

**THE UNIVERSITY OF SHEFFIELD**



**Brushless Doubly-Fed Reluctance Machines for Aerospace Electrical Power  
Generation Systems**

**By**

**Alexander Duke**

**A Thesis submitted for the degree of  
Doctor of Philosophy in the Department of  
Electronic and Electrical Engineering,  
The University of Sheffield.**

**November 2015**

## ABSTRACT

This thesis describes a programme of research encompassing the design, optimisation and experimental testing of a brushless doubly fed reluctance machine (BDFRM) for use as an aerospace electrical generator, specifically a direct line connected generator, to widen the input shaft speed beyond the normal constraints imposed by the 360-800Hz specification for a variable-frequency AC aerospace network.

BDFRMs offer the functionality of frequency correction, via a control winding, and have the advantage of using a robust reluctance rotor. A partially-rated control winding converter can, in principle, be used to provide the slip power required. A further advantage of the BDFRM is the inherent fail-safe nature of these machines, with the output voltage collapsing as soon as the control winding current has been removed.

A synchronous reluctance machine was studied as a means of providing a baseline for the BDFRM performance, including a comparison of the effect of scaling on power density.

A large number of time-stepped finite element simulations were undertaken to explore BDFRM performance, in particular, the influence of magnetic saturation in limiting the achievable power density and in compromising power quality. Detailed optimisation of a BDFRM was undertaken, including systematic mechanical design of the rotor for high speed operation. This analysis illustrates the significant compromises in machine electromagnetic performance which result from the need to accommodate mechanical stress.

The scope for employing small amounts of permanent magnet material in the rotors of both synchronous reluctance machines and BDFRMs, to improve the machine performance at the lower end of the current density range, was investigated.

Following detailed optimisation, a demonstrator machine was manufactured, which includes a skewed rotor. The performance of this machine was measured at a

number of test points to verify predictions of output power, voltage and voltage harmonics.

## **ACKNOWLEDGMENTS**

I would like to express my gratitude towards Geraint Jewell for being a vigilant supervisor and providing guidance and support throughout my PhD.

Without the financial support of the Engineering and Physical Sciences Research Council and Rolls-Royce, this PhD would not have been possible, so I am very grateful for their backing.

I would also like to thank the secretarial and technical staff in the EMD group and EEE department for their friendly advice and help during building of the demonstrator.

Thank you to my friends in the UTC and wider EMD group for their invaluable support in both technical and social matters.

Thank you to my friends for keeping the good times rolling throughout the challenging times of my PhD.

Finally, I would like to thank my parents and Miriam for keeping my head above water and for their excellent proofreading skills.

# CONTENTS

Abstract.....	ii
Acknowledgements.....	iv
Contents.....	v
Nomenclature.....	xii
<b>1 Chapter 1 – Introduction .....</b>	<b>1</b>
1.1 The More-Electric Aircraft .....	1
1.2 Methods for Increasing the Speed Range of the Generator .....	3
1.3 Scope and Contribution of the Thesis.....	7
1.4 References .....	11
<b>2 Chapter 2 – A Review of Electrical Machines with Controllable Output     Frequency.....</b>	<b>13</b>
2.1 Introduction .....	13
2.2 Cascaded Machines .....	13
2.3 Self-Cascaded Machines .....	16
2.4 Doubly-Fed Induction Generator.....	19
2.5 Brushless Doubly-Fed Machines.....	20
2.6 Brushless Doubly Fed Reluctance Machines .....	21
2.7 Control of BDFRMs.....	24
2.7.1 Scalar Control.....	24
2.7.2 Vector Control.....	24
2.7.3 Direct Torque Control .....	26
2.7.4 Torque and Reactive Power Control.....	26
2.8 BDFRM Design Considerations .....	27
2.8.1 Stator Core Features .....	27

2.8.2	Windings and Pole Numbers .....	27
2.8.3	Rotor Design .....	28
2.9	Electromagnetic Operation of the BDFRM .....	31
2.9.1	Winding Functions .....	32
2.9.2	Analytical Model of a Grid Connected BDFRM .....	35
2.9.3	Net MMF Distribution of a Grid Connected BDFRM .....	36
2.9.4	Accounting for Permeance Modulating Effect of the Salient Rotor .....	37
2.9.5	Analytical Model of a Non-Grid Connected BDFRM .....	44
2.10	Chapter 2 Summary .....	46
2.11	References .....	47
<b>3</b>	<b>Chapter 3 – The Synchronous Reluctance Machine as a Baseline Design .....</b>	<b>52</b>
3.1	Introduction .....	52
3.2	Rotor Optimisation .....	54
3.3	Baseline SyncRel Design .....	54
3.4	Airgap Flux Density Harmonics .....	62
3.5	SyncRel Scaling Study .....	64
3.6	Addition of Permanent Magnets to the Baseline SyncRel Design .....	65
3.7	Mechanically Optimised Rotor Design .....	70
3.8	Addition of PMs to Mechanically Optimised Rotor Design .....	72
3.9	Chapter 3 Summary .....	76
3.10	References .....	77
<b>4</b>	<b>Chapter 4 – Investigation of BDRFM Attributes and Design Features .....</b>	<b>78</b>
4.1	Introduction .....	78
4.2	Baseline Dimensions .....	78
4.3	Assessment of Rotor Geometries .....	80
4.3.1	Reference Machine and Rotor Designs .....	81

4.3.2	Comparison of Power Winding Voltage Magnitude at a Given Control Current Density .....	82
4.3.3	Comparison of Harmonic Content of Power Winding Voltage Waveforms.....	83
4.3.4	Comparison of Modulation of Mutual Inductance.....	85
4.4	Assessment of Alternative Pole Number Combinations .....	88
4.5	Scaling of BDFRM Performance with Rating and Size .....	92
4.6	Finite Element Investigation of Airgap Flux Density Harmonics.....	96
4.6.1	Airgap Fields with No Rotor Saliency.....	97
4.6.2	Airgap Fields with Rotor Saliency .....	100
4.7	Doubly Salient BDFRM Variants.....	106
4.7.1	Three-Phase Variants.....	106
4.7.2	Single-Phase Variants.....	108
4.8	Chapter 4 Summary .....	112
4.9	References .....	113
<b>5</b>	<b>Chapter 5 – Electromagnetic and Mechanical Optimisation of the Baseline BDFRM .....</b>	<b>114</b>
5.1	Optimisation Methodology.....	114
5.2	Selection of Stator and Rotor Core Material .....	116
5.3	Optimisation of Stator Geometry .....	117
5.3.1	Stator Winding Configuration.....	117
5.3.2	Selection of Slot Depth .....	117
5.3.3	Optimisation of Back-Iron Thickness .....	117
5.3.4	Stator tooth features .....	118
5.4	Optimisation of Rotor Geometry.....	120
5.4.1	Rotor Pole Width .....	120

5.4.2	Shaft Diameter .....	122
5.4.3	Bridges Across Flux Barriers.....	122
5.4.4	Optimisation of the Number of Rotor Flux Guides.....	122
5.4.5	Optimisation of the Relative Width of Rotor Flux Guides and Barriers.....	126
5.5	Rotor Bridge Saturation .....	127
5.6	Mechanical Optimisation of the Rotor .....	131
5.7	Power and Control Winding Design.....	142
5.7.1	Selection of the Number of Control Winding Turns .....	142
5.7.2	Selection of the Number of Power Winding Turns.....	143
5.7.3	Selection of the Relative Alignment Between the Two Windings.....	144
5.8	Final Design Operating Points.....	145
5.8.1	End Winding Inductance.....	146
5.8.2	Sampling Frequency Optimisation.....	147
5.8.3	Load Resistance Calculation.....	148
5.9	Rotor Skew .....	149
5.9.1	Skew Test Point at 4,320rpm .....	149
5.9.2	Skew Test Point at 4,860rpm .....	153
5.9.3	Skew Test Point at 9,000rpm .....	155
5.9.4	Skew Test Point at 13,200rpm.....	157
5.9.5	Skew Test Point at 14,400rpm.....	159
5.10	Final Simulation of Performance for the Optimised Design.....	163
5.11	Calculation of Losses and Efficiencies.....	163
5.11.1	Method for Calculating Copper Loss .....	164
5.11.2	Method for Calculating Iron Loss.....	165
5.11.3	Predicted Efficiencies.....	167



5.11.4	Control Winding Reactive Power Requirements .....	167
5.12	Further Studies .....	169
5.12.1	Substitution of Silicon Iron by Cobalt Iron .....	169
5.12.2	Addition of PMs to the BDFRM Rotor .....	170
5.13	Summary of Chapter 5 .....	173
5.14	References .....	176
<b>6</b>	<b>Chapter 6 – Build, Test and Analysis of a BDFRM Demonstrator .....</b>	<b>177</b>
6.1	Introduction .....	177
6.2	Demonstrator Manufacture .....	177
6.2.1	Rotor and Stator Cores .....	177
6.2.2	Stator Winding .....	178
6.2.3	Rotor Shaft .....	183
6.2.4	Machine Casing .....	185
6.3	Testing Facility .....	188
6.3.1	AVL APA 102 Dynamometer .....	189
6.3.2	Load Bank .....	190
6.3.3	Power Winding Voltage and Current Measurement .....	191
6.3.4	Control Winding Power Converter .....	192
6.3.5	Signal Conditioning .....	195
6.4	Baseline Performance Measurements .....	197
6.4.1	Test Point at 20% Below Synchronous Speed Range (4,320 rpm) .....	198
6.4.2	Test Point at 20% Above Synchronous Speed Range (14,400rpm) .....	202
6.5	Comparison of Measured Results with Finite Element Predictions .....	205
6.5.1	Operating Point at 13,200rpm .....	206
6.5.2	Operating Point at 4,860rpm .....	210
6.6	Further Investigation of Power Winding Sub-Harmonics .....	213

6.6.1	Influence of Control Winding Current on Power Winding Subharmonic at 4,860rpm.....	214
6.6.2	Influence of Control Winding Current on Power Winding Subharmonic at 13,200 rpm.....	219
6.6.3	Influence of Speed and Control Frequency on Subharmonics .....	220
6.6.4	Influence of Control Frequency Variations on Subharmonic Content	222
6.7	Investigation into Synchronous Performance .....	224
6.8	Operation at a VF Standard Operating Point.....	234
6.8.1	Thermal Characteristics of Example Operating Point.....	236
6.9	Summary of Chapter 6 .....	240
6.10	References .....	242
<b>7</b>	<b>Chapter 7 – Conclusions .....</b>	<b>243</b>
7.1	Summary of Key Findings.....	243
7.1.1	SyncRel – Influence on Performance of Rotor Flux Bridge Geometry	243
7.1.2	SyncRel – Influence of Dimension Scaling .....	243
7.1.3	BDFRM – Behaviour on a Non-Stiff AC Network .....	243
7.1.4	BDFRM – Demonstration of Limited Power Capability .....	244
7.1.5	BDFRM – Presence of Significant Second Harmonic when Operated in Synchronous Mode .....	244
7.1.6	BDFRM – Saturation Induced Sub-Harmonics .....	244
7.1.7	BDFRM – Incorporation of Permanent Magnets in SyncRel and BDFRM Rotors.....	245
7.1.8	Comparison of BDFRM Power Density with SyncRel Machines .....	245
7.1.9	Comparison of a Conventional Singly-Salient BDFRM with a Doubly-Salient Variant.....	245
7.1.10	BDFRM – Scaling Effects.....	245
7.1.11	BDFRM – Optimisation of the Number of Flux Guides .....	246

7.1.12	BDFRM – Mechanical Optimisation of the Rotor .....	246
7.1.13	BDFRM – Loss Audit .....	246
7.1.14	Influence of Rotor Skewing.....	246
7.2	Key Overall Conclusion .....	247
7.3	Proposals for Further Research .....	247
<b>8</b>	<b>Appendices .....</b>	<b>249</b>
8.1	Appendix 1 – Finite Element Analysis.....	249
8.2	Appendix 2 – Fourier Transform.....	252
8.3	Appendix 3 – Design Specification.....	254
8.4	Appendix 4 – Final Design Parameters .....	255
8.5	Appendix 5 – BDFRM Rotor and Shaft Technical Drawing .....	256
8.6	Appendix 6 – BDFRM Stator Technical Drawing.....	257
8.7	Appendix 7 – BDFRM Casing Technical Drawing .....	258

## NOMENCLATURE

$A$	Area ( $m^2$ )
$B_{c,p}$	Airgap flux density caused by the control, power windings (T)
$B_{pk}$	Peak flux density (T)
$\mathcal{F}_c$	Total MMF of control winding (A·Turns)
$\mathcal{F}_{ca,cb,cc}$	MMF of control winding phase A, B, C (A·Turns)
$\mathcal{F}_p$	Total MMF of power winding (A·Turns)
$\mathcal{F}_{pa,pb,pc}$	MMF of control winding phase A, B, C (A·Turns)
$f$	Frequency (Hz)
$G$	Peak of the inverse airgap function
$g^{-1}$	Inverse airgap function
$i_a$	Phase A current (A)
$i_b$	Phase B current (A)
$\hat{I}_c$	Peak control winding current (A)
$i_{ca,cb,cc}$	Control winding phase A, B, C current (A)
$\hat{I}_p$	Peak power winding current (A)
$i_{pa,pb,pc}$	Power winding phase A, B, C current (A)
$i_{cd}$	Control winding d-axis current (A)
$i_{cd}^*$	Reference control winding d-axis current (A)
$i_{cq}$	Control winding q-axis current (A)
$i_{cq}^*$	Reference Control winding q-axis current (A)
$J_{Max}$	Maximum current density ( $A_{rms}mm^{-2}$ )
$J_{Meas}$	Measured current density ( $A_{rms}mm^{-2}$ )
$K_{Sq}$	Skew factor
$k_{hys}$	Hysteresis loss constant ( $W/Hz/T^n$ )
$k_{anom}$	Anomalous loss constant ( $W/Hz^2/T^2$ )
$l$	Length (m)

$L_c$	Inductance in control winding (H)
$L_d$	D-axis inductance (H)
$L_{pc}$	Inductance in the power winding due to the control winding (H)
$L_p$	Inductance in the power winding (H)
$L_q$	Q-axis inductance (H)
$N$	Number of minor loops in iron loss calculation
$n_c$	Control winding number of turns
$n_p$	Power winding number of turns
$P_c$	Control winding poles
$P_{anom}$	Anomalous power loss density ( $W/m^3$ )
$P_{control}$	3-phase control winding power (W)
$P_{CuLoss}$	Total two winding 3-phase copper loss (W)
$P_{eddy}$	Eddy current power loss density ( $W/m^3$ )
$P_{hyst}$	Hysteresis power loss density ( $W/m^3$ )
$P_{iron}$	Iron power loss density ( $W/m^3$ )
$P_{load}$	3-phase load power (W)
$P_{mech}$	Mechanical power (W)
$P_{out}$	Output power (W)
$P_p$	Power winding poles
$P_{pc}$	Control winding pole pairs
$P_{power}$	3-phase power winding power (W)
$P_{pp}$	Power winding pole pairs
$P_r$	Number of rotor poles
$Q_p$	Power winding reactive power (VAr)
$Q_p^*$	Reference power winding reactive power (VAr)
$R$	Resistance ( $\Omega$ )
$S$	angle of skew ( $^\circ$ )
$T$	Time period of waveform (s)

$t$	Time (s)
$T_e$	Electromagnetic torque (Nm)
$T_e^*$	Reference electromagnetic torque (Nm)
$v$	Harmonic order
$V_{pa,b}$	Power winding phase A, B voltage (V)
$V_s$	Stator voltage as a vector (V)
$W_{ca,cb,cc}$	Control winding phase A, B, C winding function
$W_{pa,pb,pc}$	Power winding phase A, B, C winding function
$\alpha$	Offset between the control and power winding currents ( $^\circ$ )
$\alpha_{cu}$	Thermal coefficient of copper ( $K^{-1}$ )
$\alpha_p$	Pole pitch of the winding ( $^\circ$ )
$\gamma$	Rotor offset from the d-axis to phase A of the control winding ( $^\circ$ )
$\delta$	Angle between control and power winding flux ( $^\circ$ )
$\delta_{lam}$	Lamination thickness (mm)
$\Delta B_i$	Amplitude of the $i$ th minor loop in iron loss calculation (T)
$\Delta T$	Change in temperature (K)
$\theta$	Spatial angle ( $^\circ$ )
$\theta_c$	Control offset angle ( $^\circ$ )
$\theta_p$	Power offset angle ( $^\circ$ )
$\theta_{rm}$	Rotor mechanical angle ( $^\circ$ )
$\lambda_c$	Flux in the control winding (Wb)
$\lambda_{cd}$	Flux in the d-axis control winding (Wb)
$\lambda_{cq}$	Flux in the q-axis control winding (Wb)
$\lambda_p$	Flux in the power winding given by $\lambda_{pd} + j \cdot \lambda_{pq}$ (Wb)
$\mu_0$	Permeability of free space ( $N/A^2$ )
$\rho$	Resistivity of copper ( $\Omega m$ )
$\rho_{Max}$	Maximum resistivity ( $\Omega m$ )

$\rho_{\text{Meas}}$	Measured resistivity ( $\Omega\text{m}$ )
$\sigma$	Conductivity of lamination material ( $\text{Sm}^{-1}$ )
$\phi$	Angle between the control and power winding flux ( $^{\circ}$ )
$\omega_c$	Control winding angular velocity ( $\text{rads}^{-1}$ )
$\omega_p$	Power winding angular velocity ( $\text{rads}^{-1}$ )
$\omega_{\text{rm}}$	Rotor mechanical angular velocity ( $\text{rads}^{-1}$ )
$\omega_{\text{rm}}^*$	Rotor mechanical angular velocity reference ( $\text{rads}^{-1}$ )
$\omega_s$	Angular velocity of stator current ( $\text{rads}^{-1}$ )

# 1 CHAPTER 1 – INTRODUCTION

---

## 1.1 THE MORE-ELECTRIC AIRCRAFT

The concept of the so-called more-electric aircraft (MEA), in which electrical systems increasingly displace hydraulic, pneumatic and mechanical systems, has received much attention over the past twenty years [1]. Replacing these traditional systems with an electrical alternative can lead to improvements in efficiency, flexibility, reliability and reduce maintenance downtime. These benefits in turn lead to a reduction in operating costs and fuel burn, both factors which are critical to the commercial success of future civil aircraft.

Electrical systems can in principle be used to replace many different systems on an aircraft, with several such systems now in service and many more at various stages of research and testing. One early success story is the use of a combined electrical starter/generator in the Boeing 787 to start the gas turbine in place of the traditional approach of an air turbine starter [2]. This method eliminates the previously required air turbine starter and the pipework from the auxiliary power unit in the tail section to the main engines. One challenge in this application is to ensure that the machine is capable of efficient generating during normal operating conditions, yet produces sufficient torque to rotate the spools from standstill up to ignition speeds under worst-case 'cold-start' conditions.

Another important area of MEA research is the use of electrical machines to control primary and secondary flight surfaces, braking and landing gear. Historically these have been exclusively hydraulic systems but recent developments in electromechanical and electro-hydraulic actuators (EMAs and EHAs) have led to the replacement of purely hydraulic systems. In the recently launched Boeing 787, EMAs have been used for braking the aircraft and EHAs are used for various backup systems throughout the aircraft [3].

Taxiing around an airport is a large inefficiency in the operation of an aircraft which produces excess noise, fuel burn, emissions and wear in the aircraft brakes. Brake wear in particular is a concern given that brake maintenance is a costly element of



operating an aircraft. It has been suggested that using an electrical machine in the hub of an aircraft wheel could effectively mitigate all the aforementioned problems with taxiing [4]. Although earlier designs used clutches to engage the machine, newer designs now use direct drive permanent magnet machines [5, 6].

Main engine generator major enabling technology in the MEA is a high efficiency and high power density electrical generator. Even without electric taxiing and full electro-mechanical control surface actuation, neither of which have been adopted on commercial aircraft to date, the electrical loads associated with the adoption of some elements of the MEA has led to the generator ratings continuing to rise, e.g. 4 x 250kVA generators on the Boeing 787. Historically, all aircraft were supplied with fixed 400Hz AC by the engine generators. This was achieved by regulating the input speed to the generator with a hydro-mechanical device. This constant speed generator configuration is referred to as an integrated drive generator (IDG). Since the lifetime of aircraft in service is often several decades, IDGs are still widely used in service today.

However, IDGs are inefficient and require regular maintenance and as the power ratings gradually increased and the maintenance intervals of other engine components lengthened, there was increasing pressure to move away from IDGs and fixed AC supplies. This led in the 1990s [7] to the adoption of variable frequency AC (VFAC) supplies in which the frequency is allowed to vary between 360Hz and 800Hz. This frequency range allowed the supply to be produced by directly coupling a synchronous generator to the high-pressure (HP) shaft of an aircraft engine. VFAC supplies are now the standard approach to electrical networks on all new civil aircraft designs with all new airframe equipment being compatible.

However, whereas the 2.1:1 speed range permitted by the VFAC standard is more than adequate for engines which take power off the HP shaft, it can restrict the thermodynamic performance of an engine which takes power off the intermediate pressure (IP) shaft. In such cases, allowing the speed range to vary to around 2.6:1 could offer significant benefits.

## 1.2 METHODS FOR INCREASING THE SPEED RANGE OF THE GENERATOR

There are a number of key options for eliminating the stringent operating condition of the grid frequency effectively being locked to the shaft speed of the generator.

Epicyclic drive trains provide a compact and therefore high power dense solution to gearing. Although the dominant use of these drive trains is for fixed ratio applications, certain modifications can accommodate variable gear ratios. Planetary change-gears can be used to step change the gear ratio by the use of brakes to stop certain planetary systems from rotating [8].

Alternatively, a variable bicoupled transmission may be used which typically uses a variable displacement pump to allow for an infinitely variable speed ratio [8].

An alternative to requiring a fully rated converter is to only provide the required slip power to the system. This may be achieved with a powered epicyclic gearbox where the ring gear is mechanically driven by a variable speed motor, as seen in Figure 1.1. The drive to power the ring gear motor would only have to be rated to the amount of speed correction required by the epicyclic gearbox. This allows direct connection of the generator to the aircraft grid without any intermediate electronics, thus increasing system efficiency. This method requires a bulky epicyclic gear and a second electrical machine which adds both weight and mechanical complexity to the system. As with all mechanical systems, epicyclic gears tend to require lubrication and regular maintenance.

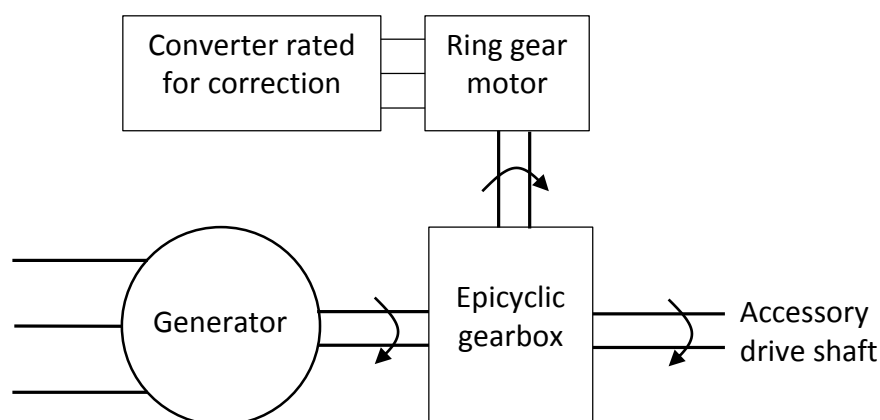


Figure 1.1 – Block diagram of a powered epicyclic gearbox arrangement

One option to increase the speed range mechanically within an electrical machine is to use a pole-changing arrangement of coils. Pole changing in induction machines has been studied since the end of the 19<sup>th</sup> century [9-11] with further development in the mid-20<sup>th</sup> century wherein pole changing was split into three major groups.

The simplest and oldest of these is the Dahlander winding configuration where a set of mechanical switches are used to switch between a delta and star connected winding configuration (Figure 1.2). In doing so the pole number of the winding can be changed in a ratio of 1:2. The major disadvantages to this design are the requirement of mechanical switches which require regular maintenance and the discontinuous nature of the pole changing which would lead to an inevitable duration of zero power. Dahlander winding configurations have seen an interest recently in new applications such as wide speed range aircraft generators [9]. In this application, conventional fixed pole machines would struggle with the large speed range requirements of a 360-800Hz aircraft grid which corresponds to a minimum to maximum speed range of 1:2.22. By using a Dahlander winding with 2 and 4 pole-pair windings, this large frequency range was realised (Figure 1.3). In this case, if a single 4-pole or 8-pole winding is used, only a 1:2 speed range can be achieved. By pole-changing between the 4- and 8-pole windings it is possible to achieve a 1:4.44 speed range whilst remaining within the 360-800Hz range. Changing the pole number in this particular case must occur anywhere between the speeds of 10,800rpm and 12,000rpm to remain between the 360Hz and 800Hz frequency limits. It was also shown that current spikes following the switching event managed to remain within aircraft standards.

Kocabas et al. [12] produced a MATLAB model to view the amount of energy that could be regenerated to the grid whilst transitioning from a lower to a higher pole number and therefore higher to lower speed.

Ionescu et al. [13] have recently used an induction machine with a Dahlander winding to model the effect of single and double layer windings on acoustic noise, demonstrating the continued interest in employing these winding configurations over a century after their first development.

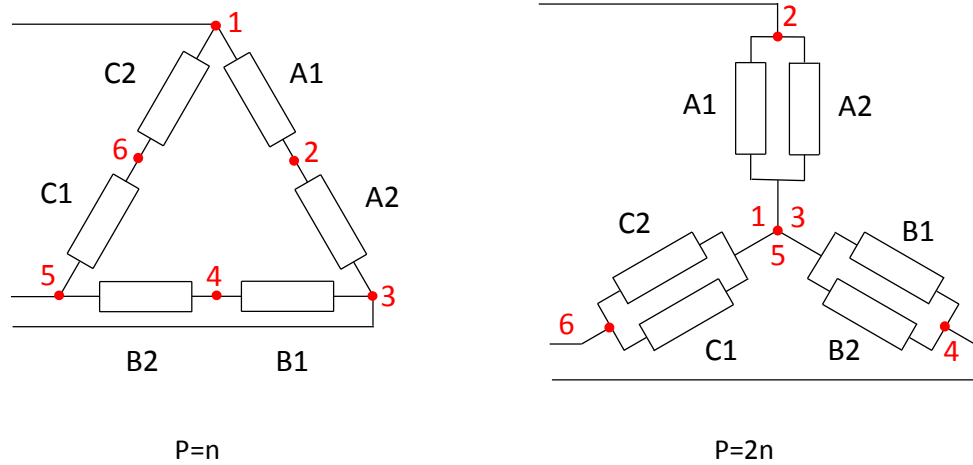


Figure 1.2 – Dahlander winding configuration with differing pole number (P)

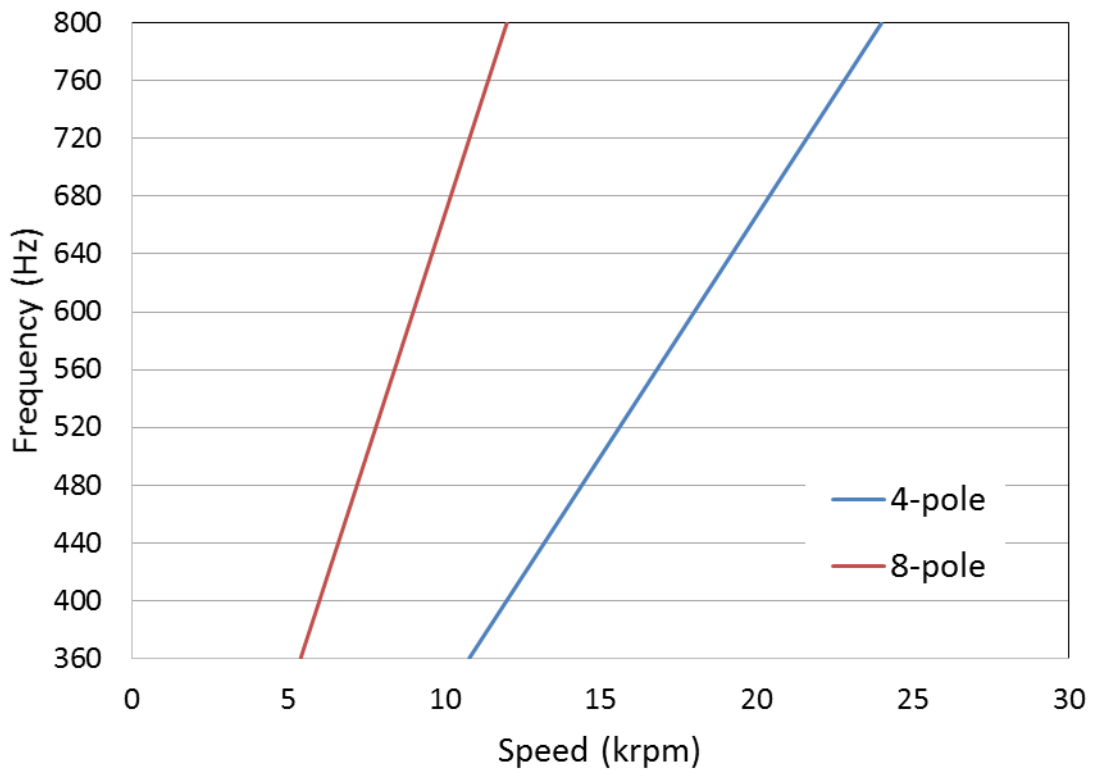


Figure 1.3 – Dahlander winding used on an aircraft grid speed characteristics with a pole change between a 4 and 8-pole winding

The second version of pole changing winding is the pole amplitude modulation (PAM) winding [14]. In this case the pole number is adjusted electromagnetically within the machine by means of adjusting the MMF distribution with a modulating signal [15]. Although speed ratios of 1:3 have been achieved [16], poor copper utilisation is seen as a major downfall of these windings.

The last of the pole-changing winding configurations is pole phase modulation (PPM), which like PAM adjusts the MMF distribution, but in this case, the phase is also modulated [17]. This leads to even higher speed ratios of 1:5 [16], which may be utilised in a range of applications such as electric vehicles.

Both PAM and PPM have the advantage of a Dahlander configuration of being capable of continuous pole-changing. This eliminated the dead period found in Dahlander connected machines while the mechanical switches are adjusted.

Within the last decade a new method of transmitting power at variable gear ratios has emerged. This started with the advent of the magnetic gearbox as patented by Martin in 1964 [18]. One method of operating the magnetic gearbox as a variable speed drive train was to control the speed of the external rotor. This was first verified by Shah et al. in 2011 [19] by using external machines to control this rotor speed.

More recently this design has been improved with the addition of a stator and coils to the outside of the actual magnetic gear [20], thereby removing the need for external machines to control the rotor speed.

These variable speed magnetic gears have been discussed for use in wind turbines and electric vehicles [19, 20]. In fact, some companies such as Magnomatics have begun commercialising these designs as a more power dense gearbox in electric vehicles, with their only major detriment being cost when compared to a standard geared system.

For a purely electrical solution, a back-to-back converter topology, as seen in Figure 1.4, could be used to completely decouple the shaft speed of the generator to the aircraft grid electrical frequency. The major disadvantage of this configuration is the necessity to use two fully rated converters alongside a standard synchronous generator. As well as increasing the weight of the overall system, the component count is also doubled which could potentially lead to reliability issues.

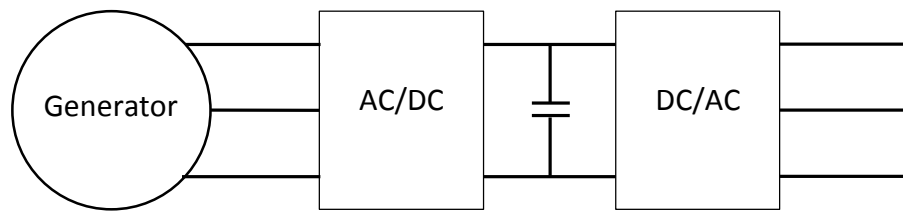


Figure 1.4 – Block diagram of a typical back-to-back converter generator arrangement

An alternative to mechanically adjusting the speed entering the generator is to allow the generator to rotate over the full speed range and electrically adjust the net output frequency within the machine by inclusion of a separate control winding and a partially rated power converter. Examples of such doubly-fed electrical machines are the doubly-fed induction generator (DFIG), the brushless doubly-fed machine (BDFM) and the brushless doubly fed reluctance machine (BDFRM). Although DFIGs are very popular in wind turbine applications, the presence of brushes and modest power densities make these unattractive for aerospace applications. One alternative is to re-locate the windings from the rotor to the stator and use a squirrel cage rotor as in the brushless doubly-fed machine (BDFM). However, the BDFM tends to suffer in terms of rotor losses in the windings and unstable operating points. The brushless doubly fed reluctance machine (BDFRM) successfully addresses all these problems by replacing the windings in the rotor with a simple reluctance rotor design.

The major benefit of these types of machine is the possibility of running the aero engine at lower speeds during some intervals in the aircraft mission cycle and using the frequency correction capability of the BDFRM to remain above the 360Hz lower threshold.

### 1.3 SCOPE AND CONTRIBUTION OF THE THESIS

This thesis explores various aspects of the behaviour and design of BDFRMs for the particular application of widening the speed range of an aerospace generator (of the order of 10-15% at either end of the VF frequency range). At various points in this thesis, additional studies are performed in parallel to the central theme, including

the addition of PM material to the rotor to aid pre-saturation and discovering the influence of saturation on voltage harmonics.

This thesis is organised as follows:

### **Chapter 2 – A Review of Electrical Machines with Controllable Output Frequency**

This chapter reviews the chronological progression of the doubly fed reluctance machine from its origins as a cascaded machine through to BDFRMs. A brief introduction to the control strategies of both brushed and brushless doubly fed machines is presented, followed by design principles for the BDFRM such as the design of the rotor and windings. A detailed section on the analytical model for the BDFRM is developed which aids in building an understanding of the complex operating conditions of the machines. Following this, a review of alternative technologies to provide frequency correction is completed as well as a brief review of control techniques for doubly-fed machines.

### **Chapter 3 – The Synchronous Reluctance Machine as a Baseline Design**

The airgap flux density of a SyncRel is analysed to provide an insight in to the prevalent harmonics for comparison to those found in the BDFRM. An inductance study is also performed to view the effect of rotor design on the torque producing capability of the SyncRel. A scaling study is then completed to view the effect of increasing the linear dimensions on power and torque densities to compare at a later stage with a scaled BDFRM. Finally, PMs are added to the rotor to view the effect on the output behaviour of the SyncRel.

### **Chapter 4 – Investigation of BDFRM Attributes and Design Features**

This chapter provides a study into various design aspects of the BDFRM, beginning with an introduction to the Fourier analysis method used throughout this thesis. A comparison between rotor topologies follows including their effect on saturation. An alternative pole number combination is then considered including a linear dimension study of this design. Doubly salient variants of the BDFRM are studied with a view to increasing the power. The baseline BDFRM is then put through a linear dimension scaling study and compared to both the SyncRel and the alternative pole number

combination. The airgap flux density harmonics of the BDFRM are then studied under various scenarios. This chapter is completed with a study into the arrangement of rotor flux barriers with respect to the rotor periphery.

#### **Chapter 5 – *Electromagnetic and Mechanical Optimisation of the Baseline BDFRM***

The baseline BDFRM design is optimised in terms of electromagnetic and mechanical considerations including a detailed design study into the rotor internal structure. The winding design including the selection of the number of turns is completed and followed by calculations of the various losses in the BDFRM. A final design is then down-selected and used to calculate the inductance and required load resistance to provide the necessary voltage and power. The rotor is then replaced with a design with a one stator slot pitch skew to reduce slotting harmonics and allow the voltage harmonics to fit within strict aerospace standards. This chapter is completed with a brief study into the replacement of lamination material as well as a look into how the addition of PMs could improve the electromagnetic operation of the machine.

#### **Chapter 6 – *Build, Test and Analysis of a BDFRM Demonstrator***

This chapter follows the build and test procedure of the demonstrator BDFRM. The test results are commented upon and compared to the finite element results obtained in preceding chapters. The subharmonics in the power winding voltage of the test machine are then studied, followed by analysis of the harmonics produced by running the BDFRM in a synchronous mode. Finally, the load bank is adjusted to provide the required output voltage with the available converter.

#### **Chapter 7 – *Conclusions***

The thesis is brought together with conclusions found in each chapter as well as ideas for further studies to be completed on this research vein.

The novel aspects of this thesis are detailed as follows:

1. The use of brushless doubly fed reluctance machines in aerospace applications as a direct replacement of the IDG



2. The design, optimisation, build and test of a BDFRM rather than the use of a stator from an alternative machine topology
3. Test data to confirm the presence of subharmonics in the power winding voltage caused by saturation
4. The use of PMs to invoke pre-saturation in the rotor mechanical supports as a means of increasing the output power in a SyncRel
5. The use of PMs to invoke pre-saturation in the rotor mechanical supports as a means of increasing the output power in a BDFRM

## 1.4 REFERENCES

- [1] B. Sarlioglu and C. T. Morris, "More Electric Aircraft: Review, Challenges, and Opportunities for Commercial Transport Aircraft," *Transportation Electrification, IEEE Transactions on*, vol. 1, pp. 54-64, 2015.
- [2] Boeing, "AERO Quarterly publication 06," [http://www.boeing.com/commercial/aeromagazine/articles/qtr\\_4\\_06/AERO\\_Q406.pdf](http://www.boeing.com/commercial/aeromagazine/articles/qtr_4_06/AERO_Q406.pdf), 2006.
- [3] A. R. Behbahani and K. J. Semega, "Control strategy for electro-mechanical actuators versus hydraulic actuation systems for aerospace applications," *SAE Tech. Pap.*, 2010.
- [4] F. Re, "Viability and state of the art of environmentally friendly aircraft taxiing systems," in *Electrical Systems for Aircraft, Railway and Ship Propulsion (ESARS), 2012*, 2012, pp. 1-6.
- [5] T. Raminosa, T. Hamiti, M. Galea, and C. Gerada, "Feasibility and electromagnetic design of direct drive wheel actuator for green taxiing," in *Energy Conversion Congress and Exposition (ECCE), 2011 IEEE*, 2011, pp. 2798-2804.
- [6] Z. Xu, C. Tighe, M. Galea, T. Hamiti, C. Gerada, and S. J. Pickering, "Thermal design of a permanent magnetic motor for direct drive wheel actuator," in *Electrical Machines (ICEM), 2014 International Conference on*, 2014, pp. 2186-2192.
- [7] C. Jie and A. Wang, "New VF-power system architecture and evaluation for future aircraft," *Aerospace and Electronic Systems, IEEE Transactions on*, vol. 42, pp. 527-539, 2006.
- [8] H. W. Müller, *Epicyclic Drive Trains - Analysis, Synthesis and Applications*. Detroit: Wayne State University Press, 1982.
- [9] M. van der Giet and K. Hameyer, "Induction motor with pole-changing winding for variable supply frequency," in *Electric Machines & Drives Conference, 2007. IEMDC '07. IEEE International*, 2007, pp. 1484-1489.
- [10] H. Sequenz, *Die Wicklungen elektrischer Maschinen* vol. 3: Springer, 1954.
- [11] H. Auinger, *Polumschaltbare Dreiphasenwicklung mit 6 Klemmen Übersicht zum Stand der Technik* vol. 69, 1978.
- [12] D. A. Kocabas, A. K. Atalay, and H. R. Ogut, "Dynamic simulation of an induction motor having a Dahlander connected winding to calculate the total energy regained in regenerative braking," in *MECHATRONIKA, 2012 15th International Symposium*, 2012, pp. 1-4.
- [13] R. M. Ionescu, G. Scutaru, I. Peter, S. Motoasca, A. Negoita, O. Plesa, *et al.*, "The influence of the winding type on the noise level of two-speed three-phase induction motors," in *Optimization of Electrical and Electronic Equipment (OPTIM), 2012 13th International Conference on*, 2012, pp. 698-705.
- [14] G. H. Rawcliffe and W. Fong, "Speed-changing induction motors: reduction of pole number by sinusoidal pole-amplitude modulation," *Proceedings of the IEE - Part A: Power Engineering*, vol. 108, pp. 357-368, 1961.
- [15] T. J. J. Pyrhönen, V. Hrabovcová, *Design of Rotating Electrical Machines*, 2nd edition ed.: Wiley, 2014.

- [16] B. S. Umesh and K. Sivakumar, "15 phase induction motor drive with 1:3:5 speed ratios using pole phase modulation," in *Power Electronics Conference (IPEC-Hiroshima 2014 - ECCE-ASIA), 2014 International*, 2014, pp. 1400-1404.
- [17] J. M. Miller, V. Stefanovic, V. Ostovic, and J. Kelly, "Design considerations for an automotive integrated starter-generator with pole-phase modulation," in *Industry Applications Conference, 2001. Thirty-Sixth IAS Annual Meeting. Conference Record of the 2001 IEEE*, 2001, pp. 2366-2373 vol.4.
- [18] T. B. M. JR, "Magnetic Transmission," US3378710A, 1968.
- [19] L. Shah, A. Cruden, and B. W. Williams, "A Variable Speed Magnetic Gear Box Using Contra-Rotating Input Shafts," *Magnetics, IEEE Transactions on*, vol. 47, pp. 431-438, 2011.
- [20] K. Atallah, W. Jiabin, S. D. Calverley, and S. Duggan, "Design and Operation of a Magnetic Continuously Variable Transmission," *Industry Applications, IEEE Transactions on*, vol. 48, pp. 1288-1295, 2012.

## **2 CHAPTER 2 – A REVIEW OF ELECTRICAL MACHINES WITH CONTROLLABLE OUTPUT FREQUENCY**

---

### **2.1 INTRODUCTION**

As discussed briefly in Chapter 1, of the many options for narrowing the output frequency produced by a generating system, those based on electrical machines, in which the output frequency can be controlled at a given speed, offer a potentially attractive solution in terms of system simplicity and reduced weight. In many applications the fact that the output frequency of an electrical generator is directly proportional to its mechanical speed is a desirable feature, e.g. in utility grids. Such behaviour is intrinsically exhibited by all wound field and permanent magnet synchronous generators irrespective of whether they are connected to large area and stiff AC grids or small islanded AC networks.

Many different machine types have been proposed and developed in order to control output frequency and de-couple it from rotor speed. This chapter reviews the key machine types, many of which are based on old concepts, and then focusses on brushless doubly fed reluctance machines (BDFRMs) as a candidate technology for the applications described in Chapter 1.

### **2.2 CASCADED MACHINES**

With the advent of alternating current in the late 19<sup>th</sup> century, a new range of alternating current electrical machines began appearing, led primarily by the work of Tesla [1]. The cascaded machine was first developed around this time by both Steinmetz in the USA and Görge in Germany while working independently [2]. In 1893, Steinmetz filed a patent [3] with 21 claims for a cascaded induction motor with various wiring configurations. This patent also details how more than two motors may be cascaded to control the speed of rotation. Cascaded machines offer the benefit of being able to uncouple the output frequency of a machine from the shaft speed. The disadvantages of this kind of cascaded machine would have been the high

cost, low power factor, low overload capacity and low efficiency due to the large copper losses and the use of brushes.

This early version of the cascaded machine consisted of two wound field induction machines, with the rotor windings of machine one connected to the stator windings of machine two as shown in Figure 2.1. The stator windings of machine one would be directly connected to the AC mains supply, with the rotor windings of machine two connected to starting and regulating resistances. Considering the case in which the windings are connected in such a way as to allow the resultant fields to rotate in the same direction, with identical pole number, the speed of the shaft would be half that of the equivalent single machine operation. If the two machines were to have different pole numbers, with contra-rotating fields, the operating speed would be equal to a single machine operating with a pole number of the difference between the pole numbers of the two machines. For example, if four pole and ten pole machines were connected in cascade with contra-rotating fields, the machine would operate at a speed identical to that of a six pole machine.

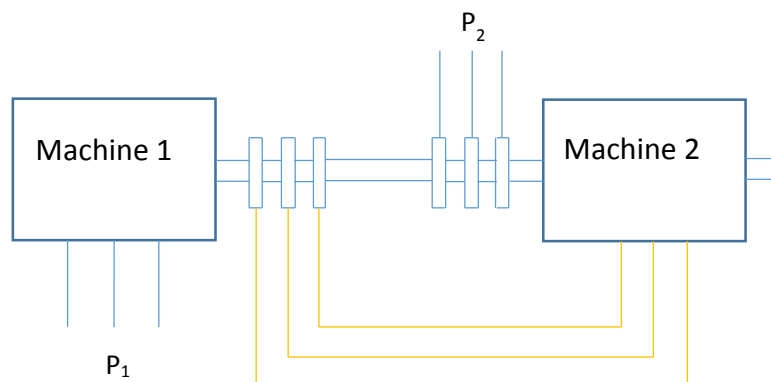


Figure 2.1 – Cascaded machine with brushes

This design could be further improved by a slight simplification of the design topology. The operational method of this type of machine was to connect two wound field induction machines mechanically to the same shaft and load (Figure 2.2). The primary (stator) windings of the first machine are connected to the supply voltage. The secondary (rotor) windings of both machines are then connected together. This allowed the slip power of the first machine to excite the second thus eliminating the

need for brushes. The stator windings of the second machine may be arranged in several ways for different desired operations. The windings could be short circuited, terminated in external resistors or supplied with variable frequency if variable speed operation was required [4].

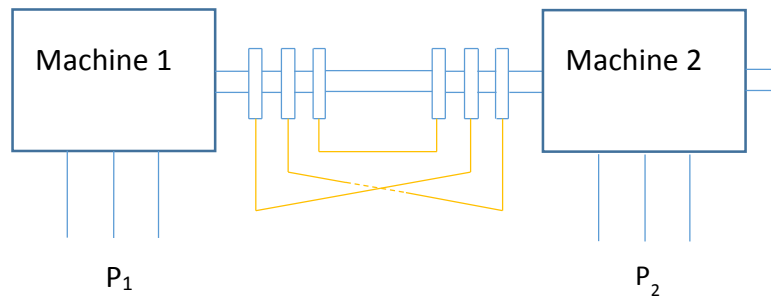


Figure 2.2 – Cascaded machine without brushes

In 1901, Thompson patented the first cascaded motor configuration to consist of only one rotor and one equivalent stator [5]. Although it seems that two separate stators are used, in reality this design consisted of one equivalent stator divided into several segments with alternating segments, carrying the primary and secondary windings. The rotor was common to both stators and consisted of distributed windings as shown in Figure 2.3.

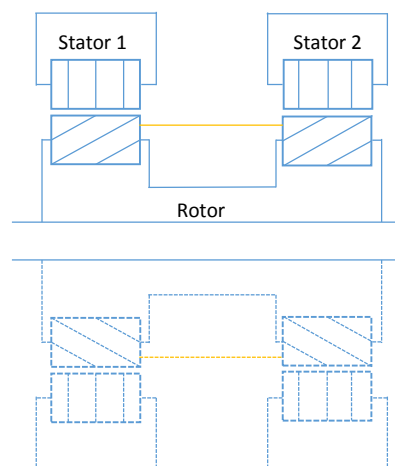


Figure 2.3 – Simplified cascaded machine design

This concept was further developed by Lydall in 1902 [6] using two sets of windings in a single stator. The problem of mutual inductance between the two windings was mitigated by using windings of different pole number. The rotor was wound in a similar way to the stator and required up to six slip rings, therefore reducing the reliability and efficiency of the machine.

### 2.3 SELF-CASCADED MACHINES

In 1907, Hunt [5] produced a detailed paper concerning a type of cascaded machine with single windings on both the stator and rotor, thereby greatly reducing the winding complexity and copper losses of these machines. A schematic of this machine is shown in Figure 2.4. The stator windings have a 6 pole pattern combined with a 3 pole. Although a very ingenious stator and rotor winding design was used, the use of slip rings and brushes meant that the Hunt motor required a regular maintenance schedule.

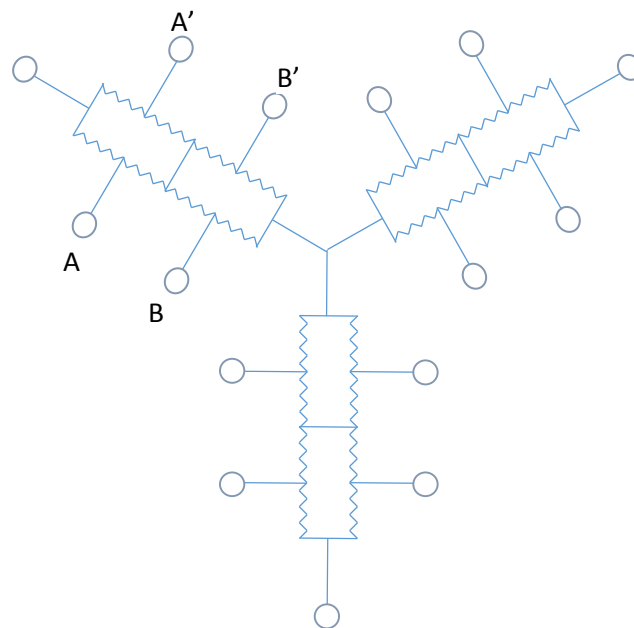


Figure 2.4 – Single stator winding of the Hunt cascaded machine

This winding layout was further improved by Creedy [7] in the 1920s by increasing the breadth of allowable pole number combinations for correct operation of the cascaded induction machine.

The Hunt motor was used extensively for low-speed long-service applications due to its high reliability. A disadvantage of this kind of motor was the double-layered irregularly grouped rotor windings, which would make the Hunt machine hard to scale down into smaller units. The Hunt motor was used as a workhorse for over half a century, before understanding and technology had progressed sufficiently to update this ageing design.

In 1970, Broadway and Burbage suggested a simpler single layer rotor winding [2], which could easily be replaced by an equivalent bar arrangement capable of supporting two fields of different pole numbers and frequencies, as shown in Figure 2.5.

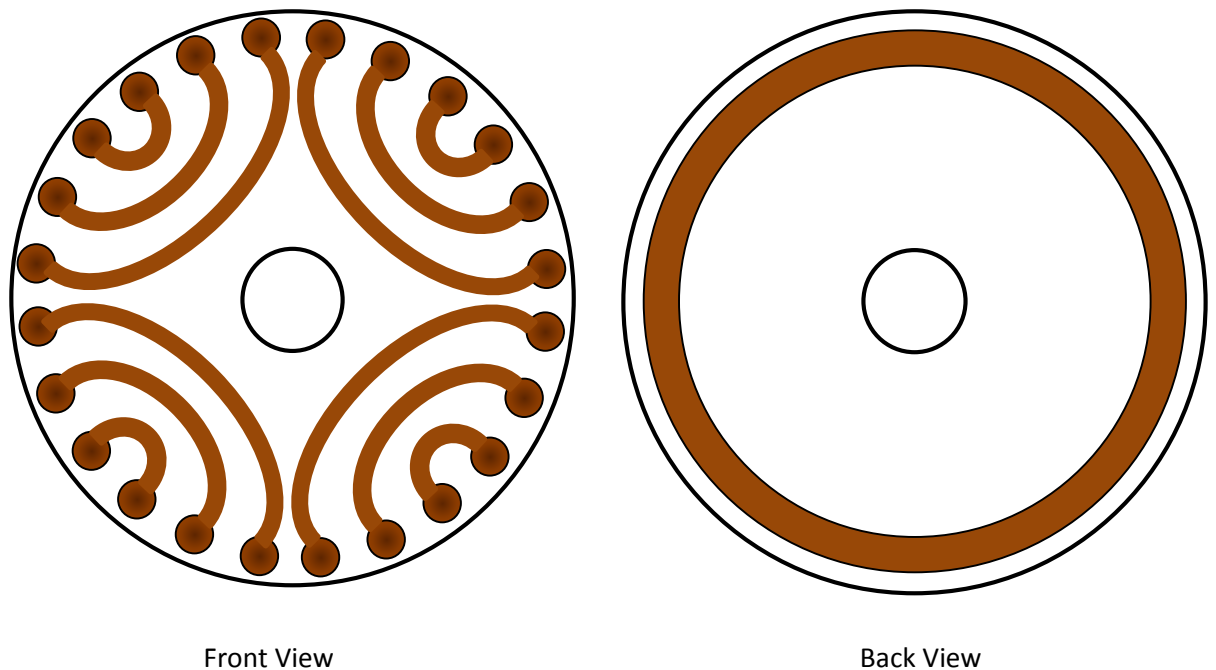


Figure 2.5 – Replacing rotor windings with bar arrangement

Broadway and Burbage also suggested a single stator winding where each phase carries a component of each of the two pole numbers used, a schematic of which is shown in Figure 2.6.



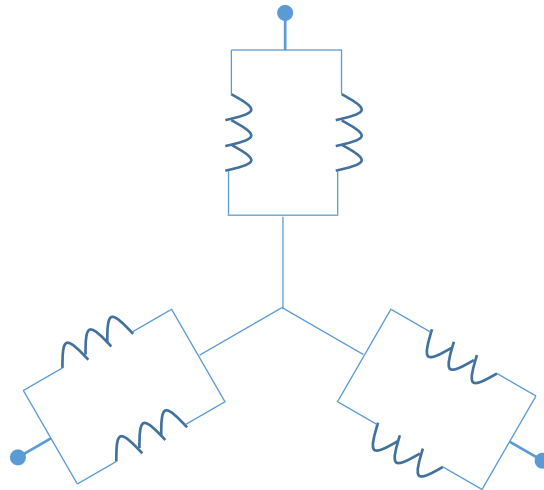


Figure 2.6 – Simplified single stator winding

Kusko and Somuah [8] constructed the equivalent of two wound rotor induction machines, built on a common set of core laminations. Two sets of 3-phase rotor windings were used to form a self-cascaded system, as shown in Figure 2.7. No slip rings or brushes were required for this design, thereby improving reliability and efficiency. The windings had to be carefully arranged and pitched so as to reduce or eliminate any undesired harmonics. As of 1978, self-cascaded induction machines could not directly compete with their conventional induction machine counterparts.

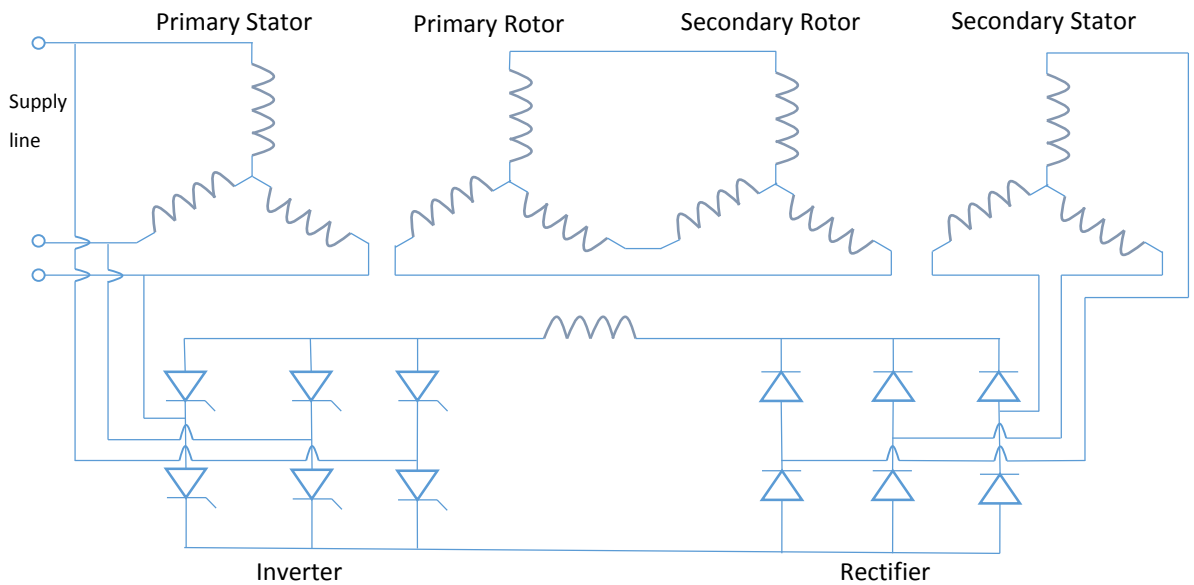


Figure 2.7 – Self-cascaded system

## 2.4 DOUBLY-FED INDUCTION GENERATOR

A major link between the standard induction machine and the BDFRM came in the form of the doubly-fed induction generator (DFIG) which is also sometimes referred to as the doubly excited wound rotor induction machine (DEWRIM). This class of machine is capable of producing a constant output frequency for a variable shaft speed input, using a partially rated power converter to supply current to the rotor windings. A disadvantage of this type of machine topology is the presence of brushes to provide this current from the partially rated converter to the rotor.

Benelghali and Charpentier [9] demonstrated the suitability of the DFIG for use in a marine tidal turbine application, and compared the performance with a PM synchronous generator (PMSG). The conclusion was that the PMSG was more suited to the application than the DFIG, owing to both a higher energy yield and a higher reliability due to the lack of brushes in the PMSG. Due to the nature of the location of many marine tidal turbines, maintenance can be a very time consuming and costly process, so a high reliability and infrequent maintenance schedule would be key to choosing a technology for this application.

Khatounian et al. [10] also published a paper concerning a PMSG and a DFIG, but this time operating in combination rather than individually as shown in Figure 2.8. In this configuration, the PMSG acts to excite the rotor windings of the DFIG via a partially rated back-to-back converter to provide power for an aircraft grid.

Although this paper concentrates on control strategies, this is one of the few papers which demonstrate the possibility of using a doubly fed machine within an airframe with an aim to reduce the rating and therefore weight of the power converter.

The DFIG has been a common choice for use in wind turbines with both fixed and variable gear ratios [11]. It was found that a DFIG configuration with either a single-stage or three-stage gearbox may be a competitive option for future wind turbines. As offshore wind turbines are becoming more prevalent, one problem with the DFIG is the maintenance required on the brushes and slip rings. In these situations, a direct drive PM generator may be better suited. However, such machines are synchronous

and therefore require a fully rated converter to produce a fixed output frequency from a variable speed input.

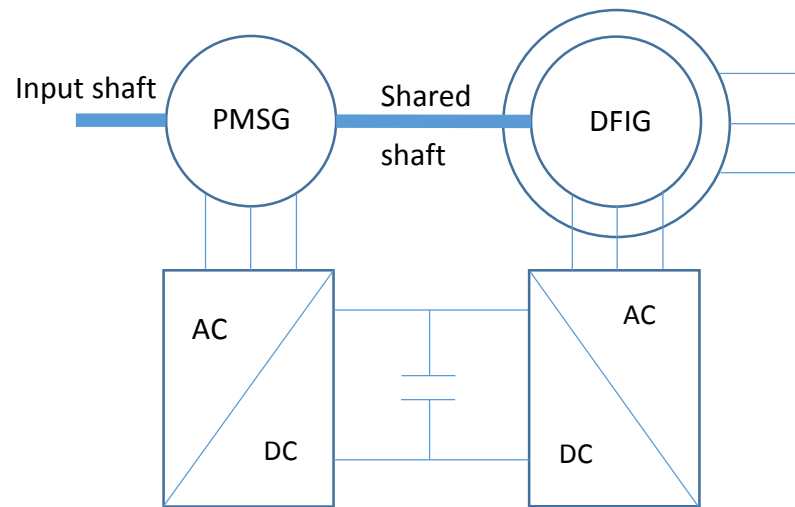


Figure 2.8 – PMSG and DFIG combination

In 2015 Feehally and Apsley [12] produced a paper on the suitability of the DFIG for use in aero generator applications. It was concluded that, even with optimised operating windows, the VA rating of the generator would have to be significantly larger than the partially rated value previously thought.

## 2.5 BRUSHLESS DOUBLY-FED MACHINES

By the late 20<sup>th</sup> century, Spee et al. [13] began exploring alternatives to adjustable speed machines, which were historically more expensive than fixed speed machines. The brushless doubly fed machine (BDFM) provided a possible solution to these cost issues. BDFMs utilise a robust cost-effective cage rotor in combination with two separate stator windings, one connected to the AC supply and the other to a partially rated power electronic converter. The rating of the converter depends upon the degree of frequency correction required. The evolution from an induction machine via a DFIG to a BDFM is shown schematically in Figure 2.9.

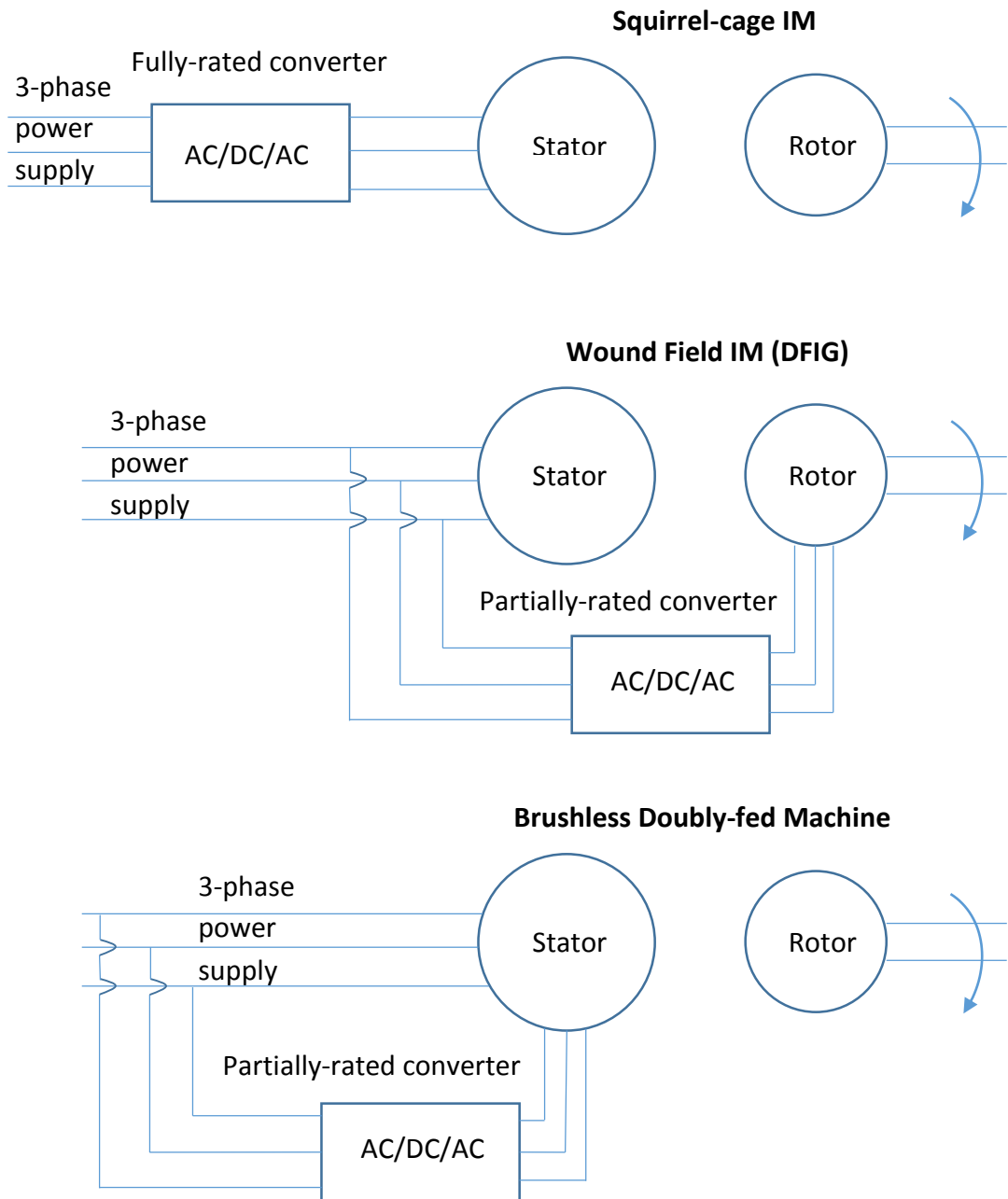


Figure 2.9 – Evolution of the induction machine to the BDFM

## 2.6 BRUSHLESS DOUBLY FED RELUCTANCE MACHINES

The Doubly Excited Reluctance Motor (DERM) emerged in 1990 which consisted of similar stator windings to the earlier Broadway designs, but using a reluctance rotor rather than a rotor winding [14]. This therefore eliminated the losses associated with rotor windings or effective rotor windings in an induction rotor.

In 1991, Xu et al. [15] proposed using Broadway's earlier design with several modifications to produce a synchronous machine. This was achieved by using only two rather than three parallel paths per phase. Synchronous operation was achieved by placing a dc source between the two star points. The doubly excited reluctance machine was found to have higher efficiencies than conventional induction machines, due to the elimination of an effective rotor winding as in the BDFM. This was the first time that doubly fed machines could directly compete with their singly fed counterparts in terms of power density.

In 2000, Betz and Jovanovic [16] compared the newly titled brushless doubly-fed reluctance machine (BDFRM) and the synchronous reluctance (SyncRel) machine, drawing several conclusions:

- The BDFRM will have a larger volume to produce the same torque as the SyncRel machine for the case of identical copper losses.
- During low torque conditions, the efficiency of the BDFRM is lower than the SyncRel machine due to the large currents required for constant flux operation.
- For a given inverter size, the BDFRM will produce twice the power of the SyncRel machine.
- To decrease the inverter rating, a maximum torque per total ampere control strategy is used but this adversely effects the torque capabilities.

Jovanovic et al. [17] in 2001 reported on the use of BDFRMs in a generating mode, adopting the terms of power and control windings for the primary and secondary stator windings respectively. Their findings indicate that a larger BDFM/BDFRM is required when compared to a standard induction machine, due to the extra winding and related flux, but the size of converter required would be significantly reduced. The BDFRM is said to have several advantages over its induction machine counterpart:

- More efficient due to lower rotor losses compared to a cage or wound rotor.
- Is likely to be able to operate at higher rotational speeds due to a more robust rotor design.

- The reluctance machine is easier to model and control due to the induction machine effectively having another winding on the rotor.
- The reluctance machine provides decoupled control of torque and reactive power to realise vector control schemes.
- Stable operation is achieved over all operating speeds (sub- and super-synchronous), whereas the induction machine experiences stability issues around the synchronous speed.

In 2002, Wang et al. [18] produced a detailed comparison between the axially laminated reluctance rotor and the cage induction rotor in the context of brushless doubly fed machines. The cage rotor was found to have superior starting and asynchronous performance, whereas the axially laminated rotor performed better at synchronous and doubly fed adjustable speed operation. Hence, the choice of rotor should be made depending upon what application the machine is required to perform. This comparison was made using the same stator winding configuration.

Variable rotor speed, constant frequency generation can be realised by combining a BDFRM with a bi-directional partially rated converter to provide a reliable and cost-effective solution. The trade-offs between generator and converter sizes will be a key factor in determining whether the BDFRM will be an attractive option for applications in the coming years [19].

BDFRMs have been proposed for use as large pumps [17] to replace the incumbent wound rotor induction machine. This leads to a partially rated converter and hence a reduction in operating costs. Using a brushless motor would also lead to a higher reliability which may make the BDFRM ideal for deep-sea oil pumps. Another potential application for BDFRMs is in large wind turbines [20-22], where energy may be harvested within a larger envelope of wind speeds and yet produce a constant output frequency.

A variant of the conventional BDFRM, proposed in [23], uses permanent magnets in the stator frame in place of the control windings. Although this leads to a reduction in total winding losses, the machine can only operate at a fixed shaft speed to output frequency relationship. This excitation method is the equivalent of feeding DC into

the control winding in a standard BDFRM. This PM design does not lend itself to increasing the shaft speed range, so will not be considered further in this thesis.

## 2.7 CONTROL OF BDFRMS

The control of BDFRMs to achieve some specified goal has received attention in published literature, and indeed is the aspect of these machines which dominates available literature. Betz and Jovanovic [24] detailed the conditions required for maximum torque per control and power ampere, as well as power factor control. In 2002, Jovanovic et al. [25] combined all of the BDFRM operating strategies into one paper.

### 2.7.1 SCALAR CONTROL

Scalar control is a suitable control technique for steady state applications such as pumps [26]. In these applications, open-loop stability problems may be mitigated due to the constant speed and therefore frequency parameters [27].

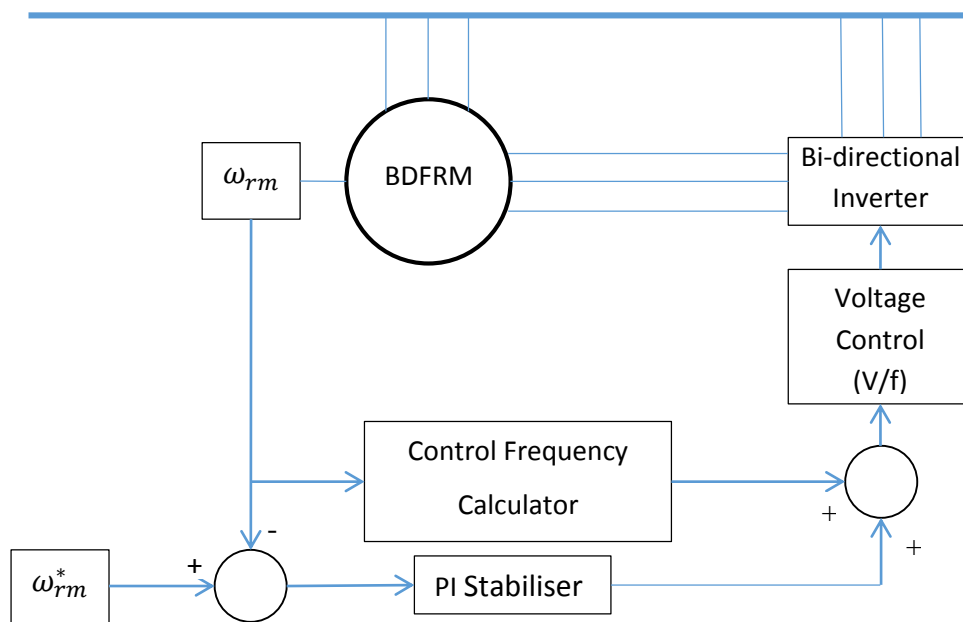


Figure 2.10 – Scalar control circuit

### 2.7.2 VECTOR CONTROL

Vector control allows faster transient response than scalar control, and is therefore more suited to dynamic systems like generators. The torque and reactive power in

the reference machine can be directly controlled using this control regime. Vector control can be realised because of the inherently decoupled control of torque and primary winding power factor [28, 29]. The control winding electromagnetic torque and real and reactive power in the BDFRM are given by:

$$T_e = \frac{P_{out}}{\omega_{rm}} = \frac{3}{2} p_r \frac{L_{pc}}{L_p} \lambda_p i_{cq} \quad (2.1)$$

$$P_{control} = \frac{\omega_c}{\omega_p + \omega_c} P_{out} = \frac{\omega_c}{\omega_p} P_{power} \quad (2.2)$$

$$Q_p = \frac{3}{2} \frac{\omega_p \lambda_p}{L_p} (\lambda_p - L_{pc} i_{cd}) \quad (2.3)$$

Where  $\lambda_p$  is the flux in the power winding given by  $\lambda_{pd} + j \cdot \lambda_{pq}$ . Figure 2.11 provides a schematic diagram of a vector control system. It can be noted that this is immediately more complex than the scalar control equivalent diagram.

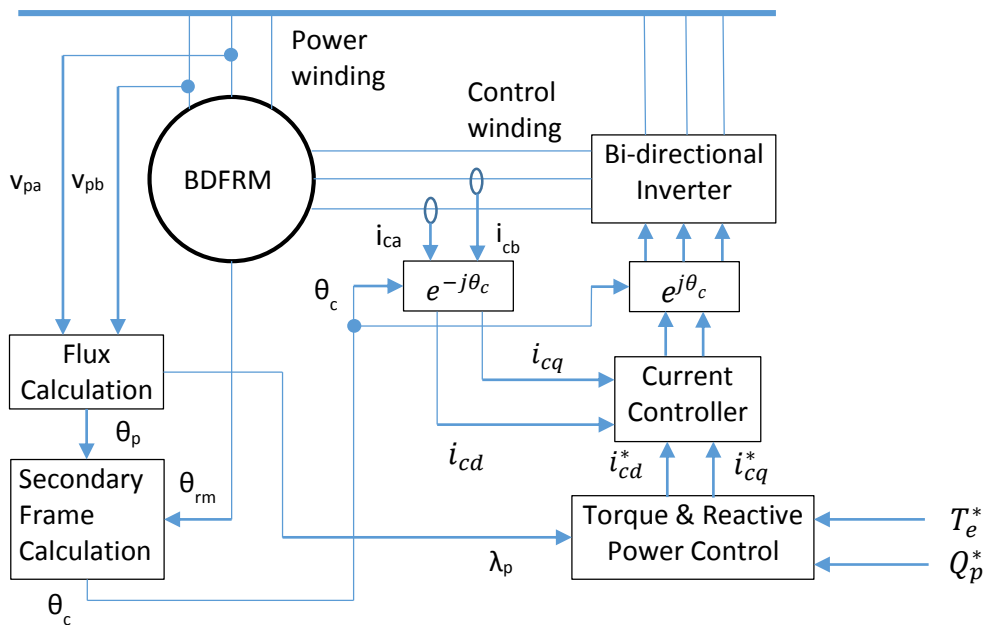


Figure 2.11 – Vector control diagram (adapted from [26])



### 2.7.3 DIRECT TORQUE CONTROL

Direct Torque Control (DTC) emerged as a control strategy in the mid-1980s [30], and provides a means for fast dynamic response without the need for quite as many machine parameters when compared to vector control. The original focus was on induction machines but can be adapted for use in BDFRMs [31-39]. A well-known limitation with DTC when applied to induction machines is the stability problems found at low frequencies, which arises because of inaccuracies in the flux estimation due to variations in resistance at low supply voltages. With the BDFRM, since both windings are accessible, these stability problems can be avoided. The BDFRM may be closely compared to an induction machine with the rotor and stator windings corresponding to the power and control windings. Hence the flux linkage in the control winding is given by:

$$\lambda_c = \lambda_{cd} + j\lambda_{cq} = \sigma L_c i_{cd} + \frac{L_{pc}}{L_p} \lambda_p + j\sigma L_c i_{cq} \quad (2.4)$$

This equation demonstrates that the control winding flux is directly proportional to the control winding quadrature axis current. This relationship therefore allows the torque to be controlled by applying a relevant voltage vector to the control winding, whilst keeping in mind the proportionality of torque and the control winding q-axis current in equation (2.1).

This strategy, which is reliant on accurate knowledge of the rotor angular position, was improved further by removing the requirement for sensors using a so-called 'sensorless' scheme [33, 40], in which an estimate of angular position is obtained by estimating the power winding flux via power winding voltage and current measurements.

### 2.7.4 TORQUE AND REACTIVE POWER CONTROL

For the new type of brushless doubly-fed machine a torque and reactive power control (TRPC) scheme may be realised [41-43]. Unlike the torque control technique, this method does not require the secondary flux amplitude or exact position

information. All that is required is the voltages and currents of two out of the three lines of the power phase windings.

## 2.8 BDFRM DESIGN CONSIDERATIONS

Although the basic configuration of a BDFRM is well established, there are many features of their design which require careful consideration to ensure that the machine both operates as expected and to its optimum level.

### 2.8.1 STATOR CORE FEATURES

Compared to a standard induction machine, BDFRMs tend to require deeper slots to accommodate the two stator windings. This leads to an increased stator outer diameter. The stator back iron and tooth width must also be increased to accommodate the extra flux present in these machines, while avoiding excessive critical saturation. As will be demonstrated on several occasions in this thesis, magnetic saturation is often a limiting factor on the performance of BDFRMs.

### 2.8.2 WINDINGS AND POLE NUMBERS

There are 4-cases for achieving coupling between the two stator windings:

$$P_r = \frac{P_p + P_c}{2} \quad \omega_{rm} = \frac{\omega_p + \omega_c}{P_r} \quad (2.5)$$

$$P_r = \frac{P_p - P_c}{2} \quad \omega_{rm} = \frac{\omega_p - \omega_c}{P_r} \quad (2.6)$$

$$P_r = \frac{-P_p + P_c}{2} \quad \omega_{rm} = \frac{-\omega_p + \omega_c}{P_r} \quad (2.7)$$

$$P_r = \frac{-P_p - P_c}{2} \quad \omega_{rm} = \frac{-\omega_p - \omega_c}{P_r} \quad (2.8)$$

[44]

Where  $P_{r,p,c}$  are the number of poles of the rotor, power winding and control winding respectively.

The rotor frequencies of (2.5) and (2.8) are identical, also the (2.6) and (2.7) rotor frequencies are identical. These equations suggest that a negative pole number may be achievable, but this is not the case as will be apparent in Section 2.9.4.

The natural speed of the BDFRM (when the control winding is fed with DC) is half that of a standard SyncRel machine. An important design consideration with doubly fed machines is the coupling achieved between the power and control windings, a feature which is demonstrated in Section 2.9.4. The mutual coupling needs to be kept to a minimum, whereas the self-coupling factor must be maximised. A two toothed rotor produces no coupling factor between the two stator windings, and is therefore not suitable for this application.

Using a four pole rotor may cause problems with harmonic interactions. If saturation causes a 3<sup>rd</sup> harmonic on the two pole winding, this would directly couple through the rotor to the six pole secondary winding.

Employing a power winding pole number larger than the control winding pole number ensures a better space utilisation for useful torque output [16, 44]. Using a lower control winding pole number leads to a reduced number of turns per phase and winding resistance value when a larger proportion of the current is in the control winding. This leads to a reduction in copper losses and, therefore, an increase in efficiency.

### 2.8.3 ROTOR DESIGN

The three main rotor types shown in Figure 2.12 have been proposed and investigated for BDFRMs. The rotor shown in Figure 2.12a consists of an axial stack of a straightforward salient pole laminated design, of the type that is widely used in SR machines. These rotors are easily manufactured and are inherently robust. A disadvantage of this type of rotor arrangement is the windage losses caused by the non-cylindrical rotor shape. However, the penalties compared to a smooth cylindrical rotor (in which losses are dominated by shear in the narrow airgap) are not as

pronounced as one might imagine, given the almost fan like structure of a typical SR rotor [45]. A method to alleviate this windage loss is to use a thin iron rib [46] to connect each tooth and thereby creating a smooth circular rotor circumference. These ribs saturate, and at low speeds, this saturation leads to slightly higher losses than a conventional rotor. At high speeds however, the windage loss is significantly reduced, thereby causing the overall machine losses to reduce at a higher rate at higher speeds compared with the conventional rotor losses. Liangzhou and Xiangyu produced a detailed paper [47] concerning the ideal design of the radially laminated rotor by using the Taguchi method to review the harmonics obtained in the torque and secondary winding current curves.

The rotor design in Figure 2.12b is the so-called axially laminated design. This design ensures high d-axis reluctance [48] by adding non-magnetic material between the laminations. Although this design is electromagnetically well founded, providing flux paths through the rotor, high iron losses can occur due to the eddy current losses along the length of the rotor. This design is also difficult to manufacture. It has been detailed in [49] that the use of axial flux barriers can effectively double the output of a BDFRM with identical stator structures.

The final design is a combination of the advantages of both the previous types of rotor in a so-called axial flux barrier rotor. This method reduces iron losses by using radial laminations, but also includes non-magnetic channels (usually consisting of air but could also be potted) to focus the flux and ensure a high saliency ratio. A comprehensive review of the six main synchronous reluctance rotor designs was produced by Staton et al. [50].

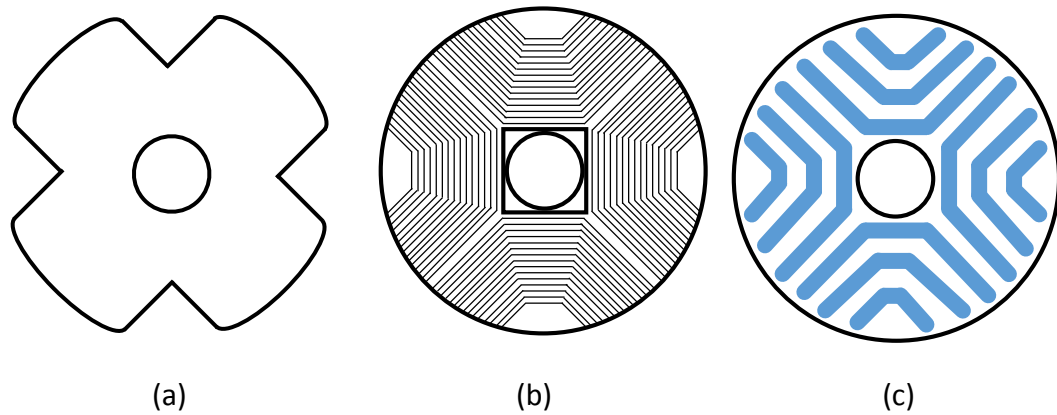


Figure 2.12 – Example rotor geometries (cruciform (a), axially laminated (b) and axial flux barrier (c))

An axial flux barrier (AFB) rotor may cause an increase in voltage ripple [51] due to the presence of some permeance modulation from the indirect effect of the channels in the rotor. This can be counteracted to some extent by splitting the rotor into two axial sections and skewing one section by half a slot. This has been proven to effectively reduce the voltage harmonics whilst maintaining the fundamental frequency of the voltage [51].

To produce effective coupling between the two stator windings, there must exist a large ratio between the d- and q- axis reluctance. The rotor eddy currents seem to depend upon the speed range that is selected as well as the winding configuration [52]. It has been shown that the winding configuration as detailed above could be affected by the speed of the rotor.

According to Schulz et al. [53], the optimal slot to tooth ratio for a radially laminated rotor is 1:1. This optimal value is obtained by ensuring that only a useful harmonic is produced by the action of the rotating rotor. An optimal stacking factor of 0.86 [49] for the radially laminated rotor is found with a requirement of maximum torque per amp. This is in contrast to the optimum stacking factor of 0.5 found for the axially laminated rotor [50].

Using an odd number of rotor poles produces a high torque density but may cause unbalanced magnetic pull (UMP) [54]. This UMP may lead to vibrations and noise within the machine and would decrease the lifetime of the bearings. The study reported in [54] also considered the merits of using higher saturation soft magnetic

cores relative to a more common material. In this case Cobalt Iron was used (Rotelloy 3) which resulted in a 27% increase in torque compared to a Silicon Iron equivalent, but with significant increase in expense.

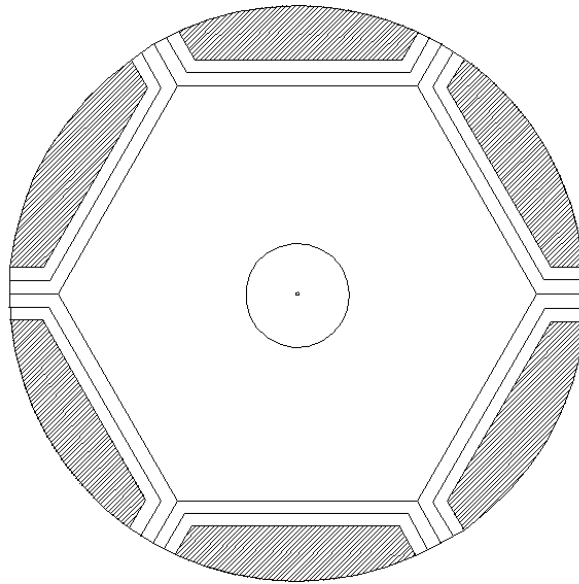


Figure 2.13 – Hybrid rotor geometry

A final design consideration for the rotor of a BDFRM is a Hybrid Rotor (Figure 2.13) which appears to be first proposed by Zhang et al. in 2009 [55]. This design combines the high saliency found in axially laminated rotors with the harmonic field suppressing qualities of cage rotors. It was stated that this design could give a marked improvement in coupling between the two windings. The geometry consists of a standard axially laminated rotor with short circuit in-fill.

## 2.9 ELECTROMAGNETIC OPERATION OF THE BDFRM

The BDFRM is generally regarded as being in a class of slip power recovery machines. This allows for a partially rated converter to be used for a speed range correction. The unique operational mode of this machine is that the permeance of the rotor modulates the MMF [56], resulting in complex analytical models for electromagnetic torque production in BDFRMs

As with all electrical machines, a detailed consideration of the airgap magnetic field provides the basis for fundamental understanding of machine behaviour. Although

ultimately, factors such as magnetic saturation, complex slot and rotor pole geometries and leakage fluxes will have an impact on performance, a simplified model based on a one-dimensional consideration of the magnetic field provides a useful starting point for understanding the various interactions, which result in useful torque.

The overwhelming majority, and indeed possibly all, previous studies have focussed on BDFRMs operating in conjunction with voltage stiff grids, which in effect fixes the power winding flux. This is entirely representative of utility grid type applications as motors or generators. However, in a VF aircraft supply, there tends to be only one generator on the localised network, and hence the voltage conditions on the power winding are not fixed. Although operation on a stiff grid and a small grid that in effect present a load to the power winding shares many elements in common, there is a need for part of the analysis to consider these cases separately.

### 2.9.1 WINDING FUNCTIONS

A useful starting point is the winding function produced by a given winding. This is a dimensionless chart displaying the spatial variation of the airgap MMF around the periphery of the airgap due to a unit DC excitation of the appropriate coils.

The winding function is assumed to be sinusoidal in most papers [57], while in others where concentrated windings are being considered, a simple squarewave function is often used [58].

An improvement to the winding function can be achieved with a stepped squarewave, which takes into account the distributed winding layout where the coils in a given phase winding might span several adjacent slots. In practice, this stepped squarewave MMF distribution would lead to a smoother spatial distribution due to leakage effects.

Due to this uncertainty in winding function shape, it is inherently difficult to obtain a truly accurate analytical result. In general, for concentrated windings, the winding function may be considered to be a squarewave, but for distributed windings, the sine wave may be closer to reality.

For the proceeding section, the control winding will be a 2-pole winding with 3 sets of nested coils per pole, and the power winding will have 6-poles with each pole containing 2 overlapping coils.

As can be deduced from Figure 2.14 and Figure 2.15, this simplification of the winding function could produce an inaccurate representation of the actual winding function depending on the winding layout. The steps seen in the actual curve in Figure 2.15 are seen to rise by different amounts. This allows the actual winding function curve to be as congruent as possible to the ideal coveted sine wave shape. To do this, varying numbers of turns are required on each of the distributed windings.

From the figures previously mentioned, it can be seen that although the control winding function seems to be more congruent to the sine wave shape, the power function is actually more akin to a squarewave. This is due to the power winding having a higher pole number and therefore less coils per pole, leading to a lower number of MMF steps per pole

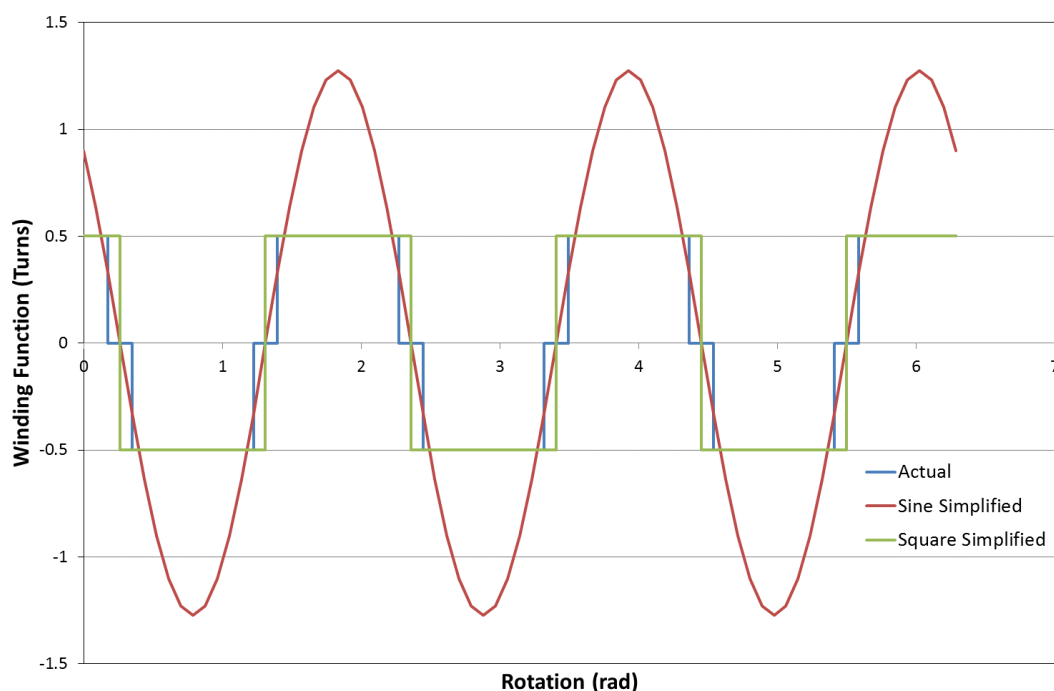


Figure 2.14 - 6-pole power winding function



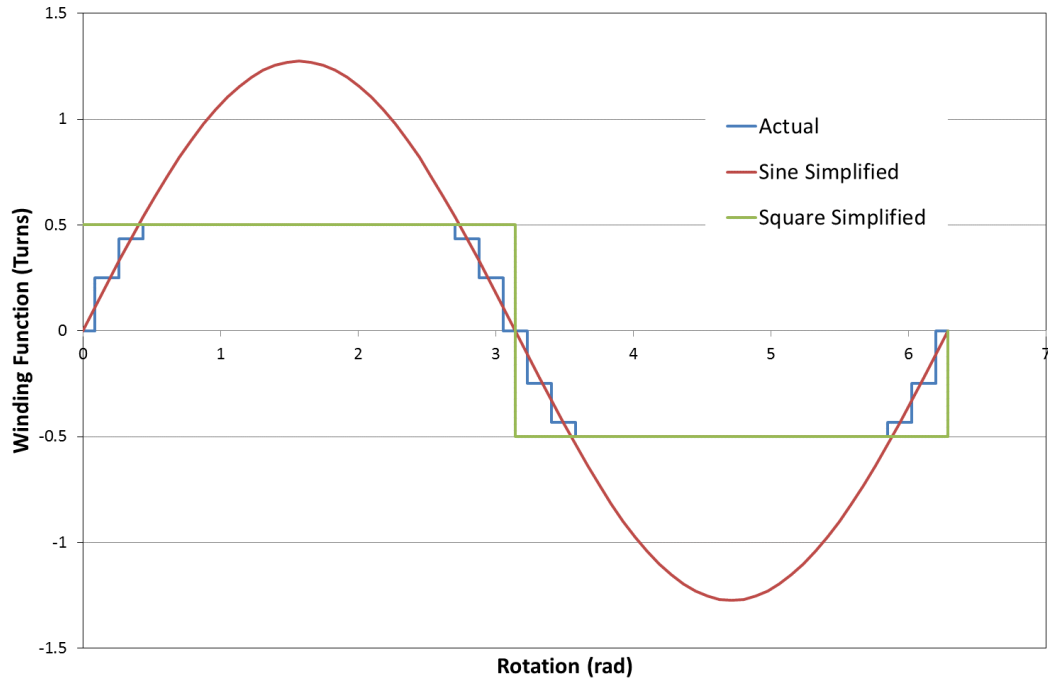


Figure 2.15 – 2-pole control winding function

For a sinusoidal assumption, the three phase power winding winding functions take the form:

$$W_{pa} = n_p \cos(p_{pp}\theta) \quad (2.9)$$

$$W_{pb} = n_p \cos\left(p_{pp}\theta - \frac{2\pi}{3}\right) \quad (2.10)$$

$$W_{pc} = n_p \cos\left(p_{pp}\theta - \frac{4\pi}{3}\right) \quad (2.11)$$

The control winding takes the form:

$$W_{ca} = n_c \cos(p_{pc}\theta) \quad (2.12)$$

$$W_{cb} = n_c \cos\left(p_{pc}\theta - \frac{2\pi}{3}\right) \quad (2.13)$$

$$W_{cc} = n_c \cos\left(p_{pc}\theta - \frac{4\pi}{3}\right) \quad (2.14)$$

For the squarewave assumption, the winding functions of the power and control windings for phase A are as follows:

$$W_{pa} = \sum_{i=1,3,\dots}^{\infty} \frac{4}{i\pi} \sin\left(\frac{i\pi}{2}\right) \cos(ip_{pp}(\theta)) \quad (2.15)$$

$$W_{ca} = \sum_{i=1,3,\dots}^{\infty} \frac{4}{i\pi} \sin\left(\frac{i\pi}{2}\right) \cos(ip_{pc}(\theta)) \quad (2.16)$$

In principle, similar Fourier expansions can be developed for more intricate representations of the spatial distribution of MMF around the airgap periphery.

### 2.9.2 ANALYTICAL MODEL OF A GRID CONNECTED BDFRM

The currents flowing through the power and control windings are assumed to be balanced three-phase sinusoidal currents. The power and control winding currents have different frequencies.

Much of the analysis presented in this section draws from and adapts a methodology proposed in [59].

In the general case, the control winding angle at  $t=0$  can be represented by an angle  $\alpha$  [53]. The six power and control winding phase currents are given by:

$$i_{pa} = \hat{I}_p \cos(\omega_p t) \quad (2.17)$$

$$i_{pb} = \hat{I}_p \cos\left(\omega_p t - \frac{2\pi}{3}\right) \quad (2.18)$$

$$i_{pc} = \hat{I}_p \cos\left(\omega_p t - \frac{4\pi}{3}\right) \quad (2.19)$$

$$i_{ca} = \hat{I}_c \cos(\omega_c t - \alpha) \quad (2.20)$$

$$i_{cb} = \hat{I}_c \cos\left(\omega_c t - \frac{2\pi}{3} - \alpha\right) \quad (2.21)$$

$$i_{cc} = \hat{I}_c \cos\left(\omega_c t - \frac{4\pi}{3} - \alpha\right) \quad (2.22)$$

### 2.9.3 NET MMF DISTRIBUTION OF A GRID CONNECTED BDFRM

The contribution to the net MMF from each phase can be calculated from the product of the winding function and phase current:

$$\mathcal{F}_{pa} = I_{pa} W_{pa} \quad (2.23)$$

$$\mathcal{F}_{pa} = \hat{I}_p \cos(\omega_p t) n_p \cos(p_{pp}\theta)$$

$$\mathcal{F}_{pb} = \hat{I}_p \cos\left(\omega_p t - \frac{2\pi}{3}\right) n_p \cos\left(p_{pp}\theta - \frac{2\pi}{3}\right) \quad (2.24)$$

$$\mathcal{F}_{pc} = \hat{I}_p \cos\left(\omega_p t - \frac{4\pi}{3}\right) n_p \cos\left(p_{pp}\theta - \frac{4\pi}{3}\right) \quad (2.25)$$

$$\mathcal{F}_{ca} = \hat{I}_c \cos(\omega_c t - \alpha) n_c \cos(p_{pc}\theta) \quad (2.26)$$

$$\mathcal{F}_{cb} = \hat{I}_c \cos\left(\omega_c t - \frac{2\pi}{3} - \alpha\right) n_c \cos\left(p_{pc}\theta - \frac{2\pi}{3}\right) \quad (2.27)$$

$$\mathcal{F}_{cc} = \hat{I}_c \cos\left(\omega_c t - \frac{4\pi}{3} - \alpha\right) n_c \cos\left(p_{pc}\theta - \frac{4\pi}{3}\right) \quad (2.28)$$

The net 3-phase rotating MMF field resulting from the power and control windings can be established following some manipulation and recognising that:

$$\cos(x)\cos(y) = \frac{\cos(x+y) + \cos(x-y)}{2} \quad (2.29)$$

The resulting MMF distributions for the power and control winding are given by:

$$\mathcal{F}_p = \frac{3}{2} \hat{I}_p n_p \cos(\omega_p t - p_{pp} \theta) \quad (2.30)$$

$$\mathcal{F}_c = \frac{3}{2} \hat{I}_c n_c \cos(\omega_c t - p_{pc} \theta - \alpha) \quad (2.31)$$

#### 2.9.4 ACCOUNTING FOR PERMEANCE MODULATING EFFECT OF THE SALIENT ROTOR

In many papers concerned with analytical modelling, the variation in permeance around the airgap is considered to be the inverse of the airgap length [57]. By way of example, Figure 2.16 shows a typical permeance variation for a 4 pole rotor. In this case, the inverse airgap model is given by:

$$g^{-1} = \frac{G}{2} + G \sum_{m=1,3,\dots}^{\infty} \left[ \frac{2}{m\pi} \sin\left(\frac{m\pi}{2}\right) \cos(mp_r \omega_{rm} t - mp_r(\theta - \gamma)) \right] \quad (2.32)$$

A further simplification often adopted is to take only the fundamental component of the permeance function. Although such assumptions are recognised to be an over simplification by some authors [53, 58], it significantly eases the following analytical model. For the case of the 4 pole rotor, considered in Figure 2.16, the simplified fundamental component model is shown in Figure 2.17, while the corresponding inverse gap expression is:

$$g^{-1} = \frac{G}{2} [1 + \cos(p_r(\theta - \theta_{rm}))] \quad (2.33)$$

In which:

$$\theta_{rm} = \omega_{rm} t + \gamma \quad (2.34)$$

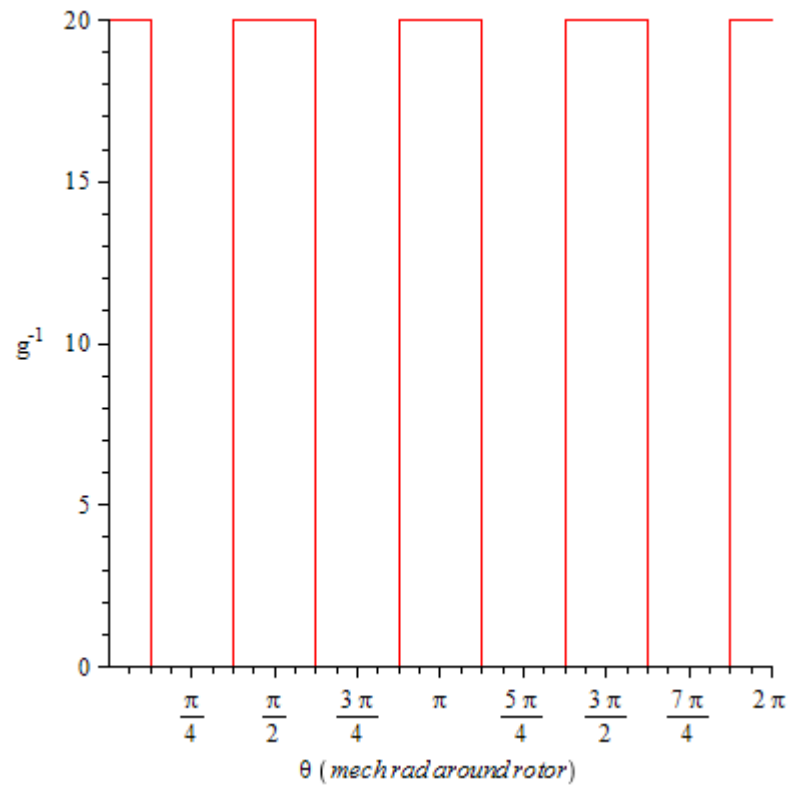


Figure 2.16 – Square-wave inverse airgap function

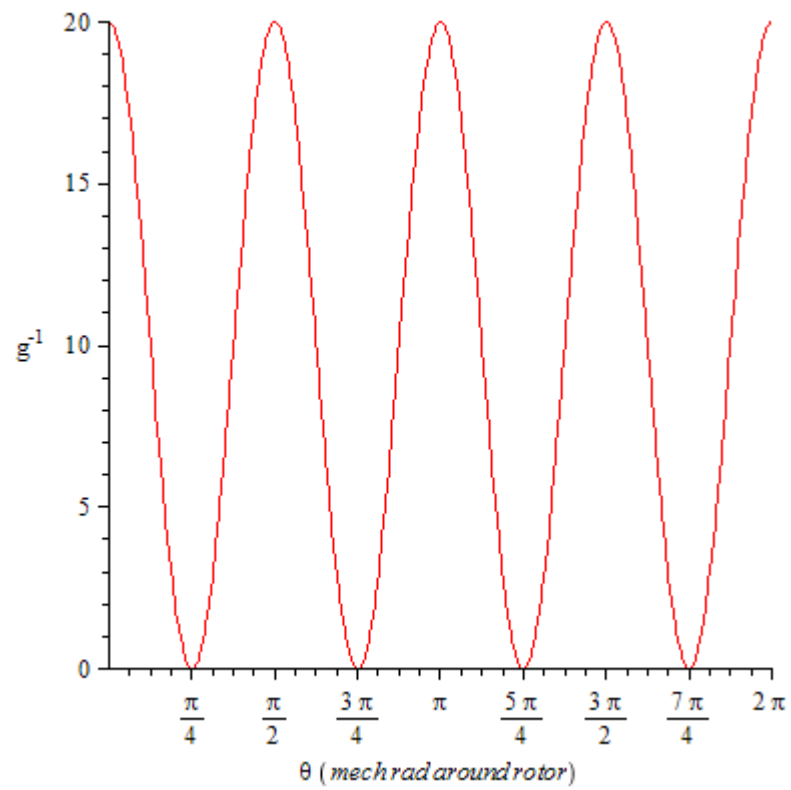


Figure 2.17 –Fundamental of inverse airgap function

Using this simplified permeance and the MMF, the airgap flux density due to the power winding can be calculated from the product of the MMF and the permeance function:

$$\begin{aligned}
B_p(\theta, \theta_{rm}) &= \mu_0 \mathcal{F}_p g^{-1} \\
&= \frac{3\mu_0 \hat{I}_p n_p}{2} \cos(\omega_p t - p_{pp} \theta) \frac{G}{2} [1 + \cos(p_r(\theta - \theta_{rm}))] \\
&= \frac{3\mu_0 \hat{I}_p n_p G}{4} \left[ \cos(\omega_p t - p_{pp} \theta) \right. \\
&\quad \left. + \frac{1}{2} \left[ \cos((\omega_p - p_r \omega_{rm})t + \theta(p_r - p_{pp})) \right. \right. \\
&\quad \left. \left. + \cos((\omega_p + p_r \omega_{rm})t - \theta(p_r + p_{pp})) \right] \right] \tag{2.35}
\end{aligned}$$

$$\langle \omega_{rm} = \frac{\theta_{rm}}{t} \rangle \tag{2.36}$$

Close inspection of equation (2.35) shows that it consists of a fundamental component of unity relative magnitude, and two side-bands of half relative magnitude as shown in Figure 2.18. This illustrates the modulating effect of the rotor permeance on the flux density produced by the power winding. In fact, after initial analysis of the airgap field in Section 4.6.2, it is apparent that these sidebands are of unequal magnitude and are not at a magnitude of half the fundamental. The gamma term in equation (2.34) may be neglected as the angle between the d-axis and phase A of the control winding has no bearing on the coupling method between the two windings.

Similarly, for the control winding:

$$\begin{aligned}
B_c(\theta, \theta_{rm}) &= \frac{3\mu_0 \hat{I}_c n_c G}{4} \left[ \cos(\omega_c t - p_{pc} \theta - \alpha) \right. \\
&\quad \left. + \frac{1}{2} \left[ \cos((\omega_c - p_r \omega_{rm})t + \theta(p_r - p_{pc}) - \alpha) \right. \right. \\
&\quad \left. \left. + \cos((\omega_c + p_r \omega_{rm})t - \theta(p_r + p_{pc}) - \alpha) \right] \right] \tag{2.37}
\end{aligned}$$

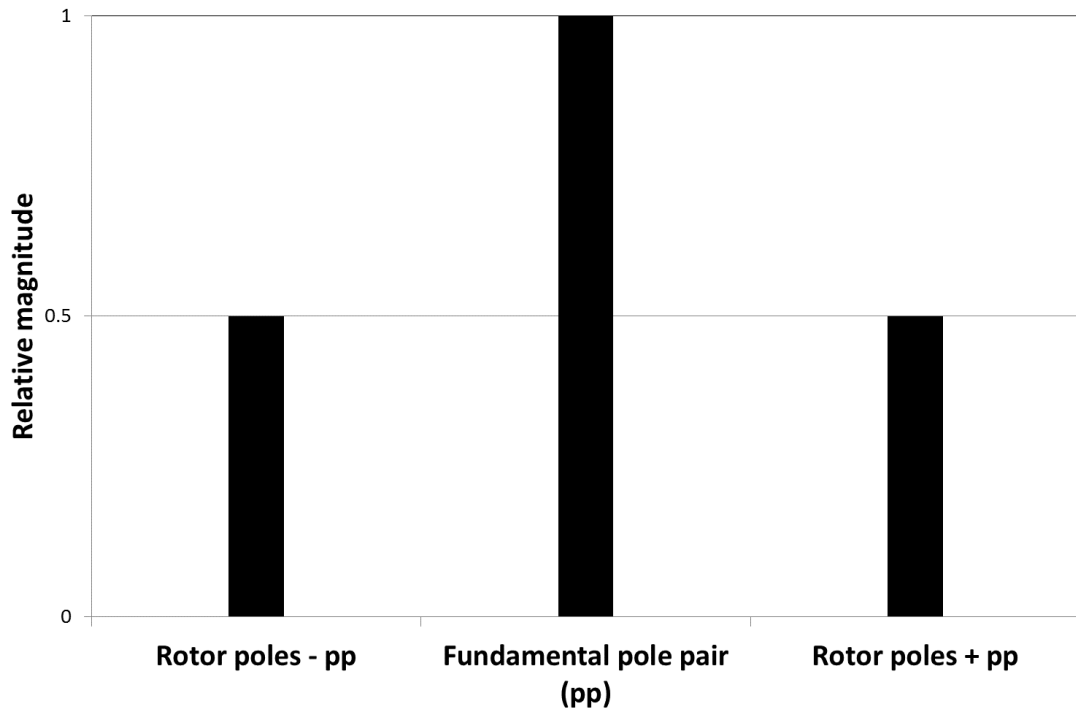


Figure 2.18 – Modulation principle on the fundamental spatial frequency

To produce useful torque in a BDFRM, these two airgap flux density components must be coupled by the rotor in such a way as to meet two criteria:

- A certain value of  $p_r$  is required to ensure that the two forward rotating components of the flux density in each winding rotate with the same electrical angular velocity.
- The two forward rotating flux density harmonics must also have the same pole number as the fundamental flux density in their counterpart winding.

These criteria may be better understood by adding both windings to the modulation principle found in Figure 2.18. Figure 2.19 demonstrates how the spatial pole numbers of each winding interact after the rotor permeance modulation. The fundamental spatial harmonic of the solid lined winding must have the same spatial pole number as the lower spatial harmonic of the hashed lined winding. Conversely, the fundamental of the hashed lined winding must have the same spatial frequency as the upper harmonic of the solid lined winding. The two outlying harmonics, at the far left and far right of Figure 2.19, are known as leakage components as they do not lead to any useful torque production in the BDFRM.

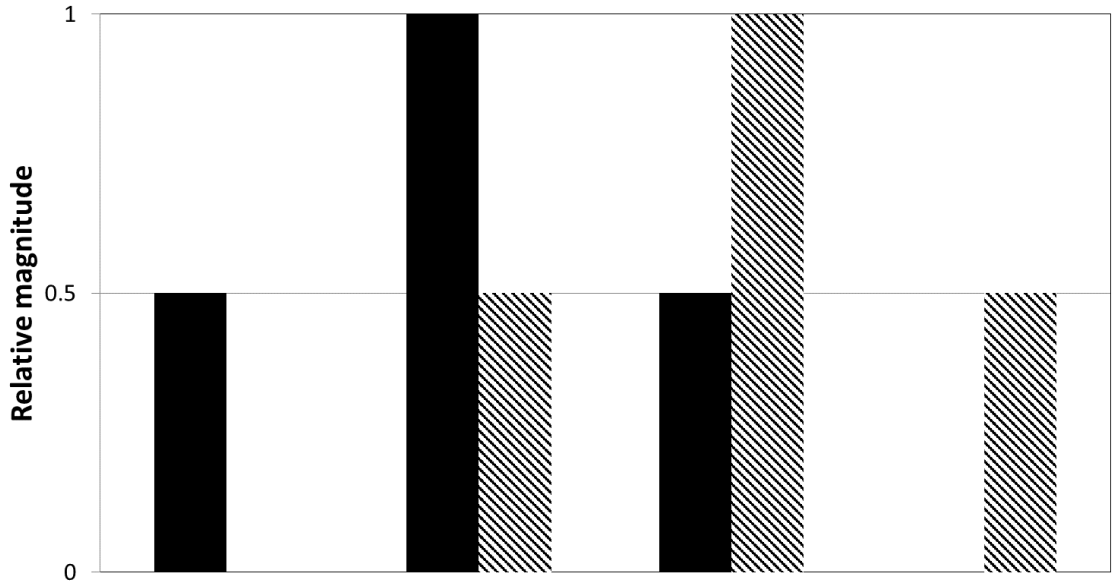


Figure 2.19 – Method of spatial harmonic coupling between the control winding (solid lines) and the power winding (hashed lines)

The nature of the coupling can be explored by considering the lower rotating sideband component of the power winding, and the fundamental of the control winding:

$$\text{Power winding lower sideband: } \cos\left((\omega_p - p_r \omega_{rm})t + \theta(p_r - p_{pp})\right)$$

$$\text{Fundamental of control winding: } \cos(\omega_c t - p_{pc} \theta - \alpha)$$

The conditions which would result in these components coupling can be established by equating them, i.e.:

$$\cos\left((\omega_p - p_r \omega_{rm})t + \theta(p_r - p_{pp})\right) = \cos(\omega_c t - p_{pc} \theta - \alpha) \quad (2.38)$$

The temporal and spatial components can then be separated out to obtain:

$$\omega_p - p_r \omega_{rm} = \omega_c \quad (2.39)$$

$$p_r - p_{pp} = -p_{pc} \quad (2.40)$$



The  $\alpha$  term may be neglected as this is simply a spatial offset and at this stage in the analysis the focus is the frequency and pole number, not the relative phase.

As the cosine function is symmetrical about zero, the left hand side of each of the above equations can be manipulated to:

$$p_r \omega_{rm} - \omega_p = \omega_c \quad (2.41)$$

$$p_{pp} - p_r = -p_{pc} \quad (2.42)$$

Following rearrangement and substitution, two alternatives for the rotor angular velocity are obtained:

$$\omega_{rm} = \frac{\omega_p - \omega_c}{p_{pp} - p_{pc}} \quad (2.43)$$

$$\omega_{rm} = \frac{\omega_p + \omega_c}{p_{pp} + p_{pc}} \quad (2.44)$$

This process can be repeated using the upper rotating sideband of the power winding and the fundamental component of the control winding:

$$(\omega_p + p_r \omega_{rm})t - \theta(p_r + p_{pp}) = (\omega_c t - p_{pc} \theta - \alpha) \quad (2.45)$$

The same manipulation procedure leads to two values for the rotor mechanical angular frequency, identical to the previous values established in equations (2.43) and (2.44), for the lower sideband.

From the first value of  $\omega_{rm}$  found, where  $p_r = p_{pp} - p_{pc}$ , a negative value of the number of rotor poles seems to be achievable if  $p_{pp} < p_{pc}$ . However, the theoretical possibility of negative pole numbers is explained when the inverse airgap function is seen to be modelled by a cosine wave. As mentioned previously, the even symmetry of the cosine function allows for both positive and negative values of the rotor pole number.

Following on from this, the two rotor pole numbers which satisfy the requirement for coupling are  $p_{pp} + p_{pc}$  and  $|p_{pp} - p_{pc}|$ .

As will be apparent only one sideband produces useful coupling between the two flux density waves in the airgap. The non-coupling unused side band manifests itself as a large leakage inductance term, in turn leading to poor dynamic torque performance [59].

The nature of the permeance modulation, and resulting coupling between the two windings, can be illustrated by a specific example with a common combination of a 6 pole power winding, a 2 pole control winding and a rotor with four teeth.

The two winding MMFs are modulated by the permeance of the rotor. This results in three modulated frequencies per winding. Two of these frequencies on one side couple with the corresponding frequencies on the other side. In this case the coupling pole numbers are the 6-pole and the 2-pole waves. But this modulation effect also produces two unwanted leakage components of 10-pole and 14-pole. This is illustrated in normalised terms in Figure 2.20.

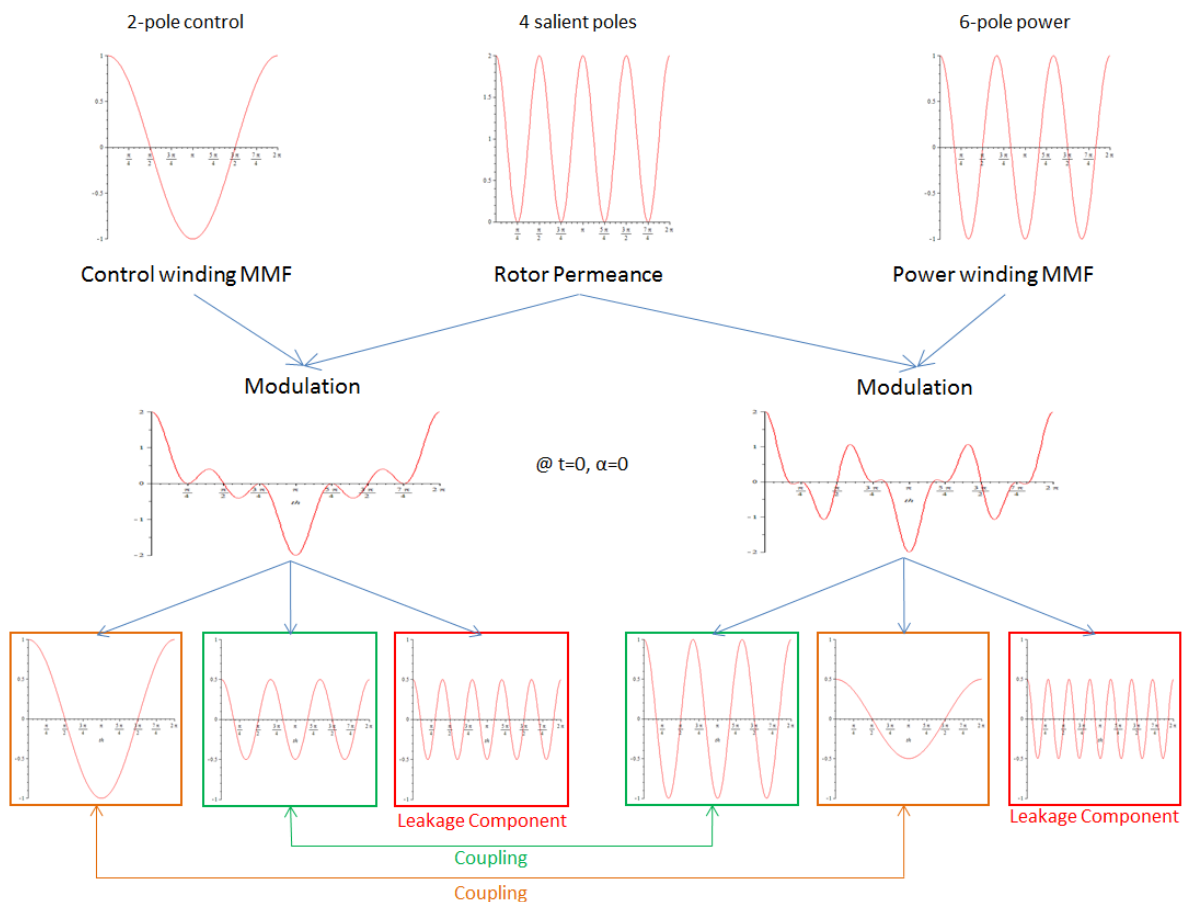


Figure 2.20 – Modulation example with a 2-pole control winding, 6-pole power winding and a 4 pole rotor

The coupled airgap fields then produce the torque due to the fields rotating at the same speed with identical pole numbers. More information on this torque producing mechanism as well as the key equations for calculating reactive power and torque etc. may be found in the comprehensive BDFRM report produced by Betz and Jovanovic [59].

As noted previously this analytical model covers the case of a stiff grid, in which the power winding voltage is governed by the grid. In order to cater for an isolated load, several modifications are necessary.

### 2.9.5 ANALYTICAL MODEL OF A NON-GRID CONNECTED BDFRM

For this different set of operating conditions on an isolated (i.e. un-stiff) grid, the expressions for the control winding current (equations (2.20) to (2.22)), MMF (equations (2.26) to (2.28)) and flux density (equation (2.37)) remain. However, the equations for the power winding must be derived from the control winding flux density via the pole number and frequency relationships, since they are no longer set by a stiff grid.

It should be noted that to the author's best knowledge, a model to cater for these conditions has not been published in literature.

Starting with equation (2.37) for the airgap flux density due to the control winding current:

$$\begin{aligned}
 B_c(\theta, \theta_{rm}) = \frac{3\mu_0 \hat{I}_c n_c G}{4} & \left[ \cos(\omega_c t - p_{pc} \theta - \alpha) \right. \\
 & + \frac{1}{2} \left[ \cos((\omega_c - p_r \omega_{rm})t + \theta(p_r - p_{pc}) - \alpha) \right. \\
 & \left. \left. + \cos((\omega_c + p_r \omega_{rm})t - \theta(p_r + p_{pc}) - \alpha) \right] \right] \quad (2.37)
 \end{aligned}$$

As discussed previously, there are two possible combinations of pole number and frequency that ensure coupling between the windings, via the modulating effect of rotor permeance. The four equations which will be used in this case are (2.39) to (2.42).

First taking equations (2.39) and (2.40) and rearranging for  $p_{pc}$  and  $\omega_c$  yields:

$$p_{pc} = p_{pp} - p_r \quad \omega_c = \omega_p - p_r \omega_{rm} \quad (2.46)$$

Substituting this into the above equation for  $B_c(\theta, \theta_{rm})$  produces:

$$B_p(\theta, \theta_{rm}) = \frac{3\mu_0 \hat{I}_p n_p G}{4} \left[ \cos((\omega_p - p_r \omega_{rm})t - \theta(p_{pp} - p_r) - \alpha) \right. \\ \left. + \frac{1}{2} \left[ \cos((\omega_p - p_r \omega_{rm} - p_r \omega_{rm})t + \theta(p_r - p_{pp} + p_r) - \alpha) \right. \right. \\ \left. \left. + \cos((\omega_p - p_r \omega_{rm} + p_r \omega_{rm})t - \theta(p_r + p_{pp} - p_r) - \alpha) \right] \right] \quad (2.47)$$

$$B_p(\theta, \theta_{rm}) = \frac{3\mu_0 \hat{I}_p n_p G}{4} \left[ \cos((\omega_p - p_r \omega_{rm})t + \theta(p_r - p_{pp}) - \alpha) \right. \\ \left. + \frac{1}{2} \left[ \cos((\omega_p - 2p_r \omega_{rm})t + \theta(2p_r - p_{pp}) - \alpha) \right. \right. \\ \left. \left. + \cos(\omega_p t - \theta p_{pp} - \alpha) \right] \right]$$

Equation (2.47) must then be compared to equation (2.37) to establish the coupling between the two windings.

The fundamental term of the control winding airgap flux density links to produce the lower sideband of the power winding flux density. Similarly, the upper sideband of  $B_c$  links to produce the fundamental component of  $B_p$ . Finally, the lower sideband of  $B_c$  does not couple so is regarded as a leakage term in  $B_p$ .

Taking a similar approach for equations (2.41) and (2.42) yields:

$$p_{pc} = p_r - p_{pp} \quad \omega_c = p_r \omega_{rm} - \omega_p \quad (2.48)$$

$$\begin{aligned}
B_p(\theta, \theta_{rm}) &= \frac{3\mu_0 \hat{I}_p n_p G}{4} \left[ \cos((p_r \omega_{rm} - \omega_p)t - \theta(p_r - p_{pp}) - \alpha) \right. \\
&\quad + \frac{1}{2} \left[ \cos((p_r \omega_{rm} - \omega_p - p_r \omega_{rm})t + \theta(p_r - p_r + p_{pp}) - \alpha) \right. \\
&\quad \left. \left. + \cos((p_r \omega_{rm} - \omega_p + p_r \omega_{rm})t - \theta(p_r + p_r - p_{pp}) - \alpha) \right] \right] \quad (2.49) \\
B_p(\theta, \theta_{rm}) &= \frac{3\mu_0 \hat{I}_p n_p G}{4} \left[ \cos((p_r \omega_{rm} - \omega_p)t - \theta(p_r - p_{pp}) - \alpha) \right. \\
&\quad + \frac{1}{2} \left[ \cos(\omega_p t - \theta p_{pp} - \alpha) \right. \\
&\quad \left. \left. + \cos((2p_r \omega_{rm} - \omega_p)t - \theta(2p_r - p_{pp}) - \alpha) \right] \right]
\end{aligned}$$

Using this second set of equations leads to the same control winding term producing the active sideband of the power winding flux density. However, in this second case, the leakage and fundamental terms are now produced by the upper and lower sidebands of  $B_c$  respectively.

This airgap flux density is then demodulated by the rotor to produce the correct power winding MMF, resulting in the desired frequency of current in the power winding.

## 2.10 CHAPTER 2 SUMMARY

This chapter has detailed the chronological evolution of the BDFRM from its origins as a cascaded machine over a century ago. This was then followed by a section of available control schemes for the BDFRM and some key design considerations for the stator, rotor and windings.

Analytical models were then presented for both a stiff grid and a non-grid connected BDFRM, detailing the complex nature of the airgap modulation process to facilitate torque production in these machines.

The findings from this chapter can be developed in Chapters 4 and 5 to facilitate electromagnetic studies and to find an optimised BDFRM design.

## 2.11 REFERENCES

- [1] N. Tesla, "A New System of Alternate Current Motors and Transformers," *American Institute of Electrical Engineers, Transactions of the*, vol. V, pp. 308-327, 1888.
- [2] A. R. W. Broadway and L. Burbridge, "Self-cascaded machine: a low-speed motor or high-frequency brushless alternator," *Electrical Engineers, Proceedings of the Institution of*, vol. 117, pp. 1277-1290, 1970.
- [3] C. P. Steinmetz, "Operating Alternating Motors," US Patent 587340, 03/08/87, 1897.
- [4] L. Yuefeng, "Design of a brushless doubly-fed induction motor for adjustable speed drive applications," in *Industry Applications Conference, 1996. Thirty-First IAS Annual Meeting, IAS '96., Conference Record of the 1996 IEEE*, 1996, pp. 850-855 vol.2.
- [5] L. J. Hunt, "A new type of induction motor," *Electrical Engineers, Journal of the Institution of*, vol. 39, pp. 648-667, 1907.
- [6] S. B. L. a. F. Lydall, "Improvements in poly-phase induction motors," Britain Patent 16839, 1902.
- [7] F. Creedy, "Some developments in multi-speed cascade induction motors," *Electrical Engineers, Journal of the Institution of*, vol. 59, pp. 511-532, 1921.
- [8] A. Kusko and C. B. Somuah, "Speed Control of a Single-Frame Cascade Induction Motor with Slip-Power Pump Back," *Industry Applications, IEEE Transactions on*, vol. IA-14, pp. 97-105, 1978.
- [9] S. Benelghali, M. E. H. Benbouzid, and J. F. Charpentier, "Comparison of PMSG and DFIG for marine current turbine applications," in *Electrical Machines (ICEM), 2010 XIX International Conference on*, 2010, pp. 1-6.
- [10] F. Khatounian, E. Monmasson, F. Berthereau, E. Delaleau, and J. P. Louis, "Control of a doubly fed induction generator for aircraft application," in *Industrial Electronics Society, 2003. IECON '03. The 29th Annual Conference of the IEEE*, 2003, pp. 2711-2716 Vol.3.
- [11] H. Polinder, F. F. A. van der Pijl, G. J. de Vilder, and P. J. Tavner, "Comparison of direct-drive and geared generator concepts for wind turbines," *Energy Conversion, IEEE Transactions on*, vol. 21, pp. 725-733, 2006.
- [12] T. Feehally and J. Apsley, "The doubly-fed induction machine as an aero generator," in *Energy Conversion Congress and Exposition (ECCE), 2014 IEEE*, 2014, pp. 1340-1347.
- [13] R. Spee, A. K. Wallace, and H. K. Lauw, "Performance simulation of brushless doubly-fed adjustable speed drives," in *Industry Applications Society Annual Meeting, 1989., Conference Record of the 1989 IEEE*, 1989, pp. 738-743 vol.1.
- [14] L. X. a. T. A. L. Feng Liang, "d-q Analysis of a Variable Speed Doubly AC Excited Reluctance Motor," 1990.
- [15] L. Xu, F. Liang, and T. A. Lipo, "Transient model of a doubly excited reluctance motor," *Energy Conversion, IEEE Transactions on*, vol. 6, pp. 126-133, 1991.

- [16] R. E. Betz and M. G. Jovanovic, "The brushless doubly fed reluctance machine and the synchronous reluctance machine-a comparison," *Industry Applications, IEEE Transactions on*, vol. 36, pp. 1103-1110, 2000.
- [17] M. G. Jovanovic, R. E. Betz, and Y. Jian, "The use of doubly fed reluctance machines for large pumps and wind turbines," in *Industry Applications Conference, 2001. Thirty-Sixth IAS Annual Meeting. Conference Record of the 2001 IEEE*, 2001, pp. 2318-2325 vol.4.
- [18] W. Fengxiang, Z. Fengge, and X. Longya, "Parameter and performance comparison of doubly fed brushless machine with cage and reluctance rotors," *Industry Applications, IEEE Transactions on*, vol. 38, pp. 1237-1243, 2002.
- [19] M. G. Jovanovic, "Power factor and inverter rating. A compromise in doubly fed reluctance machine drives," in *Power Electronics and Variable Speed Drives, 2000. Eighth International Conference on (IEE Conf. Publ. No. 475)*, 2000, pp. 311-316.
- [20] D. G. Dorrell and M. Jovanovic, "On the Possibilities of Using a Brushless Doubly-Fed Reluctance Generator in a 2 MW Wind Turbine," in *Industry Applications Society Annual Meeting, 2008. IAS '08. IEEE*, 2008, pp. 1-8.
- [21] E. M. Schulz and R. E. Betz, "Use of Doubly Fed Reluctance Machines in Wind Power Generation," in *Power Electronics and Motion Control Conference, 2006. EPE-PEMC 2006. 12th International*, 2006, pp. 1901-1906.
- [22] F. Valenciaga and P. F. Puleston, "Variable Structure Control of a Wind Energy Conversion System Based on a Brushless Doubly Fed Reluctance Generator," *Energy Conversion, IEEE Transactions on*, vol. 22, pp. 499-506, 2007.
- [23] K. Xiaoguang, W. Fengxiang, and S. Yan, "Comparison of High Speed PM Generator with PM Doubly Fed Reluctance Generator for Distributed Power Generation System," in *Industrial Electronics and Applications, 2007. ICIEA 2007. 2nd IEEE Conference on*, 2007, pp. 1193-1197.
- [24] R. E. Betz and M. G. Jovanovic, "Theoretical analysis of control properties for the brushless doubly fed reluctance machine," *Energy Conversion, IEEE Transactions on*, vol. 17, pp. 332-339, 2002.
- [25] M. G. Jovanovic, J. Yu, and E. Levi, "A review of control methods for brushless doubly-fed reluctance machines," in *Power Electronics, Machines and Drives, 2002. International Conference on (Conf. Publ. No. 487)*, 2002, pp. 528-533.
- [26] M. Jovanovic, "Sensored and sensorless speed control methods for brushless doubly fed reluctance motors," *Electric Power Applications, IET*, vol. 3, pp. 503-513, 2009.
- [27] M. Hassan and M. Jovanovic, "Improved scalar control using flexible DC-Link voltage in Brushless Doubly-Fed Reluctance Machines for wind applications," in *Environment Friendly Energies and Applications (EFEA), 2012 2nd International Symposium on*, 2012, pp. 482-487.
- [28] M. G. Jovanovic and R. E. Betz, "Slip power recovery systems based on brushless doubly fed reluctance machines," in *Power Conversion Conference, 2002. PCC Osaka 2002. Proceedings of the*, 2002, pp. 987-992 vol.3.

- [29] S. Ademi and M. Jovanovic, "Vector control strategies for brushless doubly-fed reluctance wind generators," in *Environment Friendly Energies and Applications (EFEA), 2012 2nd International Symposium on*, 2012, pp. 44-49.
- [30] I. Takahashi and T. Noguchi, "A New Quick-Response and High-Efficiency Control Strategy of an Induction Motor," *Industry Applications, IEEE Transactions on*, vol. IA-22, pp. 820-827, 1986.
- [31] M. G. Jovanovic and J. Yu, "An optimal direct torque control strategy for brushless doubly-fed reluctance motors," in *Power Electronics and Drive Systems, 2003. PEDS 2003. The Fifth International Conference on*, 2003, pp. 1229-1234 Vol.2.
- [32] M. G. Jovanovic, Y. Jian, and E. Levi, "Encoderless direct torque controller for limited speed range applications of brushless doubly fed reluctance motors," *Industry Applications, IEEE Transactions on*, vol. 42, pp. 712-722, 2006.
- [33] M. G. Jovanovic and D. G. Dorrell, "Sensorless Control of Brushless Doubly-Fed Reluctance Machines using an Angular Velocity Observer," in *Power Electronics and Drive Systems, 2007. PEDS '07. 7th International Conference on*, 2007, pp. 717-724.
- [34] H. Chaal, M. Jovanovic, and K. Busawon, "Sliding Mode Observer based direct torque control of a Brushless Doubly-Fed Reluctance Machine," in *Industrial Electronics & Applications, 2009. ISIEA 2009. IEEE Symposium on*, 2009, pp. 866-871.
- [35] M. Jovanovic, Y. Jian, and E. Levi, "A direct torque controller for limited speed range applications of brushless doubly-fed reluctance motors," in *Industry Applications Conference, 2004. 39th IAS Annual Meeting. Conference Record of the 2004 IEEE*, 2004, pp. 2403-2410 vol.4.
- [36] M. G. Jovanovic, J. Yu, and E. Levi, "Real-time implementation of direct torque control scheme for brushless doubly-fed reluctance motors," in *Power Electronics, Machines and Drives, 2004. (PEMD 2004). Second International Conference on (Conf. Publ. No. 498)*, 2004, pp. 752-757 Vol.2.
- [37] Y. Jian and M. Jovanovic, "Direct torque control on a brushless doubly fed reluctance machine," in *Universities Power Engineering Conference, 2004. UPEC 2004. 39th International*, 2004, pp. 587-590 vol. 1.
- [38] M. Jovanovic and Y. Jian, "A direct torque controlled brushless doubly-fed reluctance machine drive system," in *Industrial Electronics, 2004 IEEE International Symposium on*, 2004, pp. 917-922 vol. 2.
- [39] M. G. Jovanovic and M. M. R. Ahmed, "Sensorless Speed Control Strategy for Brushless Doubly-Fed Reluctance Machines," in *Electric Machines & Drives Conference, 2007. IEMDC '07. IEEE International*, 2007, pp. 1514-1519.
- [40] M. G. Jovanovic, J. Yu, and E. Levi, "A doubly-fed reluctance motor drive with sensorless direct torque control," in *Electric Machines and Drives Conference, 2003. IEMDC'03. IEEE International*, 2003, pp. 1518-1524 vol.3.
- [41] H. Chaal and M. Jovanovic, "Towards a Generic Torque and Reactive Power Controller for Doubly-Fed Machines," *Power Electronics, IEEE Transactions on*, vol. PP, pp. 1-1, 2011.



- [42] H. Chaal and M. Jovanovic, "Direct Power Control of Brushless Doubly-Fed Reluctance Machines," in *Power Electronics, Machines and Drives (PEMD 2010), 5th IET International Conference on*, 2010, pp. 1-6.
- [43] H. Chaal and M. Jovanovic, "A new sensorless torque and reactive power controller for doubly-fed machines," in *Electrical Machines (ICEM), 2010 XIX International Conference on*, 2010, pp. 1-6.
- [44] A. M. Knight, R. E. Betz, and D. Dorrell, "Design and analysis of Brushless Doubly Fed Reluctance Machines," in *Energy Conversion Congress and Exposition (ECCE), 2011 IEEE*, 2011, pp. 3128-3135.
- [45] S. D. Calverley, G. W. Jewell, and R. J. Saunders, "Aerodynamic losses in switched reluctance machines," *Electric Power Applications, IEE Proceedings* -, vol. 147, pp. 443-448, 2000.
- [46] W. Sung Hong, C. Jaehoon, and L. Ju, "Windage Loss Reduction of High-Speed SRM Using Rotor Magnetic Saturation," *Magnetics, IEEE Transactions on*, vol. 44, pp. 4147-4150, 2008.
- [47] L. Ji and X. Yang, "Optimization design on salient pole rotor of BDFRM using the Taguchi method," in *Power Electronics Systems and Applications (PESA), 2011 4th International Conference on*, 2011, pp. 1-4.
- [48] I. Scian, D. G. Dorrell, and P. Holik, "Assessment of Losses in a Brushless Doubly-Fed Reluctance Machine," in *Magnetics Conference, 2006. INTERMAG 2006. IEEE International*, 2006, pp. 196-196.
- [49] E. M. Schulz and R. E. Betz, "Optimal torque per amp for brushless doubly fed reluctance machines," in *Industry Applications Conference, 2005. Fourtieth IAS Annual Meeting. Conference Record of the 2005*, 2005, pp. 1749-1753 Vol. 3.
- [50] D. A. Staton, T. J. E. Miller, and S. E. Wood, "Maximising the saliency ratio of the synchronous reluctance motor," *Electric Power Applications, IEE Proceedings B*, vol. 140, pp. 249-259, 1993.
- [51] D. G. Dorrell, A. M. Knight, and R. E. Betz, "Issues with the design of brushless doubly-fed reluctance machines: Unbalanced magnetic pull, skew and iron losses," in *Electric Machines & Drives Conference (IEMDC), 2011 IEEE International*, 2011, pp. 663-668.
- [52] D. G. Dorrell, I. Scian, E. M. Schulz, R. B. Betz, and M. Jovanovic, "Electromagnetic Considerations in the Design of Doubly-Fed Reluctance Generators for use in Wind Turbines," in *IEEE Industrial Electronics, IECON 2006 - 32nd Annual Conference on*, 2006, pp. 4272-4277.
- [53] E. M. Schulz and R. E. Betz, "Optimal rotor design for brushless doubly fed reluctance machines," in *Industry Applications Conference, 2003. 38th IAS Annual Meeting. Conference Record of the*, 2003, pp. 256-261 vol.1.
- [54] D. G. Dorrell, A. M. Knight, and R. E. Betz, "Improvements in Brushless Doubly Fed Reluctance Generators Using High-Flux-Density Steels and Selection of the Correct Pole Numbers," *Magnetics, IEEE Transactions on*, vol. 47, pp. 4092-4095, 2011.
- [55] Z. Fengge, L. Yongxin, and W. Xiuping, "The design and FEA of brushless doubly-fed machine with hybrid rotor," in *Applied Superconductivity and Electromagnetic Devices, 2009. ASEMD 2009. International Conference on*, 2009, pp. 324-327.

- [56] L. Xu, "Analysis of a doubly-excited brushless reluctance machine by finite element method," in *Industry Applications Society Annual Meeting, 1992., Conference Record of the 1992 IEEE*, 1992, pp. 171-177 vol.1.
- [57] Y. Liao, L. Xu, and L. Zhen, "Design of a doubly fed reluctance motor for adjustable-speed drives," *Industry Applications, IEEE Transactions on*, vol. 32, pp. 1195-1203, 1996.
- [58] E. M. Schulz and R. E. Betz, "Impact of winding and gap flux density harmonics on brushless doubly fed reluctance machines," in *Power Electronics, Machines and Drives, 2004. (PEMD 2004). Second International Conference on (Conf. Publ. No. 498)*, 2004, pp. 487-491 Vol.2.
- [59] M. J. R. Betz. (1998, 02/04/2012). Introduction to Brushless Doubly Fed Reluctance Machines - The Basic Equations. *EE0023*.

## **3 CHAPTER 3 – THE SYNCHRONOUS RELUCTANCE MACHINE AS A BASELINE DESIGN**

---

### **3.1 INTRODUCTION**

Synchronous reluctance (SyncRel) machines, operating directly from AC supplies, have been studied for nearly a century [1], with early designs suffering from the limited performance of magnetic material properties of the time. This resulted in uncompetitive power and torque densities, and limited functionality for many applications compared to induction machines, e.g. reliable direct on-line starting, response to load changes etc. The last 30 years or so has seen a resurgence in interest in SyncRel machines due to advances in both magnetic materials research and in particular high frequency power electronics. One sector of particular interest has been the use of SyncRel in the expanding electric vehicle market [2-4]. SyncRel offer the prospect of high efficiencies, relatively low cost components (notably the absence of permanent magnets) and a robust rotor structure, which lends itself to use in hazardous environments.

The rotor of a SyncRel must exhibit the highest possible degree of magnetic saliency. The design of the rotor can be split into three main groups; axially laminated cruciform, radially laminated and axial flux barrier (AFB). Figure 3.1 shows the three most common topologies of rotor, in all cases for a 4 pole rotor. The simple cruciform rotor has been shown to offer poor performance in terms of average torque and torque ripple. Although offering high levels of inductance ratio, the radially laminated design is difficult to manufacture and also produces large amounts of eddy current losses, due to the laminations running parallel to the airgap field. The favoured rotor for modern reluctance machines therefore is the AFB rotor, which offers large inductance ratios with a relatively simple rotor construction.

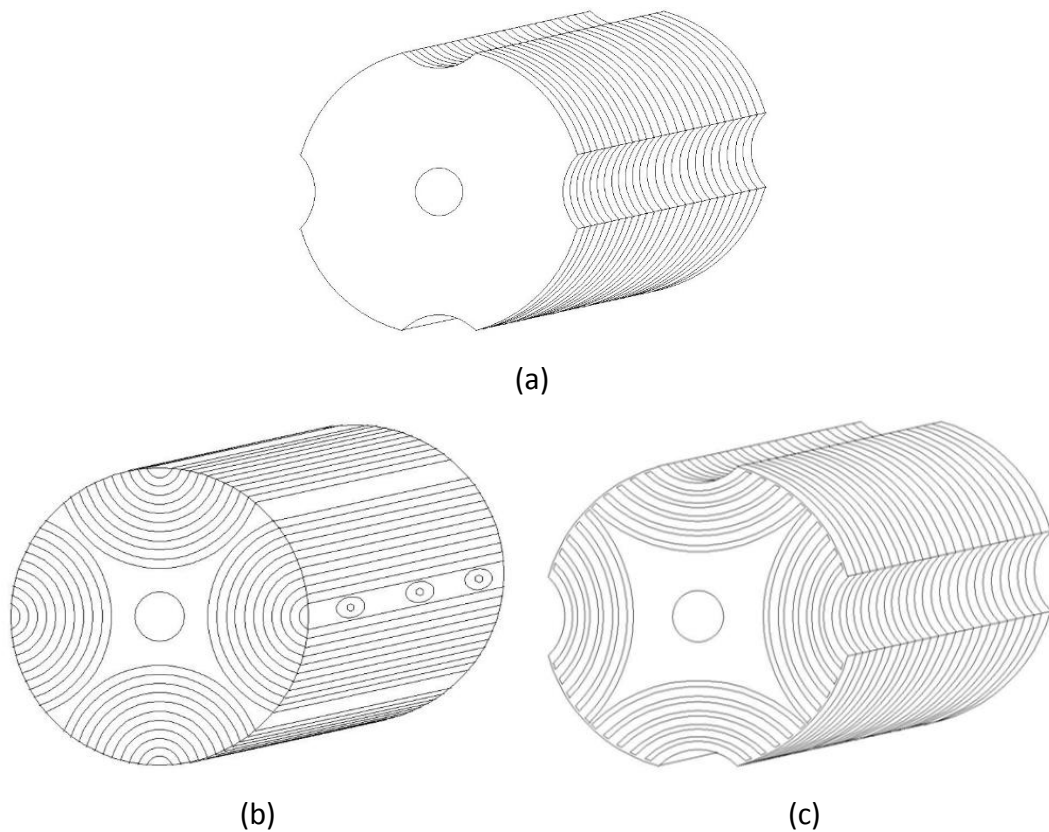


Figure 3.1 Simple cruciform (a), axially laminated (b) and AFB (c) rotor designs

In applications which give rise to modest centrifugal loading of the rotor (i.e. a combination of low rotational speed and diameter), the rotor geometry can be optimised almost solely with regard to electromagnetic torque production, although issues such as manufacturability and parasitic losses in support and clamping structures might also feature. In applications with a combination of rotor diameter and rotational speeds that can give rise to significant localised mechanical stress in regions of the rotor, there is often a need to compromise the electromagnetic performance to ensure the requisite mechanical integrity of the rotor.

As a benchmark for assessing the torque and power density capabilities of a BDFRM, a SyncRel provides a useful singly-fed comparison, when an identical frame size is used.

As a standalone piece of research concerning the SyncRel machine, there is an opportunity to use small amounts of permanent magnets in axial flux barrier rotors to instigate pre-saturation of the structural areas of the rotor. Without these magnets, magnetising current is required to saturate these bridge regions before flux

will travel along the preferred paths. The inductance ratio of the SyncRel is also studied with various rotor rib configurations and current densities to demonstrate the traverse between localised and bulk saturation.

### **3.2 ROTOR OPTIMISATION**

Even with the relatively simple rotor construction of a SyncRel, there are several dimensions which can be optimised, such as the width [5] and number of flux guides. Some previous studies start from a solid rotor cross-section (i.e. no flux barriers) and then determine the most effective barrier layouts by inspection of the flux paths in this solid rotor [6], while other studies have taken an analytical approach to obtaining the optimised rotor design for a particular set of defined output parameters [7].

The axial flux barrier rotor incorporates a series of flux barriers, in the form of slots in the rotor cross-section, which can be filled with non-conducting material, e.g. cast polymer, or simply left as airgaps. At the end of each barrier, a thin section must be used to maintain the single piece nature of the rotor lamination. It is desirable that these connecting sections should have a small magnetic cross-section, such that they saturate at low levels of stator excitation, in order to prevent excess leakage flux.

This chapter includes an assessment of the scope for employing permanent magnets to pre-saturate these regions. Several different permanent magnet enhanced AFB rotor topologies were considered, with varying degrees of benefit being derived.

### **3.3 BASELINE SYNCREL DESIGN**

The baseline synchronous reluctance machine design considered in this chapter is shown in Figure 3.2. The leading dimensions and design features are detailed in Table 3.1, and a winding diagram is shown in Figure 3.3. The four-pole winding consists of three nested coils per pole, with a double-layered arrangement in the slots. The start and direction of the winding diagram of Figure 3.3 is shown as a red line and arrow in Figure 3.2. This SyncRel baseline design studied here has identical dimensions to that of the initial baseline BDFRM used in Section 4.2. Although it is a relatively conventional 3-phase, 36 slot, 4 pole configuration, it is notable for employing Cobalt Iron in the stator and rotor cores. This latter issue, and the significant influence that

magnetic saturation will inevitably bring to bear, does not play to the recognised strengths of synchronous reluctance machines.

Table 3.1 – Leading machine dimensions and design features

Stator Dimensions	(mm)	Rotor Dimensions	(mm)
Stator outer diameter	209	Rotor inner diameter	40
Stator back iron thickness	22	Rotor outer diameter	120
Tooth body height	19	Rotor rib thickness	1.0
Tooth body width	5.5	Active axial length	100
Tooth shoulder height	1	Airgap length	0.5
Tooth tip height	2		
Winding packing factor	0.5	Number of stator slots	36
Dual-layer winding area ratio	1:1	Number of flux barriers	3
Tooth tip to slot pitch ratio	0.8:1	Flux guide:barrier ratio	1:0.67

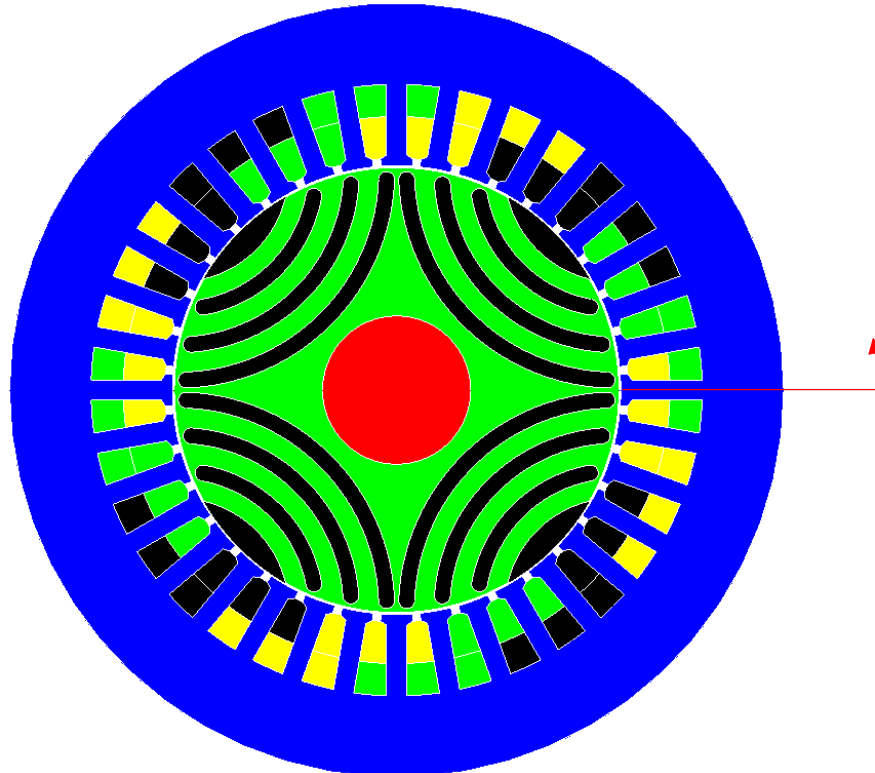


Figure 3.2 – Cross-section of baseline SyncRel with OD of 209mm including the start and direction of the winding diagram in Figure 3.3

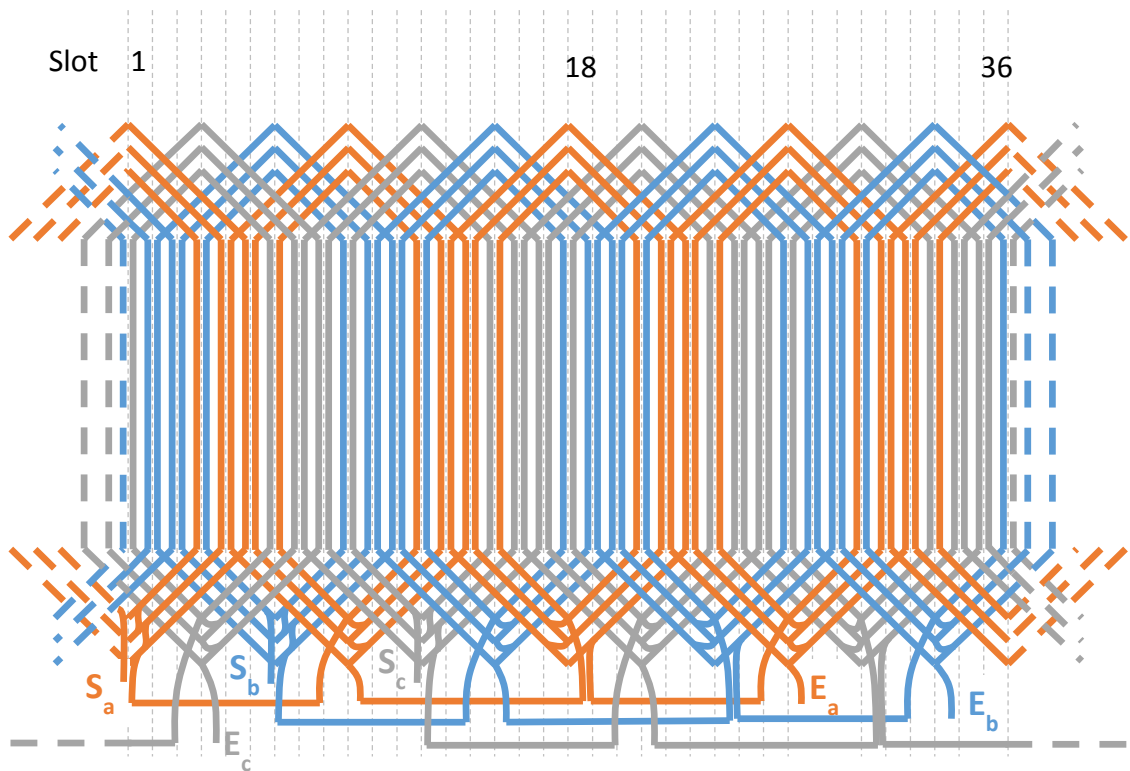


Figure 3.3 – Winding diagram of the baseline SyncRel design with the start (S) and end (E) of each phase indicated

The likely upper limit on the torque capability for this stator design, from the perspective of pure electromagnetic considerations, can be established from an idealised rotor design with no bridging sections as shown in Figure 3.4. Although such a rotor is not impossible to manufacture (e.g. by over moulding the various core regions in a non-magnetic and non-conducting polymer or composite [8]) it is likely to be impractical for applications requiring a robust rotor structure such as high speed operation. It nevertheless provides a useful baseline, against which to judge the degradation in electromagnetic performance with increasing influence from mechanical design considerations.

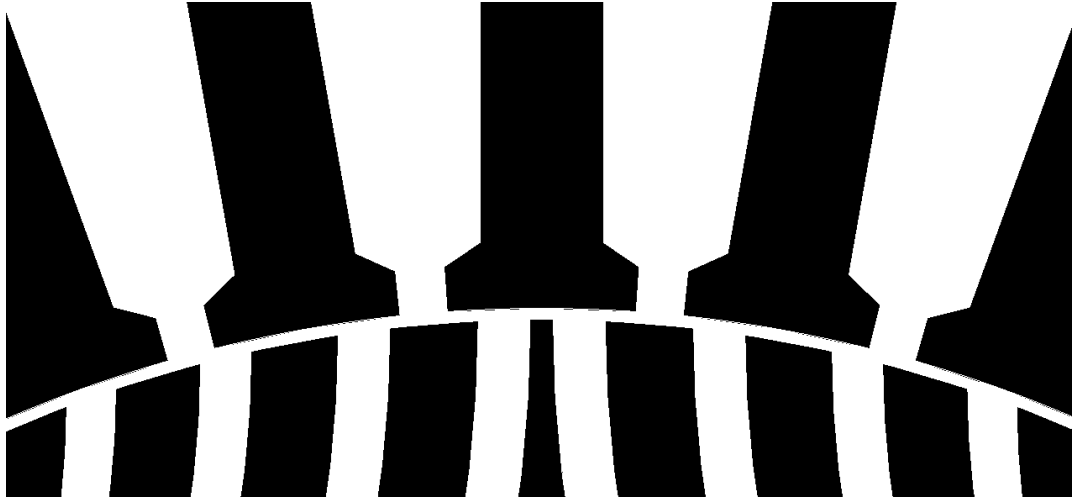


Figure 3.4 – SyncRel rotor design with bridges set to air

It is commonplace to calculate the torque of a SyncRel machine from consideration of the direct ( $L_d$ ) and quadrature ( $L_q$ ) axes inductances [9], e.g. by dividing the power (equation (3.1)) by  $\omega_r$ .

$$P = \frac{3V_s^2}{2\omega_s} \left( \frac{1 - \frac{L_q}{L_d}}{L_q} \right) \sin 2\delta \quad (3.1)$$

The load angle  $\delta$  in equation (3.1) is defined as the angle between the d-axis of the rotor and the position of Phase A peak MMF on the stator. In the case of an ideal SyncRel (i.e. not subject to magnetic saturation) operating in generating mode, the delta should be maintained at  $270^\circ$  electrical (equivalent to  $135^\circ$  mechanical with a two pole pair machine). However, magnetic saturation within the stator and/or rotor core can lead to a shift in this peak torque angle at high current densities. Figure 3.6 shows the two-dimensional finite element calculated static torque as a function of the load angle at three different rms current densities in the stator conductors for the reference design detailed in Table 3.1. As will be apparent, where the optimum delta for generating shifts from around  $135^\circ$  mechanical, at a current density of  $1.41A_{rms}mm^{-2}$ , to  $\sim 160^\circ$  mechanical at a current density of  $10.61A_{rms}mm^{-2}$ .

Additional information about the finite element procedure used throughout this thesis can be found in Appendix 1 (Section 8.1).



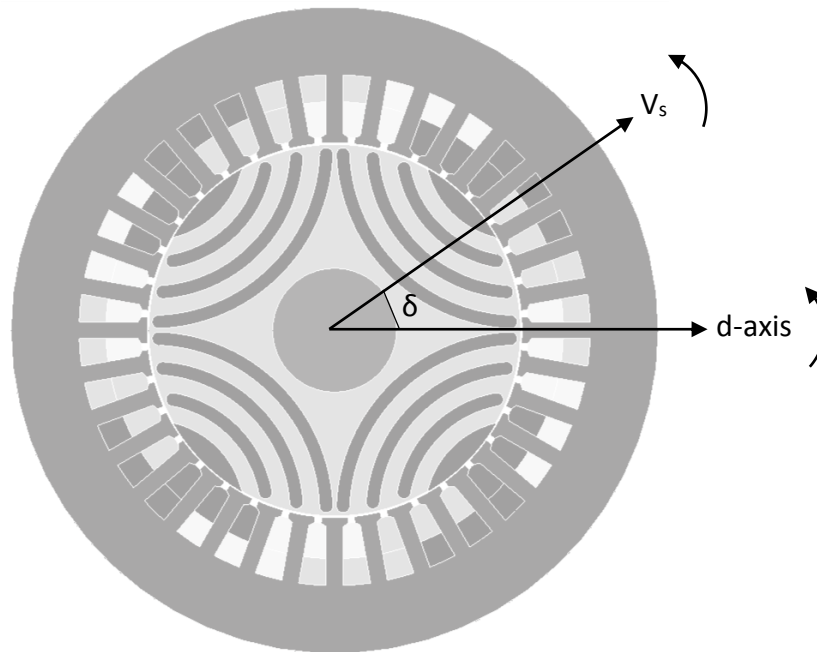


Figure 3.5 – Definition of  $\delta$  used in equation **Error! Reference source not found.**

Figure 3.6 – Average torque as a function of load angle with a range of control winding current densities

In machines subjected to appreciable magnetic saturation, the values of direct and quadrature axis inductance will inevitably vary significantly over the range of operating stator currents. One means of capturing much, but by no means all, of this

behaviour is to calculate these components of self-inductance with current in one phase. Another more accurate route to follow is to control the d- and q-axis currents, by adjusting the three phase currents. This gives a much more accurate representation of how the SyncRel will operate in real world situations, with full appreciation of the saturation effects within the machine.

The resulting saliency ratios for the idealised baseline rotor (where the bridges have been replaced with air) and the electromagnetically optimised rotor design are shown in Figure 3.7. These saliency ratio results are calculated by means of controlling the dq axis currents, in a set of magneto-static FEA solvers. This provides considerable insight into the effect of bulk saturation, notably the marked reduction in saliency ratio at higher levels of excitation, specifically a reduction of 16% from 4.72 to 3.96, for the idealised air bridged rotor case at a current density of  $14.14A_{rms}mm^{-2}$ . As expected, the saliency ratio of the idealised rotor is consistently higher than that of the electromagnetically optimised rotor, due to the leakage through these additional cobalt iron bridges. The initial lower saliency ratio in the cobalt iron bridges case may be attributed to the fact that the bridges have not fully saturated, so a significant leakage flux is flowing between these bridges and the stator teeth.

Although inductance variations with stator current provides a useful insight, ultimately the most significant measure of machine performance is the variation in torque as a function of stator current density. These results were calculated by means of transient magnetic 2D FEA solvers. For the baseline design in which rotor bridges have been incorporated (Figure 3.2) there is, as would be expected, a small penalty incurred in torque performance, compared to the idealised rotor with no bridges. This is illustrated in Figure 3.8, which shows the variation in finite element predicted average torque for both rotor geometries (assuming in all cases that the load angle remains at  $130^\circ$  mechanical for maximum generating torque). At the higher end of the current density range ( $14.14A_{rms}mm^{-2}$ ) the reduction is 4%, which can be attributed to the increased saturation of the main rotor and stator core flux paths from the additional leakage flux. As shown by the torque waveforms in Figure 3.9, which were predicted at a low current density of  $1.41A_{rms}mm^{-2}$ , the behaviour in

terms of torque ripple is similar apart from a discernible increase in rotor slotting harmonics for the design without rotor bridges.

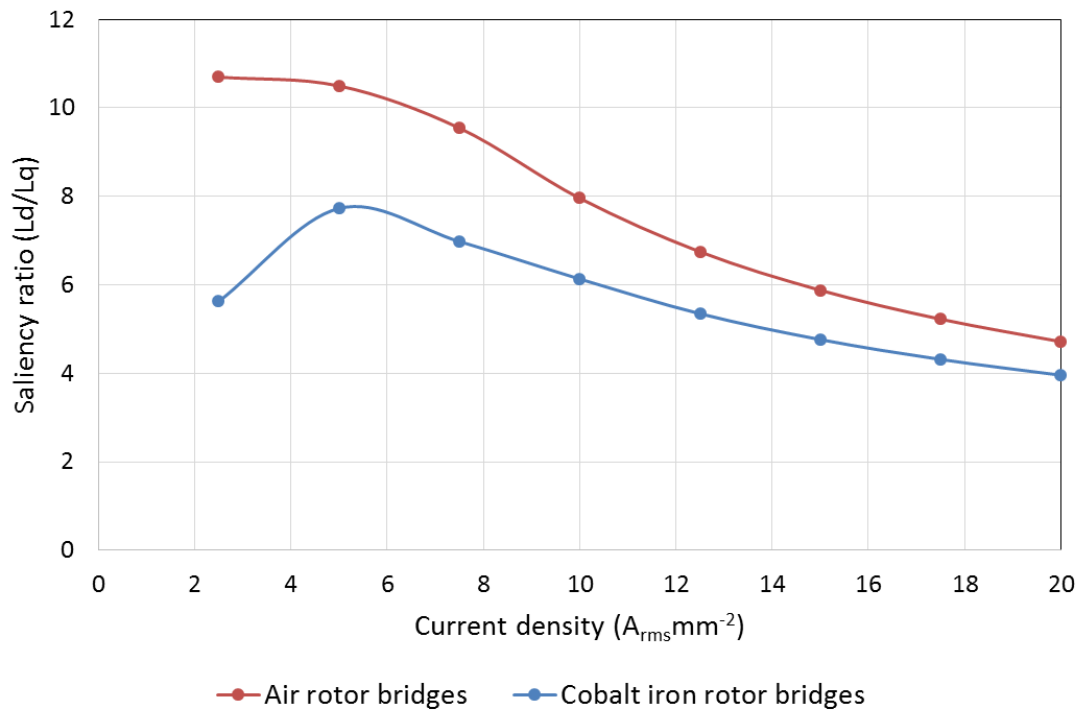


Figure 3.7 – 2D FEA calculated saliency ratio of the SyncRel with an electromagnetically optimised rotor with both air rotor bridges and Cobalt Iron rotor bridges over a range of current densities and a fixed load angle of 135°

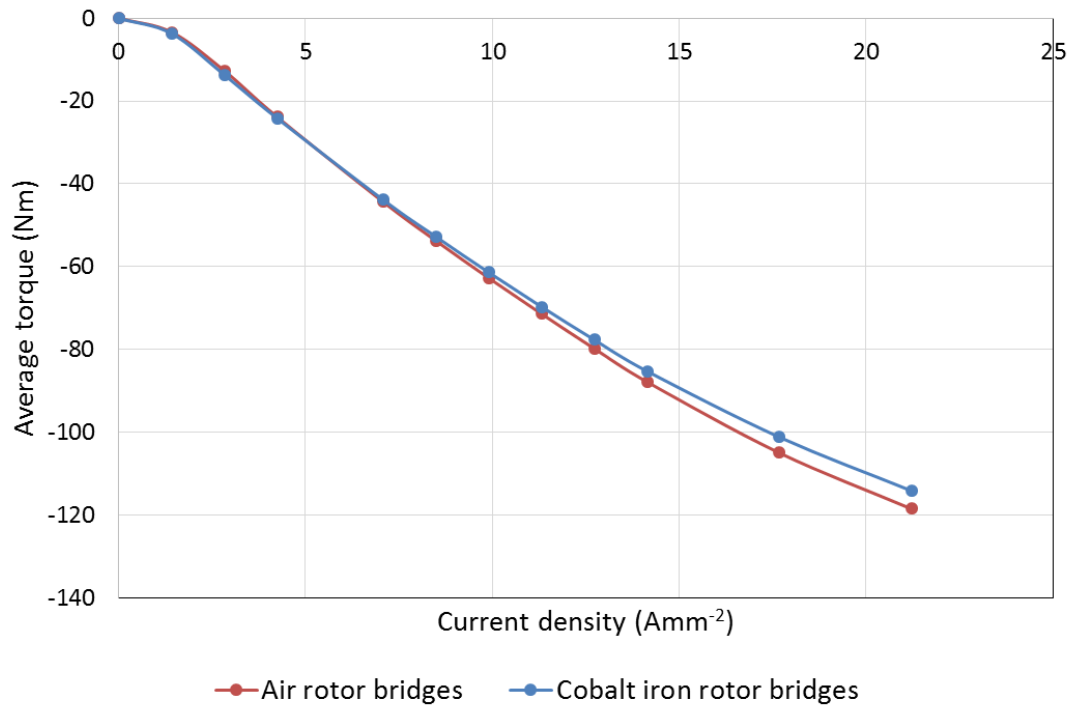


Figure 3.8 – Comparison of 2D FEA calculated torque with and without rotor bridges at a fixed load angle of 130°

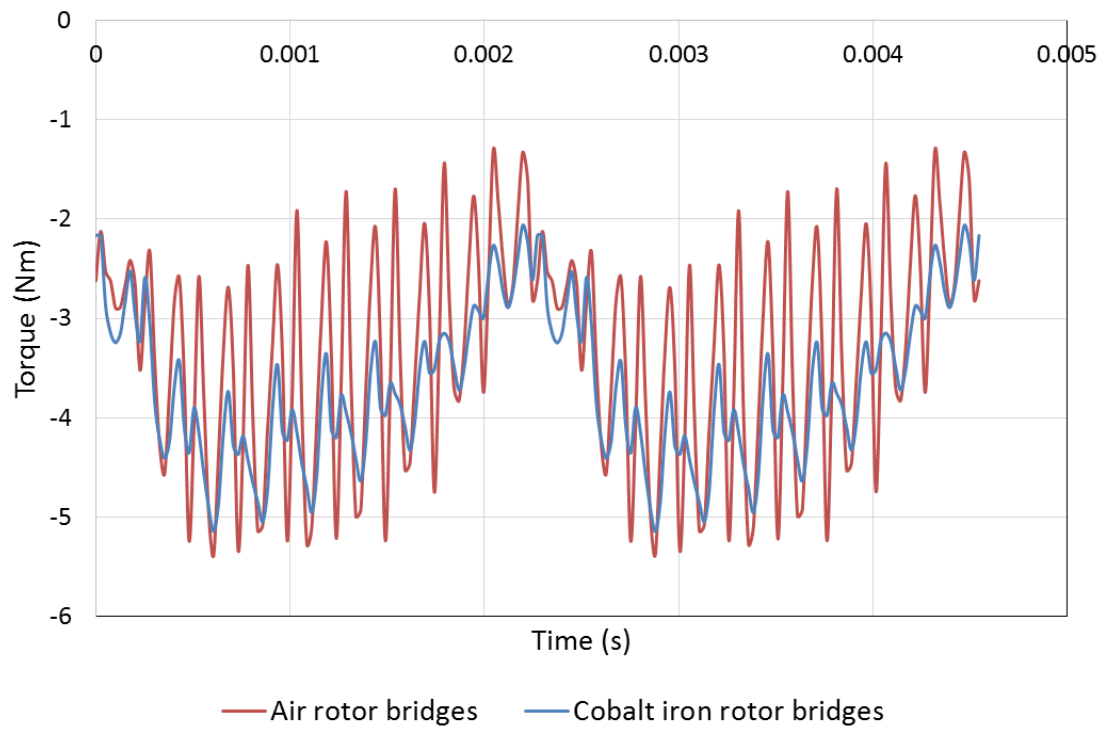


Figure 3.9 – 2D finite element calculated torque waveforms for the SyncRel at a current density of  $1.14A_{rms}mm^{-2}$  and a load angle of 130°

### 3.4 AIRGAP FLUX DENSITY HARMONICS

As will be discussed in more detail in successive chapters, airgap flux density harmonics are a key stepping stone in understanding the operation of BDFRMs. Although the airgap flux density is more straightforward in a SyncRel, due to the presence of only one winding and synchronous operation, an analysis of airgap flux density harmonics in the SyncRel provides a useful starting point.

As expected, a dominant four-pole field in the SyncRel airgap flux density is observed when the airgap flux density of the cobalt iron bridged design is studied (Figure 3.10). As will be apparent from the corresponding Fourier transform of the airgap flux density in Figure 3.11 and Figure 3.12, in addition to this four-pole field, there are significant spatial harmonics in the airgap. The 36 and 72 order harmonics can be attributed to the slotting of the stator core and the reluctance modulation caused by the saturating sections of the rotor respectively. The theory behind the use of this fast Fourier transform may be found in Appendix 2 (Section 8.2).

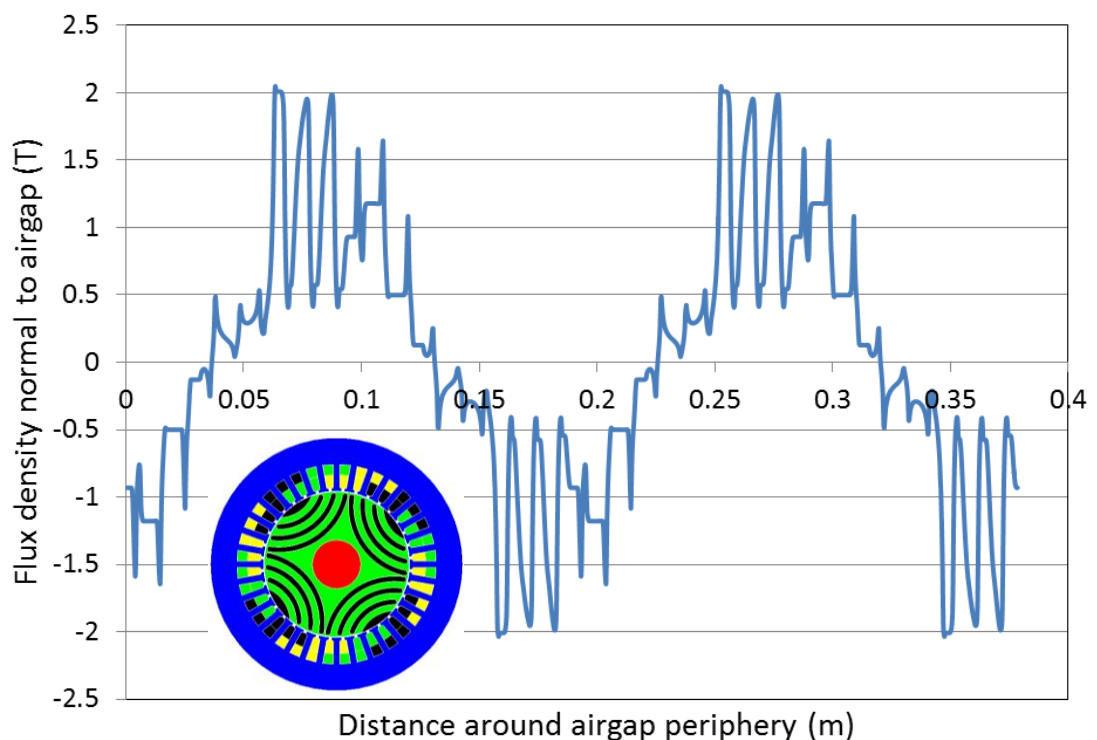


Figure 3.10 – Airgap flux density normal to airgap around rotor periphery of baseline SyncRel machine with control winding currents of  $I_A=0$ ,  $I_B=-612.28\text{A}$  and  $I_C=612.28\text{A}$  and a rotor alignment as displayed

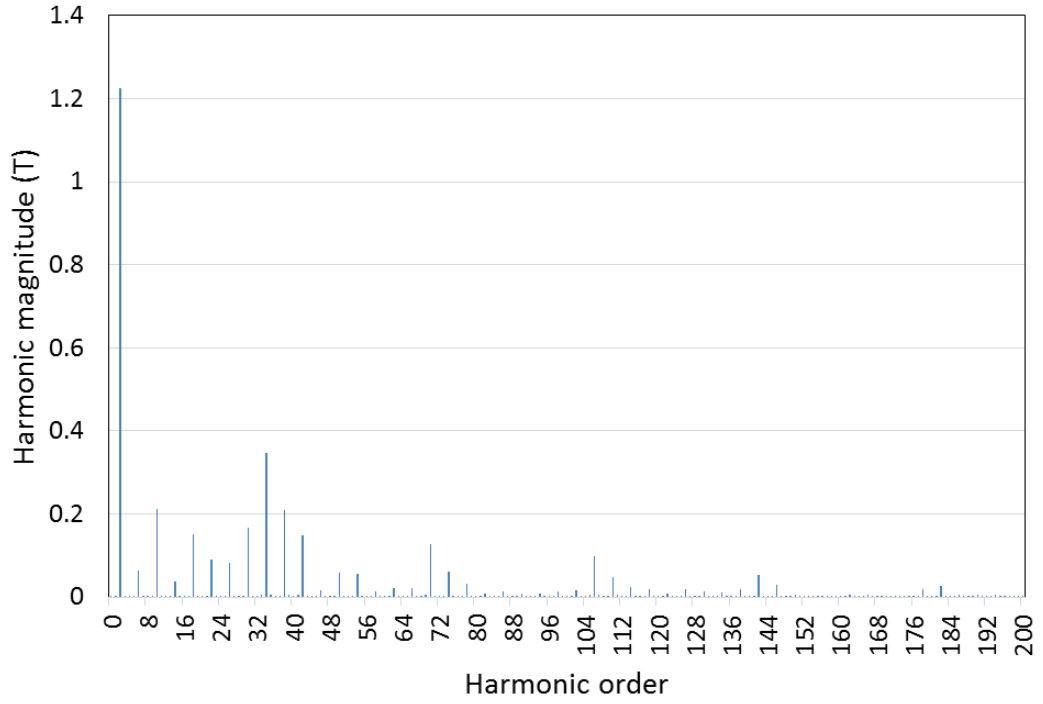


Figure 3.11 – Fourier transform of airgap flux density profile of Figure 3.10

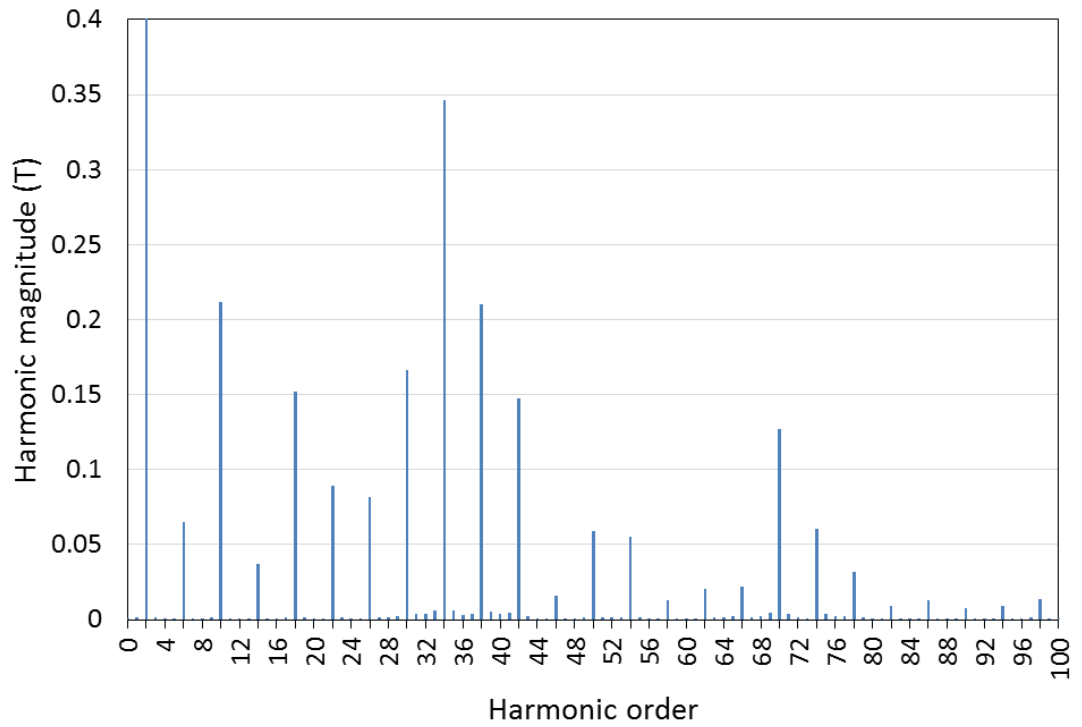


Figure 3.12 – Magnified version of the airgap Fourier transform of Figure 3.11

### 3.5 SYNCREL SCALING STUDY

As with all singly-excited machines, scaling effects can be significant when trying to establish torque densities for particular topologies. It is well known for example that wound field or singly excited machines only become competitive with PM machines at larger frame sizes, where the winding volume required to produce competitive MMF per pole can be accommodated. In order to establish the scaling behaviour of SyncRel machines, seven designs of increasing frame size are considered by applying a linear scaling factor to the dimensions of the baseline design. Only two design parameters remain constant throughout this study, viz. the airgap at 0.5mm and the active axial length at 100mm. It should be noted that alternative scaling methods are available, such as increasing the axial length along with the other dimensions.

Two operating parameters are also maintained at fixed values, the stator current density at  $14.14A_{rms}mm^{-2}$  and the load angle at  $160^\circ$  electrical, which corresponds to the peak generating torque point as found in Figure 3.6. This constant current density leads to an increase in current as the linear dimensions of the slot increase. The remaining key dimensions and weights for the scaled designs are summarised in Table 3.2 (a scaling factor of 1.0 corresponding to the baseline design). In each case, the quoted mass includes the end-windings, which were estimated by taking the cross-section of copper from each slot and extruding this around the periphery of the stator by the relevant angle.

It should be noted at this point that the various scaled designs, which are generated by simple linear scaling from the baseline design, are not necessarily optimal in themselves, and some further optimisation might be possible in each case, albeit that this would be at the expense of a systematic basis for the study.

The finite element predicted power and torque densities for these seven designs are shown in Figure 3.13. The power and torque densities calculated in this figure include the weights of the rotor, stator, slot copper and end windings. As would be expected, there is some improvement in power density with increasing scaling factor, although the advantage with scaling begins to tail off.

Table 3.2 – Leading dimensions and masses of scaled SyncRel designs

Design parameter	Scaling factor						
	1	1.25	1.5	1.75	2	2.5	3
Stator OD (mm)	209	261	313	365	417	521	625
Rotor OD (mm)	120	150	180	210	240	300	360
Stator mass (kg)	14.3	22.2	32.0	43.6	56.9	88.8	127.9
Rotor mass (kg)	4.9	7.6	10.9	14.9	19.4	30.4	43.7
Slot copper mass (kg)	2.3	3.5	5.0	6.8	8.8	13.7	19.7
End winding mass (kg)	1.0	2.0	3.4	5.3	7.9	15.3	26.2

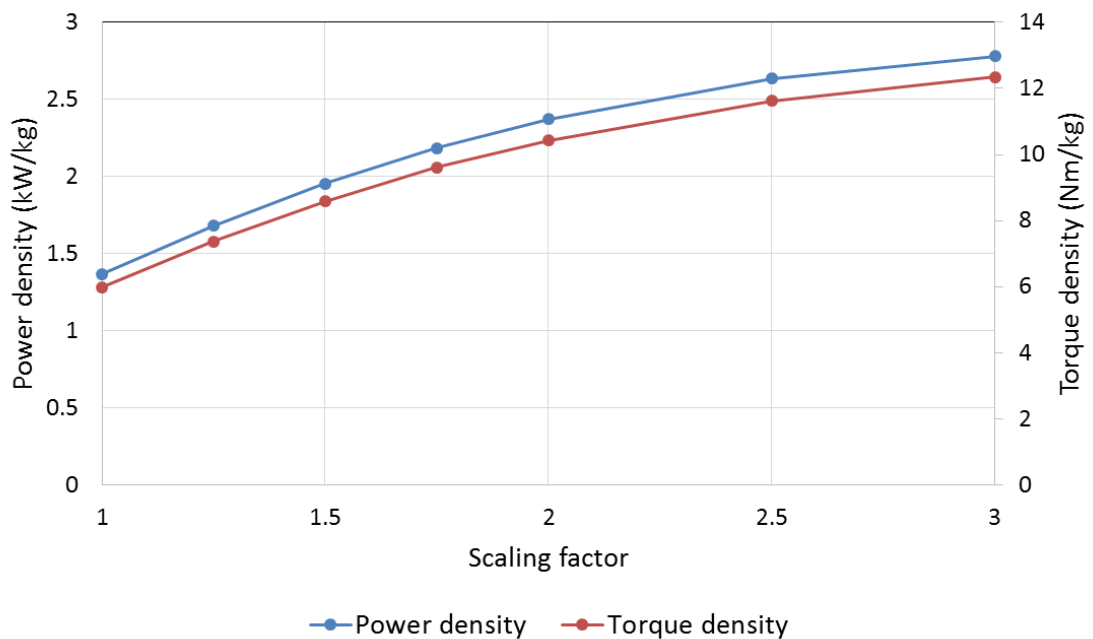


Figure 3.13 – Variation with scaling factor of the torque and power density of the baseline SyncRel at 6,600 rpm including the weight of the end windings

### 3.6 ADDITION OF PERMANENT MAGNETS TO THE BASELINE SYNCREL DESIGN

As noted previously, in order to maintain the single-piece nature of the core cross-section, a series of small bridging regions are necessary to connect various regions of the core together. These bridging regions are not required for electromagnetic purposes, and indeed detract from the saliency ratio of the rotor by promoting unwanted leakage flux. As illustrated in Section 3.3, it is necessary to ensure that these regions are heavily saturated under rated conditions in order to limit the leakage flux and promote the passage of flux through the rotor flux guides.



As proposed in [10], there is scope to employ permanent magnets within the salient rotor structure in order to pre-saturate the bridging regions (i.e. ensure they are saturated at zero stator excitation). However, the PM configuration proposed in [10], which is shown in Figure 3.14, can also result in saturation in the main flux path of the rotor, in turn leading to some compromising of the potential advantages of incorporating PMs. Moreover, the rotor barriers were completely filled with PM material, leading to additional mass and a significant additional cost of manufacture.

The incorporation of PMs into the rotor can also provide a route to improving the power factor, as demonstrated by Vartanian et al. [11], in turn leading to a reduction in the required converter rating. However, in this case, the PMs provide a source of excitation flux to increase the saliency ratio, rather than being incorporated to promote localised magnetic saturation.

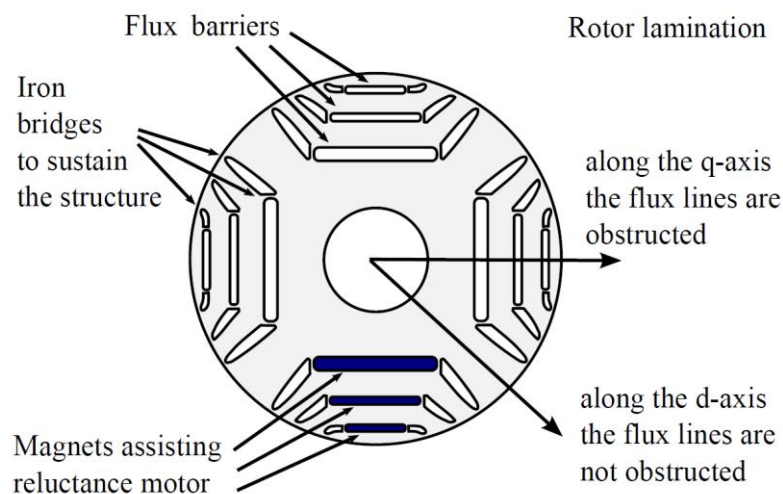


Figure 3.14 - Permanent magnet arrangement taken from [10]

In assessing the scope for incorporating PMs into the rotor, due account may need to be taken of the need to incorporate additional mechanical ribs (as illustrated later in Section 5.6). This can limit the locations and size of the magnets.

The location, size and direction of magnetisation of the PMs are all important factors in ensuring that the rotor bridges are sufficiently saturated, so as to avoid desaturation under normal operating conditions, as well as minimising the degree of saturation of the main flux path through the rotor. In addition, the design requires consideration of the need to avoid irreversible demagnetisation.

For the baseline SyncRel considered in this chapter (whose leading dimensions were summarised in Table 3.1), the magnet arrangement shown in Figure 3.15 was adopted. The magnets are 4.3mm along their longest side 2.1mm tall and span the full 100mm axial length of the machine. Adjacent magnets are all of the same pole type to avoid unwanted saturation in the main flux paths of the rotor. The resulting finite element predicted magnetic field distribution for this arrangement is shown in Figure 3.16 for zero stator excitation. This illustrates the effectiveness of the magnets in both achieving localised saturation and limiting the region over which saturation occurs.

The resulting torque produced with this arrangements of PMs was calculated from a series of magneto-static finite element field calculations. The resulting torque waveform is shown in Figure 3.17, alongside the corresponding waveform for the original baseline design at a modest current density of  $1.41A_{rms}mm^{-2}$ . At this level of excitation, the inclusion of the PMs results in an increase in average torque of 10%, while at the same time achieving a reduction of 10% in the magnitude of the torque ripple.

However, these benefits do not remain constant over the full range of stator current densities, as illustrated by Figure 3.18, which shows the torque benefits achieved by incorporating PMs as a function of current density. As would be expected, the benefits are more pronounced at lower excitation levels, where the pre-saturation is useful. However, some benefits are still gained at the upper end due to the reduced leakage component of flux in the main flux paths.

Along with modest improvements in average torque, the torque ripple is more appreciably reduced (by up to 23% at higher current densities of  $14.14A_{rms}mm^{-2}$ ), as seen in Figure 3.19.

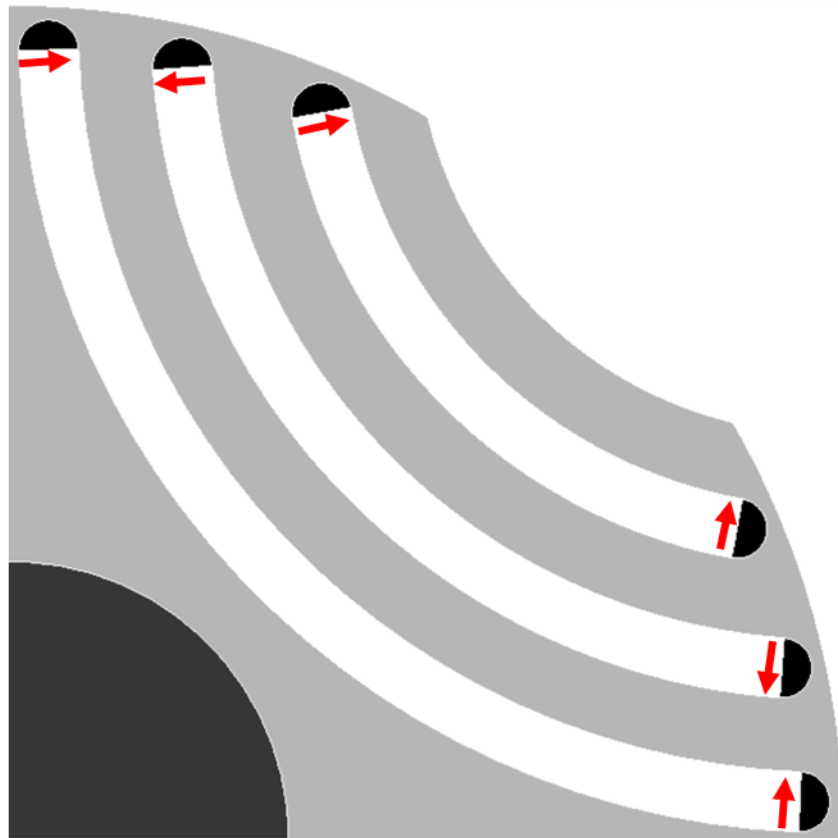


Figure 3.15 – PM magnetisation orientation in the electromagnetically optimised rotor

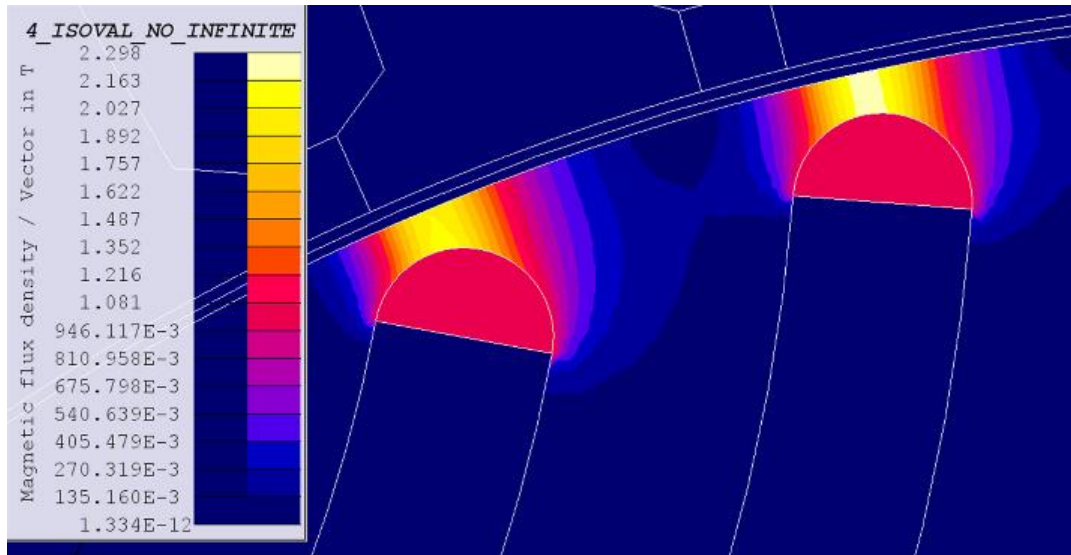


Figure 3.16 – Magnet saturation of the rotor bridges

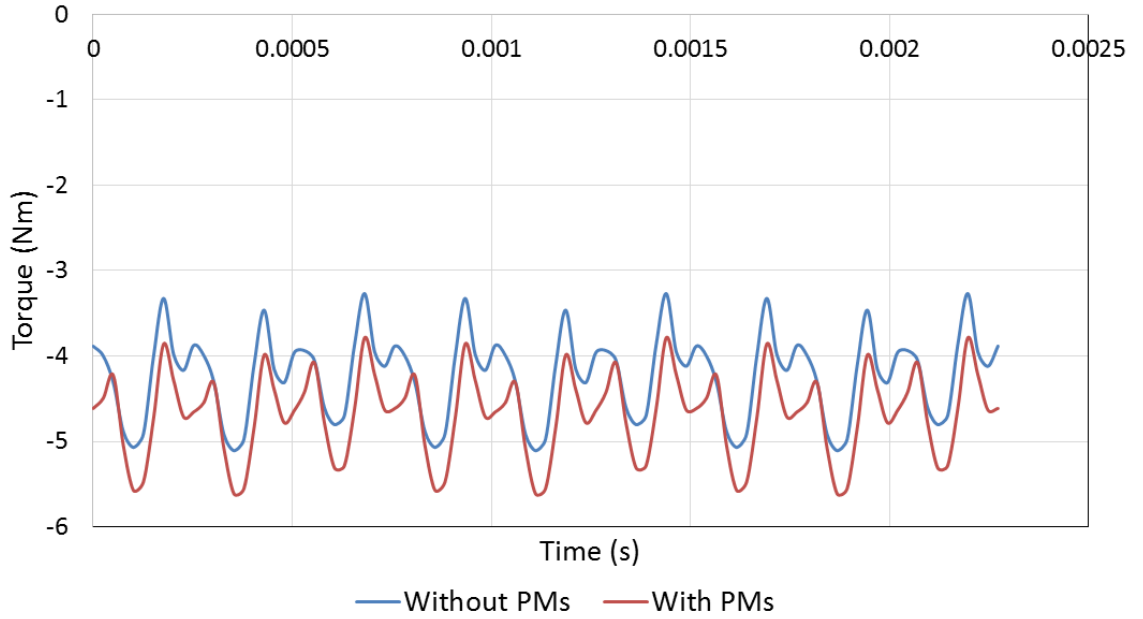


Figure 3.17 – 2D FEA calculated torque for the electromagnetically optimised rotor with and without PMs at a current density of  $1.41A_{rms}mm^{-2}$  and a load angle of  $130^\circ$  and a rotor speed of 6,600rpm

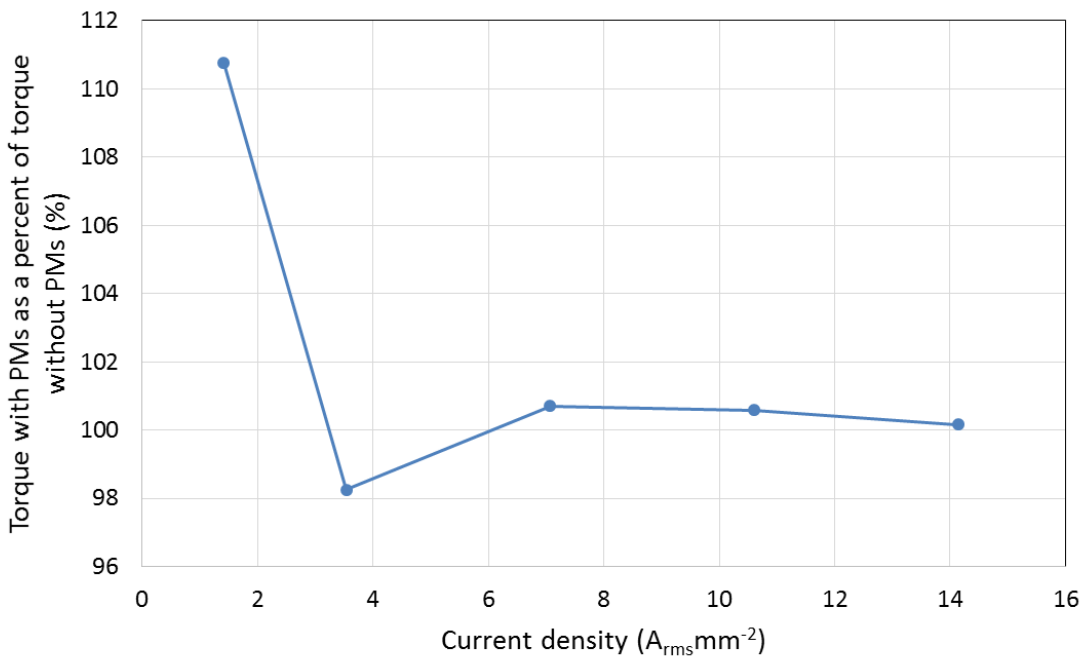


Figure 3.18 – 2D FEA calculated change in torque from a baseline without PMs (set to 100%) to a model with the addition of PMs for the electromagnetically optimised rotor over a range of current densities at a rotor speed of 6,600rpm

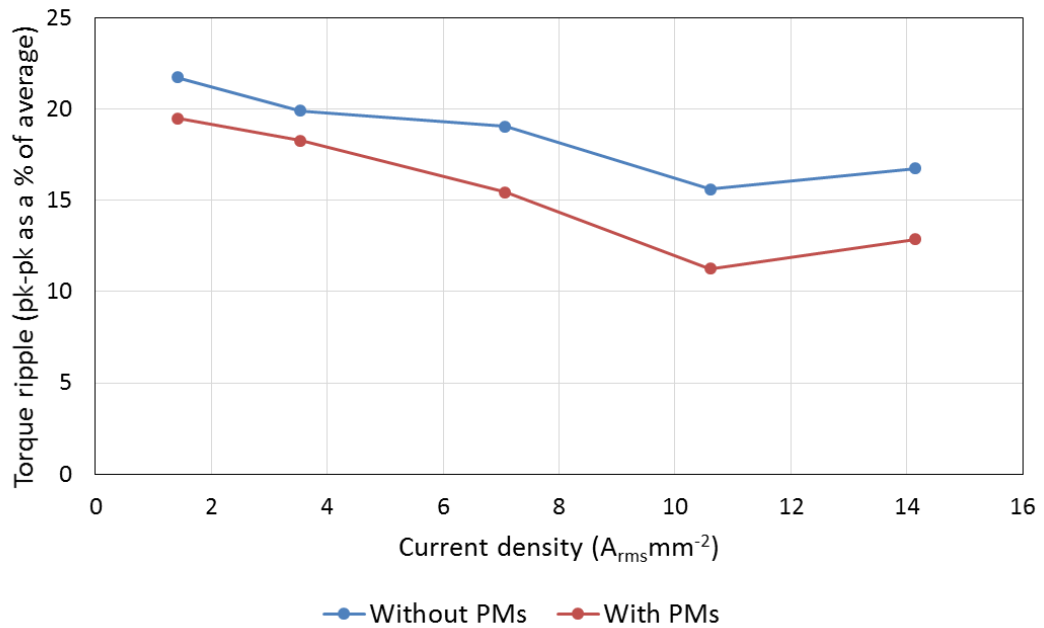


Figure 3.19 – 2D FEA calculated torque ripple produced over a range of current densities with and without the addition of PMs with an electromagnetically optimised rotor with a speed of 6,600rpm

### 3.7 MECHANICALLY OPTIMISED ROTOR DESIGN

Although the baseline design of the rotor is well-suited from an electromagnetic point of view to maximising torque, the structure is not well-suited to withstanding high mechanical loadings, which can occur in high speed applications. In fact, as will be covered more thoroughly in Chapter 5, the electromagnetically optimised rotor design would critically deform at only a third of the intended top speed for the BDFRM.

With this in mind, additional cross-barrier supports must be included to avoid this deformation (Figure 3.20). As these extra supports span the flux barriers, a reduction in performance would be expected, as confirmed in Figure 3.21, where the torque of the SyncRel has reduced to 80% of the original electromagnetically optimised design (at a current density of  $14.14A_{rms}mm^{-2}$ ), due to the flux traversing the cross-barrier supports rather than remaining in the flux guides. Further information on the optimisation study of the mechanical design of this rotor may be found in the BDFRM optimisation chapter (Section 5.6) of this thesis.



Figure 3.20 – Mechanically optimised rotor design

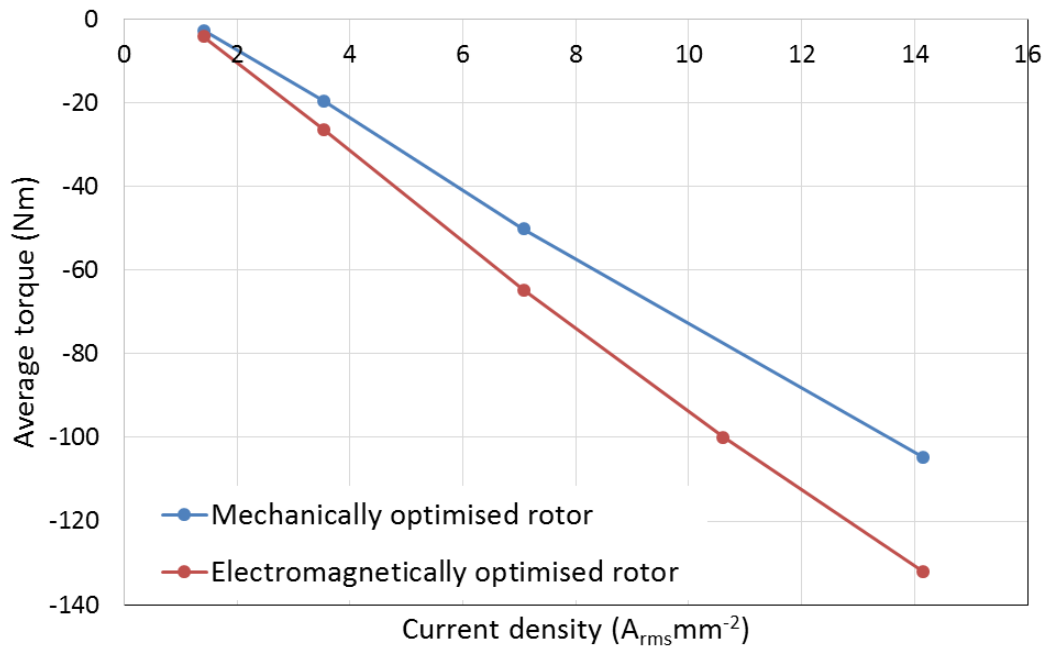


Figure 3.21 - Torque comparison between a mechanically optimised and electromagnetically optimised SyncRel rotor over a range of control winding current densities and a rotor speed of 6,600rpm

### 3.8 ADDITION OF PMs TO MECHANICALLY OPTIMISED ROTOR DESIGN

As with the baseline design, PMs can be incorporated into the flux barriers to pre-saturate the additional supporting ribs. One arrangement, which was found to produce saturation in the cross-barrier supports and hence improve the electromagnetic torque capability of the machine, is shown in Figure 3.22.

Figure 3.23 shows the resulting finite element predicted flux density distribution in the rotor at zero stator excitation. As will be apparent, the flux density at the midpoint of each supporting rib is  $\sim 2.2\text{T}$  (exhibiting significant if not complete magnetic saturation in Cobalt Iron), while the flux density in the centre of each flux guide is close to  $0\text{T}$ . The variation in torque for this design as a function of stator current density is shown in Figure 3.25, alongside that for the mechanically optimised rotor with no PMs. As will be apparent, including PMs results in an increase in torque at a current density of  $1.41\text{A}_{\text{rms}}\text{mm}^{-2}$  from  $2.8\text{Nm}$  to  $4.35\text{Nm}$  (a 55% increase). The gap narrows at the upper end of the current density range ( $14.14\text{A}_{\text{rms}}\text{mm}^{-2}$ ), to a still appreciable, 3.6%. In addition, the torque ripple is reduced across the whole current density range, as may be seen in Figure 3.26. Table 3.3 provides a summary of these gains in torque, and reductions in torque ripple found for machines incorporating PMs across a range of current densities.

This study provides a sound baseline in the performance effects of adding PMs to the reluctance rotors of SyncRels, and suggests that the knowledge gained here could be transferred to the BDFRM in a later chapter.

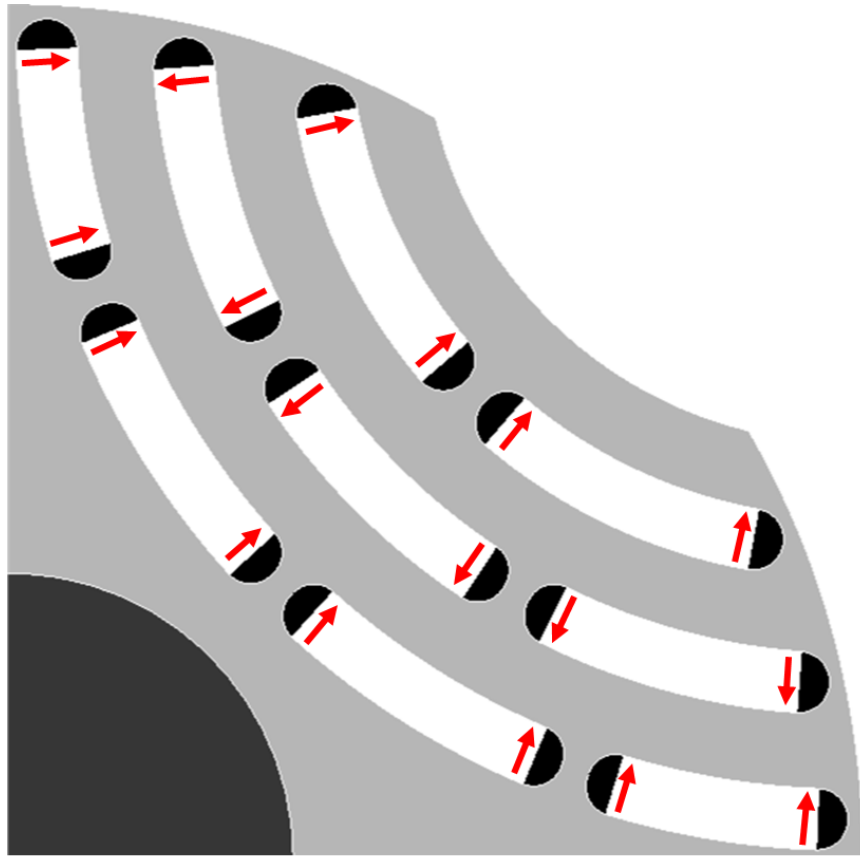


Figure 3.22 - Location and magnetisation of PMs in the mechanically optimised rotor design



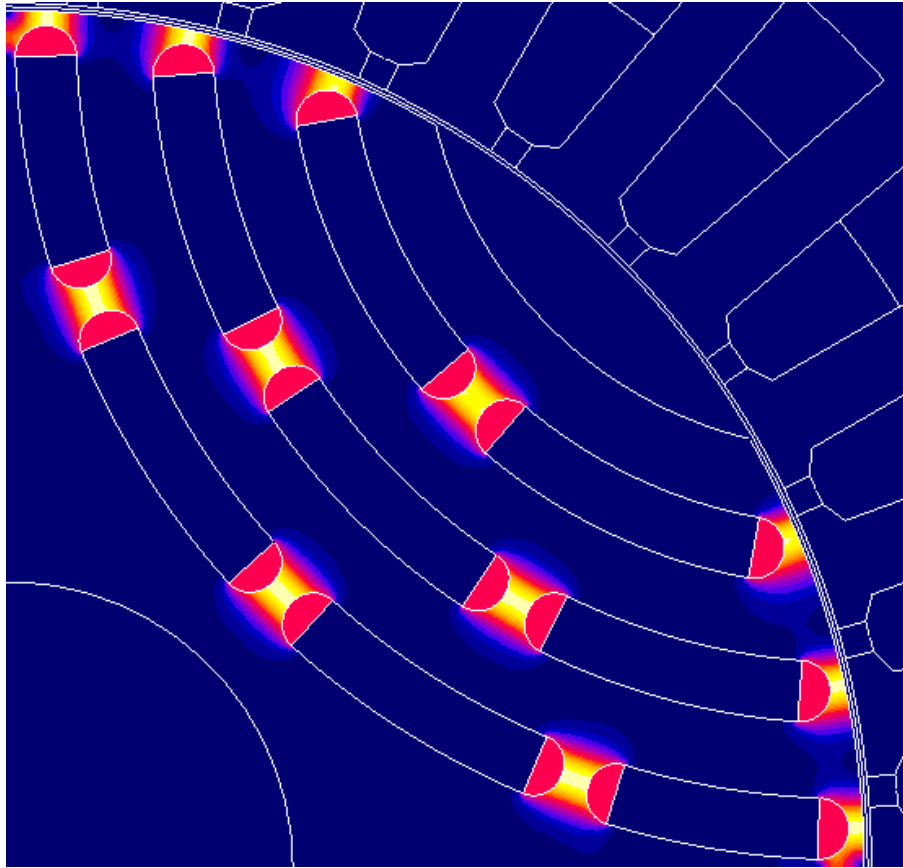


Figure 3.23 – Finite element predicted flux density distribution for a mechanically optimised rotor with permanent magnets

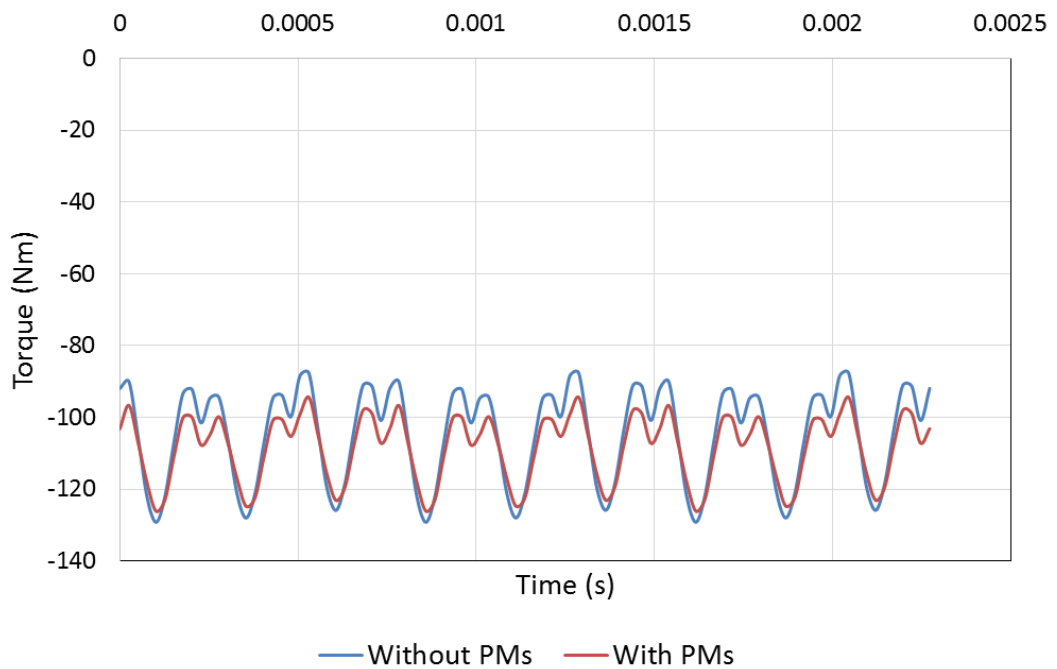


Figure 3.24 – 2D FEA calculated torque in the baseline SyncRel design with a mechanically optimised rotor at 6,600rpm with and without the addition of PMs at a current density of  $14.14A_{rms}mm^{-2}$

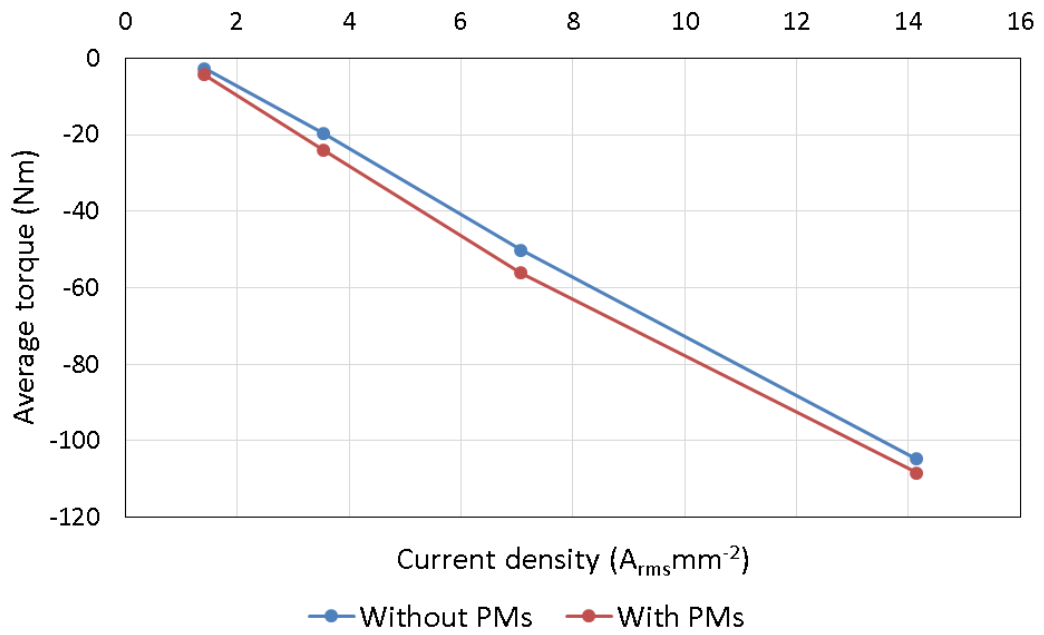


Figure 3.25 – 2D FEA calculated torque in the baseline SyncRel design with a mechanically optimised rotor at 6,600rpm with and without the addition of PMs across a range of current densities

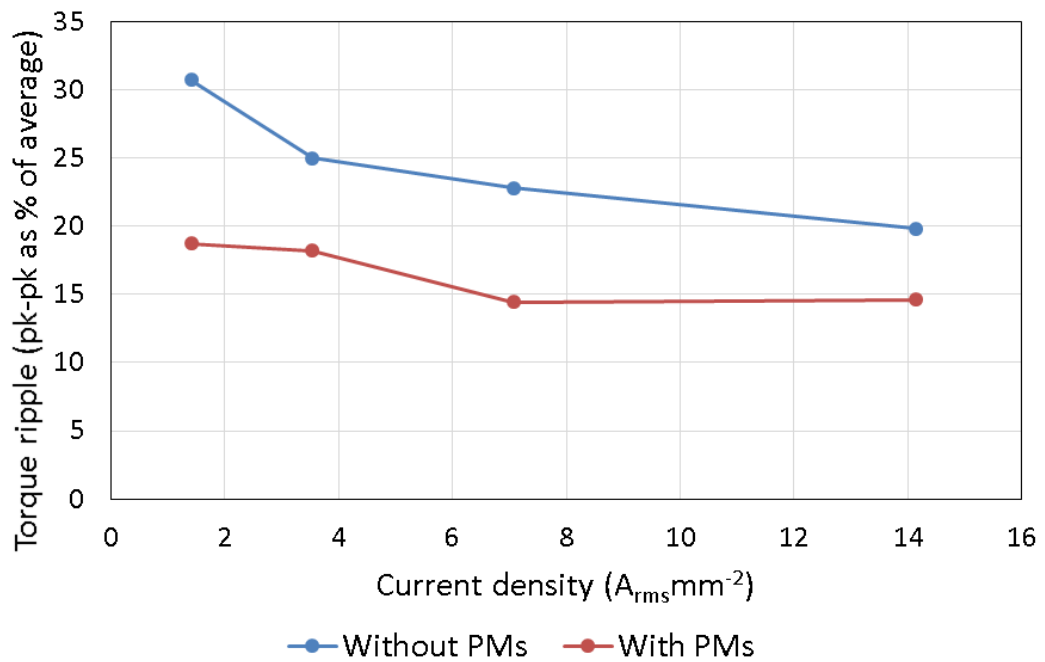


Figure 3.26 – 2D FEA calculated torque ripple as a percentage of the average torque across a range of current densities in the baseline SyncRel design with a mechanically optimised rotor at 6,600rpm with and without the addition of PMs

Table 3.3 – Comparison of torque with and without the addition of magnets to a mechanically optimised rotor at 6,600rpm across a range of current densities

Current Density ( $A_{rms}mm^{-2}$ )	Mechanically optimised rotor		Addition of PMs	
	Average torque (Nm)	Torque ripple (pk-pk as % of average) (%)	Average torque (Nm)	Torque ripple (pk-pk as % of average) (%)
1.41	-2.80	61.46	-4.35	37.48
3.54	-19.61	49.94	-24.07	36.38
7.07	-50.14	45.60	-56.20	28.84
14.14	-104.72	39.68	-108.44	29.24

### 3.9 CHAPTER 3 SUMMARY

This chapter has provided some background of the SyncRel machine, and has produced a baseline characterised design to use in future comparisons with the BDFRM.

Also, novel placement of magnets to pre-saturate the iron bridges has led to improvements in output power, average torque and torque ripple over the baseline SyncRel design.

Finally, a mechanically optimised rotor is used in place of the electromagnetically optimised design. Permanent magnets were then added to this rotor design, leading to appreciable improvements in electromagnetic performance.

### 3.10 REFERENCES

- [1] J. K. Kostko, "Polyphase reaction synchronous motors," *American Institute of Electrical Engineers, Journal of the*, vol. 42, pp. 1162-1168, 1923.
- [2] S. Taghavi and P. Pillay, "A core analysis of the synchronous reluctance motor for automotive applications," in *Electrical Machines (ICEM), 2014 International Conference on*, 2014, pp. 961-967.
- [3] M. Morandin, E. Fornasiero, N. Bianchi, and S. Bolognani, "A robust integrated starter/alternator drive adopting a synchronous reluctance machine for automotive applications," in *Transportation Electrification Conference and Expo (ITEC), 2014 IEEE*, 2014, pp. 1-6.
- [4] Ricardo. (2015, 17/03/2015). Ricardo develops next-generation electric vehicle motor.
- [5] T. A. L. Takayoshi Matsuo, "Rotor Design Optimization of Synchronous Reluctance Machine," *IEEE Transactions on Energy Conversion*, vol. 9, pp. 359-365, 1994.
- [6] S. Yammine, C. Henaux, M. Fadel, S. Desharnais, and L. Calegari, "Synchronous reluctance machine flux barrier design based on the flux line patterns in a solid rotor," in *Electrical Machines (ICEM), 2014 International Conference on*, 2014, pp. 297-302.
- [7] R. R. Moghaddam and F. Gyllensten, "Novel High-Performance SynRM Design Method: An Easy Approach for A Complicated Rotor Topology," *Industrial Electronics, IEEE Transactions on*, vol. 61, pp. 5058-5065, 2014.
- [8] P. B. Reddy, K. Grace, and A. El-Rafaie, "Conceptual Design of Sleeve Rotor Synchronous Reluctance Motor for Traction Applications," *IEMDC 2015*, 2015.
- [9] T. J. J. Pyrhönen, V. Hrabovcová, *Design of Rotating Electrical Machines*, 2nd edition ed.: Wiley, 2014.
- [10] N. Bianchi, E. Fornasiero, M. Ferrari, and M. Castiello, "Experimental comparison of PM assisted synchronous reluctance motors," in *Energy Conversion Congress and Exposition (ECCE), 2014 IEEE*, 2014, pp. 4499-4506.
- [11] R. Vartanian, H. A. Toliyat, B. Akin, and R. Poley, "Power factor improvement of synchronous reluctance motors (SynRM) using permanent magnets for drive size reduction," in *Applied Power Electronics Conference and Exposition (APEC), 2012 Twenty-Seventh Annual IEEE*, 2012, pp. 628-633.

## **4 CHAPTER 4 – INVESTIGATION OF BDRFM ATTRIBUTES AND DESIGN FEATURES**

---

### **4.1 INTRODUCTION**

This chapter explores some of the key electromagnetic design features which are important in determining the performance of BDRMs, with particular reference to achieving the high power densities required for the target application. In many cases, there are general statements in published literature on some of these aspects, but little supporting quantitative or systematic evidence. As a pre-requisite for the design optimisation described in Chapter 5, several important aspects of design were systematically investigated, within the context of a reference BDRM machine design.

### **4.2 BASELINE DIMENSIONS**

To provide a consistent basis for comparing machine designs and performance in several chapters of this thesis, the baseline set of leading dimensions summarised in Table 4.1 were adopted. Although a nominal stator outer diameter of 209mm was chosen, this value was adjusted in proceeding sections due to ongoing optimisations throughout the PhD. The value of stator outer diameter only varies between 206-209mm, and the slot depth and airgap length remain constant throughout this chapter. In each section of this chapter, the stator outer diameter will be stated to make clear the value used. The lamination material chosen for the following studies was a Vacuumschmelze Cobalt Iron (VACOFLUX50), with a BH curve as shown in Figure 4.1.

Throughout this thesis, a pole number combination of 2/4/6 will be used, which corresponds to a 2-pole control winding, 4-pole rotor and a 6-pole power winding. This combination was chosen due to the high speed aerospace application, which lends itself to requiring a low pole number to produce a relatively low output frequency within the VF range [1]. One major downfall of this pole number combination is the subharmonic content of the power winding voltage waveform due

to the saturation induced 3<sup>rd</sup> harmonic in the control winding linking directly to the 6-pole power winding [2]. The only lower alternative pole number combination which would allow the coupling method discussed in Section 2.9 is a 2/3/4 combination. Although this would be advantageous in the high speed aerospace application of this thesis, the odd number of rotor poles could lead to unbalanced magnetic pull, thus leading to a reduction in bearing life and excess noise.

The winding diagram for the baseline BDFRM design is shown in Figure 4.2, with Figure 4.3 outlining the location of slot one and the numbering direction.

Table 4.1 – Design parameters of the initial baseline design

Design parameter	Value (mm)
Stator outer diameter	209
Rotor outer diameter	120
Stator and rotor core axial length	100
Airgap length	0.5

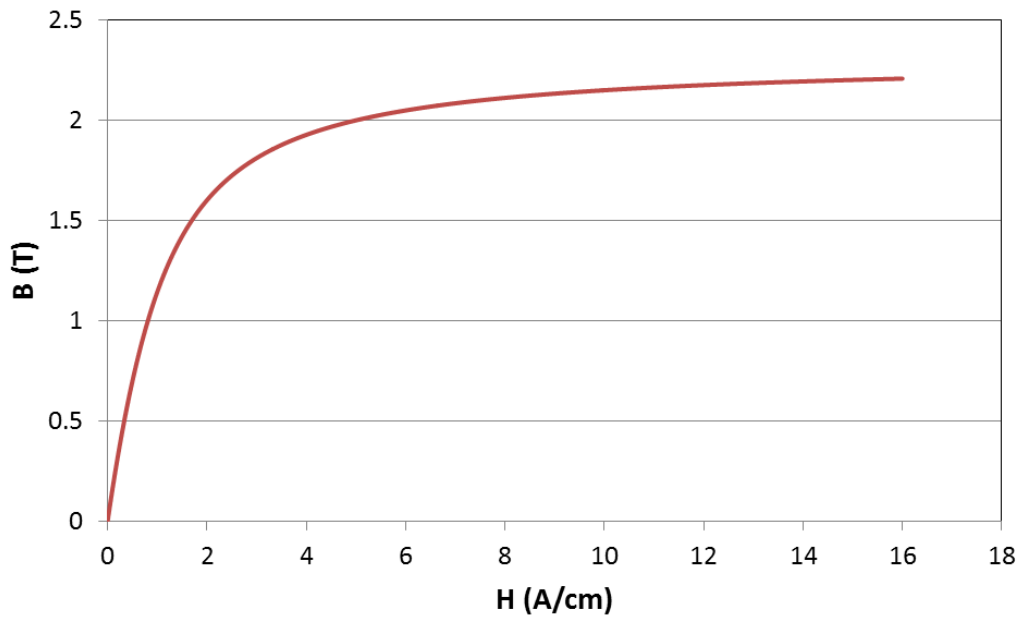


Figure 4.1 – BH curve of Vacuumschmelze VACOFLUX50 Cobalt Iron [3]

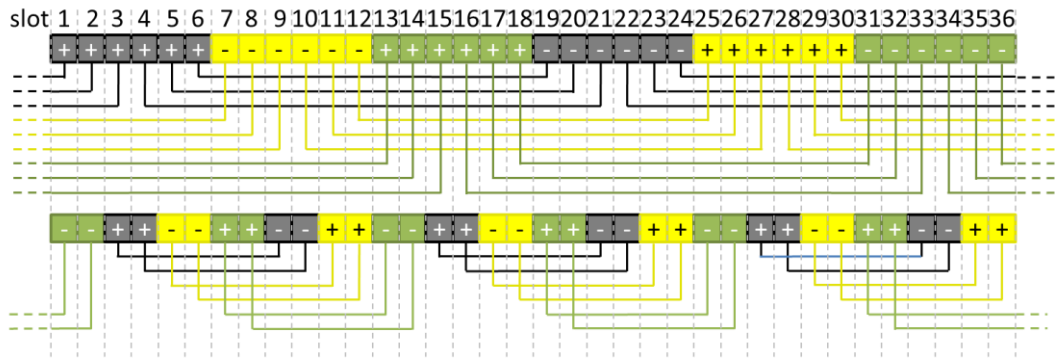


Figure 4.2 – Power and control winding diagram for the baseline BDFRM

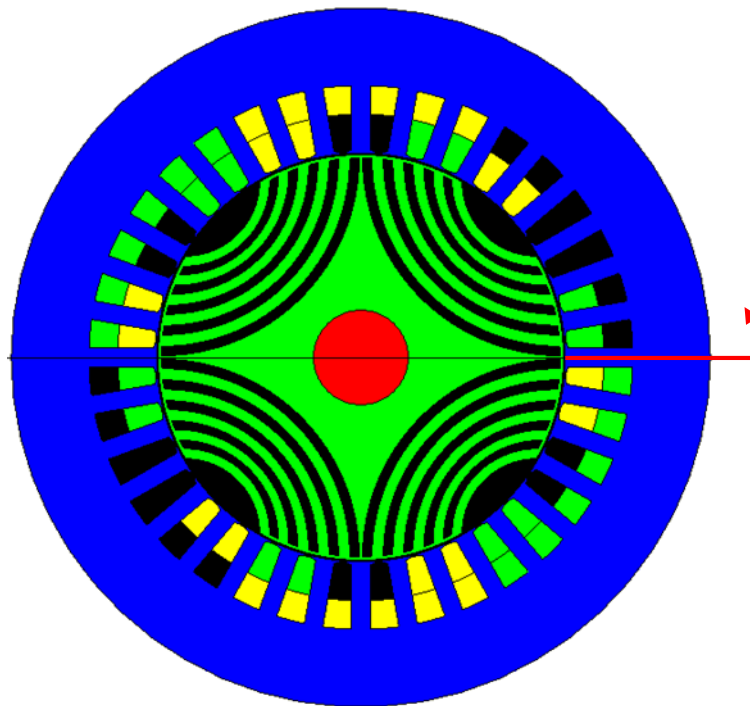


Figure 4.3 – Cross-section of the baseline BDFRM to demonstrate the location of slot one and direction of slot numbering for the winding diagram of Figure 4.2 where the colours refer to the following phases; Black – A, Green – B, Yellow – C

### 4.3 ASSESSMENT OF ROTOR GEOMETRIES

As noted in Section 2.8.3, there are 3 geometries of rotors which are suitable for SyncRel machines and BDFRMs, specifically the simple cruciform, the axially laminated and the axial flux barrier (AFB). Rotors based on axial laminations do not lend themselves to high speed applications, such as the proposed VF generator, where speeds of the order of 14,400rpm will be encountered. Of the remaining two geometries, there are two aspects of performance that will be key in determining which is best suited to the target application:

- Magnitude of power winding voltage at a given control current density
- Harmonics produced in the power winding output voltage

#### 4.3.1 REFERENCE MACHINE AND ROTOR DESIGNS

In order to explore these factors within the context of the target applications, initial four-pole rotor designs were established for use in combination with the same 36 slot stator having the key dimensions listed in Table 4.1. Cross-sections through the resulting machine designs are shown in Figure 4.4 and Figure 4.5.

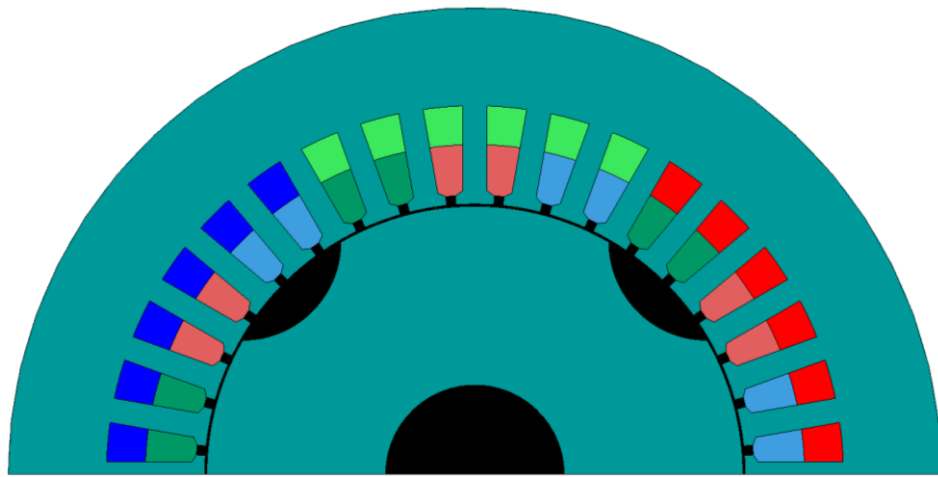


Figure 4.4 – BDFRM design with cruciform rotor and reference dimensions of Table 4.1

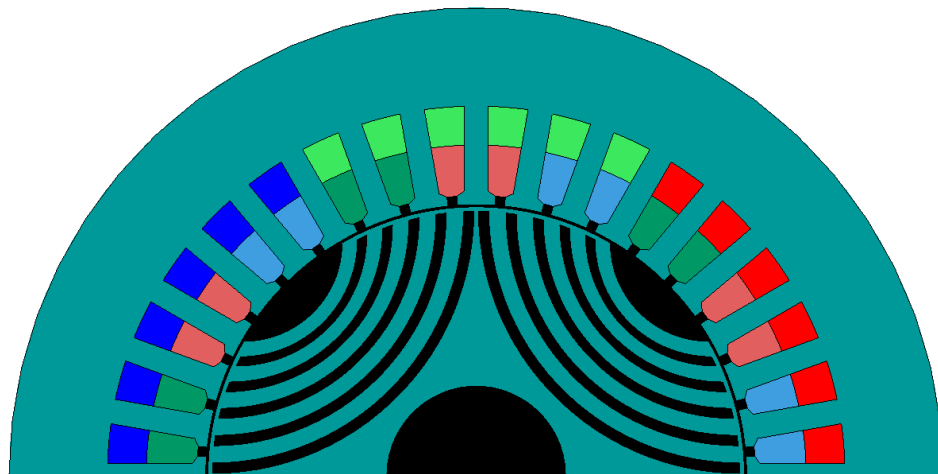


Figure 4.5 – BDFRM design with AFB rotor and reference dimensions of Table 4.1



#### 4.3.2 COMPARISON OF POWER WINDING VOLTAGE MAGNITUDE AT A GIVEN CONTROL CURRENT DENSITY

A series of time-stepped finite element simulations were performed for increasing values of control winding current density, for the following operating point:

- Rotor mechanical speed – 6,600rpm
- Control winding frequency – 40Hz (contra-rotating)
- Open-circuit power winding

In each test case of this section the stator outer diameter is fixed at 209mm. Figure 4.6 shows the predicted variation in the open-circuit power winding voltage as a function of control winding current density for both the AFB and cruciform rotors. As will be apparent, the open-circuit voltage achieved with the AFB is significantly higher than for the cruciform rotor.

Both rotor types are subject to significant saturation for control winding current densities beyond  $4A_{rms}mm^{-2}$ . This is illustrated by the equivalent characteristic for a cruciform rotor, in which both the stator and rotor cores are modelled with a linear B-H characteristic with a fixed relative permeability of 13,000. It is also interesting to note that the performance of the non-linear AFB machine is superior to its linear equivalent up to the onset of saturation, behaviour that can be attributed to the saturation of the bridges at the end of the flux barriers.

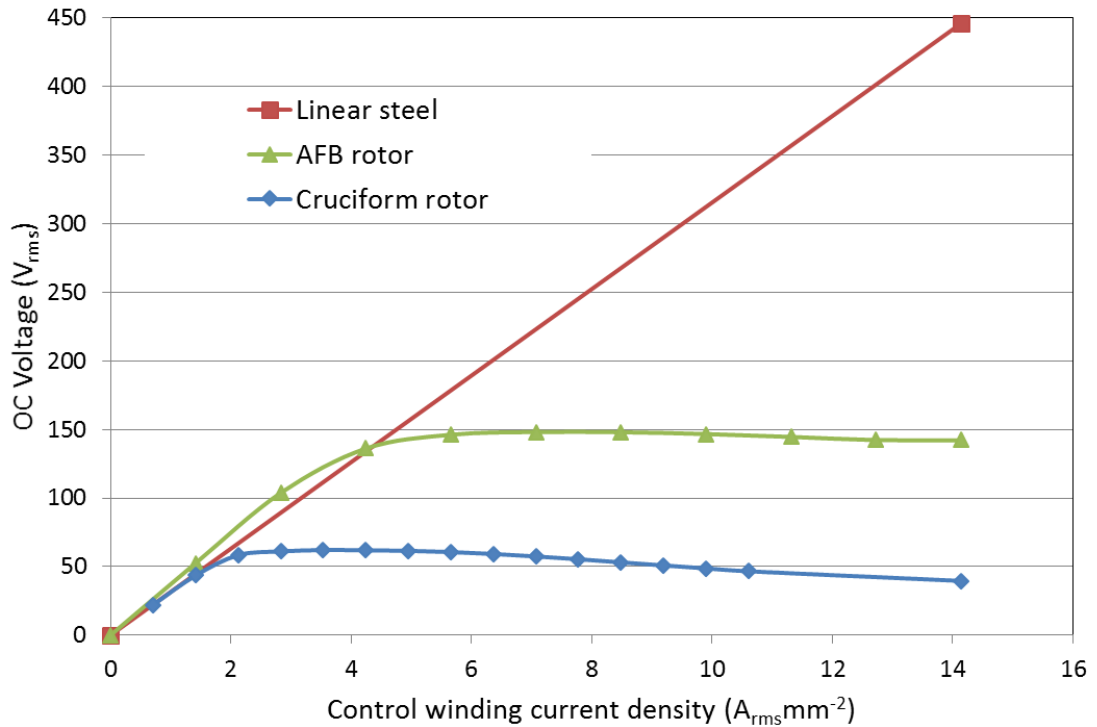


Figure 4.6 – Variation of open-circuit power winding voltage as a function of control winding current density using an AFB and a cruciform rotor (also shown is the characteristic for a cruciform rotor with a fixed relative permeability of 13,000)

#### 4.3.3 COMPARISON OF HARMONIC CONTENT OF POWER WINDING VOLTAGE WAVEFORMS

The harmonic content of the voltage waveform was explored for the particular case of a control winding current density of 14.14A<sub>rms</sub>mm<sup>-2</sup>. In each test case of this section the stator outer diameter is fixed at 209mm. The predicted open-circuit output voltage waveform under these conditions for both the cruciform and AFB rotor are shown in Figure 4.7 and Figure 4.8 respectively. The corresponding FFTs of these open-circuit voltage waveforms are shown in Figure 4.9. As will be apparent, at this operating point the harmonics introduced by the cruciform are far more prominent than those from the AFB. The THD for the cruciform and AFB rotors are 51.17% and 22.17% respectively. Of particular prominence in the spectrum for both rotors is the harmonic at 680Hz, which is thought to originate from the significant 18 pole spatial harmonic in the 2 pole winding, discussed later with Figure 4.25, which is then modulated by the rotor to create a 680Hz harmonic. Both spectra contain a significant subharmonic at 120Hz, which is due to a saturation induced 3<sup>rd</sup> harmonic as will be discussed in Section 5.9.

In both cases, further benefits in harmonic suppression are likely to be realised by skewing the rotor by one stator slot pitch as discussed later in Section 5.9.

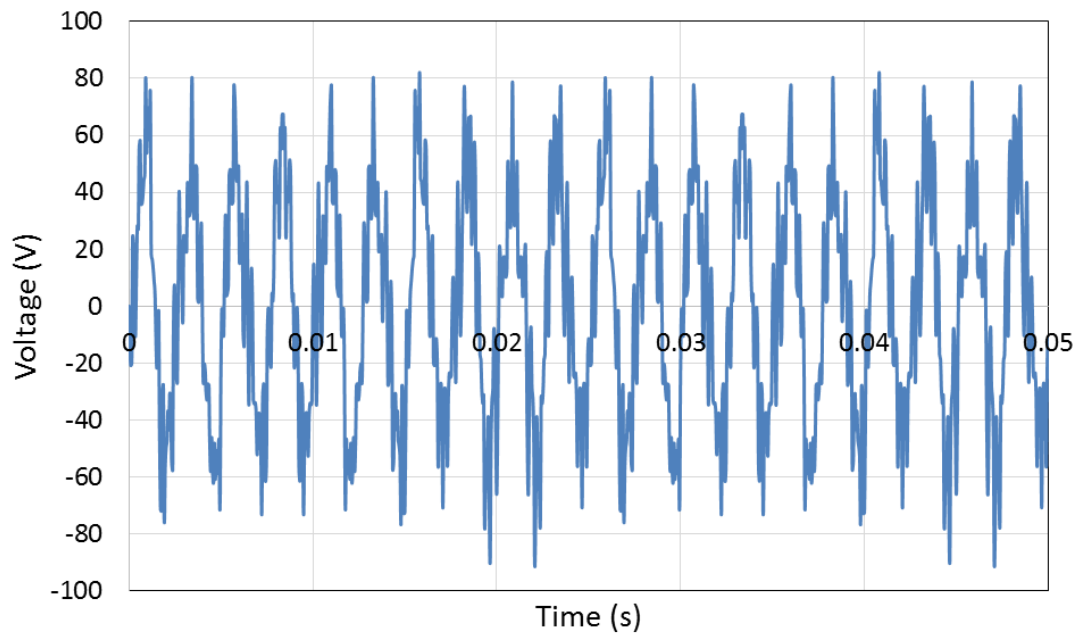


Figure 4.7 – Power winding phase A open circuit voltage with a cruciform rotor rotating at 6,600rpm and a  $14.14A_{rms}mm^{-2}$  40Hz contra-rotating control winding current density

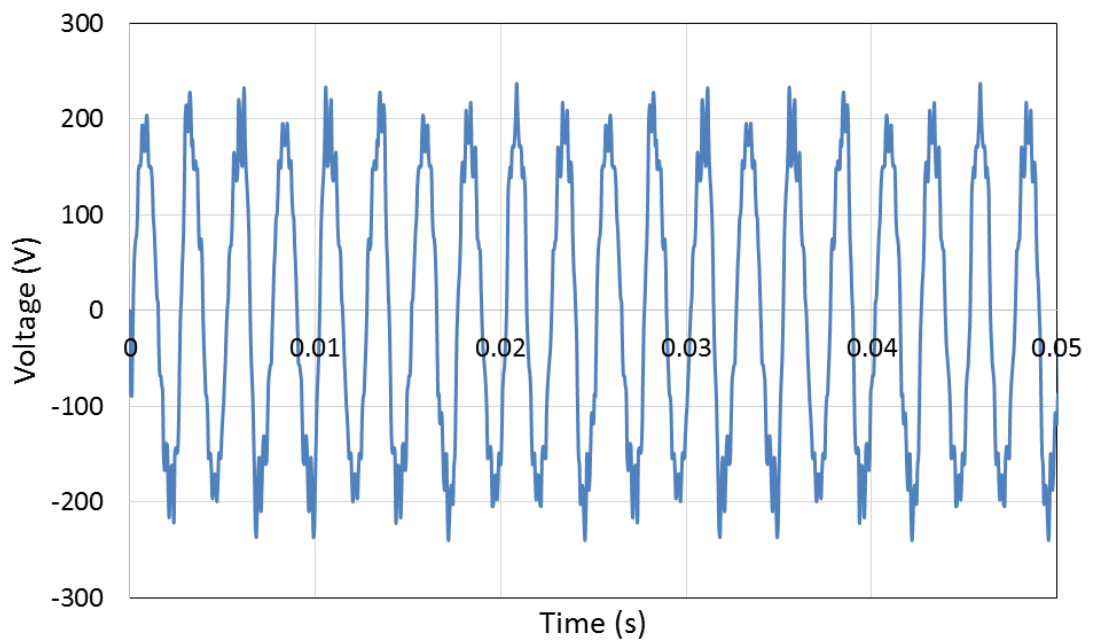


Figure 4.8 – Power winding phase A open circuit voltage with an AFB rotor rotating at 6,600rpm and a  $14.14A_{rms}mm^{-2}$  40Hz contra-rotating control winding current density

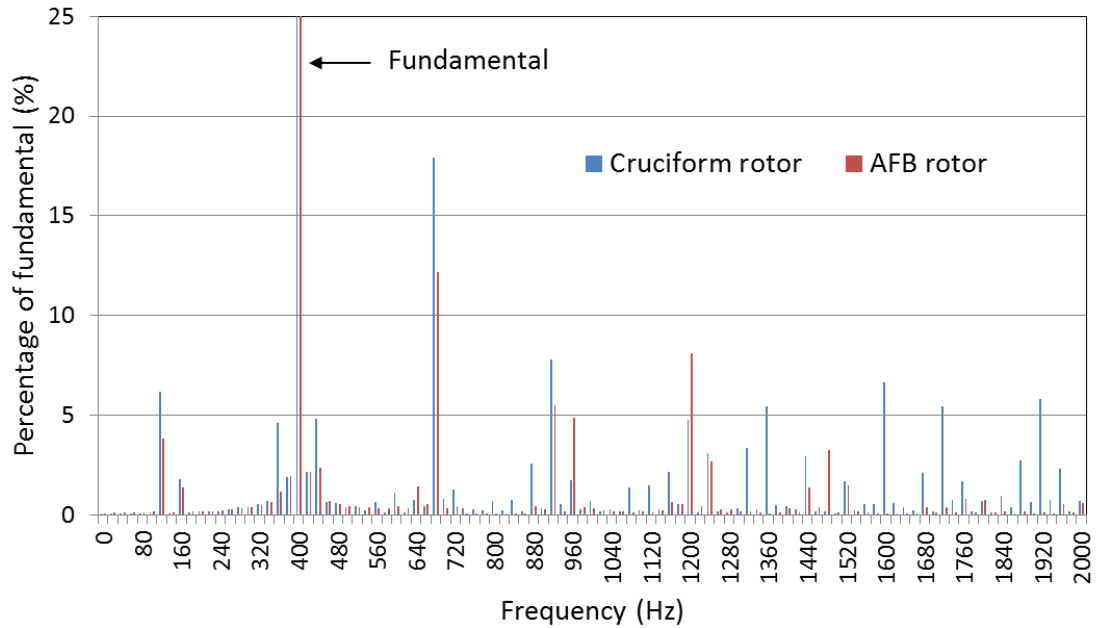


Figure 4.9– Comparison of the harmonics in the power winding voltage produced with a cruciform and AFB rotor with an open circuit power winding, a  $14.14A_{rms}mm^{-2}$  40Hz contra-rotating control winding current density and a speed of 6,600rpm

#### 4.3.4 COMPARISON OF MODULATION OF MUTUAL INDUCTANCE

An important and useful indicator of BDFRM rotor performance is the degree to which the mutual coupling between the control winding and the power winding is modulated by the rotor. It is useful to quantify this as the difference between the maximum and minimum value, with a higher value indicating improved performance. This value will be influenced by magnetic saturation and the relationship will depend on the rotor type. Hence, it is useful to calculate this indicator across the operating range of control winding current densities.

The method used to calculate this performance indicator was to set a fixed DC current in phase A of the control winding only, and extract the power winding flux-linkage of phase A. Representative time stepped simulations, at a rotor speed of 4,800rpm, for both rotor types at current densities of 1 and 20  $Amm^{-2}$  are shown in Figure 4.10 and Figure 4.11 respectively. In each test case of this section the stator outer diameter is fixed at 209mm.

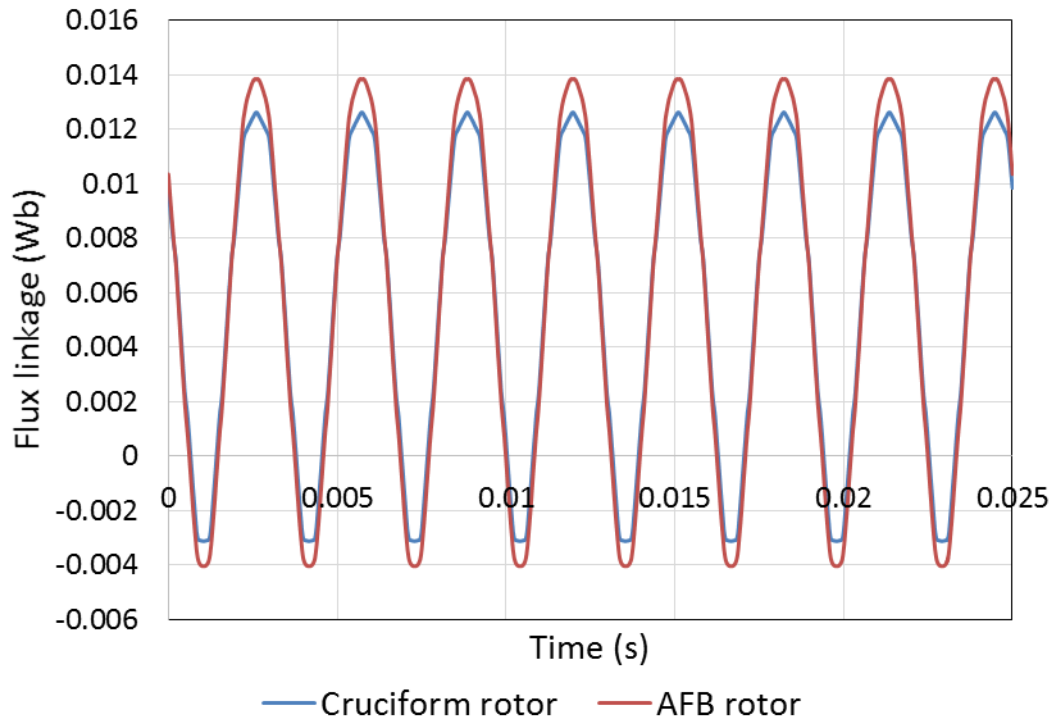


Figure 4.10 – Power winding phase A flux linkage due to a phase A control winding DC current with a  $1\text{Amm}^{-2}$  at a speed of 4,800rpm and an open circuit power winding for both the cruciform and AFB rotors

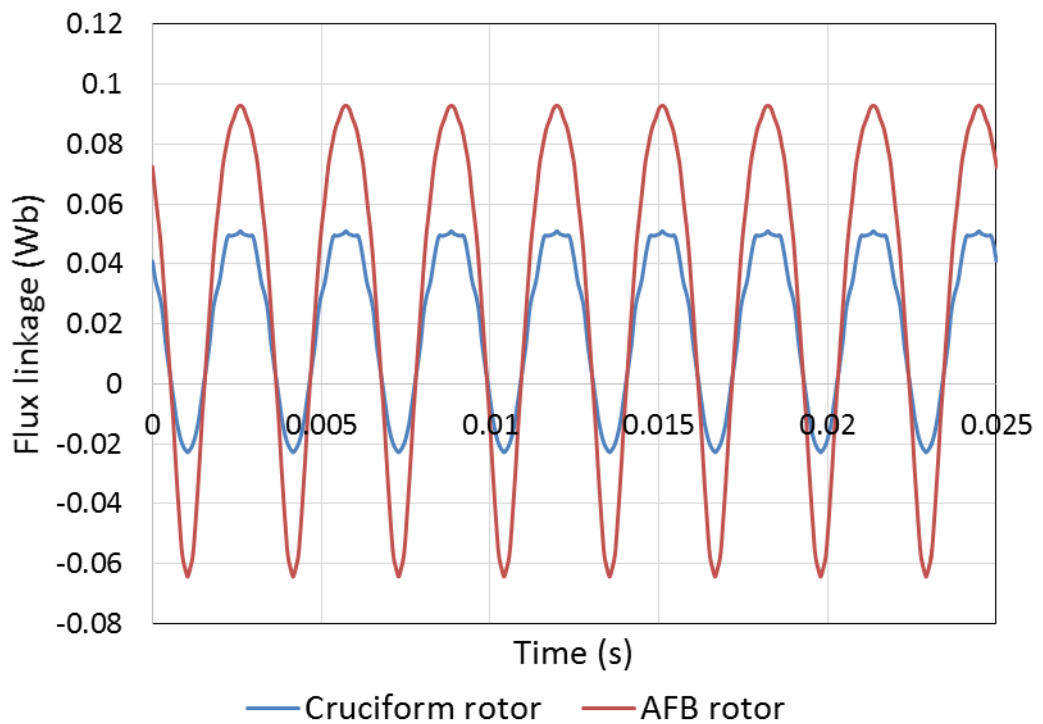


Figure 4.11 – Power winding phase A flux linkage due to a phase A control winding DC current with a  $20\text{Amm}^{-2}$  at a speed of 4,800rpm and an open circuit power winding

Figure 4.12 shows the variation in this ratio for both types of rotor structure, for control winding current densities between 1 and 20  $\text{Amm}^{-2}$ . As shown by Figure 4.12, the main advantage of the AFB rotor comes at the higher current densities when the bridges at the end of the flux barriers saturate. In both cases, there is an obvious tailing-off of the benefits in the flux-linkage by increasing the control winding current density further, due to the presence of bulk saturation. For the cruciform rotor this occurs at low current densities of  $\sim 4\text{Amm}^{-2}$ , whereas the AFB rotor maintains a roughly linear increase in flux linkage excursion up to  $\sim 15\text{Amm}^{-2}$ . In the cases of these two specific rotor and stator designs, the main location of saturation was the stator back iron, particularly in the case of the cruciform rotor. To demonstrate this Figure 4.13 and Figure 4.14 show flux density plots for areas over 2.3T (the magnetising limit for Cobalt Iron) for the cruciform and AFB rotors respectively.

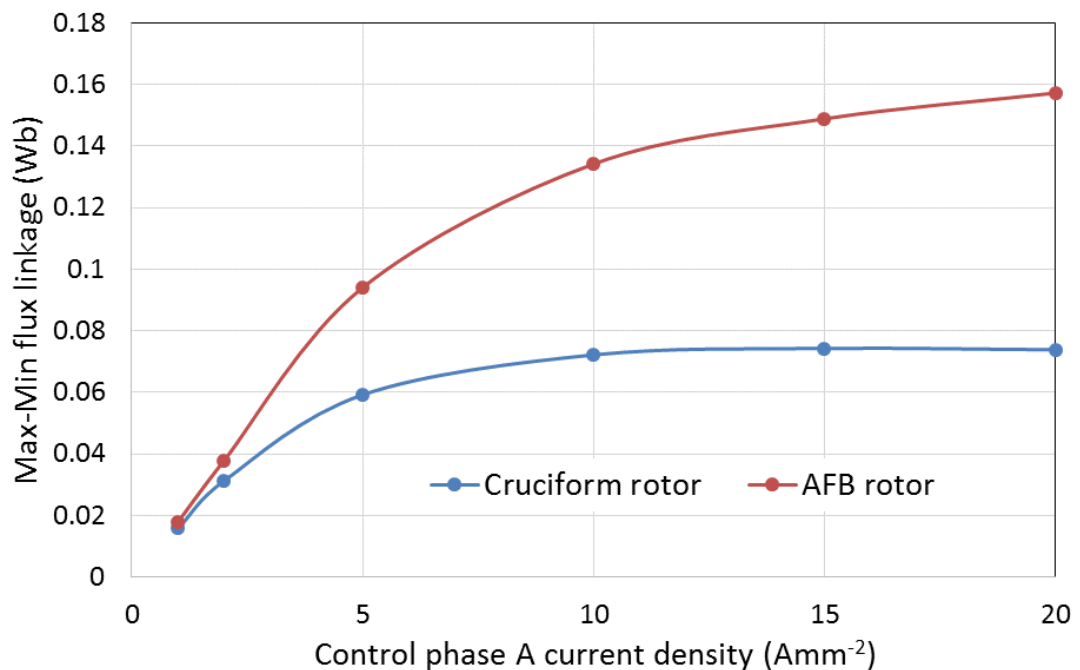


Figure 4.12 – Max-min flux linkage in phase A of the power winding for both the cruciform and AFB rotors at a speed of 4,800rpm with a range of control winding DC phase A current densities and an open circuit load

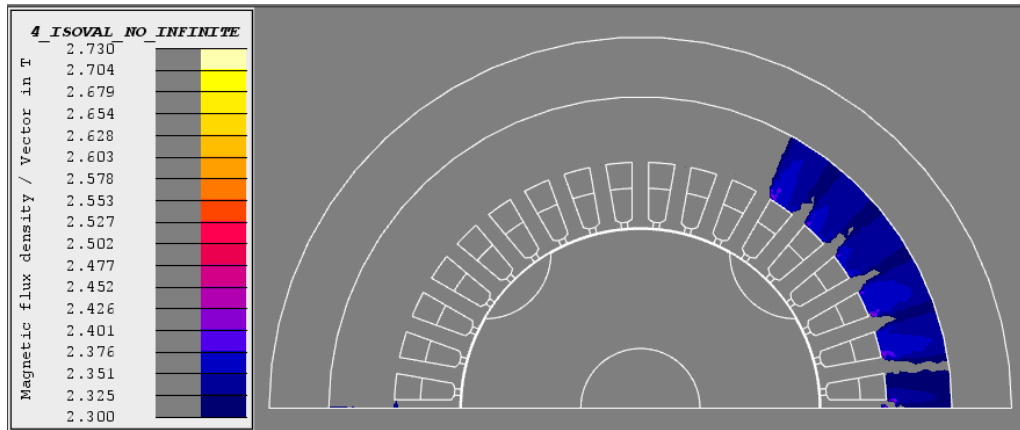


Figure 4.13 – Areas of saturation (above 2.3T in Cobalt Iron) in the FE model with a cruciform rotor at a control winding phase A current density of  $20\text{Amm}^{-2}$  with a rotor speed of 4,800rpm and an open circuit power winding

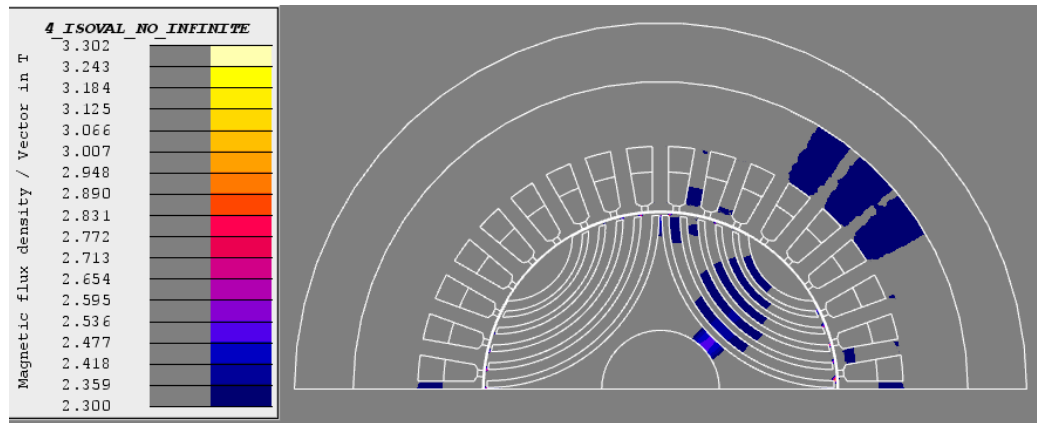


Figure 4.14 – Areas of saturation (above 2.3T in Cobalt Iron) in the FE model with an AFB rotor at a control winding phase A current density of  $20\text{Amm}^{-2}$  with a rotor speed of 4,800rpm and an open circuit power winding

#### 4.4 ASSESSMENT OF ALTERNATIVE POLE NUMBER COMBINATIONS

Published studies [2] have identified, albeit only qualitatively, that the 2/4/6 pole number combination exhibits a tendency under saturation of direct coupling of the 3<sup>rd</sup> harmonic of the 2-pole field as discussed in the previous section. Since this has a direct bearing on the achievable power density and the control winding converter rating, alternative pole combinations were considered. One option would be to select the only viable combination of lower pole numbers, viz. a 2 pole control winding, 3 pole salient rotor and a 4 pole power winding (2/3/4 in the standard designation adopted). However, this combination is inherently asymmetric with regard to radial force distribution, and would hence give rise to

significant, and potentially, unsustainable levels of unbalanced magnetic pull on the rotor, in turn giving rise to additional bearing wear and increased mechanical vibration.

The next viable 3-phase combination is a 4/6/8 pole machine, which in common with the baseline 2/4/6 machine, is symmetrical and balanced in terms of radial forces. A design was established for this combination using the basic principles established for the 2/4/6 baseline machine. Figure 4.15 shows a cross-section through the 4/6/8 design, which has an identical stator core outer diameter of 206mm as the baseline design.

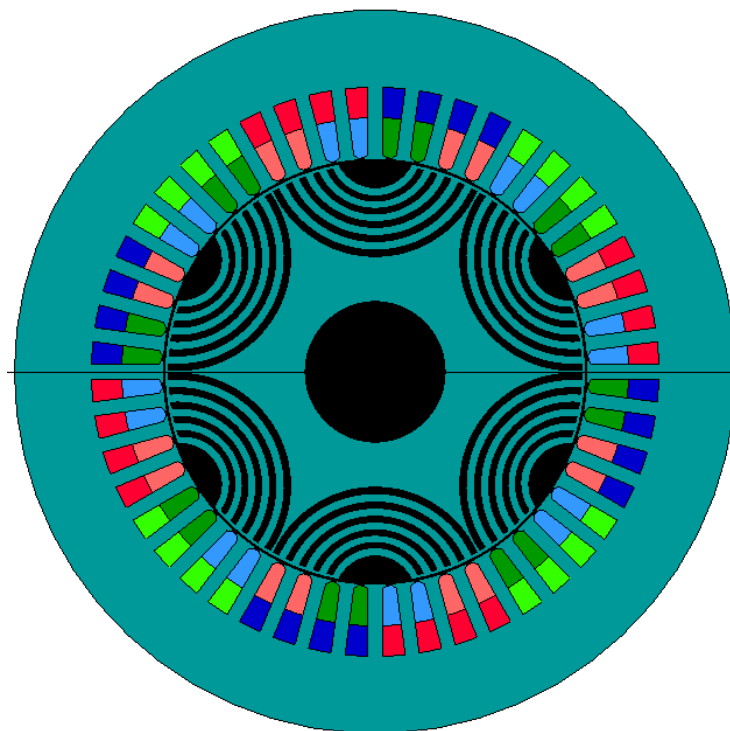


Figure 4.15 – Cross-section of the 4/6/8 pole combination BDFRM design

The performance of this 4/6/8 design was predicted using a circuit-coupled finite element simulation, in which the control winding current level was identical to the 2/4/6 design. The higher pole number necessarily dictates that the machine rotates at a lower speed in order to remain within the lower end of the 360-800Hz VF range. More specifically, for the same benchmark operating point of 11% frequency correction at 360Hz, the rotational speed is 3,200rpm as compared to 4,800rpm for the baseline 2/4/6 design. A summary of the performance of this machine compared to the baseline design is contained in Table 4.2. As will be



apparent, when compared to the baseline design, the 4/6/8 design exhibits a markedly lower torque density. This is to be expected given the difficulty already encountered with the 2/4/6 design of accommodating sufficient control winding MMF per pole in a relatively small frame size. The increased number of poles in the 4/6/8 design compounds this difficulty. Even more marked is the reduction in power capability, which is a consequence of both the reduced torque density and the necessarily lower rotational speed which can be used to produce a 360Hz output.

Table 4.2 – BDFRM pole number combination comparison

Pole number combination (control/rotor/power)	2/4/6	4/6/8
Control winding current ( $A_{rms}$ )	250	250
Rotor speed (rpm)	4,800	3,200
Power winding frequency (Hz)	360	360
Active torque density* (Nm/kg)	2.00	1.34
Active power density* (kW/kg)	1.12	0.39

\* Active weight includes the stator, rotor and slot copper only (i.e. excludes end-winding)

As briefly mentioned in Section 4.3.3, the 2/4/6 pole number combination tends to give rise to a subharmonic in the power winding voltage, due to the saturation-induced third harmonic in the 2-pole control winding that links directly to the 6-pole power winding. To ensure that this is not the case in a 4/6/8 pole number combination BDFRM, a FE-calculated power winding phase A voltage waveform is captured in Figure 4.16. To complement Figure 4.16, the FFT of this voltage waveform is provided in Figure 4.17. The fundamental frequency can be seen as 360Hz, with the only other appreciable harmonic at 520Hz, thus confirming the absence of the subharmonic seen in the 2/4/6 pole number case.

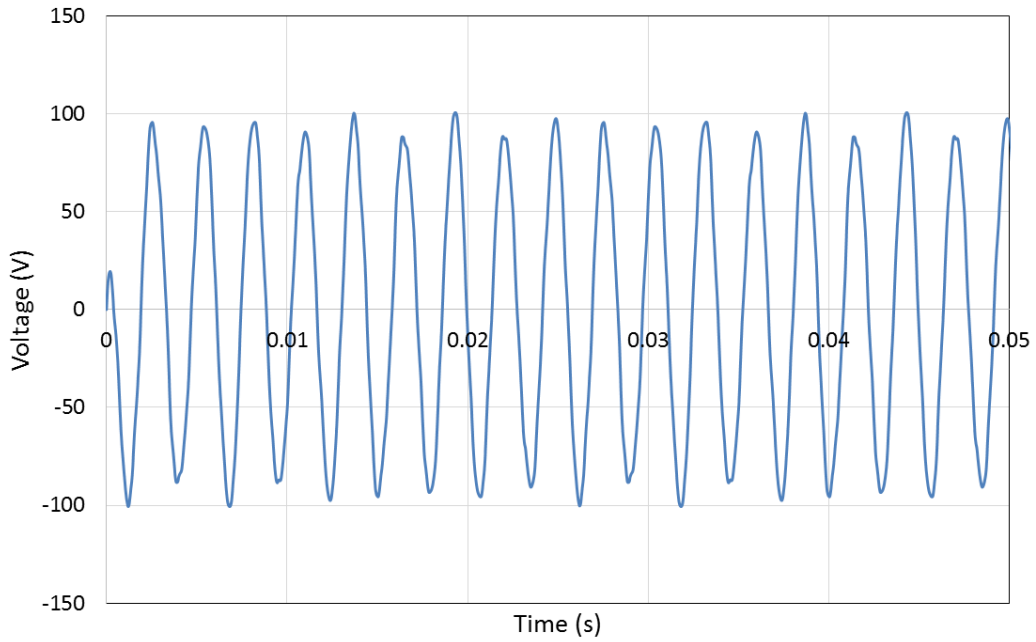


Figure 4.16 – Phase A power winding voltage with a speed of 3,200rpm, a power winding load of 1Ω and a 40Hz co-rotating control winding current with a current density of  $14.14A_{rms}mm^{-2}$

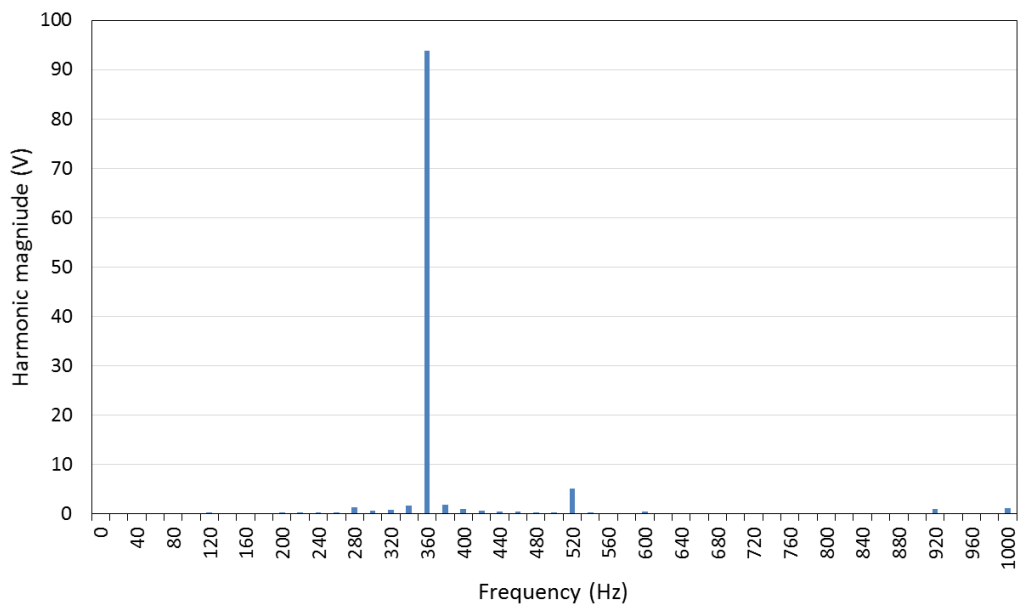


Figure 4.17 – FFT of phase A power winding voltage with a speed of 3,200rpm, a power winding load of 1Ω and a 40Hz co-rotating control winding current with a current density of  $14.14A_{rms}mm^{-2}$

## 4.5 SCALING OF BDFRM PERFORMANCE WITH RATING AND SIZE

It is important to recognise that although simple linear scaling of all the machine dimensions provides a consistent and straightforward means of scaling from a baseline design, it may not necessarily lead to optimal design at larger diameters, where some differences in relative proportions of the stator features may prove beneficial in terms of power density. Notwithstanding this limitation, it provides a useful means of understanding the scalability of BDFRMs. The following scaling rules were applied:

- All the linear dimensions in the machine cross-section were increased by a prescribed scaling factor with the exception of the airgap which remained constant at 0.5mm
- The axial length of the stator and rotor cores remained fixed at 100mm
- The control winding current density remained fixed at  $10.6A_{rms}mm^{-2}$ . In this regard, the increased slot area which results with increasing scaling factor is exploited to increase the MMF per slot and not reduce the loss density by reducing the current density

These scaling rules were applied to values of scaling factors up to three times the original baseline design. It should be noted that alternative scaling options are possible. A summary of the scaled designs is shown in Table 4.3. For each scaling factor, the output power density and torque density were calculated from time-stepped finite element simulations, for an operating point of 4,800rpm, with a control winding current density of  $10.61A_{rms}mm^{-2}$ . The load resistance at each scaling factor was calculated, by an iterative FE process, to provide maximum power winding load power.

In assessing the performance of each scaled design, two alternative measures of power and torque density were used, one based on the total active machine mass (excl. casing and shaft), and the other based on the active elements within the core (excl. end-windings, casing and shaft). This separating out of the end-windings provides some additional insight into the scaling.

Table 4.3 – Leading dimensions and masses of the scaled BDFRM designs

Scaling factor	1.00	1.25	1.50	1.75	2.00	2.50	3.00
<b>Stator outer diameter (mm)</b>	206	257	309	360	411	514	616
<b>Rotor outer diameter (mm)</b>	120	150	180	210	240	300	360
<b>Cross-sectional area of slot (mm<sup>2</sup>)</b>	136	212	306	414	542	422	1216
<b>Stator core mass (kg)</b>	13.70	21.39	30.79	41.89	54.69	85.42	122.97
<b>Rotor core mass (kg)</b>	5.25	8.18	11.76	15.98	20.85	32.53	46.80
<b>Active region coil mass (kg)</b>	2.20	3.42	4.94	6.68	8.74	13.61	19.61
<b>End-winding coil mass (kg)</b>	2.99	5.80	10.01	15.68	23.60	45.99	79.69

The resulting variations in torque and power density with scaling factor are shown in Figure 4.18. As would be expected, the torque density which does not include the end-windings (which arguably provides a more meaningful comparison of the underlying scalability) increases appreciably, albeit with diminishing returns as magnetic saturation becomes more pronounced, recalling that the MMF per slot increases in proportion to the increase in slot cross-sectional area. When the end-windings are included, the benefits are less significant and eventually lead to a marginal reduction in torque density. This is largely a consequence of the fixed axial length of each of the seven designs, which increasingly results in aspect ratios in which the end-winding begins to dominate.

The trends shown in Figure 4.18 support the assertion that BDFRMs are not well suited to smaller frame sizes. On the basis of this scaling study, larger diameter machines are likely to yield torque density improvements of the order of 50%, compared to the baseline dimensions, although more definitive figures would require optimisation of the design at each diameter, notably in terms of adjusting the proportions in favour of the core over the slot, as diameter is increased.

Comparing the BDFRM scaling study to the SyncRel scaling study of Section 3.5, the BDFRM seems to have reached a peak in power and torque density (with end windings included) whereas the SyncRel densities are still increasing past a scaling factor of 3. This may be attributed to the necessity of the BDFRM core steel to carry more flux, due to the presence of two windings, therefore saturation is much more of a problem in these machines. Another restricting factor on BDFRM power and torque densities is the end windings required for two 3-phase windings, with a relatively low pole number, and therefore high arc length.

For the readers interest the shear stress at each scaling factor is also provided in Figure 4.19.

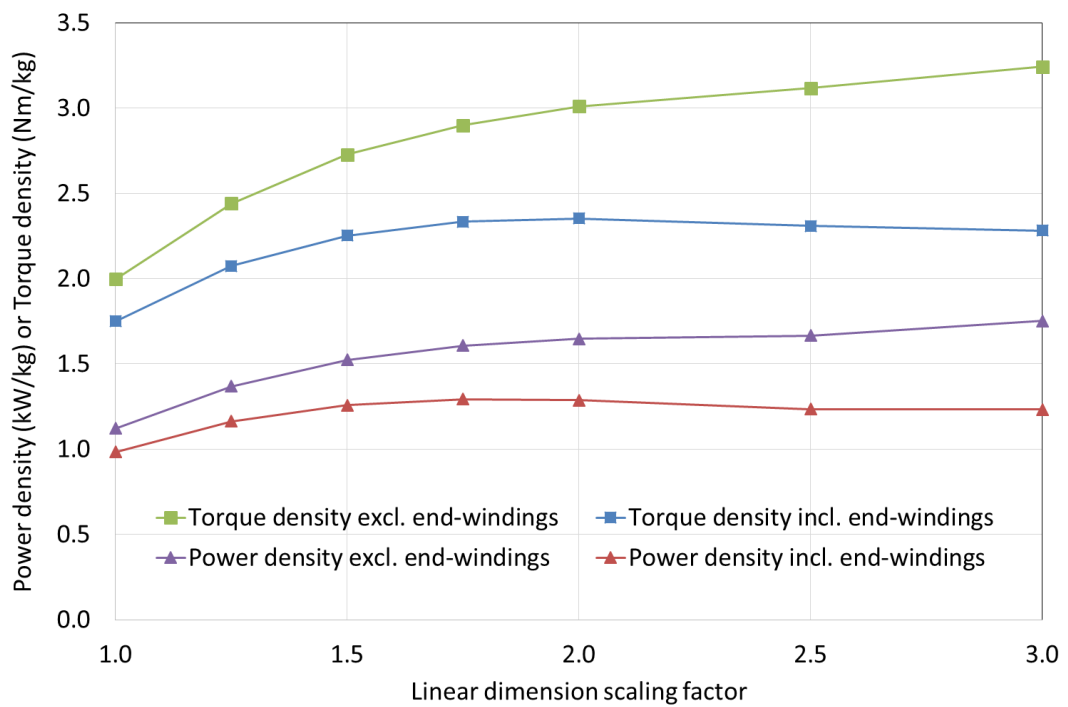


Figure 4.18 – Variation with scaling factor of the torque and power density of the baseline 2/4/6 BDFRM at 4,800rpm with a 40Hz contra-rotating control winding current density of  $10.61A_{rms}mm^{-2}$

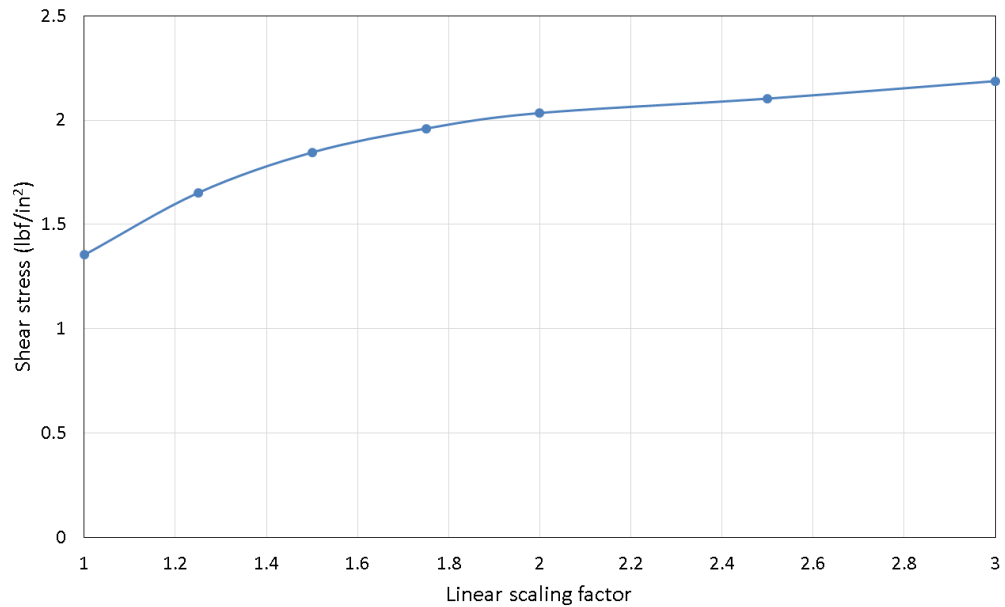


Figure 4.19 – Variation with scaling factor of the shear stress of the baseline 2/4/6 BDFRM at 4,800rpm with a 40Hz contra-rotating control winding current density of  $10.61A_{rms}mm^{-2}$

To complete this section of BDFRM scaling, a further scaling study was carried out to establish whether the 4/6/8 combination would scale differently from the 2/4/6 case. As was the case with 2/4/6 model, there is an appreciable increase in torque density as the machine dimensions are scaled as seen in Figure 4.20. However, the nature of the scaling with the 4/6/8 combination does not overcome the shortfall in performance compared to the corresponding 2/4/6 combination across the entire range of scaling considered, there is no evidence that further scaling will meaningfully close the gap. Hence, despite the penalty which is incurred by the presence of a third harmonic of the control winding, which couples with the power winding in the 2/4/6 combination, selecting the next available symmetrical 3-phase combination of pole numbers results in lower levels of performance.

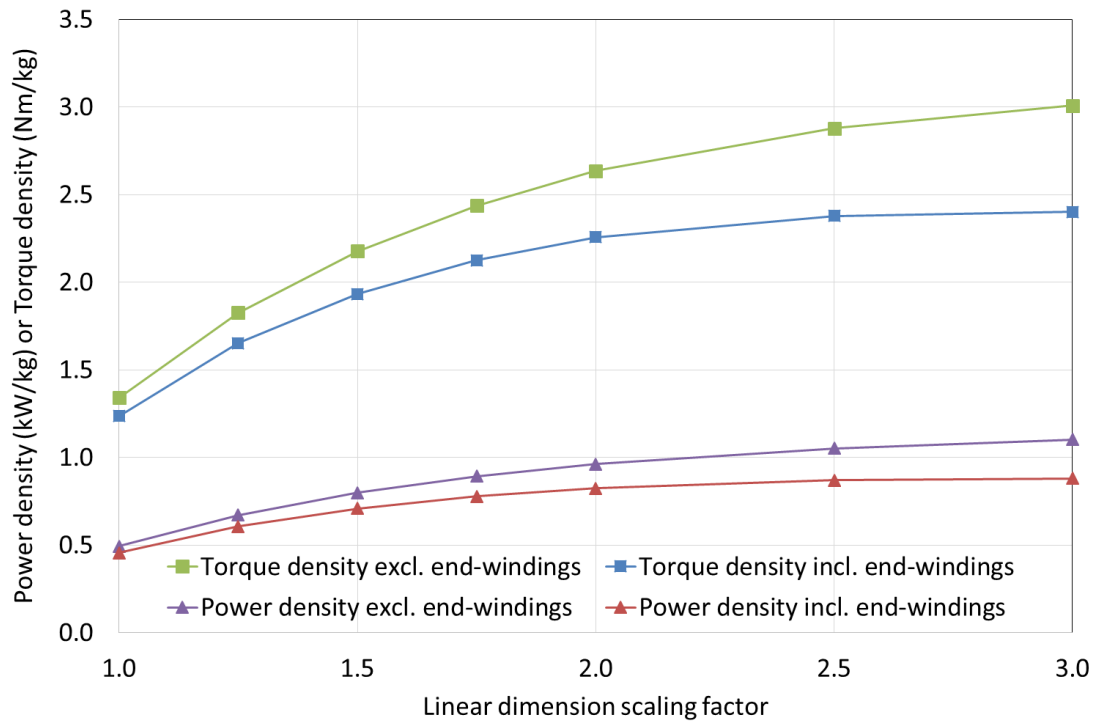


Figure 4.20 – 4/6/8 pole combination BDFRM scaling study at 4,800rpm with a 40Hz contra-rotating control winding current density of  $10.61A_{rms}mm^{-2}$

#### 4.6 FINITE ELEMENT INVESTIGATION OF AIRGAP FLUX DENSITY HARMONICS

The underlying operation of a BDFRM is based on the modulation of the airgap fields produced by the two windings, in a manner which results in interactions that produce net torque on the rotor. The analytical basis of this behaviour is reasonably well established, if rather simplified and limited, when very high levels of electric loadings give rise to appreciable saturation of the stator and/or rotor cores. Moreover, the permeance modulation introduced by a practical design of the rotor, and the means by which this changes with increasing magnetic saturation, dictates that BDFRMs will tend to depart in performance from that anticipated from analytical models, particularly in applications which demand high power densities.

Given the relatively modest performance predicted for the baseline machine using time-stepped, circuit coupled, finite element simulations, a series of finite element models were used in an attempt to provide some further insight into the role of the various harmonics and couplings present in a practical design of a machine. More specifically, a series of finite element models were solved for a

rotor speed of 4,860rpm, a load resistance of  $3\Omega$ , a control winding current density of  $14.14A_{rms}mm^{-2}$  and a control winding frequency of 36Hz, which corresponds to a 10% frequency correction. In all cases, a fast Fourier transform (FFT) was performed on the airgap flux density waveforms, in order to establish the various harmonics at play. In each test case of this section the stator outer diameter is fixed at 207mm.

#### 4.6.1 AIRGAP FIELDS WITH NO ROTOR SALIENCY

A useful starting point, albeit not one representative of an actual BDFRM machine, is to replace the salient rotor with a plain cylindrical Silicon-Iron rotor of the same outer diameter. Taking the control and power windings separately and in turn, magneto-static finite element calculations were performed with this plain cylindrical rotor, with the winding under consideration having a static current in each slot, which is based on a representative time-snapshot of the currents that would be present under normal BDFRM operation at the reference conditions. The resulting spatial harmonics in the airgap field, when the control and power windings are excited, are shown in Figure 4.21 and Figure 4.22 respectively.



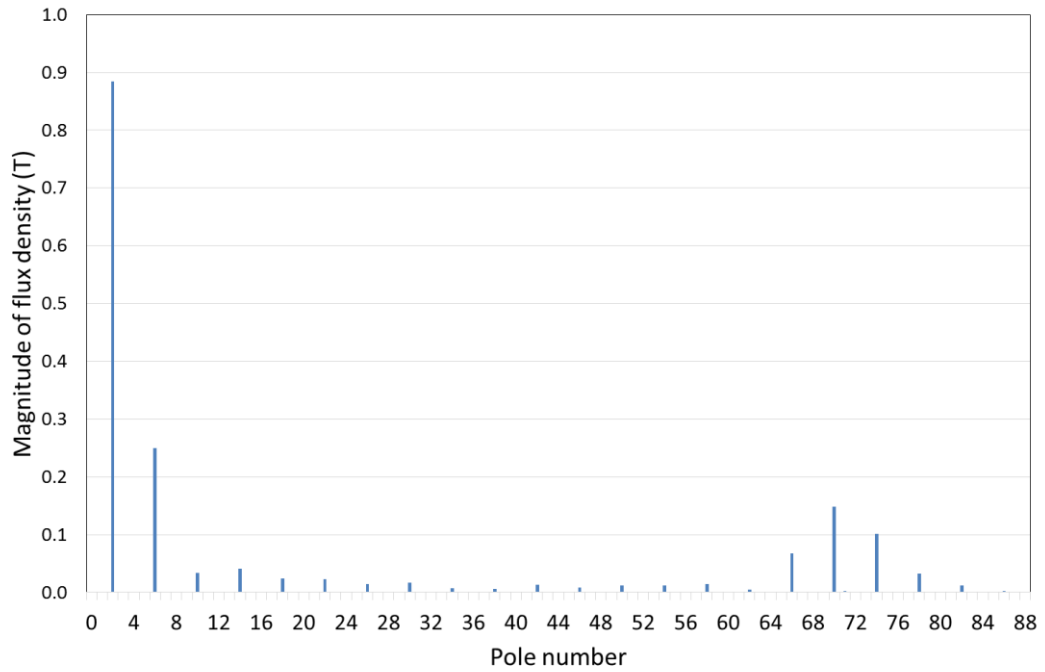


Figure 4.21 – Spatial harmonic spectrum of the airgap flux density with 2-pole control winding excited with a fixed snapshot of a  $14.14A_{rms}mm^{-2}$  stator current and a plain cylindrical rotor and a power winding load of  $3\Omega$

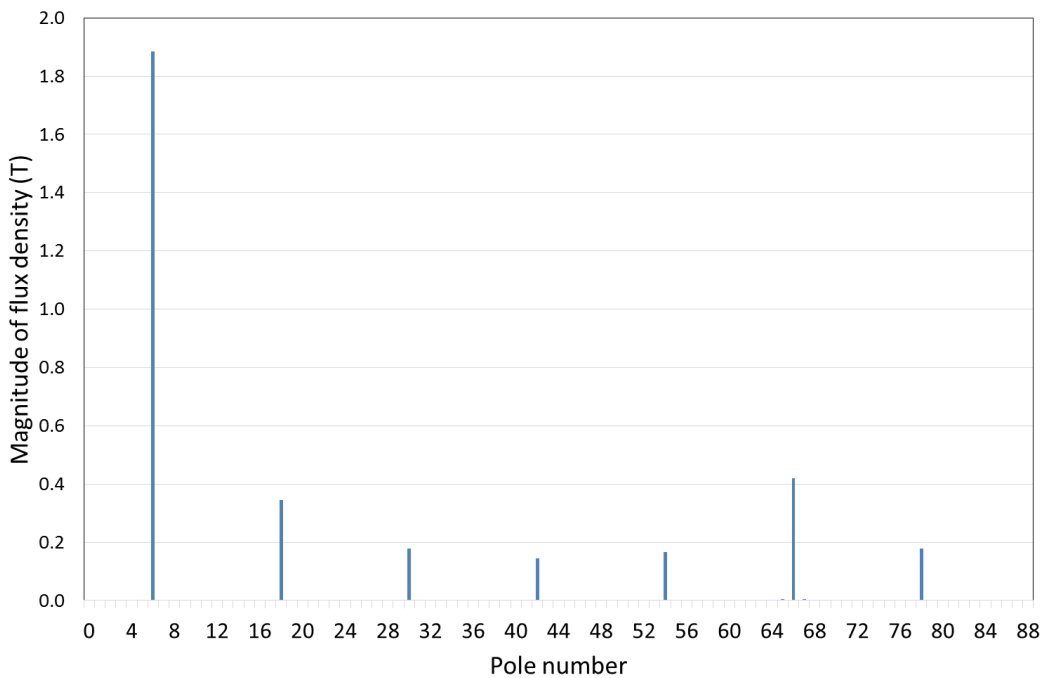


Figure 4.22 – Spatial harmonic spectrum of the airgap flux density with 6-pole power winding excited with a fixed snapshot of a  $14.14A_{rms}mm^{-2}$  stator current and a plain cylindrical rotor and a power winding load of  $3\Omega$

As would be expected, the spectra are dominated by the fundamental components predicted by an analytical model, although there is significant harmonic content in both cases. The majority of the harmonics of significance are due to entirely predictable winding and slotting harmonics. In both spatial harmonic spectra there is, as would be expected, significant harmonics centred around 72 poles, which can be attributed to slotting effects from the 36 slot stator.

Another notable similarity between these two spectra is the presence of appreciable third order harmonics, having magnitudes relative to the fundamental of 28% and 16% for the 2 and 6 pole windings respectively. These harmonics, which are not predicted by the analytical model, are due to the onset of significant magnetic saturation in the rotor and/or stator cores. It is important to bear in mind that magnetic saturation acts in such a way as to suppress the flux around the peak of the fundamental. It is this suppression of the peak that results in an apparent increase in the third harmonic. This magnetic saturation in the stator and/or rotor core leads to saturation induced 6-pole flux harmonic from the 2-pole control winding excitation, and an 18-pole flux harmonic from the 6-pole winding.

In the case of the 6-pole power winding, the 18-pole spatial harmonic does not pose a first-order problem, as this field harmonic does not couple directly with the 2-pole control winding. However, the 6-pole harmonic from the 2-pole control winding couples directly with the 6-pole power winding. This in effect is a transformer EMF between the two windings, which does not rely on the rotor permeance modulation, and hence does not contribute any useful torque-producing interactions with the rotor. The variation in the relative magnitude of this 6-pole saturation harmonic from the 2-pole control winding as a function of control winding current density is shown in Figure 4.23. As will be apparent, even for relatively modest control winding current densities of  $5A_{rms}mm^{-2}$  (modest in the sense of thermal consequences), the third harmonic constitutes a significant 20% of the fundamental. This issue of the presence of significant 3<sup>rd</sup> harmonic in a 2/4/6 pole combination BDFRM has been discussed in general in previous literature [2, 4] as a basis for considering alternative pole number combinations.

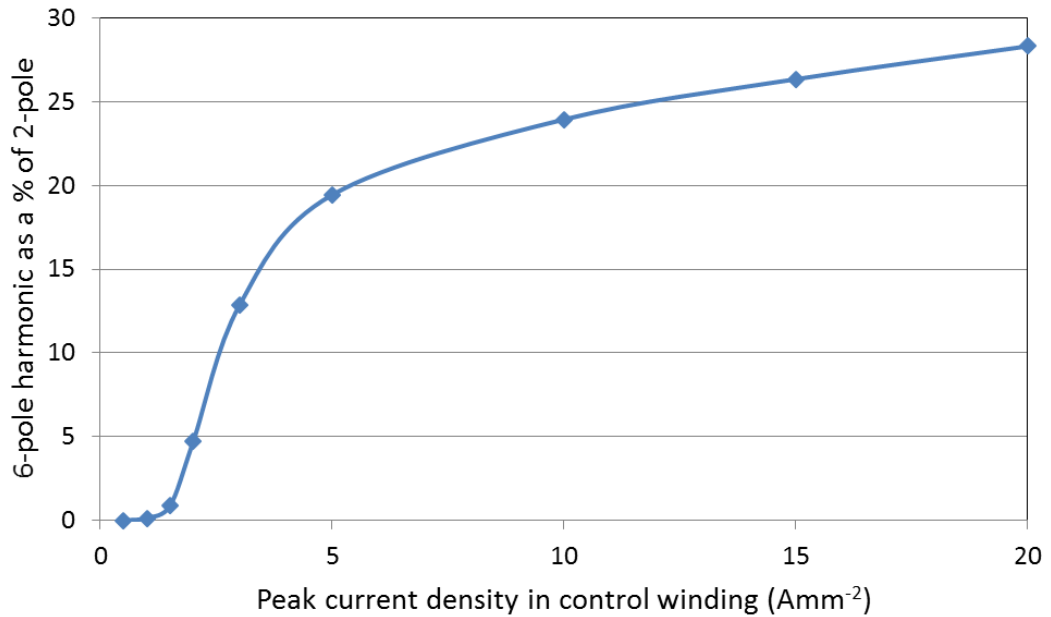


Figure 4.23 – Variation in the magnitude of 6-pole spatial harmonic resulting from saturation with the 2-pole control winding

#### 4.6.2 AIRGAP FIELDS WITH ROTOR SALIENCY

Having explored the spatial harmonics arising from a combination of winding distribution and the slotting using a plain cylindrical rotor, the next series of magneto-static models reinstated the AFB rotor to establish the influence of the rotor permeance modulation on the harmonic content of the airgap flux density. As was the case with the plain rotor, again the control and power windings were excited separately with a single ‘snapshot’ set of static currents in the appropriate phase windings. Clearly, the relative angular displacement between the rotor and stator used in the single magneto-static field calculation will have some bearing on the magnitude of the harmonics observed. For this stage of the analysis, the relative orientation shown in Figure 4.24 was adopted.

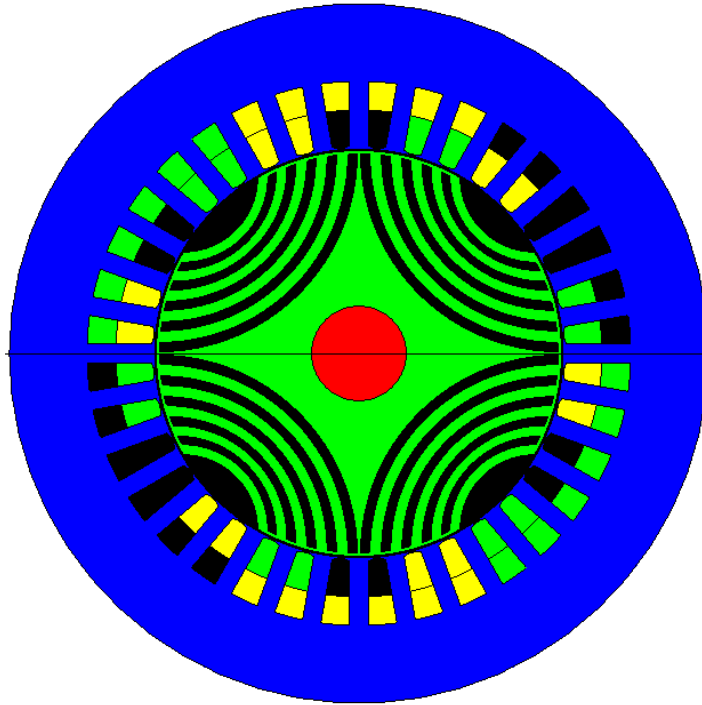


Figure 4.24 – Relative orientations of rotor and stator used to generate spatial harmonic spectra where the inner and outer windings are the power and control windings respectively and the colours refer to the following phases; Black – A, Green – B, Yellow – C

The resulting spatial harmonic spectra for the 2-pole control winding and the 6-pole power winding are shown in Figure 4.25 and Figure 4.26 respectively, in both cases with a snapshot of a control winding current density of  $14.14A_{rms}mm^{-2}$ . In the control winding spectrum of Figure 4.25, the 4-pole permeance modulation of the rotor acts on the 2-pole excitation to create significant 6-pole and 10-pole components. Although the production of the 6-pole harmonic arising from permeance modulation is desirable, and indeed fundamental to the production of torque, its magnitude relative to the 2-pole harmonic is rather larger than expected from permeance modulation alone. This is consistent with the observation that some 20% of the 6-pole harmonic is contributed by saturation, although it is recognised that the 20% magnitude observed in Figure 4.23 is predicted for a slightly different saturation conditions given the different rotors. In addition to the slotting harmonics expected, a further notable harmonic is at 18-poles which is again largely attributable to magnetic saturation. The other harmonics of interest are at 42 and 50 poles, which can be attributed to the effective permeance modulating effects of the bridges which close off each flux barrier and are very prone to localised magnetic saturation. The

corresponding spectrum in Figure 4.26, for the 6-pole power winding, exhibits many of the same features, albeit that the degree of third harmonic introduced by saturation is less pronounced, which in large part is a consequence of the considerably lower MMF per pole.

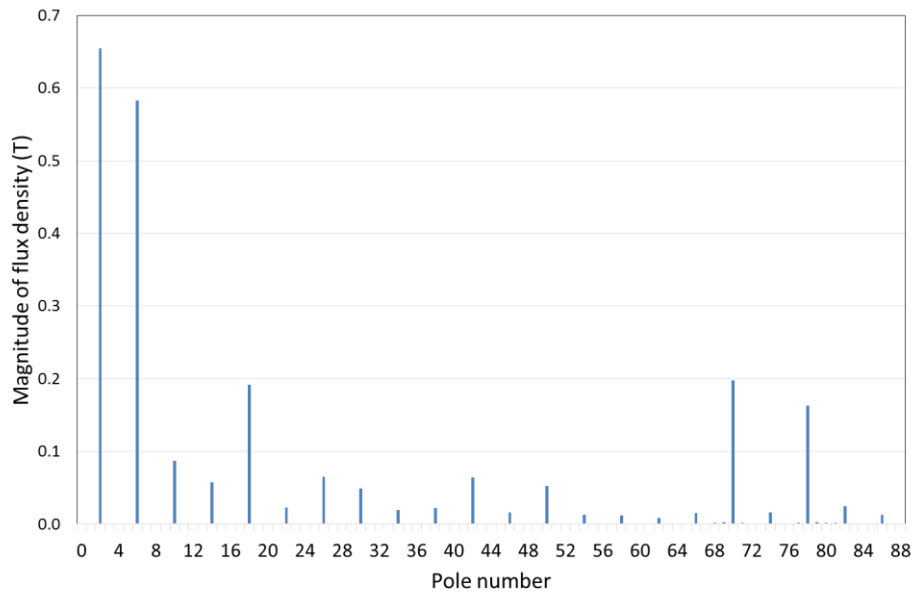


Figure 4.25 – Spatial harmonic spectrum of the airgap flux density with 2-pole control winding excited with a fixed snapshot of stator current at a current density of  $14.14A_{rms}mm^{-2}$  and a salient AFB rotor

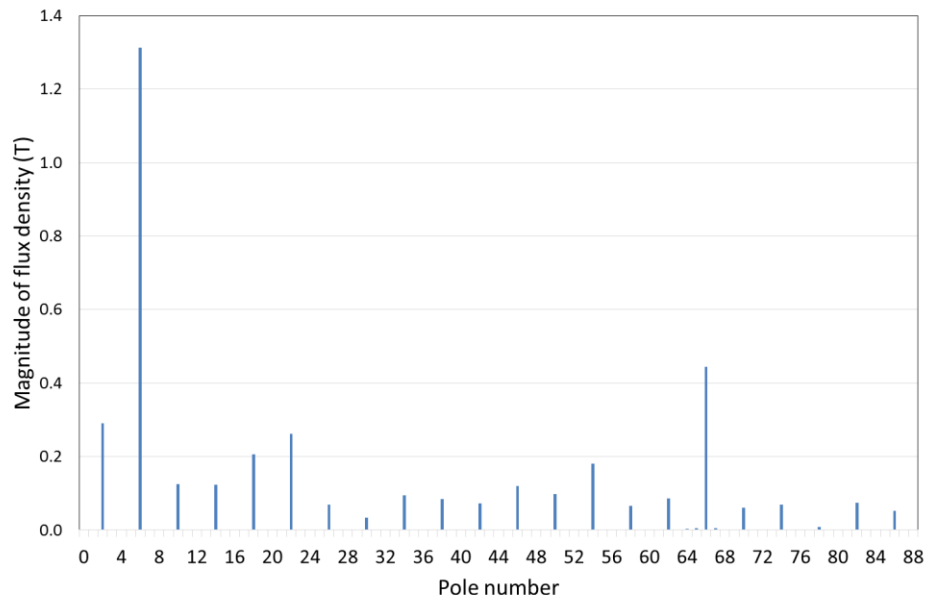


Figure 4.26 - Spatial harmonic spectrum of the airgap flux density with 6-pole power winding excited with a fixed snapshot of stator current at a current density of  $14.14A_{rms}mm^{-2}$  and a salient AFB rotor

The time domain power winding voltage waveform was then analysed to determine the extent of the influence of the third harmonic, introduced by saturation, caused by the 2-pole control winding excitation. Two cases were considered in an attempt to draw out the effect of saturation, viz. a model with a non-linear magnetisation curve for the stator and rotor and a further model with a linear representation of the magnetisation characteristic, i.e. a fixed relative magnetic permeability of 9,766.

In the case of the non-linear representation of the core material, Figure 4.28 shows the presence of a harmonic at  $\sim 108\text{Hz}$  (3x the control winding frequency of 36Hz). In the time domain, as shown in the output voltage waveform of Figure 4.27, this manifests itself as a low frequency modulation of the 360Hz fundamental. However, as shown by Figure 4.30, the corresponding harmonic analysis of the waveform predicted with linear magnetic material does not contain the 108Hz component, which in turn ensures that there is no low frequency modulation of the fundamental. This can also be clearly identified when comparing the voltage waveforms of the non-linear material and the linear material as seen in Figure 4.27 and Figure 4.29 respectively. One means of alleviating this undesirable cross-coupling and voltage modulation is to use alternative pole number combinations such as a 4/6/8 configuration, albeit at the expense of lower shaft speed for the same output frequency.

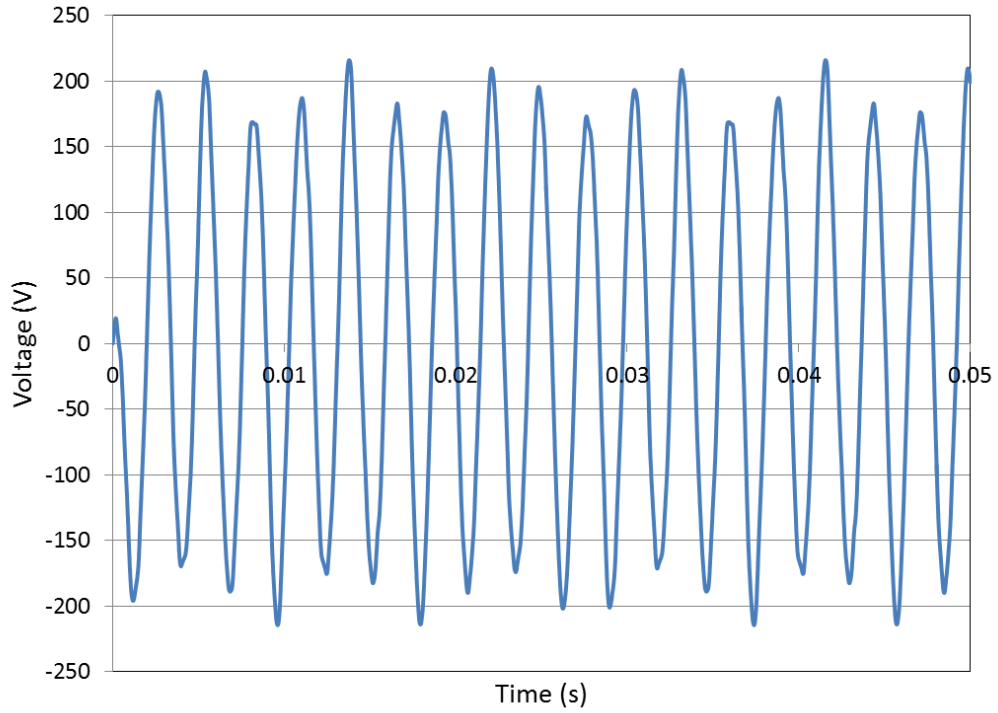


Figure 4.27 – Power winding phase A voltage with AFB rotor in place and non-linear lamination material at a speed of 4,860rpm, a control winding current density of  $14.14A_{rms}mm^{-2}$ , a control frequency of 36Hz and a load of  $3\Omega$

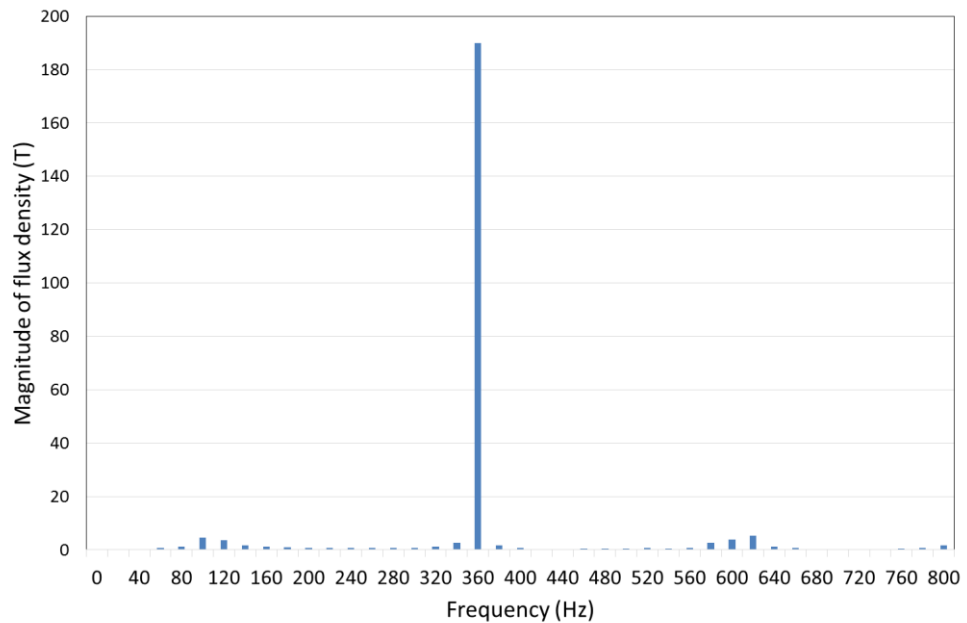


Figure 4.28 – FFT of power winding voltage (Figure 4.27) with AFB rotor in place and non-linear material at a speed of 4,860rpm, a control winding current density of  $14.14A_{rms}mm^{-2}$ , a control frequency of 36Hz and a load of  $3\Omega$

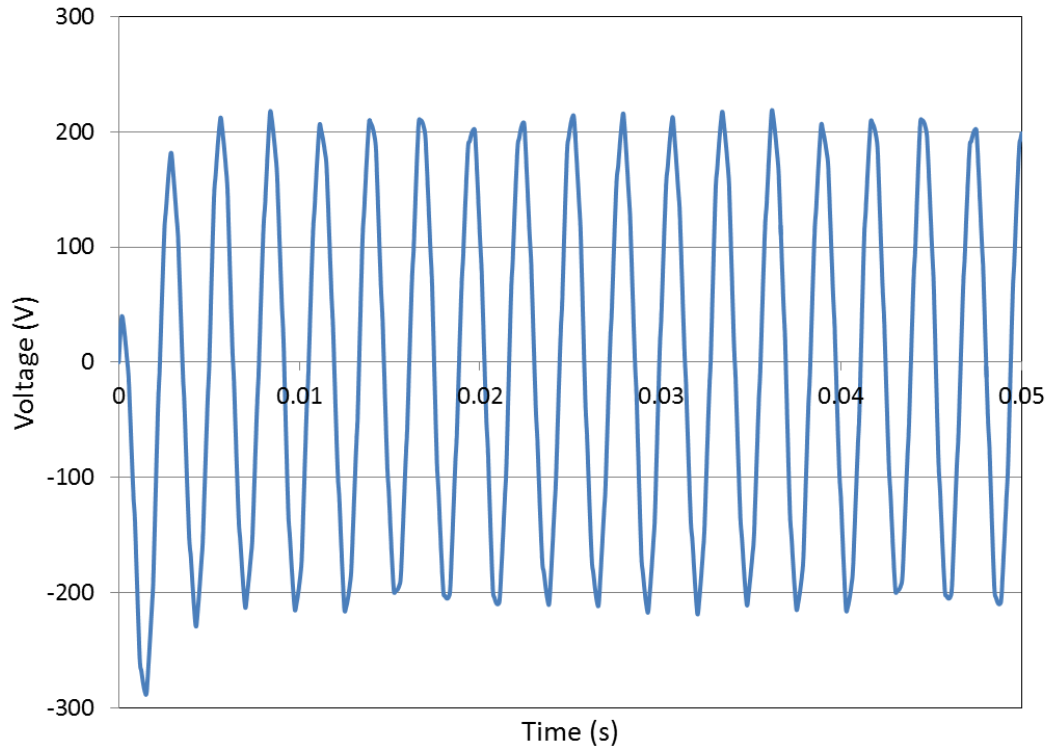


Figure 4.29 – Power winding phase A voltage with AFB rotor in place and linear lamination material at a speed of 4,860rpm, a control winding current density of  $14.14A_{rms}mm^{-2}$ , a control frequency of 36Hz and a load of  $3\Omega$

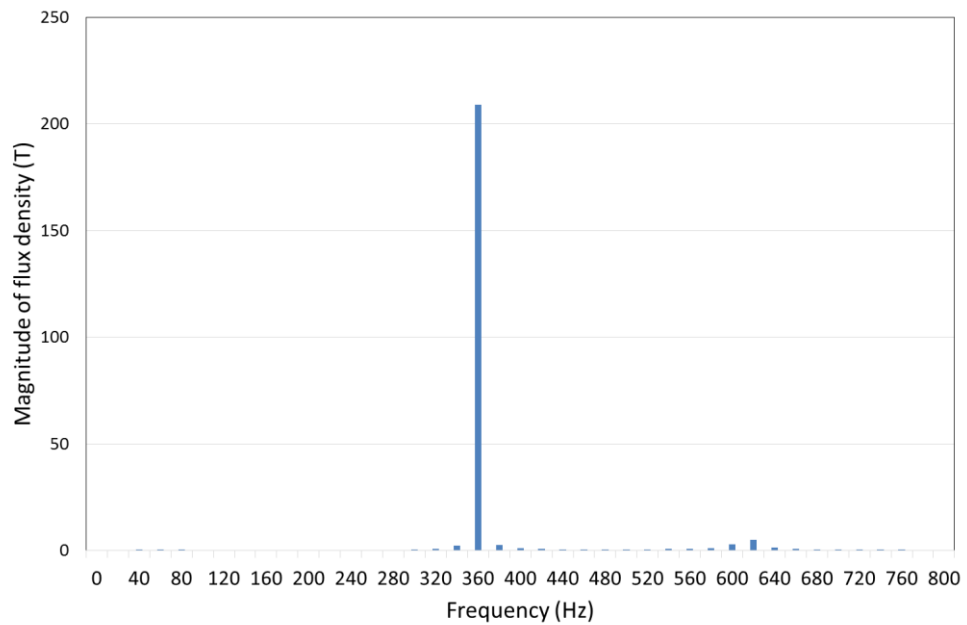


Figure 4.30 – FFT of power winding voltage (Figure 4.29) with AFB rotor in place and linear lamination material at a speed of 4,860rpm, a control winding current density of  $14.14A_{rms}mm^{-2}$ , a control frequency of 36Hz and a load of  $3\Omega$



## 4.7 DOUBLY SALIENT BDFRM VARIANTS

The singly salient nature of the BDFRMs considered up to this point inevitably compromise the achievable saliency ratio and hence torque density. It is possible that a doubly salient variant (i.e. a machine which also exhibits pronounced stator core saliency) would increase the saliency ratio, and therefore could potentially increase the torque production of the BDFRM. In each test case of this section the stator outer diameter is fixed at 209mm.

### 4.7.1 THREE-PHASE VARIANTS

To produce a doubly salient variant of a three-phase BDFRM, the stator must have a number of teeth non-divisible by the number of rotor teeth. As the rotor must have four teeth to ensure correct modulation, the lowest number of stator teeth possible is 18 teeth for a 3-phase 6-pole winding. This leads to very poor utilisation of the airgap periphery as shown in the representative cross-section of Figure 4.31.

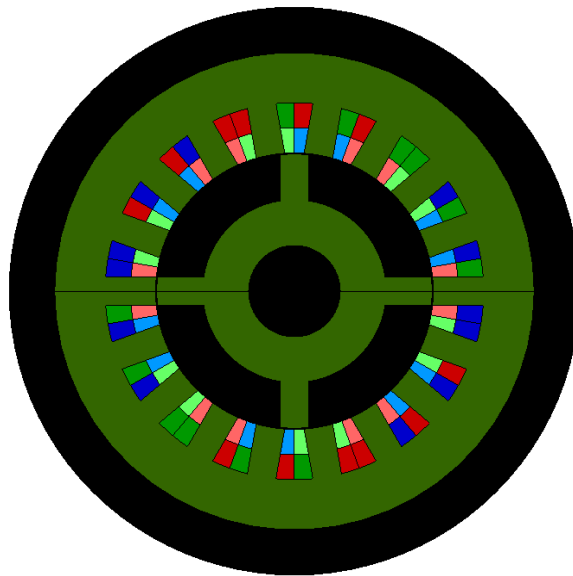


Figure 4.31 – 3-phase doubly salient BDFRM design

Compared to a 36 slot singly-salient design the control winding self-inductance ratio is 51% larger in the doubly-salient design. As a consequence of the concentrated coil winding in the doubly-salient variant, the cross-sectional area per coil is lower than in the singly salient variant. If the magnitude of the current density is to be maintained between the two models, this would lead to a lower control winding

MMF in the doubly-salient variant. The performance of this doubly-salient design (with the same rotor and stator outer diameter) was simulated at an operating point of 4,800rpm with a contra-rotating  $14.14A_{rms}mm^{-2}$  40Hz control current.

The power winding load in each case was chosen to produce a maximum output power at a control current density of  $14.14A_{rms}mm^{-2}$ . For the original singly salient design of Figure 4.24 and the new doubly salient design of Figure 4.31, a power winding load of  $0.9\Omega$  and  $0.15\Omega$  was chosen respectively. This poor rotor utilisation leads to a decrease in output power by 56%, from 28.81kW for the singly salient machine to 12.57kW for the doubly salient machine.

Along with a large reduction in power by using a doubly-salient design, the torque ripple of the doubly-salient model is also appreciably larger than that of the singly-salient machine. In fact the ripple of the doubly salient design causes the torque to vary between generating and motoring as seen in Figure 4.32.

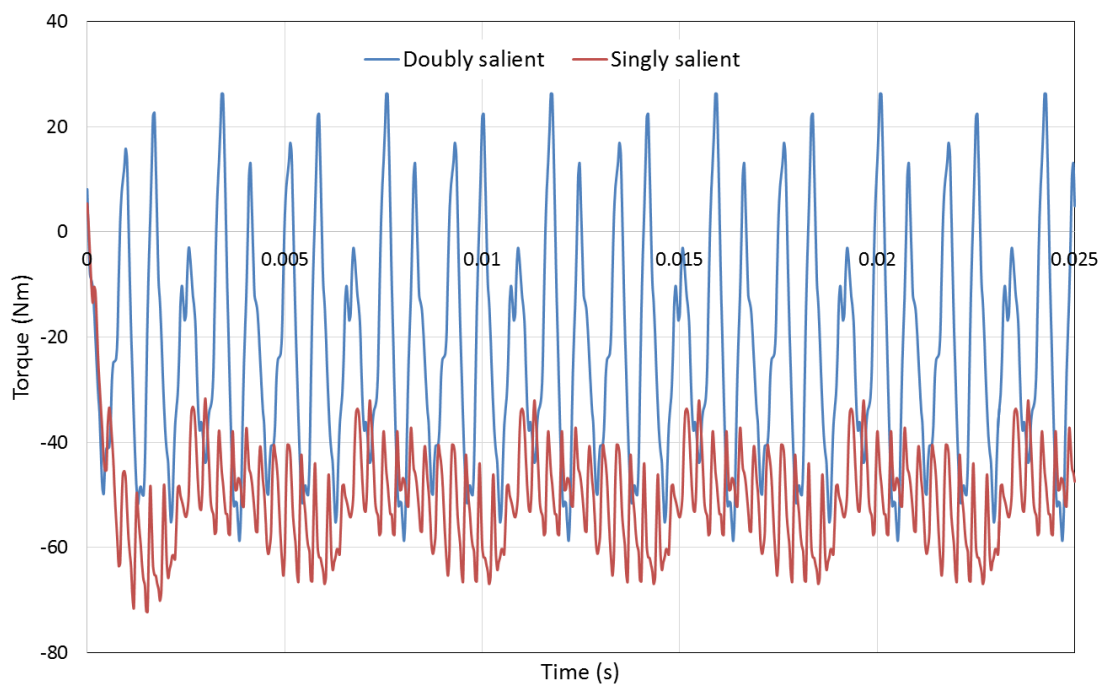


Figure 4.32 – Torque waveform of the singly and doubly salient BDFRM designs at a control winding current density of  $14.14A_{rms}mm^{-2}$ , a 40Hz contra-rotating control winding frequency and a 4,800rpm rotor

#### 4.7.2 SINGLE-PHASE VARIANTS

One option to increase the utilisation of the airgap periphery is to use three separate single phase machines (Figure 4.33). These would be cascaded on the same shaft, with appropriate offsetting of the rotor and/or stator angular positions. Such an approach would also have the advantage of some level of fault tolerance, due to the independent electromagnetic paths in each phase, although mechanically the phases are still coupled.

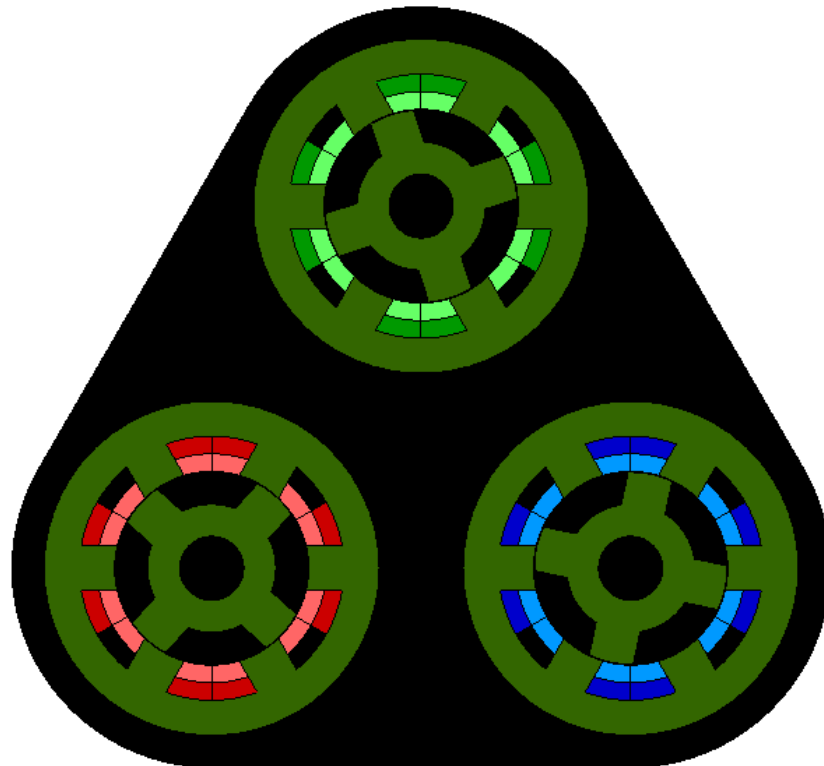


Figure 4.33 – 3 single phase cascaded BDFRMs

A major problem identified with using only a single control winding per machine is the presence of a zero excitation point twice every electrical cycle. In order to determine the effect of the interval during which the single-phase excitation is close to zero, the performance of a single-phase BDFRM was simulated for the following conditions:

- Rotational speed – 4,800rpm
- Control winding frequency – 40Hz (co-rotating)
- Control winding current density –  $14.14A_{rms}mm^{-2}$

- Power winding load –  $0.2\Omega$

The resulting power winding output voltage is shown in Figure 4.34. The correct level of frequency correction is achieved with this single-phase machine (320Hz synchronous output corrected to 360Hz output). However, the zero excitation points lead to a collapse of the power winding voltage, causing unacceptable levels of THD which are well outside the limitations of the VF standard, even when a star connected arrangement of coils is used, as some superposition of power winding voltages is present. As an example, Figure 4.35 shows the line-to-line voltage created by a star-connection of three phases, each with an appropriately phase-shifted version of the waveform in Figure 4.34.

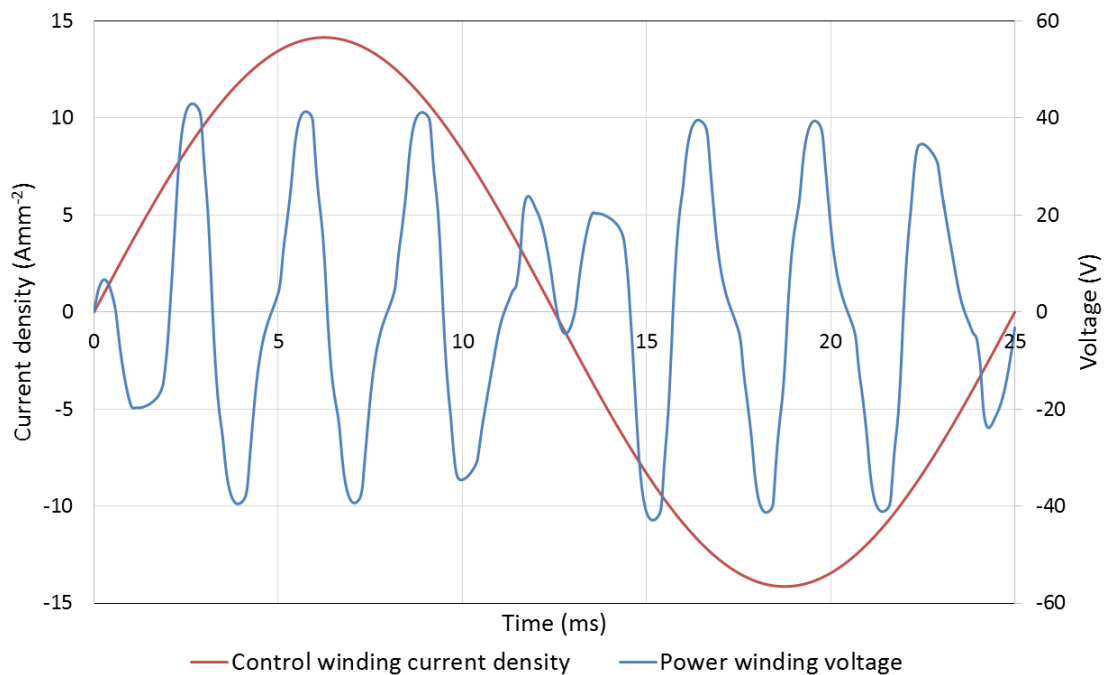


Figure 4.34 – Control winding current density and power winding voltage produced with a single phase BDFRM at 4,800rpm with a 40Hz co-rotating control winding current and a power winding load of  $0.2\Omega$

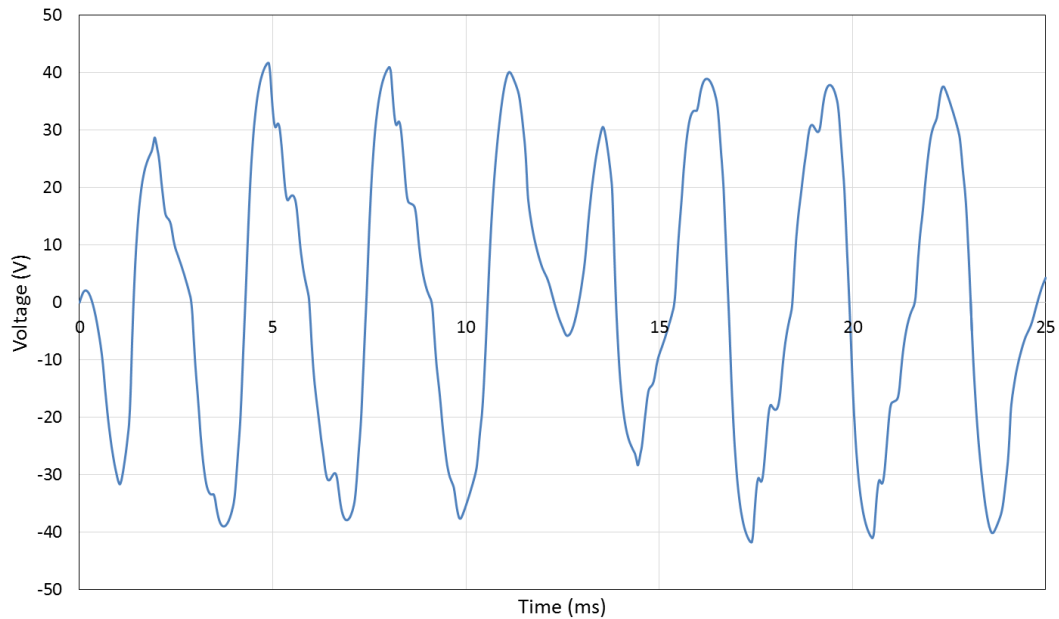


Figure 4.35 – AB line to line voltage produced with two single phase BDFRMs at 4,800rpm with a 40Hz co-rotating control winding current and a power winding load of  $0.2\Omega$

Two solutions to this problem of zero / very low excitation intervals were then reviewed. The first option considered each individual machine with a single power winding and three control winding phases. This eliminated the excitation dead time seen in the previous design, but still led to high power winding voltage THD and torque ripple.

The second solution considered was applying a DC offset to the control winding current to eliminate all zero crossing points as shown in Figure 4.36. Although this leads to fewer and smaller harmonics in the power winding voltage, both the high control winding RMS current required, and the torque ripple were undesirable.

Various alternative stator designs incorporating PMs were considered as a means of providing a DC offset flux to aid the control winding current. However, having explored several design variants with PMs placed in both the stator tooth body and tooth tips, it was found that the PMs were detrimental to the power winding voltage, rather than eliminating the zero excitation point.

For the reasons stated above it was deemed that, without significant further investigation, the doubly-salient BDFRM machine was unsuitable to operate within

the specification of this thesis, therefore no further research was carried out on this design.

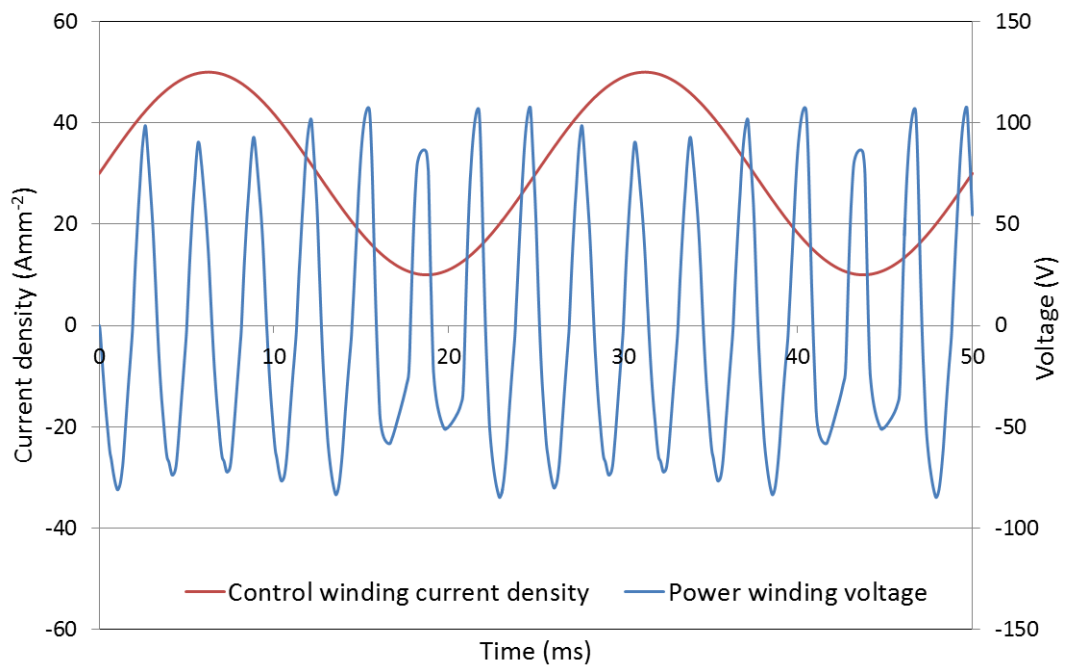


Figure 4.36 – Offset control winding current and power winding voltage produced with a single phase BDFRM at 4,800rpm with a 40Hz co-rotating control winding current and a power winding load of  $0.2\Omega$

## 4.8 CHAPTER 4 SUMMARY

This chapter has put forward several interesting design studies regarding the design of the BDFRM which affects saturation, harmonic content and output power.

The AFB rotor was seen to be the best choice for rotor design, with a higher output voltage fundamental and a lower harmonic content than the simple cruciform design. This was found to be primarily due to a more efficient distribution of flux in the core, so as to reduce saturation.

An alternative pole number combination was considered which demonstrated reductions in power and torque densities but proved to eliminate the direct coupling between the two windings seen in the 2/4/6 pole combination case.

A scaling study was performed on both the 2/4/6 and the 4/6/8 pole number combinations, with a conclusion that advantages in power density by scaling tend to tail off after a linear scaling factor of three. The weight of the end windings plays a big part in the poor torque and power densities of these machines, due to bulky low pole number distributed windings required to give a more sinusoidal MMF.

An initial study in to the airgap flux density harmonics was performed to provide a better understanding of the operation of the BDFRM and to view which harmonics are primarily a result of saturation within the machine.

Doubly salient variants of the BDFRM were studied in an attempt to increase the saliency ratio of the BDFRM, but poor rotor periphery utilisation led these to be unfeasible. One option to combat this was to use three single-phase cascaded machines, but dead times in the single-phase current waveforms would lead to a collapse in voltage twice every control winding electrical cycle.

The findings of this chapter will be taken forward in to the next chapter for the optimisation of a BDFRM demonstrator.

## 4.9 REFERENCES

- [1] U. D. o. Defense, "Aircraft Electric Power Characteristics - MIL-STD-704F," ed, 2004.
- [2] A. M. Knight, R. E. Betz, and D. G. Dorrell, "Design and Analysis of Brushless Doubly Fed Reluctance Machines," *Industry Applications, IEEE Transactions on*, vol. 49, pp. 50-58, 2013.
- [3] Vacuumschmelze. Soft Magnetic Cobalt-Iron-Alloys [Online]. Available: [http://www.vacuumschmelze.com/fileadmin/Medienbibliothek\\_2010/Downloads/HT/PHT\\_004\\_Vacoflux-Vacodur\\_engl.pdf](http://www.vacuumschmelze.com/fileadmin/Medienbibliothek_2010/Downloads/HT/PHT_004_Vacoflux-Vacodur_engl.pdf)
- [4] E. M. Schulz and R. E. Betz, "Impact of winding and gap flux density harmonics on brushless doubly fed reluctance machines," in *Power Electronics, Machines and Drives, 2004. (PEMD 2004). Second International Conference on (Conf. Publ. No. 498)*, 2004, pp. 487-491 Vol.2.



## 5 CHAPTER 5 – ELECTROMAGNETIC AND MECHANICAL OPTIMISATION OF THE BASELINE BDFRM

---

### 5.1 OPTIMISATION METHODOLOGY

The preceding chapter has described several of the operating features of a BDFRM. The next stage was to begin to optimise the design to enable a best case demonstrator to be constructed.

Before optimisation could take place, a detailed specification must be drafted to ensure the demonstrator is both effective in confirming analytical models, and capable of operating within the ranges of test equipment available. The detailed specification can be found in Appendix 3 (Section 8.3).

It should be noted that the proceeding optimisation study is performed based on a fixed (before back iron optimisation) stator frame size of 209mm as set out in Table 4.1. This frame size would produce a machine with an active mass of roughly 24kg. A conservatively designed PM machine would be expected to produce over 50kW with this frame size.

Taking the leading dimensions of the stator and rotor core listed in Table 4.1 as a starting point, there are several dimensions and features which could be optimised in order to enhance performance. In the case of the demonstrator machine, there are many different aspects of performance that could be selected as the criteria for optimality. For the purposes of this study, the optimisation (Sections 5.3.3 to 5.3.4) was performed by exploring the sensitivity of machine output power at a specific operating point described in Table 5.1. This provided a typical operating point of the BDFRM over a range of current densities.

The parameters to be optimised are done so in parallel in individual FE solvers. Whilst each parameter is adjusted, the other accompanying parameters remain constant throughout this study, as demonstrated in Table 5.2.

Table 5.1 – Operating point used throughout the BDFRM optimisation

Parameter	Value
<b>Rotor speed (rpm)</b>	4,800
<b>Control winding current densities (<math>A_{rms}mm^{-2}</math>)</b>	1.41, 7.07, 14.14
<b>Control winding frequency (Hz)</b>	40
<b>Correction factor (%)</b>	12.5
<b>Power winding frequency (Hz)</b>	360
<b>Load resistance (<math>\Omega</math>)</b>	3

Table 5.2 – Base values of parameters to be optimised

Parameter	Value
<b>Stator back iron thickness (mm)</b>	23
<b>Rotor pole width (fraction of <math>90^\circ</math>)</b>	0.67
<b>Number of flux guides</b>	5
<b>Ratio of rotor guide:barrier</b>	50:50
<b>Tooth tip height (mm)</b>	0.5
<b>Tooth shoulder height (mm)</b>	1

As is the case in the remainder of this thesis, the current density values quoted are rms in the conductors themselves assuming a conductor packing factor in the slot of 0.5. In the case of the highest values of  $14.14A_{rms}mm^{-2}$ , this corresponds to a magneto-motive force in the control winding in each slot of 612.9Ampere-turns.

For each combination of dimensions and features, a full electric-circuit coupled finite element simulation was performed, reaching steady-state conditions. For each simulation, the output power delivered, the power winding copper loss and the torque were calculated. Although this a computationally intensive undertaking, it does ensure that the full saturation conditions are captured, this factor being key in sizing the various regions of the stator and rotor cores.

The power factor of the load remains at zero throughout these simulations, although the author acknowledges that aerospace generated are often designed with a power factor of around 0.8 lagging [1]. This would lead to an increase in requirement for the converter VA rating.

## 5.2 SELECTION OF STATOR AND ROTOR CORE MATERIAL

The reference design established in Chapter 4 was based on Cobalt Iron stator and rotor cores, as is likely to be the case in any eventual aerospace application. However, to provide a more cost effective means of producing a prototype of reasonable rating (i.e. >10kW) for this thesis, Silicon Iron was adopted for both the stator and rotor cores. The specific grade of Silicon Iron selected was NO20 which is a 0.2mm thick, non-oriented, high performance material manufactured by Surahammar.

The initial magnetisation curve for Surahammar NO20 Silicon Iron is shown in Figure 5.1 along with the corresponding curve for Vacoflux 50 Cobalt Iron considered in the design study of Chapter 4. The lower saturation flux density of NO20 compared to Vacoflux50 will inevitably result in some reduction in the achievable torque density, in particular at higher levels of stator excitation.

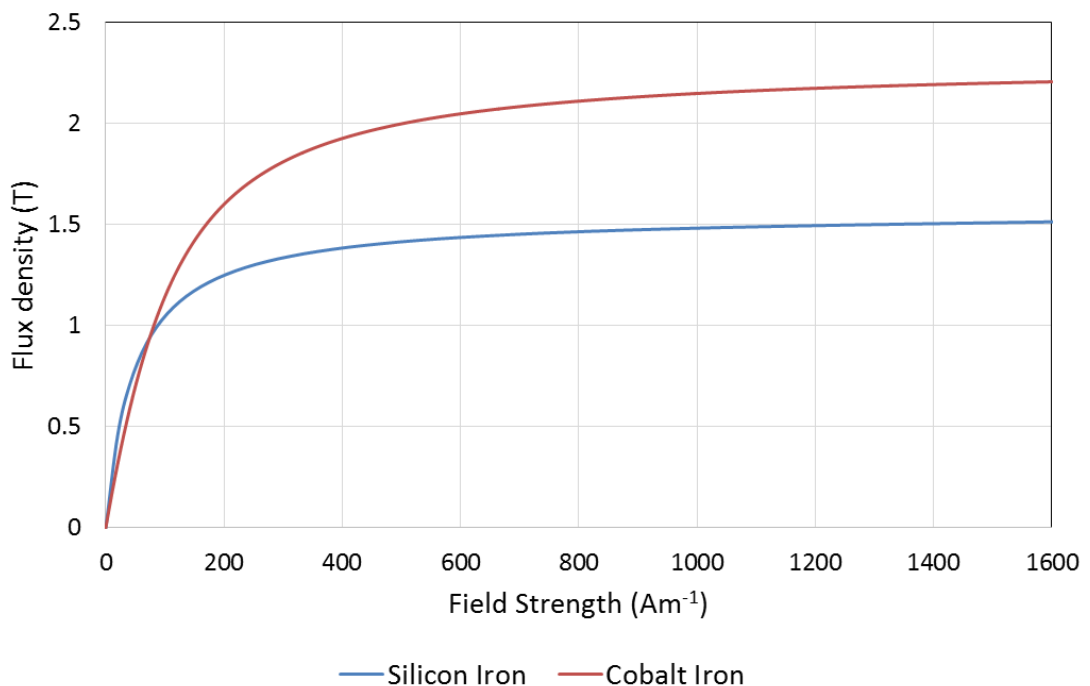


Figure 5.1 – Initial magnetisation curve for Surahammar NO20 [2] Silicon Iron and Vacuumschmelze VACOFLUX 50 [3] Cobalt Iron

## 5.3 OPTIMISATION OF STATOR GEOMETRY

### 5.3.1 STATOR WINDING CONFIGURATION

The stator winding configuration is the same as that adopted in Chapter 4 and shown previously in Figure 4.2. The stator is equipped with 36 slots, with the power and control windings arranged in two distinct layers within the slots with the power winding located nearer the airgap. The individual control and power windings are in themselves rather traditional distributed 2 and 6 pole windings.

### 5.3.2 SELECTION OF SLOT DEPTH

The stator slot depth in a doubly-fed machine must, inevitably, be made larger than that of a singly-fed machine, so as to accommodate the two windings. With this in mind a slot depth of 20.5mm has been used throughout this optimisation, and indeed throughout this thesis.

### 5.3.3 OPTIMISATION OF BACK-IRON THICKNESS

The first dimension optimised was the stator back iron thickness, defined as  $T_{BI}$  in Figure 5.2. The selection of the back iron thickness involves a compromise between ensuring that rated flux can pass through this region without excessive magnetic saturation and the mass of the stator core. Employing insufficient back iron thickness can adversely affect the achievable torque and power densities. In this study, the stator inner diameter was fixed, with a moving outer diameter.

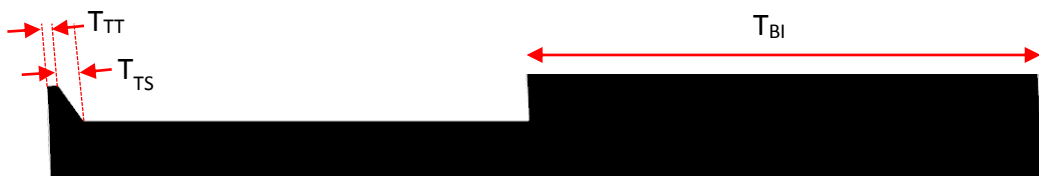


Figure 5.2 – Half of a stator slot/tooth to demonstrate the stator attributes to be optimised  
Figure 5.3 shows the simulated variation in the power winding output power for the reference operating conditions defined in Table 5.1. It can be seen that at each value of control winding peak current density, there is a point at which the machine output power ceases to increase with increasing back iron thickness, indicating a back iron

which is sufficiently thick to eliminate significant magnetic saturation. A more comprehensive view of the trade-off between electromagnetic performance and mass can be obtained by plotting the variation in power density as a function of back iron thickness. In this study, the power density refers to the active mass of the machine only (stator, rotor and windings) and excludes the casing and shaft. As would be expected, there is an optimum in terms of power density, which occurs at a value of back-iron thickness well before the output power levels off. On the basis of the simulated results in Figure 5.3, a back iron thickness of 22mm was selected. This corresponds to the optimal for the highest level of control winding current density considered. As would be expected, this value is greater than the optimal point for lower current densities, leading to under-utilisation of the stator core over some of the operating points.

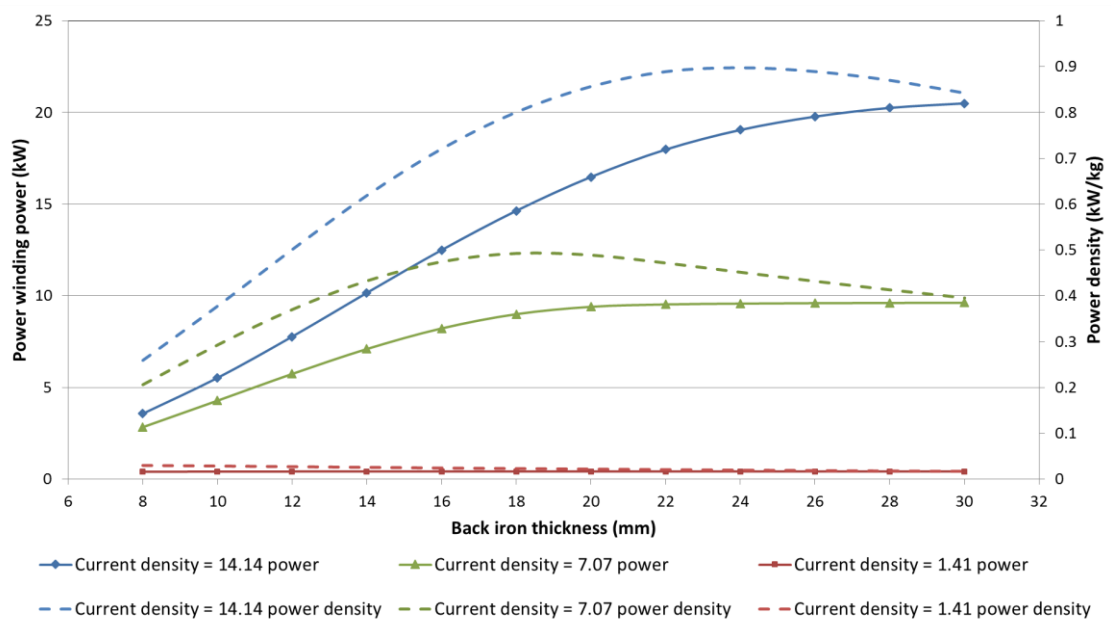


Figure 5.3 – Predicted variation in 3-phase load power produced as a function of stator back iron thickness for three distinct values of control winding current density where all current densities are measured in  $A_{rms}mm^{-2}$

#### 5.3.4 STATOR TOOTH FEATURES

The final aspects of the stator design to be optimised were the various dimensions of the stator teeth, specifically the tooth tip height and the tooth shoulder height, both of which are illustrated in Figure 5.2 as  $T_{TT}$  and  $T_{TS}$  respectively. Figure 5.4 shows the variation in the output power at the reference operating condition as a function of

tooth tip height. As will be apparent, although the sensitivity is not pronounced, adopting a smaller tooth tip height brings some advantages in output power. Reducing the height of the tooth tip acts to reduce cross-slot leakage between adjacent teeth, therefore directing more flux across the airgap to the rotor. A value of 0.5mm was selected, this being deemed to be the smallest that could be practically manufactured while also remaining mechanically robust. A similar level of relative insensitivity was observed with the tooth shoulder height as shown in Figure 5.5, and again a value of 0.5mm was selected.

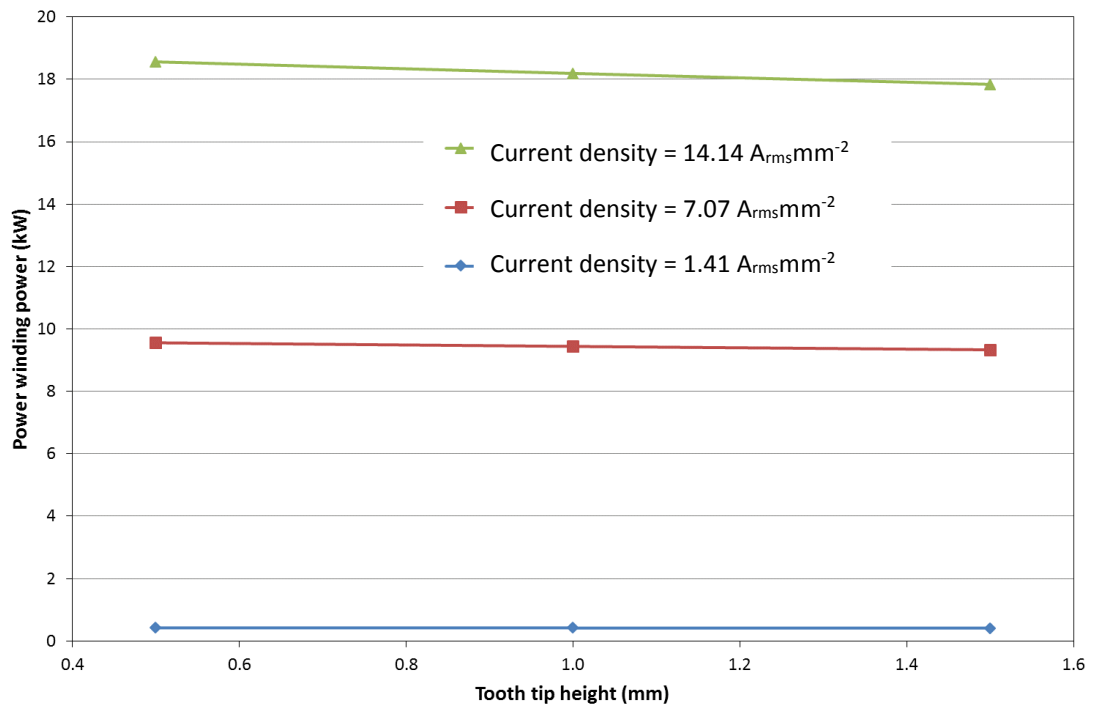


Figure 5.4 – Stator tooth tip height optimisation with regards to total 3-phase load power

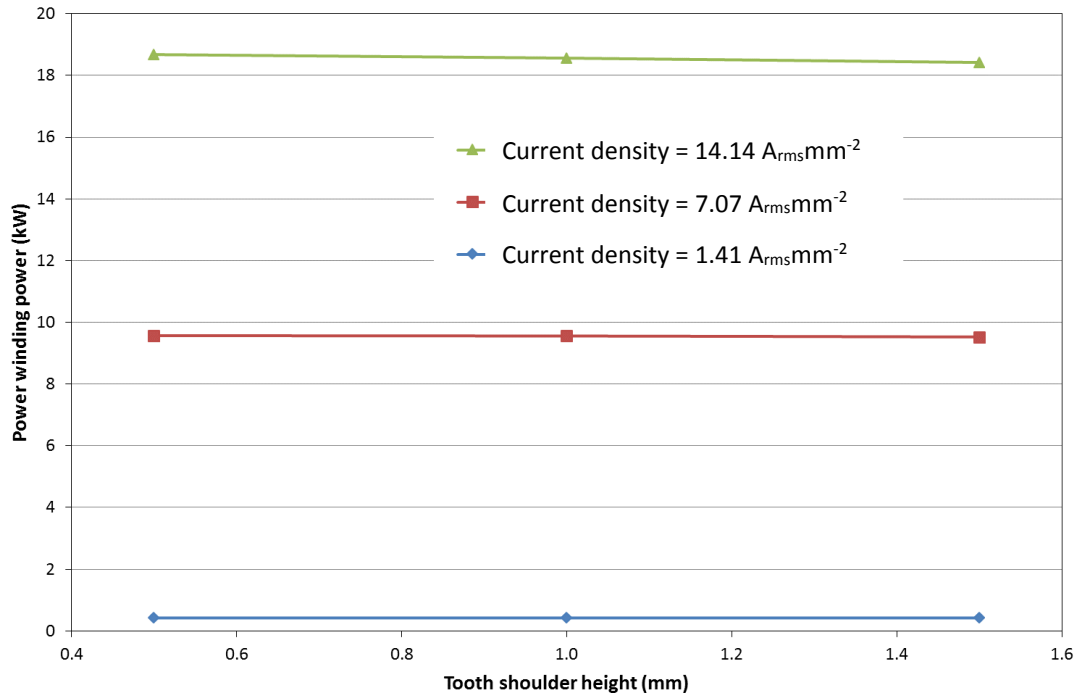


Figure 5.5 – Stator tooth shoulder height optimisation with regards to total 3-phase load power

## 5.4 OPTIMISATION OF ROTOR GEOMETRY

### 5.4.1 ROTOR POLE WIDTH

Although the AFB rotor described previously in Chapter 2 contains many intricate features, a major parameter is the angular span of each pole. It is often useful to express this in terms of a proportion of the available periphery for each pole, e.g. as a fraction of 90° in the case of a four-pole rotor. Figure 5.6 shows rotor designs that are at the extremes of the reasonable range, viz. 0.9 and 0.4.

A series of simulations at the reference operating point in Table 5.1 were performed for rotors with poles which occupy between 0.4 and 0.9 of the 90° span. As shown, there is an optimum, albeit not very pronounced, for ratios of ~0.65. This value was adopted for subsequent optimisation.

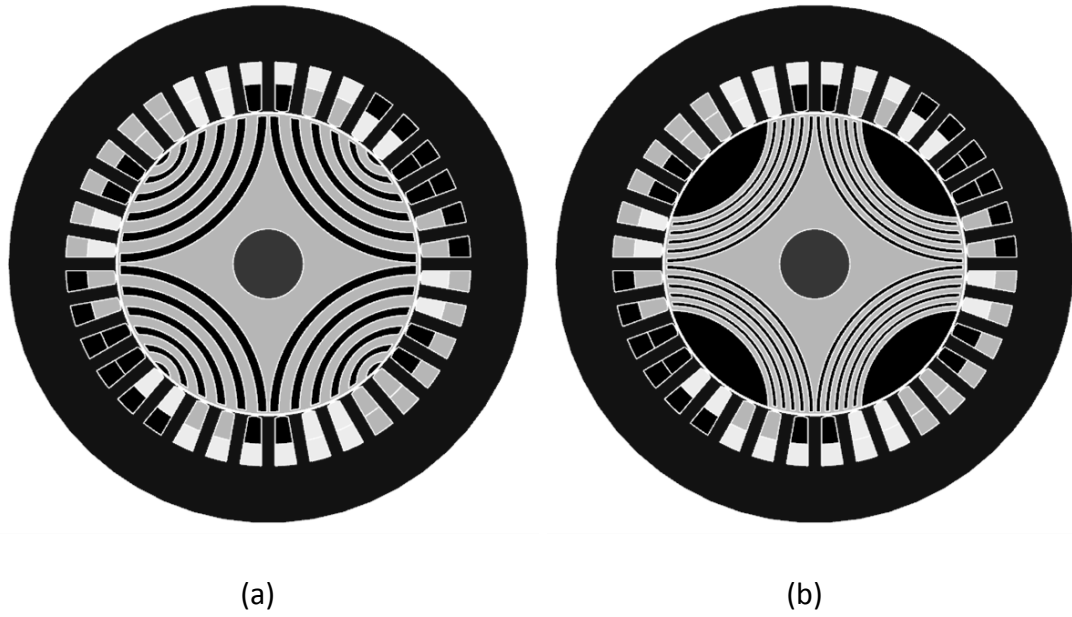


Figure 5.6 – Rotor pole-arc to rotor pole pitch ratio of 0.9 (a) and 0.4 (b)

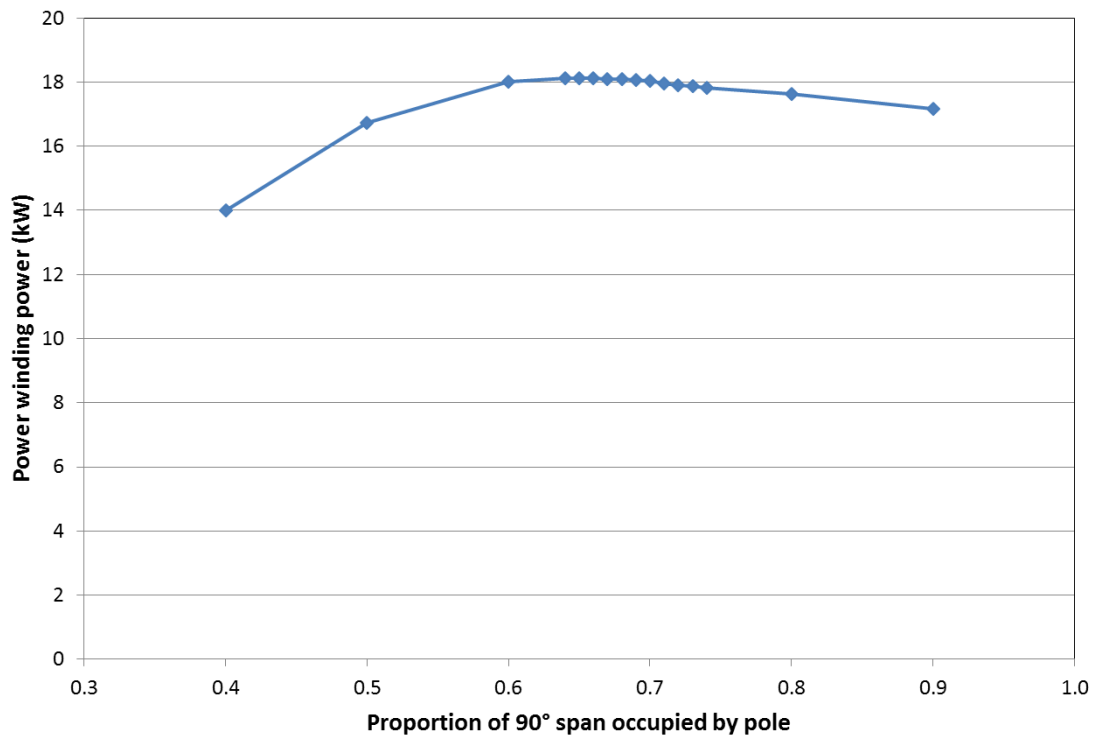


Figure 5.7 – Optimisation of the proportion of 90° rotor periphery span occupied by rotor pole



#### 5.4.2 SHAFT DIAMETER

The shaft diameter does not play a first-order role in the electromagnetic performance of the rotor, providing it is not required to occupy a significant proportion of the overall rotor cross-section (as might be the case with a fully embedded generator mounted on an engine shaft). It must have sufficient strength and stiffness to transmit the rated torque, with significant margin and avoid any problems with rotor dynamics, e.g. whirl of the shaft [4]. The shaft diameter was set to 28mm to provide ample rigidity [5] whilst being readily coupled to the dynamometer used to test the demonstrator. In order to promote the passage of flux in the desired four-pole pattern, the shaft should be non-magnetic, e.g. 316 stainless steel.

#### 5.4.3 BRIDGES ACROSS FLUX BARRIERS

As discussed previously in Chapter 3, in order to produce a single piece lamination, it is necessary to incorporate bridging regions at the end of each flux guide near to the airgap. From an electromagnetic point of view, these bridges should be as thin as possible, to promote localised saturation. However, even when the emphasis is entirely on electromagnetic design (i.e. no account of mechanical stress considerations at this stage) they must be sufficiently wide to be able to be manufactured by a wire eroder to a predetermined tolerance and maintain the overall rotor geometry during assembly. Based on these considerations, the bridges were kept to 1mm which is a practical trade-off between the two objectives above.

To encourage a reduction in torque ripple [6], the closures of each flux barrier were curved rather than given a sharp corner. This will also help to reduce point loading of stress, when the rotor is subject to a centrifugal load. More on the mechanical optimisation of the rotor will be discussed in a later section.

#### 5.4.4 OPTIMISATION OF THE NUMBER OF ROTOR FLUX GUIDES

These flux guides, some examples of which are shown in Figure 5.8, are key in directing the flux to the appropriate location around the rotor periphery, and therefore maximising the saliency ratio of the rotor. If a fixed ratio of the flux barrier

and guide widths is adopted, then the number of rotor guides has no effect on the overall weight of the rotor. The power winding output power, at the reference operating condition detailed in Table 5.1, was calculated for rotor designs having a number of flux guides between zero (i.e. the rotor in Figure 5.8a) and seven (shown in Figure 5.8c). In each case, the width of the flux guides and barriers was kept at the same 50:50 ratio. The resulting variation in stator output power, as a function of the number of flux guides, is shown in Figure 5.9.

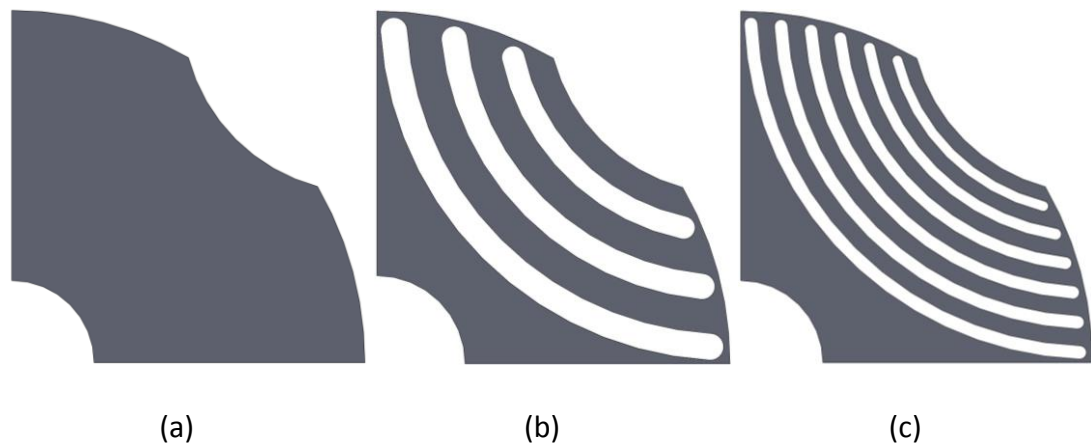


Figure 5.8 – Rotor designs with zero (a), three (b) and seven (c) rotor flux guides

As shown in Figure 5.9, there are no further benefits in power winding power, at any of the control winding current densities, for a number of flux guides beyond three. This said, published studies [6, 7] suggest that at least 4 or 5 flux barriers are required for four-pole rotors to minimise ripple in the torque and harmonics in the output voltage. To ensure that benefits in torque ripple and/or voltage harmonics were not being over-looked, further analysis was performed. Figure 5.10 shows the predicted total harmonic distortion of the output voltage waveform, as a function of the number of flux guides, for 3 different stator current density levels. This illustrated that there is little, if any, benefit in increasing the number of rotor flux guides beyond three. Similar conclusions may be drawn from the corresponding predicted torque ripple variations in Figure 5.11. It is interesting to note the torque waveform in Figure 5.12, which includes an appreciable ripple due to both the slotting effects and the interaction of the airgap flux harmonics. Further harmonic study will follow in Section 5.9, where a skewed rotor is implemented in an effort to dampen and eliminate some of these high frequency harmonics.

One possible advantage to having more rotor guides than 3, which will be discussed more thoroughly in Section 5.6, is concerned with the mechanical stress.

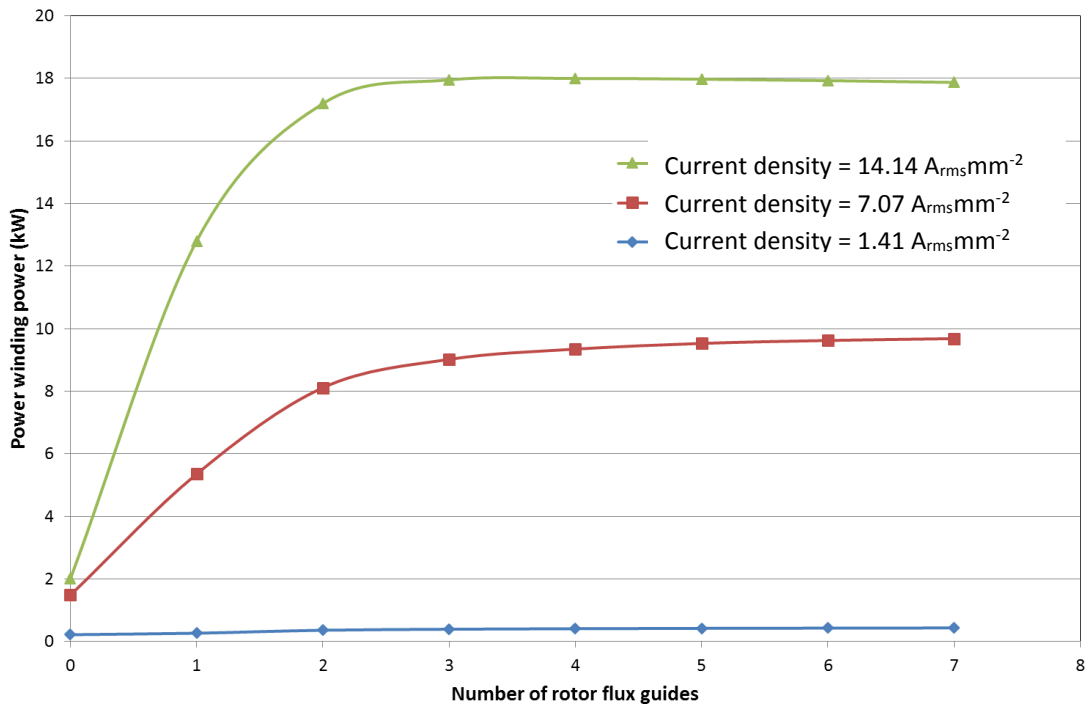


Figure 5.9 – 3-phase load power produced with incremental numbers of flux guides

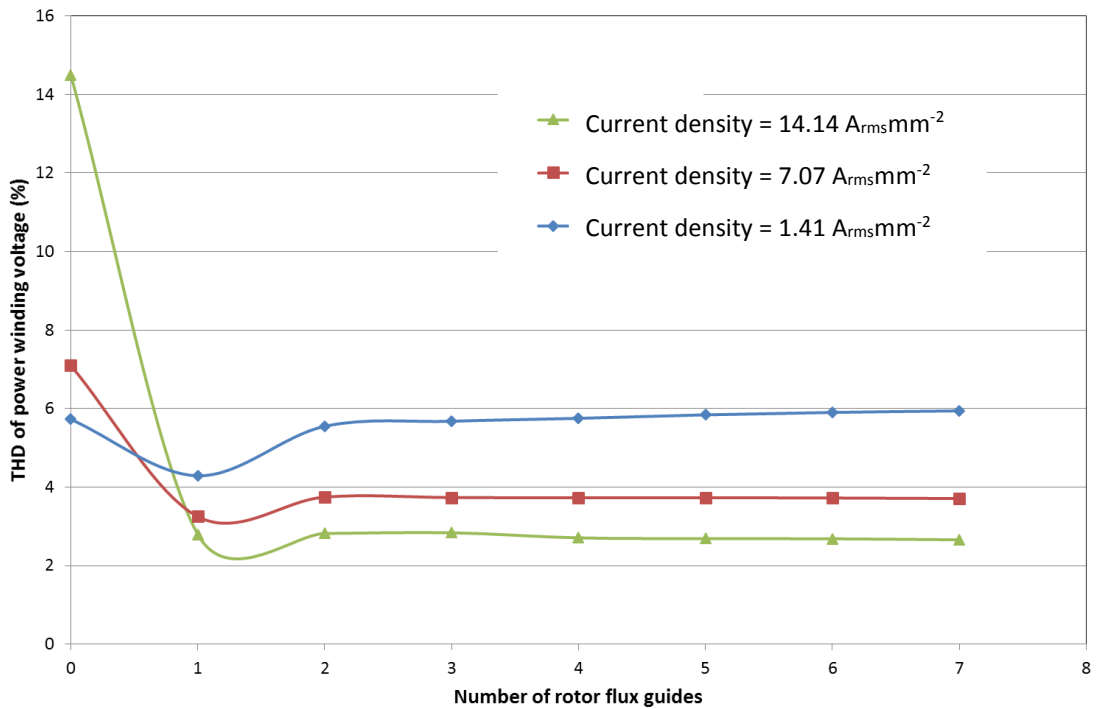


Figure 5.10 – Power winding RMS voltage and THD produced with incremental numbers of flux guides

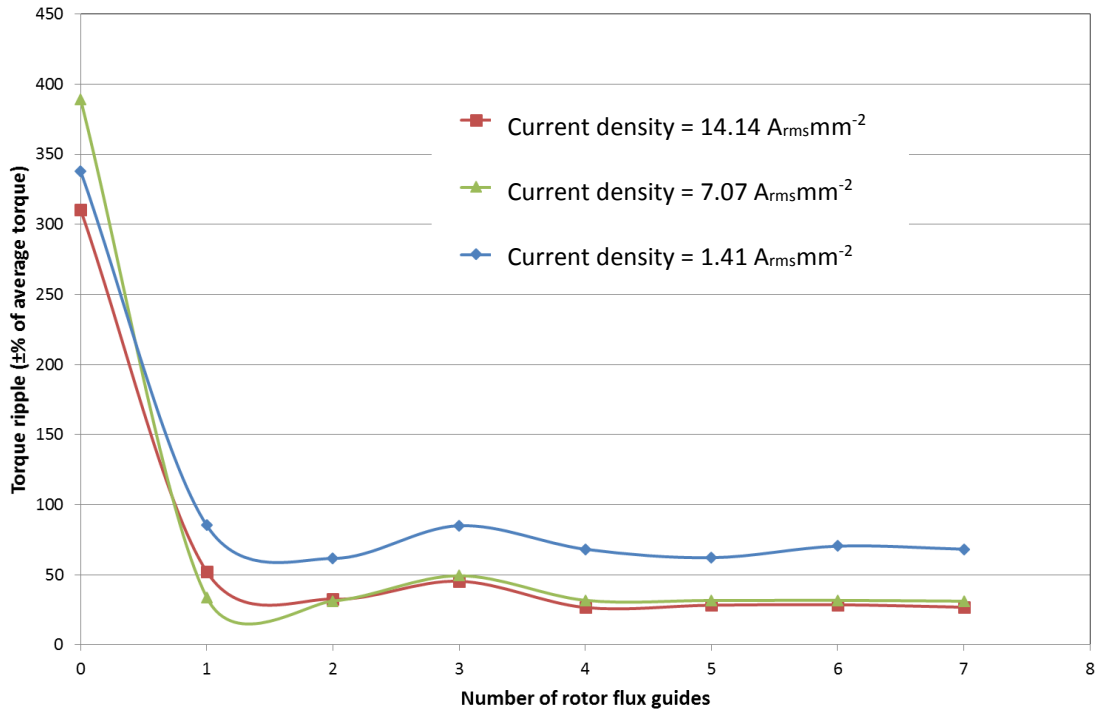


Figure 5.11 – Torque ripple produced with incremental number of flux guides with a range of current densities

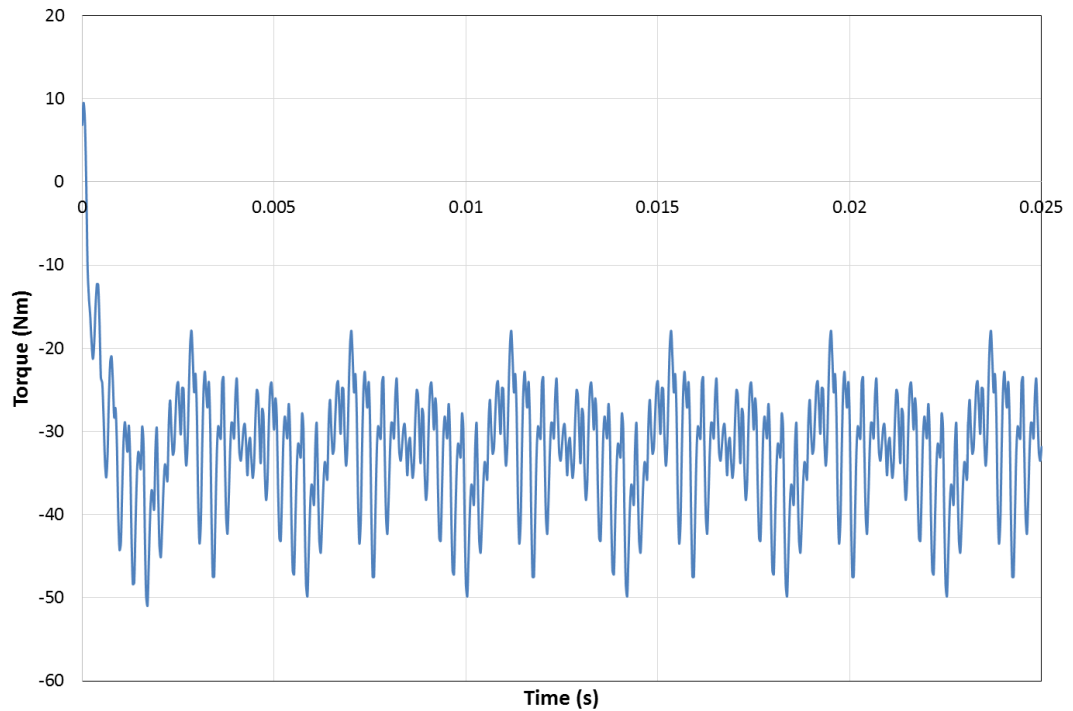


Figure 5.12 – Torque produced with three rotor flux barriers and a control winding excitation of 14.14A<sub>rms</sub>mm<sup>-2</sup> with a load of 3Ω (N.B initial transient is a consequence of the electrical time constant and zero current starting assumption)

#### 5.4.5 OPTIMISATION OF THE RELATIVE WIDTH OF ROTOR FLUX GUIDES AND BARRIERS

A further rotor parameter that can be optimised is the percentage of the combination of the flux barrier and guide that is taken up with flux guide (which was previously set to equal 50% in Table 5.1). If the width of the flux guide is reduced too far then magnetic saturation could occur even at modest levels of excitation, causing a reduction in torque. However, if the width of the rotor flux guides is increased too far, causing the barriers to reduce, then their effectiveness in directing flux along the guides will be reduced due to greater flux leakage across the barriers. This in turn, would lead to a loss of saliency ratio and hence torque. To investigate this behaviour systematically, the percentage of the total flux guide and barrier width taken up as flux guide was varied over the range 5% to 100%, and the output power calculated for the reference operating point, defined previously in Table 5.1. The resulting variation in the output power with this ratio is shown in Figure 5.13, while Figure 5.14 displays the two rotor cross-sections at the extremes of this range and the optimal rotor with a percentage of 55%, which produces an output power of 18.0kW at  $14.14A_{rms}mm^{-2}$ .

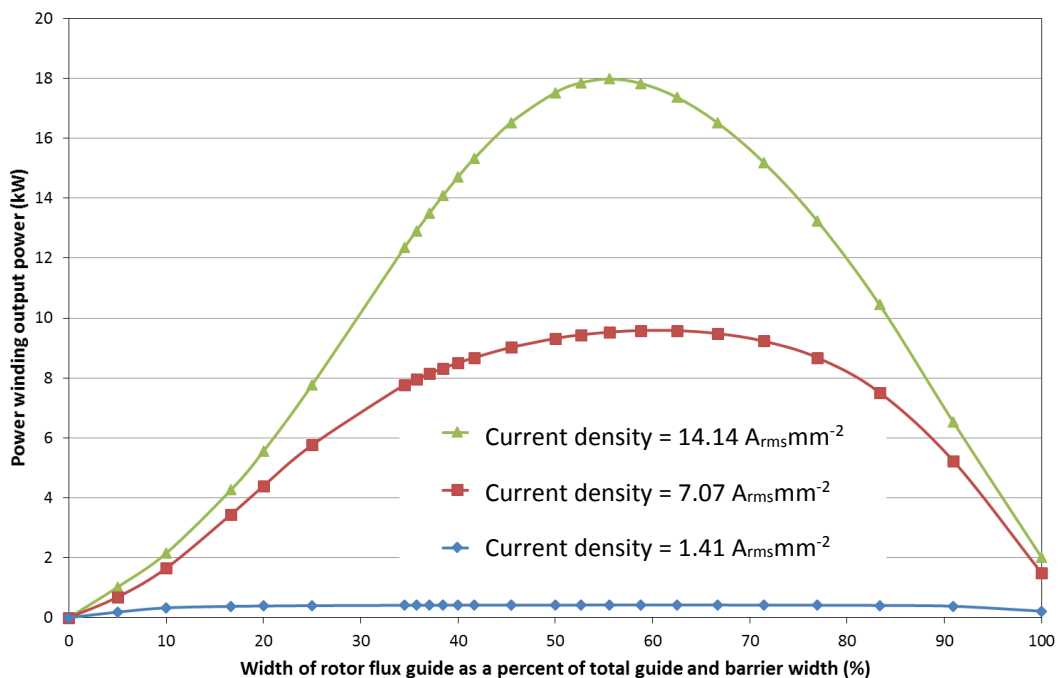


Figure 5.13 – Rotor flux guide width optimisation with regards to total 3-phase output power

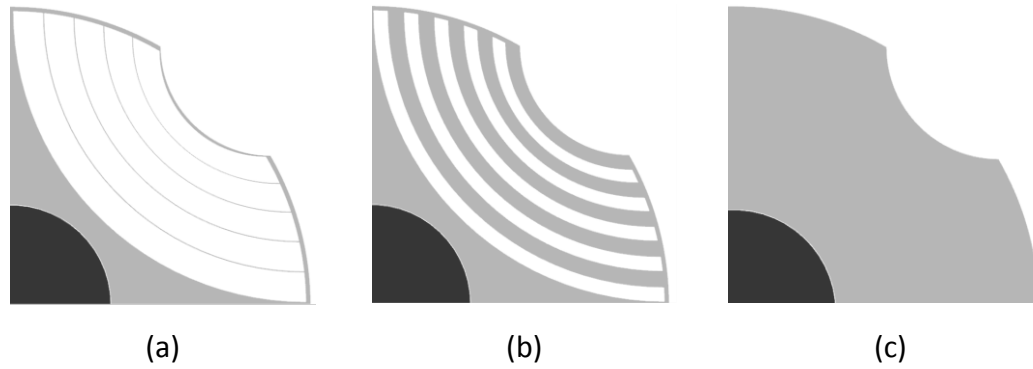


Figure 5.14 – Cross-sections of a 5% rotor flux guide (a) the optimal 55% flux guide (b) and a 100% rotor flux guide (c)

A summary of the original and optimised stator and rotor dimensions can be found in Table 5.3.

Table 5.3 – A summary of the dimensions optimised in Sections 5.3 and 5.4

Parameter	Original value	Optimised value
Stator back iron thickness (mm)	23	22
Rotor pole width (fraction of 90°)	0.67	0.65
Number of flux guides	5	3
Ratio of rotor guide:barrier	50:50	55:45
Tooth tip height (mm)	0.5	0.5
Tooth shoulder height (mm)	1	0.5

## 5.5 ROTOR BRIDGE SATURATION

In order to be effective, it is important that the rotor bridges are magnetically saturated at the lowest possible excitation current, thus preventing excessive leakage flux through the bridges, which both reduces the saliency ratio and increases the flux in the stator core. The role of bridge saturation is illustrated in Figure 5.15, which compares the output power predicted from a series of transient finite element simulations for cases with both the non-linear B-H characteristic for Silicon Iron, and with a linear fixed magnetic permeability of  $13,000\mu_0$ . As will be apparent, for values of current density up to  $\sim 12.6A_{rms}mm^{-2}$ , the machine with non-linear bridges produces more power due to saturation of the bridges. However, beyond a current density of  $\sim 12.6A_{rms}mm^{-2}$ , bulk saturation begins to occur in the rotor and stator cores and the non-linear and linear power curves cross-over.

A further useful comparison can be obtained by comparing output power predicted with non-linear and linear ( $13,000\mu_0$ ) B-H characteristics, in both cases with the bridge regions having a permeability of  $\mu_0$  (i.e. non-magnetic). As expected, the resulting comparison, which is shown in Figure 5.16, demonstrates that with non-magnetic bridges, all operating points with the linear material produce a higher power than that with non-linear material.

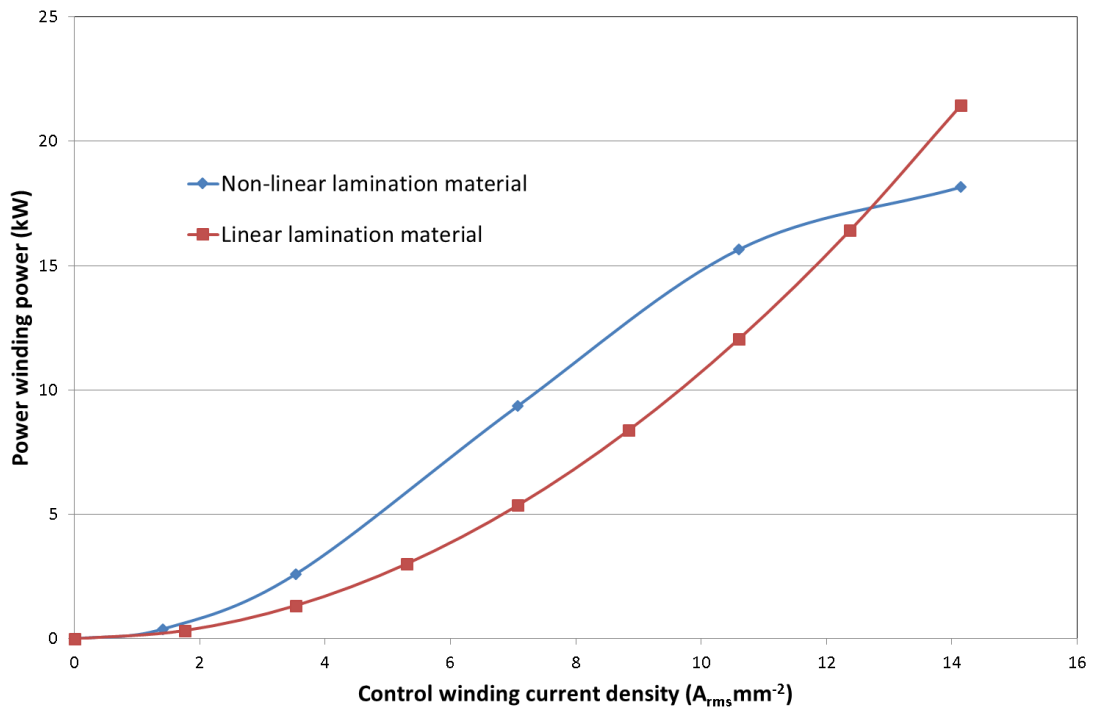


Figure 5.15 – 3-phase load power produced with the use of both linear and non-linear lamination materials with the rotor bridges in place at 10% below the VF range (4,860rpm) with a co-rotating 36Hz control winding current and a power winding load resistance of  $3\Omega$

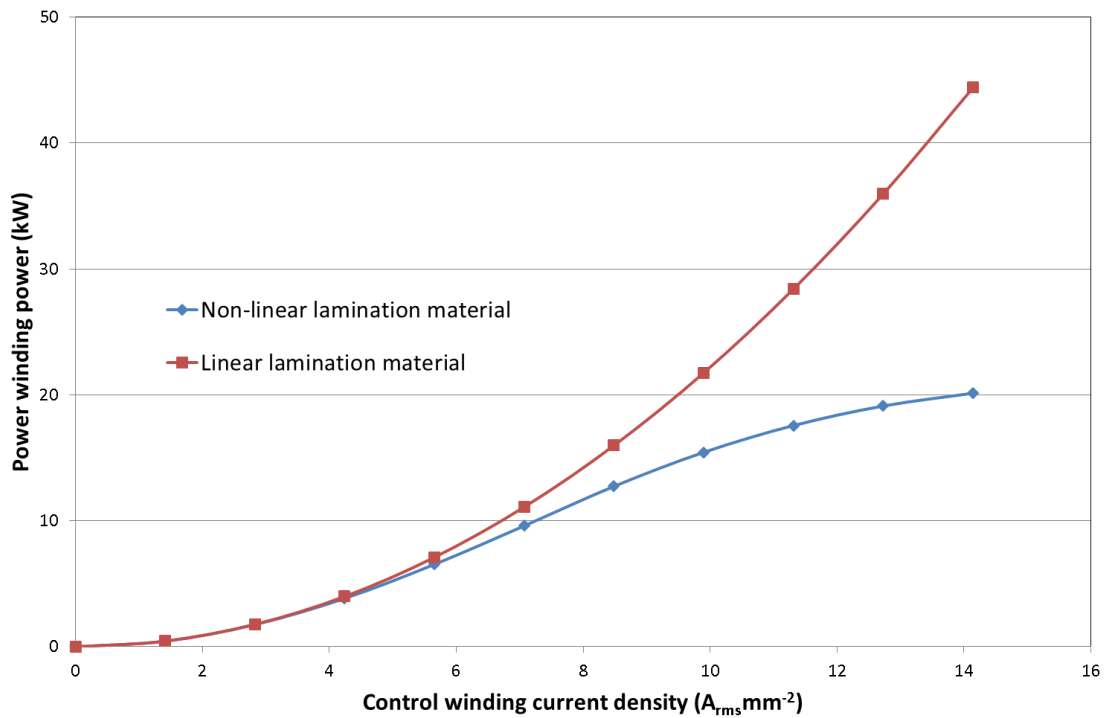


Figure 5.16 – 3-phase load power produced with the use of both linear and non-linear lamination materials and with rotor bridges set to air at 10% below the VF range (4,860rpm) with a co-rotating 36Hz control winding current and a power winding load resistance of  $3\Omega$

A better understanding of the nature of bridge saturation can be established from the predicted distribution of magnetic equipotential contours in the FEA model, for the rotor with magnetic bridges of the same properties as the remainder of the rotor. Firstly, for the case of a non-linear core at a current density of  $8.5A_{rms}mm^{-2}$ , it is clear from Figure 5.17 that only a small proportion of the flux crossing the airgap passes through the bridges before returning to the stator, with the majority of flux in this case passing along the rotor flux guides as expected. However, the corresponding field distribution for the linear core material, which is shown in Figure 5.18 illustrates that a significant proportion of the airgap flux passes through the rotor bridges, thus leading to a reduced output power seen in Figure 5.15.



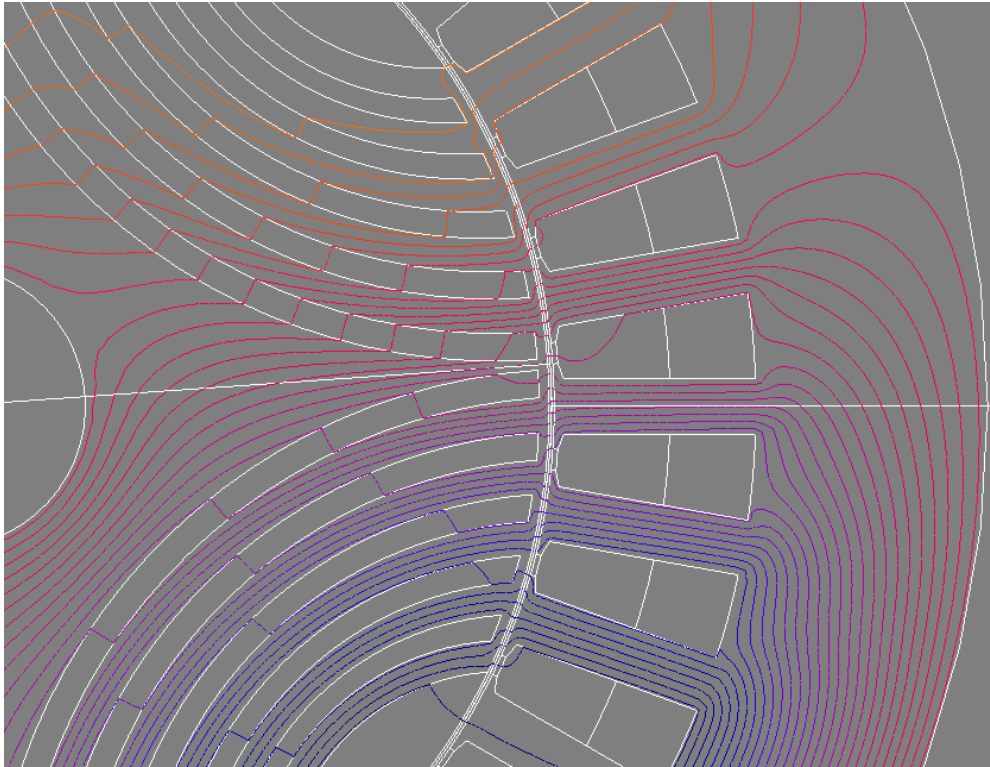


Figure 5.17 – Isovalue flux plot of a model with non-linear lamination material at a current density of  $8.5A_{rms}mm^{-2}$

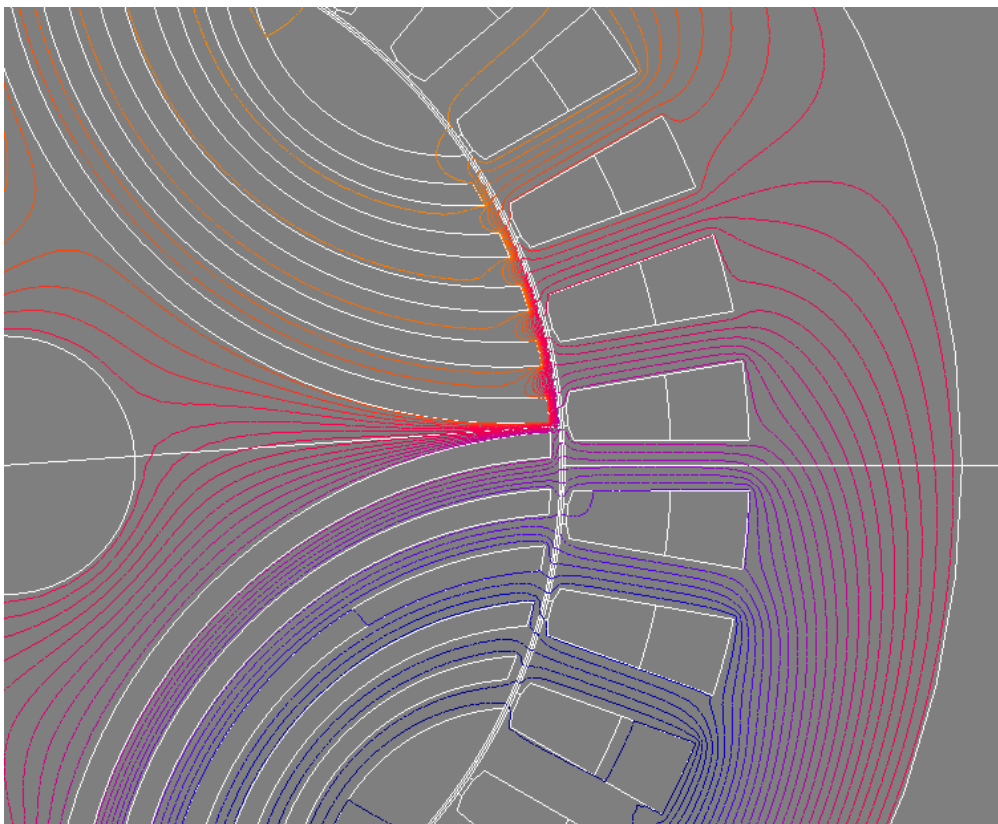


Figure 5.18 – Isovalue flux plot of a model with linear lamination material at a current density of  $8.5A_{rms}mm^{-2}$

## 5.6 MECHANICAL OPTIMISATION OF THE ROTOR

Previous published studies [7, 8] have demonstrated that when the rotor structure is subjected to significant centrifugal loading (through a combination of speed and diameter), cross-barrier supports are often required in order to limit deformation of the rotor and maintain localised stress levels below some specified maximum service stress, e.g. some proportion of the yield strength of the rotor core material. As the rotor in this design study was subjected to speeds of up to 14,400rpm (assuming a frequency correction of up to 20% at the upper end of its operating range), it was important to ensure that the rotor structure would remain intact at these high rotational speeds (surface velocity of  $90\text{ms}^{-1}$ ). To this end, a series of two- and three-dimensional mechanical finite element models were solved using ANSYS, in all cases assuming linear, isotropic material behaviour (i.e. the mechanical anisotropy of a laminated stack was not considered). This is a reasonable approximation as the mechanical loading is dominated by the in-plane centrifugal loading. The physical properties assigned to the rotor core, which were drawn from manufacturer supplied data for NO20 Silicon Iron, are summarised in Table 5.4. Although the data in Table 1.3 is useful to undertake the modelling and assess the results, it does not in itself set the upper limit of the stress that could be accommodated. Clearly, the UTS sets an absolute limit, but it would also be desirable to avoid any significant yield. Furthermore, in order to have some overhead to allow for fatigue, it is common design practice for many metals to set a design stress as some proportion of the yield stress, often 50-60% although this is influenced by factors such as temperature and uncertainty in service loads. For this design study, a conservative but representative limit of 50% of the yield stress was imposed.

As discussed in Section 5.4.4, little electromagnetic benefit is gained from increasing the number of rotor barriers beyond three. A similar study was performed for mechanical behaviour. A series of three-dimensional mechanical finite element models, with no cross-barriers supports and an increasing number of flux guides were solved. In each case the bridging regions, which close off the flux barriers, are 1mm thick as was the case for the rotor considered in Section 5.4.4. It should be noted that

the curved ending of the rotor flux barrier proves both to improve the mechanical integrity of the rotor, as well as reducing the torque ripple [6].

The resulting predicted variation in peak stress as a function of the number of flux guides is shown in Figure 5.19, while Figure 5.20 shows a typical predicted stress distribution. As will be apparent in the more detailed Figure 5.21, in the absence of cross-barrier support, the levels of stress in the regions at the end of each barrier are much greater than could be sustained by NO20.

Indeed, for the case of a rotor with three flux barriers and 1mm thick bridging regions, the maximum allowable speed for the peak localised stress to remain below 50% of yield strength is only 5,000rpm as compared to the rated speed of 14,400rpm. There is an indication that there is a penalty associated with increasing the number of barriers, but without cross-supports all the variants are impractical and hence no mechanical optimum can be established. However, given that there is little electromagnetic benefit in going beyond three flux barriers and this would furthermore increase the levels of localised stress, only designs with three flux barriers were subsequently considered.

Table 5.4 – Material specific parameters used in ANSYS to represent NO20 Silicon Iron

Constant	Value
Yield strength (0.2% proof strength) (MPa)	400
Ultimate tensile strength (MPa)	505
Young's modulus (GPa)	185

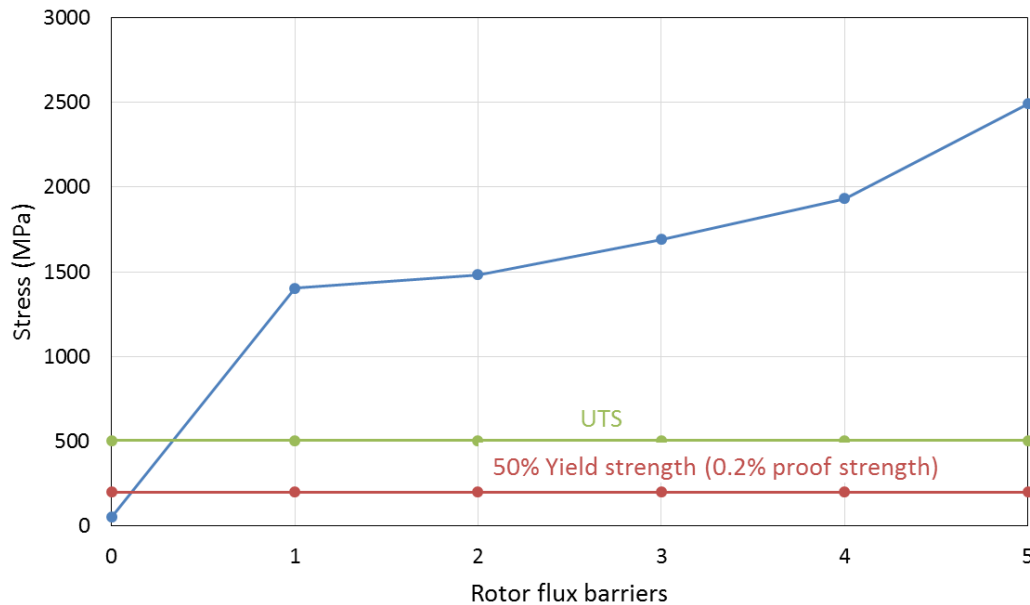


Figure 5.19 – Influence of the number of rotor flux barriers on the peak localised stress in the rotor at 14,400rpm (rotor not equipped with any cross-barrier supports)

Of the various modifications that can be made to the rotor geometry to alleviate localised stress concentrations, two specific features were investigated systematically, viz. the thickness of the outermost bridge that closes off the flux barrier (which as shown previously in Figure 5.20 is the region of highest stress concentration), and the incorporation of cross-barrier supports.

Firstly, the thickness of the bridge was varied from 1mm to 10mm in 4 equal incremental steps. The two rotor geometries at the extremes of this range are shown in Figure 5.22. As will be apparent, although the 10mm bridge thickness will tend to alleviate the mechanical stress concentration around the flux barriers, it will tend to reduce the saliency ratio of the machine. The resulting predicted variation in peak localised stress with bridge thickness is shown in Figure 5.23. Even with the uppermost thickness of bridge of 10mm, which would significantly diminish the electromagnetic effectiveness of the flux barriers, the localised stress levels remain too high for reliable operation.

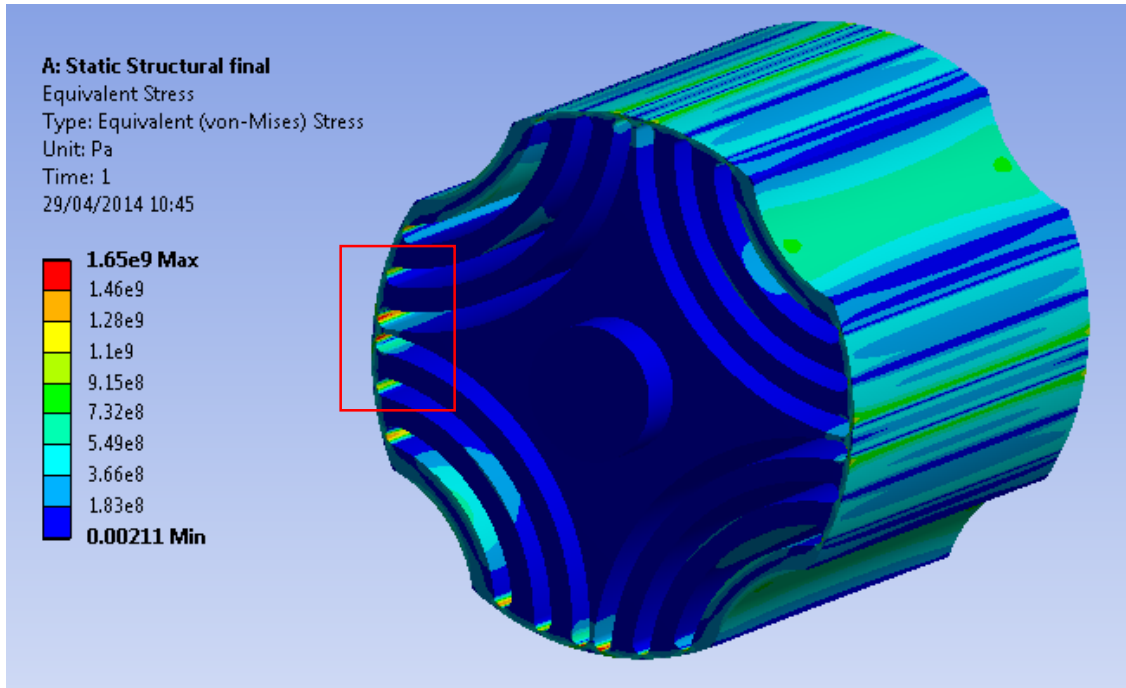


Figure 5.20 – Predicted stress distribution in an NO20 Silicon Iron rotor with three flux guides at 14,400rpm

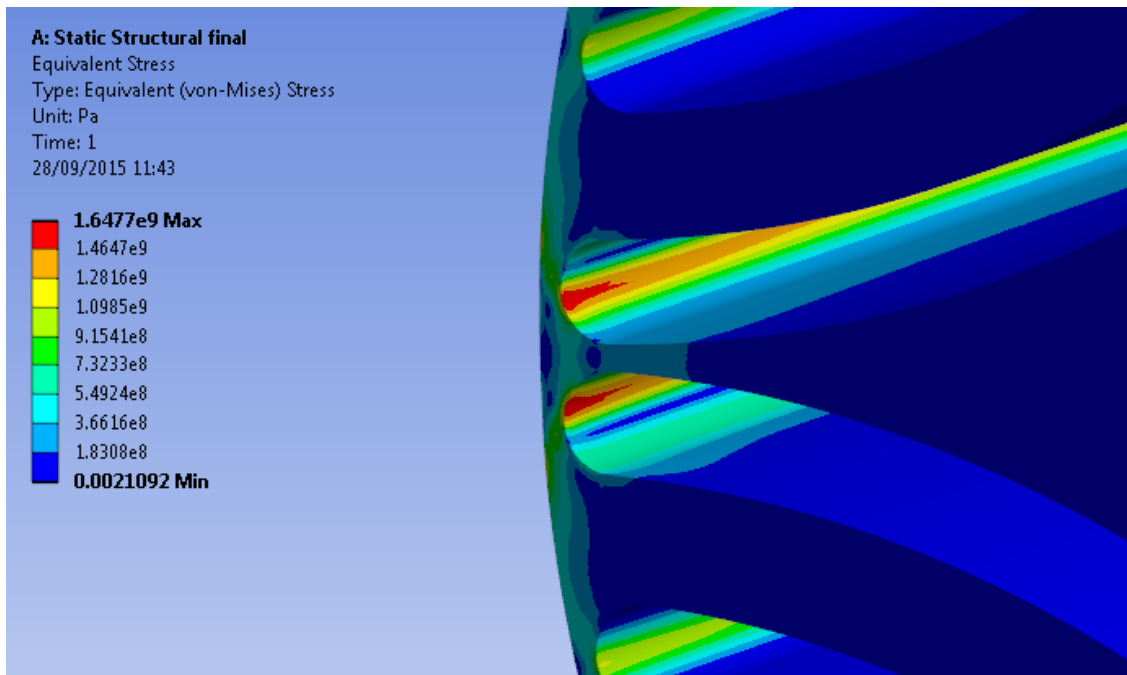


Figure 5.21 – Detailed view of the stress distribution as highlighted with a red square in Figure 5.20

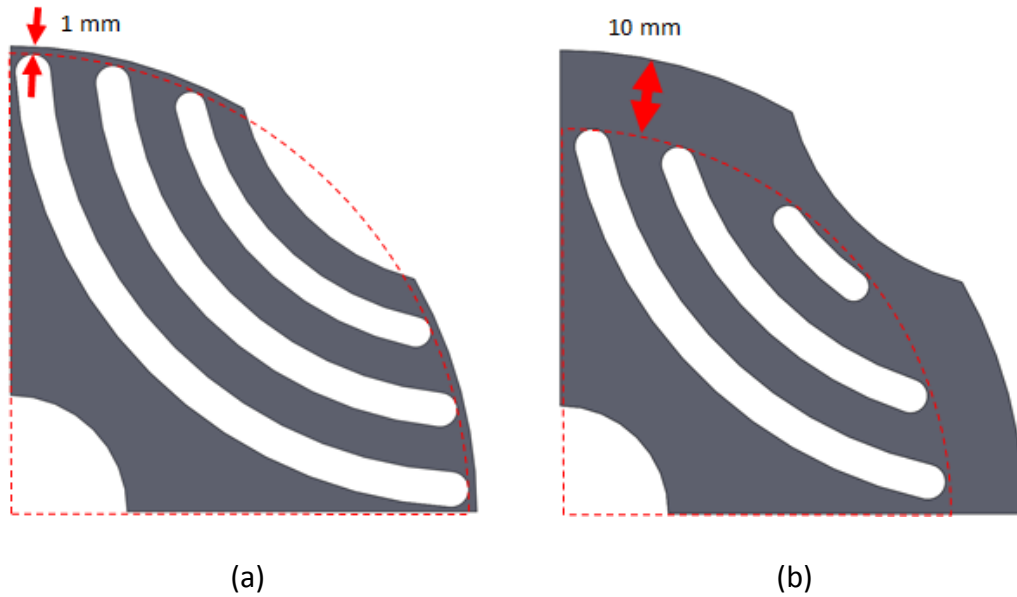


Figure 5.22 – Rotor designs with 1mm (a) and 10mm (b) rotor bridge thickness

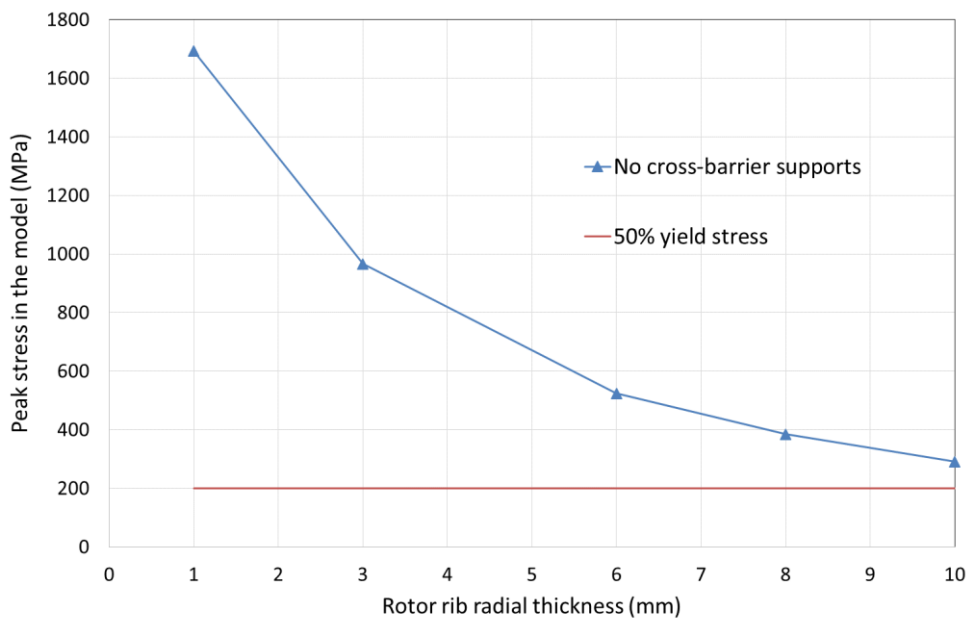


Figure 5.23 – Finite element predicted variation of peak localised stress in the rotor with increasing rotor bridge radial thickness at a speed of 14,400rpm

The inability to produce a viable mechanical design, even with excessively thick bridges (excessive in the sense of electromagnetic considerations), demonstrates that the major challenge is the large span of the flux guides in the core and their tendency to bend under the action of centrifugal loading, in turn loading the regions near the ends of the flux guides. This can be addressed, albeit with some

electromagnetic penalty, by incorporating small intermediate supports at points along the span of the flux guides. A number of alternative arrangements of cross-barrier support limbs were analysed, such as a design with a single cross-barrier support per barrier (Figure 5.24). This design was modelled with both a 1mm and 2mm support over a range of rotor bridge radial thicknesses. As can be seen in Figure 5.25 even with the thickest 2mm support and the thickest 10mm rotor bridge, the peak stress of 258.8MPa remains above the 50% yield strength limit of 200MPa.

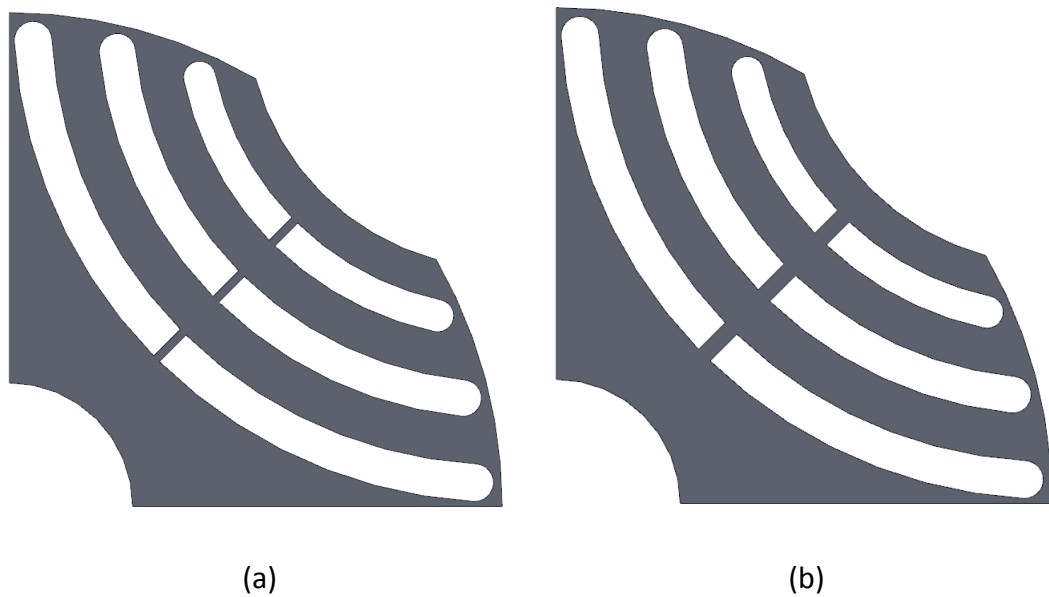


Figure 5.24 – Cross-section of a quarter of a rotor used during the mechanical optimisation process with one 1mm support per barrier (a) and with one 2mm support per barrier (b) both shown with a rotor bridge thickness of 1mm

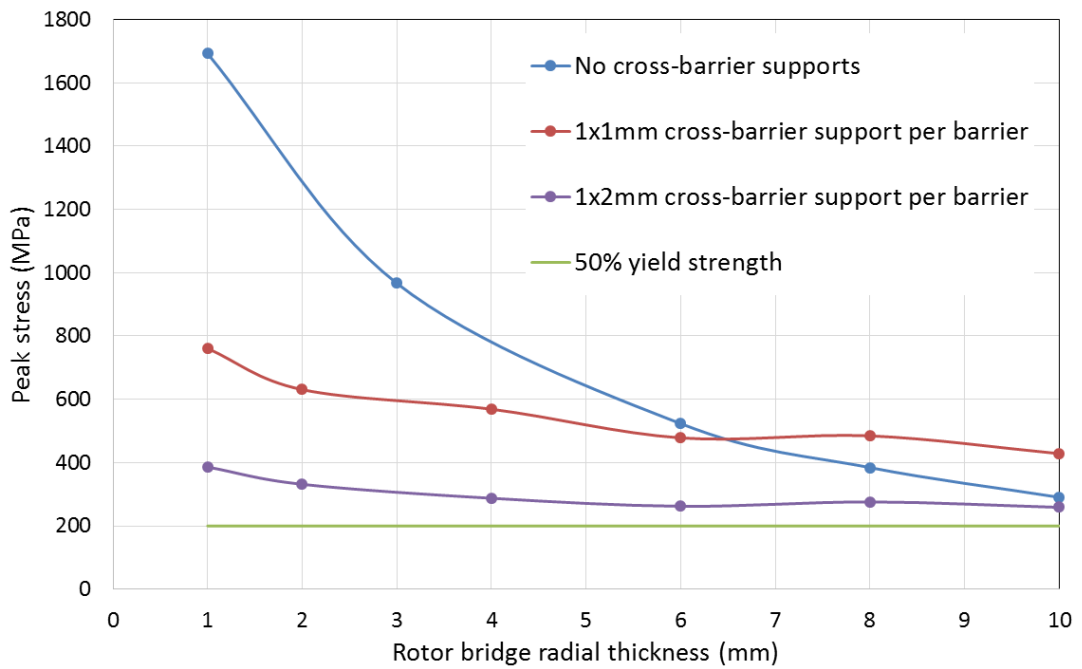


Figure 5.25 – Peak stresses in the two rotors found in Figure 5.24 while rotating at 14,400rpm

Rotor designs which incorporate additional supports between the flux guides were considered, in an attempt to further reduce the peak stress towards a value of ~200MPa. It is not necessary to incorporate an equal number of supports in all the flux barriers and there are many options for minimising the peak stress. By way of example, Figure 5.26a shows a rotor with a 1/2/3 support arrangement while Figure 5.26b shows a 3/2/3 arrangement. These are both effective in reducing stress, but only down to 229MPa and 237MPa respectively. The resulting stress distributions are shown in Figure 5.27 and Figure 5.28 from which it will be apparent that although the supports significantly reduce the stress at the ends of the flux barriers, the peak stress now occurs at the intersection of the support and flux guide. More detailed views of these high stress areas are included in Figure 5.29a and Figure 5.29b for the 1/2/3 and 3/2/3 support arrangement cases respectively.

However, although the supports are effective in reducing stress, they are likely to be detrimental to electromagnetic performance. In order to establish the level of compromise in electromagnetic performance which is introduced, the performance of both of the rotors shown in Figure 5.26 were predicted using time-stepped electric-circuit coupled finite element analysis with both cases utilising the same



reference stator design. The power produced by the rotor models shown in Figure 5.26a and Figure 5.26b are 12.14kW and 11.09kW respectively. This 8.6% decrease in output power is entirely due to the addition of the two extra supports in the outer-most flux barrier. The FE calculation of power for these two models was performed with a  $3\Omega$  load resistor and uses the optimised stator as detailed in Appendix 4 (Section 8.4) and a control winding current density of  $14.14A_{rms}mm^{-2}$ .

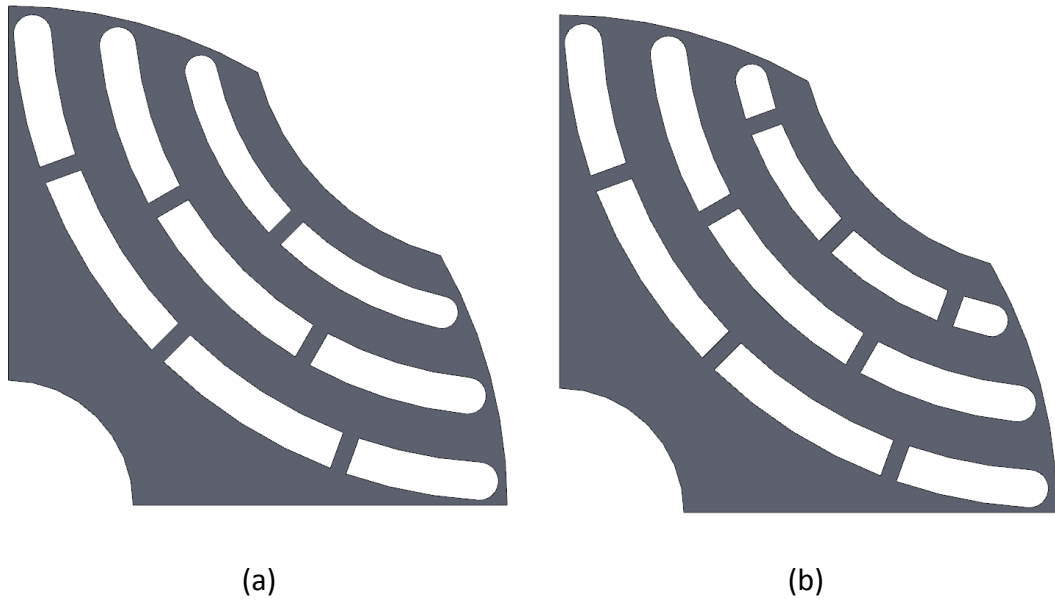


Figure 5.26 – Cross-section of a quarter of a rotor used during the mechanical optimisation process with 1/2/3 2mm supports per barrier (a) and with 3/2/3 2mm supports per barrier (b) both shown with a rotor bridge thickness of 1mm

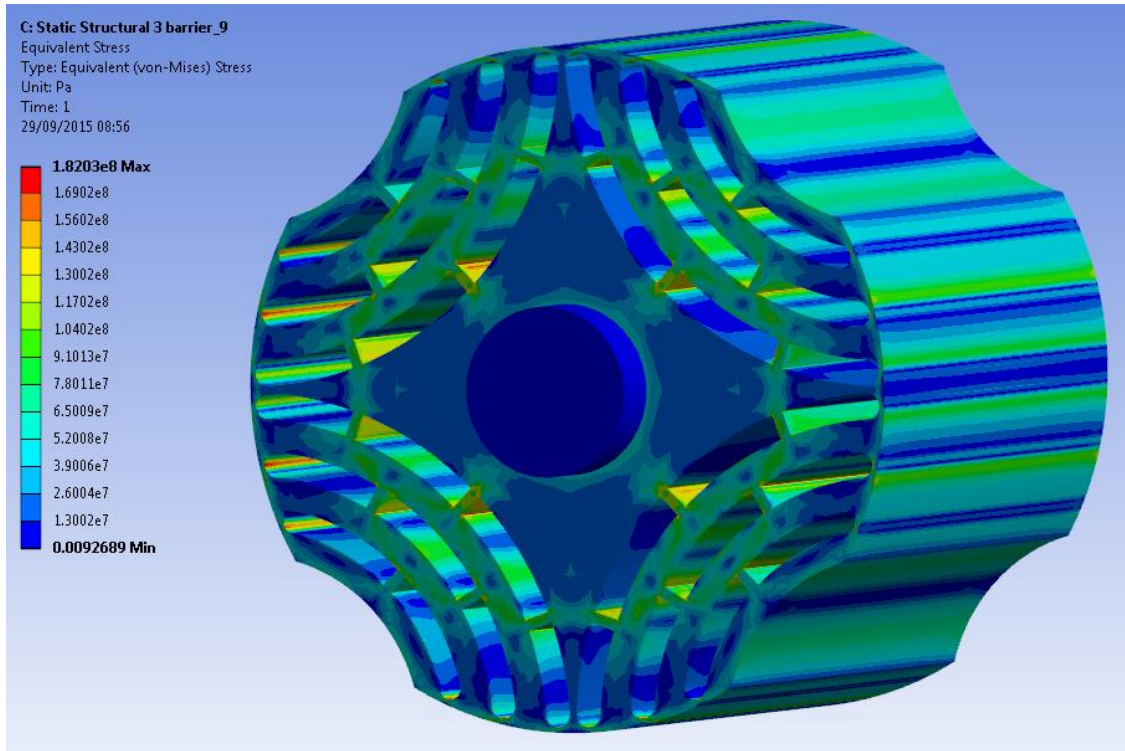


Figure 5.27 - Predicted stress distribution in an NO20 Silicon Iron rotor with three flux guides and a 1/2/3 cross-barrier support arrangement at 14,400rpm

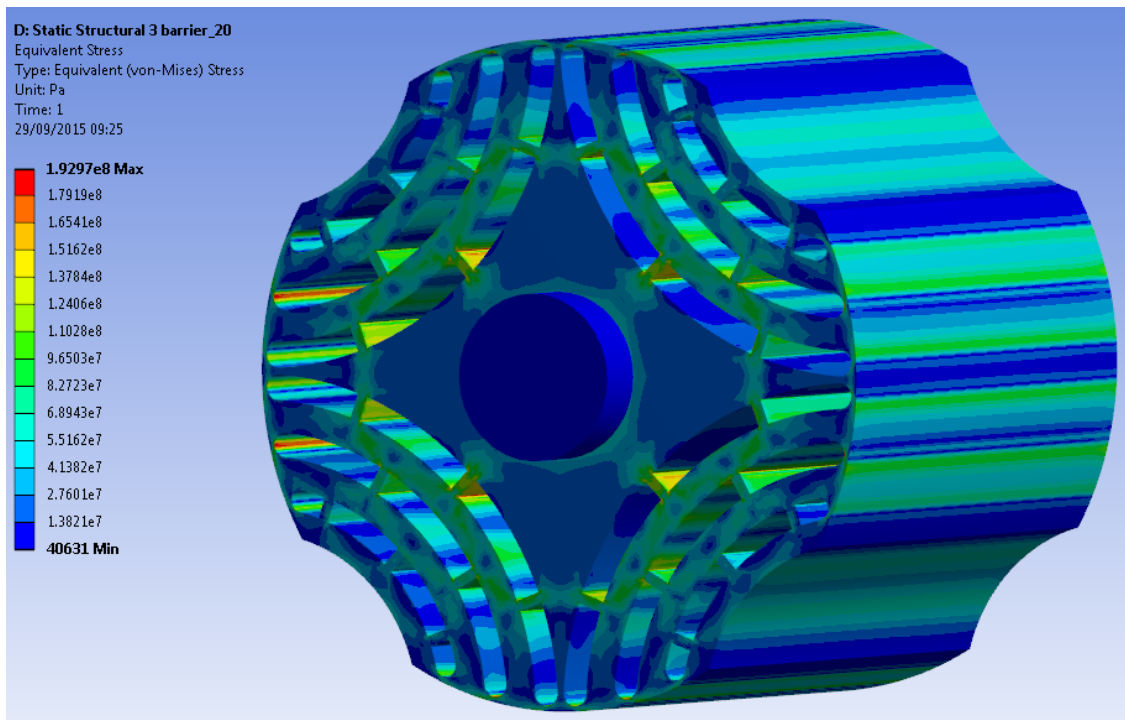
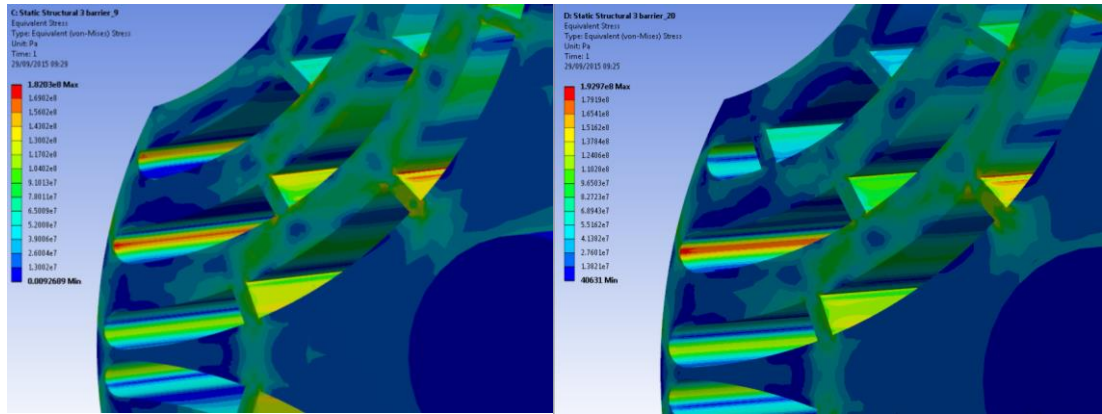


Figure 5.28 - Predicted stress distribution in an NO20 Silicon Iron rotor with three flux guides and a 3/2/3 cross-barrier support arrangement at 14,400rpm



(a)

(b)

Figure 5.29 – Detailed view of the high stress areas of an NO20 Silicon Iron rotor with three flux guides and a 1/2/3 (a) and 3/2/3 (b) cross-barrier support arrangement at 14,400rpm

Adding a fillet radius where the cross-barrier supports meet the flux guides is likely to yield dividends in reducing these peak stress points. Adding a fillet of radius 2mm to all the supports in Figure 5.26a and Figure 5.26b results in a further reduction in peak stress to 192MPa and 188MPa respectively, i.e. within the imposed 200MPa limit.

For the reasons stated above, the final rotor design shown in Figure 5.30b (shown alongside the electromagnetically optimised rotor in Figure 5.30a) was selected. This has a predicted peak stress of 192MPa which is below the 200MPa target (50% of yield strength) as compared to 1,648MPa of the electromagnetically optimised design. However, the various supports will inevitably diminish the electromagnetic effectiveness of the flux barriers, resulting in an inevitable penalty in electrical performance of the machine.

In order to quantify this penalty, electric-circuit coupled finite element simulations were performed for the now optimised stator with the dimensions outlined in Appendix 4 (Section 8.4). The resulting performance at two specific operating points are compared in Table 5.5 and Table 5.6. As will be apparent, in order to bring the peak rotor stress to below 50% of the yield stress of NO20, the output power is reduced by 34%. The reduction is slightly less pronounced at a higher speed point (13,200rpm) with only a 25% reduction. It should however be recalled that the electromagnetically optimised rotor can only operate within this defined stress limit

up to 5,000rpm. The power density calculations in Table 5.5 and Table 5.6 are calculated without considering the control winding power. If this control winding power is included, the power density would be expected to reduce further.

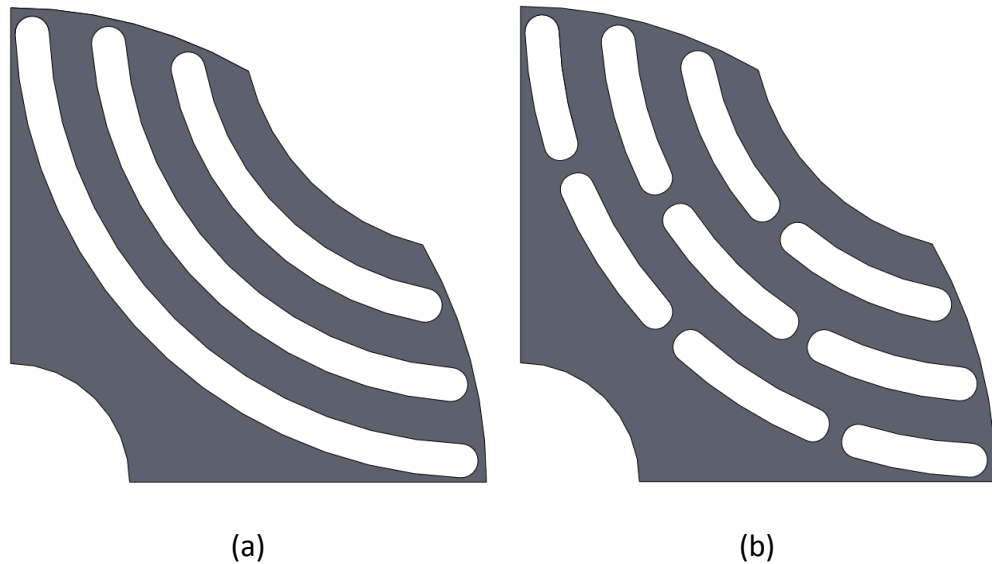


Figure 5.30 – Cross-section of the electro-magnetically optimised rotor (a) and the mechanically robust variant (b)

Table 5.5 – Comparison of electromagnetic performance at 4,860rpm for a load resistance of  $3\Omega$  (synchronous frequency of 324Hz)

	Electromagnetically optimised	Mechanically robust
<b>Rotor speed (rpm)</b>	4,860	
<b>Control frequency (Hz)</b>	36	
<b>Power frequency (Hz)</b>	360	
<b>Torque (Nm)</b>	-30.5	-20.5
<b>Control winding power (kW) (Current density=<math>14.14 A_{rms}mm^{-2}</math>)</b>	2.3	2.0
<b>Power winding power (kW)</b>	16.8	11.1
<b>Active* power density** (kW/kg)</b>	0.76	0.50

\* Active weight includes the stator, rotor and slot copper

\*\*Power density excludes the control winding power

Table 5.6 – Comparison of electromagnetic performance at 13,200rpm for a load resistance of  $3\Omega$  (synchronous frequency of 880Hz)

	Electromagnetically optimised	Mechanically robust
<b>Rotor speed (rpm)</b>	13,200	
<b>Control frequency (Hz)</b>	80	
<b>Power frequency (Hz)</b>	800	
<b>Torque (Nm)</b>	-25.0	-18.8
<b>Control winding power (kW)</b> (Current density= $14.14 A_{rms}mm^{-2}$ )	2.8	2.1
<b>Power winding power (kW)</b>	31.3	23.4
<b>Active* power density** (kW/kg)</b>	1.42	1.05

\* Active weight includes the stator, rotor and slot copper

\*\*Power density excludes the control winding power

## 5.7 POWER AND CONTROL WINDING DESIGN

Although the basic layouts of the individual windings have been established in Section 4.2, it is necessary to specify a particular number of turns for each of the star-connected windings and their relative orientation.

### 5.7.1 SELECTION OF THE NUMBER OF CONTROL WINDING TURNS

Whereas the analysis up to this point has been based on a normalised current fed control winding, in which a prescribed sinusoidal MMF has been assigned to the control winding, in practice, it is necessary to fix a specific number of turns to interface with a practical 3-phase inverter. A control winding voltage of  $230V_{rms}$  was chosen and the number of turns on the control winding was adjusted to match this voltage, with a control winding current density of  $14.14A_{rms}mm^{-2}$ . Table 5.7 provides an example of the process involved in finding the optimum number of turns for a control winding voltage of  $230V_{rms}$ .

Table 5.7 – Example results of adjusting the number of control winding turns to produce a voltage of  $230V_{rms}$

Control winding turns	Control winding voltage ( $V_{rms}$ )	Control winding current ( $A_{rms}$ )
1	12.58	410.25
44	553.79	9.37
30	377.44	13.67
20	251.63	20.51
18	248.66	21.54
17	234.85	22.81
<b>16</b>	<b>221.15</b>	<b>24.24</b>

It is difficult to optimise the number of turns to operate over the whole frequency and speed range, so the key operating point chosen to determine the number of turns for the control and power windings was at 4,860rpm, with a control winding frequency of 36Hz. This operating point was chosen to be representative of BDFRM operation during most of its lifetime. An operating point at 10% below the synchronous speed range corresponds to lowering the gas turbine cruise rotational velocity by 10%, whilst still remaining above the lower 360Hz limit of the VF standard.

After repeated FE simulations and reviewing the control winding voltage, the final control winding design has 16 turns with a control winding voltage of  $221.15V_{rms}$  which corresponds to a current of  $24.24A_{rms}$ . This gives rise to a calculated control winding phase resistance of  $0.719\Omega$  and a FE-calculated control winding self-inductance of 2.77mH. To calculate the phase resistance, the end winding lengths are calculated by estimating the arc length, by taking the average radius of the coil in the slot and the angle of each arc. Further information on the calculation of end winding lengths can be found in Section 5.11.1.

### 5.7.2 SELECTION OF THE NUMBER OF POWER WINDING TURNS

In order to comply with one of the key elements of MIL-STD-704F standard, the nominal output voltage of the line to neutral power winding is chosen to be  $115V_{rms}$ , although the standard allows this to vary between 108 and 118  $V_{rms}$ . The aim of this

study was to match the power winding MMF with the control winding MMF, as well as producing an output voltage near the  $115V_{rms}$  target. Table 5.8 demonstrates an example of several iterations, which were completed to discover the optimum number of power winding turns. In this case, to achieve the required voltage and MMF balance for 10% below the synchronous speed range, 13 series turns per coil are required on the power winding. This corresponds to a phase resistance of  $0.289\Omega$  and a self inductance of  $1.07mH$ .

Table 5.8 – Example results of adjusting the number of power winding turns to match the MMF of the control winding and to achieve a power winding voltage of around  $115 V_{rms}$

Power winding turns	Load resistance ( $\Omega$ )	Control winding MMF (Aturns)	Power winding MMF (Aturns)	Power winding phase voltage ( $V_{rms}$ )
8	2.0	388	350.0	87.5
11	2.0	388	416.1	75.7
11	2.6	388	395.7	93.5
13	3.5	388	397.0	106.9
<b>13</b>	<b>3.7</b>	<b>388</b>	<b>391.8</b>	<b>111.5</b>

### 5.7.3 SELECTION OF THE RELATIVE ALIGNMENT BETWEEN THE TWO WINDINGS

With two windings on the stator, there is a degree of design freedom as to the relative angular displacement of these two windings. Due to there being 36 slots accommodating a 2-pole and 6-pole winding, there are 12 possible combinations of relative alignment between the control and power windings. To establish the influence on the electromagnetic operation of the BDFRM of this relative alignment, the mutual inductance from the control winding to the power winding was calculated for all combinations.

This procedure demonstrated that this particular component of mutual inductance is inherently unsymmetrical, but altering the relative alignment has a negligible effect on the overall output power produced by the BDFRM. As seen in Figure 5.31,

although the inductance for each phase changes with each alignment setting, the overall 3-phase inductance does not change. This asymmetry leads to slight differences in each of the power winding phase powers, but neither presents an opportunity to increase power nor is likely to present a problem with demonstrator testing.

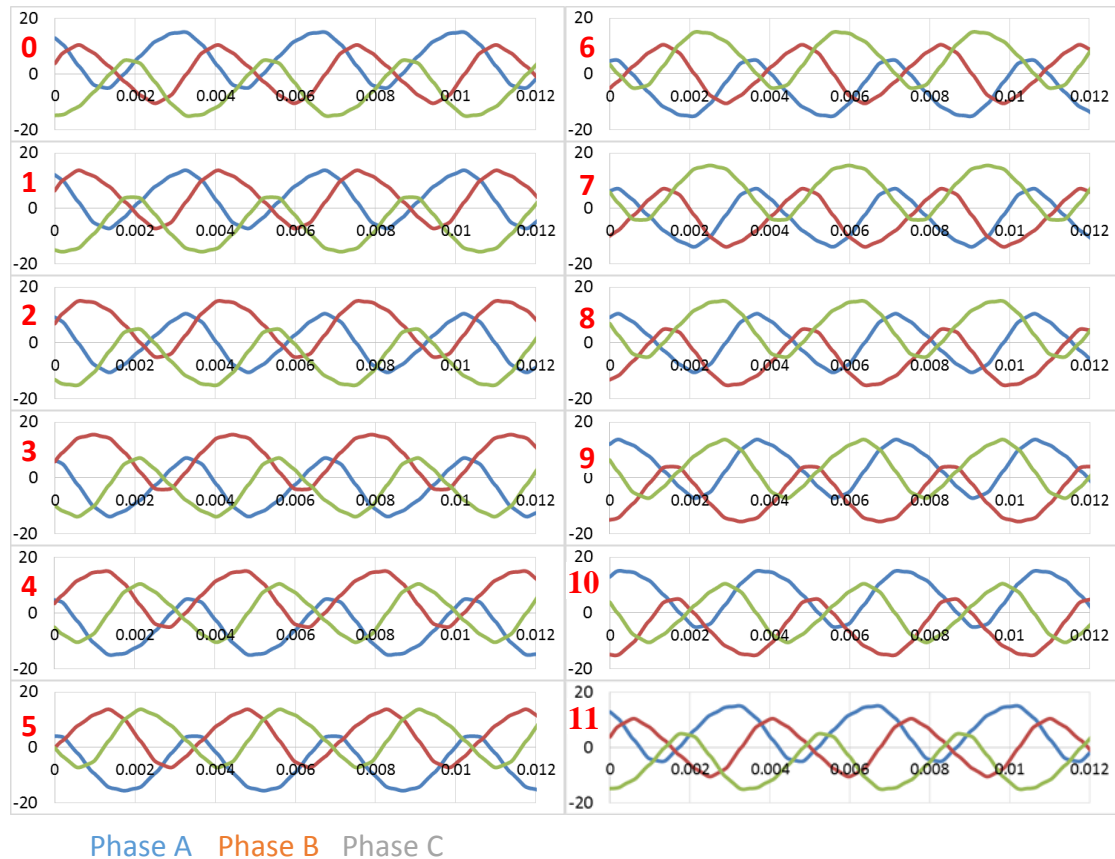


Figure 5.31 – Mutual inductance in the power winding at 12 winding alignments at  $10^\circ$  mechanical increments and a control winding current density of  $1.41A_{rms}mm^{-2}$  where the x-axis is the distance around the rotor periphery (m) and the y-axis is the inductance (mH)

## 5.8 FINAL DESIGN OPERATING POINTS

Following the significant electromagnetic and mechanical optimisation described above, a final design was selected to be taken forward as a demonstrator. Having established the many design features and dimensions, the performance was predicted at various test points. Prior to predicting performance, several important features of the machine B and its model needed to be finalised.

- End winding inductance must be calculated to add into the electric-circuit coupled FE model (as a fixed inductance external to the FE region).



- The load resistance required to load the power winding must be established for each operating point to ensure the machine is operating at maximum efficiency, but still remaining within the VF standard output voltage of 108-118V<sub>rms</sub>.
- The influence of the number of sampling steps used in the finite model on the accuracy of the calculated power.

### 5.8.1 END WINDING INDUCTANCE

There are two main methods for calculating the end winding inductance of an electrical machine. Firstly, a full 3D FE model could be constructed to calculate directly the effect of the end windings upon the total inductance. Although in principle, providing a route to accurate values, the complicated distributed winding layouts with 2 and 6 pole windings intertwined in the end-region and the uncertainty over the exact geometry of coils which could be manufactured (notably the length of the end-windings) will limit the accuracy of this approach.

The preferred method, which was adopted in this thesis, was to measure the total inductance of each phase post-winding. The end-winding component in the FE model can then be calculated by subtracting the value of inductance found in the FE software under the same excitation conditions. Both conditions were without a rotor in the stator bore.

Table 5.9 – Inductance measurements and calculations

Winding and phase	Calculated inductance from 2D FEA model (mH)	Measured inductance (mH)	End winding contribution (mH)
<b>Control Phase A</b>	2.77	4.73	1.96
<b>Control Phase B</b>	2.77	4.63	1.86
<b>Control Phase C</b>	2.77	4.66	1.89
<b>Power Phase A</b>	0.81	1.07	0.26
<b>Power Phase B</b>	0.81	1.07	0.26
<b>Power Phase C</b>	0.81	1.07	0.26

## 5.8.2 SAMPLING FREQUENCY OPTIMISATION

Initial time-stepped electric-circuit coupled finite element simulations exhibited some problems with ensuring power balance with the problem domain, an issue that was quickly established as being sensitive to the time step duration. In order to reduce computation time in FE analysis it is usually beneficial to reduce the number of time steps employed by the solver until such time as it begins to adversely affect the accuracy of the results. However, although only small discrepancies were evident in the individual current and voltage waveforms (which might have been regarded as an acceptable trade-off with computation time), the power balance was far more sensitive. These discrepancies in the powers within the BDFRM were established using (5.1), noting that iron loss is not included with Flux 2D time stepped model (it is calculated separately as a post-processing activity).

If this equation balances within a reasonable tolerance, then the sampling frequency is deemed to be high enough to yield an accurate result.

$$P_{\text{load}} + P_{\text{CuLoss}} = P_{\text{control}} + P_{\text{mech}} \quad (5.1)$$

The relationship between time-step duration and power balance was investigated systematically at one particular test-point at 14,400rpm which is 20% above the top end of the 360 to 800 Hz VF frequency range. The control winding current was set to 14.14A<sub>rms</sub>mm<sup>-2</sup> with a power winding load resistance of 3.7Ω.

Figure 5.32 shows the variation in power imbalance as a function of time step durations. For this operating point, the peak 3-phase output power is 13.45kW. If this curve was to be extrapolated downwards it may be reasonably assumed that it would pass through zero, if numerical errors in the FE analysis were eliminated. On the basis of the findings in Figure 5.32, all the time-stepped simulations performed for optimising geometry were completed with a 35μs time step. Although this would lead to inaccuracies in the power calculations, a peak power point can still be found and is useful for relative comparisons for design optimisation. However, for accurate final performance predictions for the down-selected design, time steps of the order of 25μs were used (leading to 48 hour solve times for each test point).

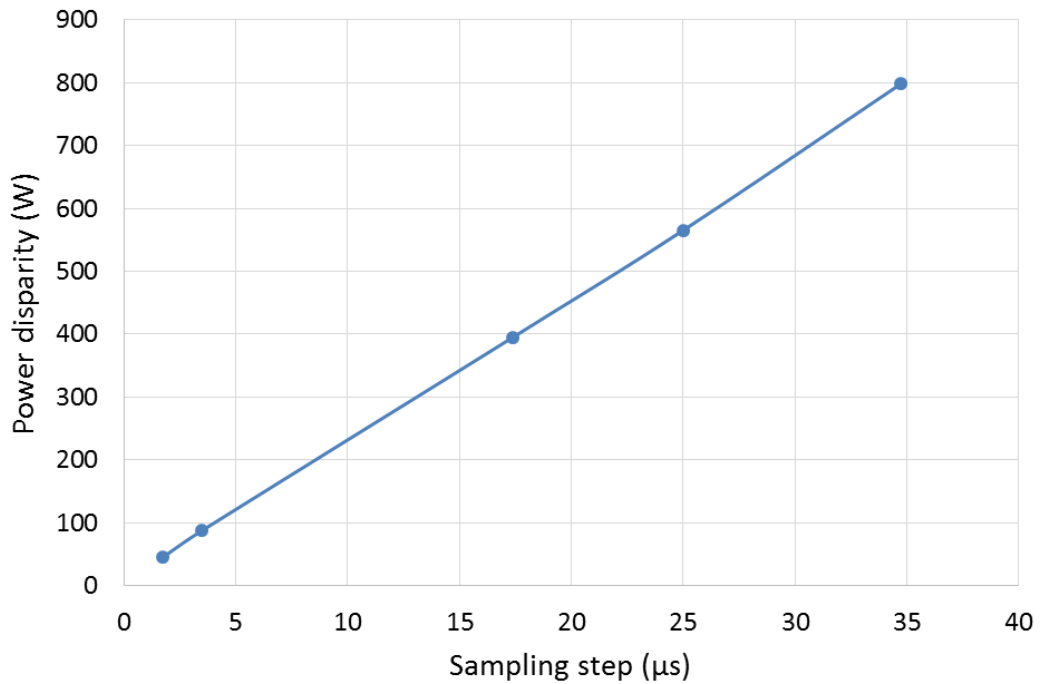


Figure 5.32 – Power disparity due to certain sampling steps for an operating point at 20% above the VF frequency range (14,400rpm) with a  $14.14\text{A}_{\text{rms}}\text{mm}^{-2}$  160Hz contra-rotating control winding current and a  $3.7\Omega$  load resistance

### 5.8.3 LOAD RESISTANCE CALCULATION

The load resistance (to a resolution of  $0.1\Omega$ ) at each operating point was selected to give a power winding output voltage value of between 108 and 118  $V_{\text{rms}}$ . This corresponds to the variable frequency voltage requirements for Mil-Std-704F[9] which must be adhered to in aerospace applications. The calculated load resistances for the power winding at several operating points are summarised in Table 5.10. It is recognised that the machine was loaded with a unity power factor load, whereas in practice, typical aircraft networks have power factor of between 0.85 lagging and 1 [9].

Table 5.10 – Power winding load resistances used at a range of operating points

Operating point	Rotor speed (rpm)	Control winding frequency (Hz)	Load resistor ( $\Omega$ )
-20%	4,320	160	4.1
-10%	4,860	80	4.7
Mid-range	9,000	0	3.7
+10%	13,200	36	3.7
+20%	14,400	72	3.7

## 5.9 ROTOR SKEW

By adding a  $10^\circ$  (one stator slot pitch) skew to the rotor it is anticipated that slotting harmonics in the output voltage would be reduced at the expense of a reduction in the fundamental magnitude. By using the Skewed add-on available for the Flux 2D package, it was possible to model the effect of this skew on the power winding load voltage harmonics in time domain simulations. As these solvers are computationally expensive, only key operating points were investigated.

### 5.9.1 SKEW TEST POINT AT 4,320RPM

The effect of skew can be illustrated by considering a specific test point at 4,320rpm with a control winding current density of  $14.14A_{rms}mm^{-2}$  and a load resistance of  $4.1\Omega$ . This rotor speed corresponds to the BDFRM operating at 20% below the VF frequency range, requiring a control winding frequency of 72Hz to bring the power winding frequency up to 360Hz.

The resulting predicted output voltage waveforms derived from time-stepped FEA solutions are shown in Figure 5.33. The corresponding FFT of the power winding load voltages are shown in Figure 5.34 and Figure 5.35. The FFTs shown have a frequency span which is large enough to ensure all harmonics of interest are displayed. To aid clarity, the fundamental harmonic is excluded from these FFTs, and to provide some context to the magnitude of the harmonics, the military standard 704F[9] variable frequency harmonic limit is superimposed onto each FFT. One consequence of adopting a wide frequency range, and the limited number of time steps in the time domain FEA coupled simulations, is the presence of significant side-lobes, in particular around the fundamental. By scaling the magnitude axis for display

purposes without the fundamental, these side-lobes around the fundamental become apparent. It is therefore important to recall that apparent components centred around the fundamental are artefacts of the FFTs and not identifiable harmonics of the voltage waveform as discussed in detail in Appendix 2 (Section 8.2).

In the case of a rotor without a skew (Figure 5.34) it can be seen that several harmonics have a RMS value that exceeds the MIL704F limit, notably those at ~220Hz, ~500Hz and ~2240Hz. The 220Hz can be attributed to a saturation induced third harmonic from the control winding linking directly to the power winding. With a 72Hz control winding frequency this would lead to a 216Hz 3<sup>rd</sup> harmonic which corresponds to the nominal 220Hz sub-harmonic in the FFT. The 500Hz harmonic can be attributed to an artefact of the modulation principle as will be discussed further in Section 6.4.1. The other high harmonic at 2240Hz can be attributed to slotting effects of both the rotor and stator. The attribution of these higher harmonics to slotting is vindicated when the predicted voltage harmonics produced by a rotor with a skew are considered (Figure 5.35). Whereas little difference in RMS value can be seen in the 220Hz harmonic, large reductions in the other two major harmonics are observed. In fact, the 500Hz and 2240Hz harmonics have reduced by 46% and 74% respectively from their pre-skew values.

This reduction in slotting harmonics has led to the 2240Hz harmonic falling comfortably inside the VF limit, but the 500Hz and 220Hz remain over the more onerous low frequency limit of the VF standard.

Although skew is beneficial in terms of reducing the slotting harmonics, this will always come at the expense of reduction in fundamental magnitude. Without skewing the magnitude of the fundamental power winding voltage at this specific load condition was 157.59V whereas with a skew, the fundamental magnitude reduces by 4.4% to 150.60V. It is also worth noting that adopting this particular skew results in a reduction in THD of the voltage waveform from 8.6% to 6.9%.

Skewing of the rotor has also adversely affected the torque as shown in Figure 5.36, with the average torque reducing from -17.59Nm to -15.97Nm. However, one benefit accrued from the skewing is a 60% reduction in the THD of the torque.

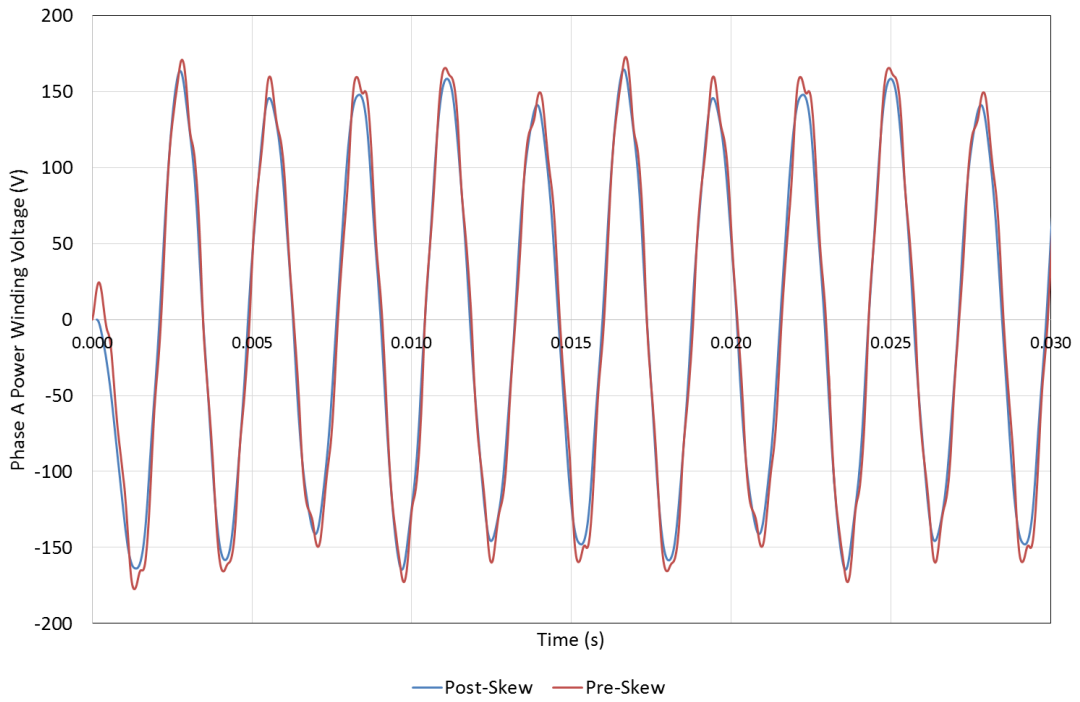


Figure 5.33 – 20% below VF range (4,320rpm) power winding phase A voltage waveform for pre- and post-skew with a 72Hz co-rotating  $14.14A_{rms}mm^{-2}$  control winding current and a load resistance of  $4.1\Omega$

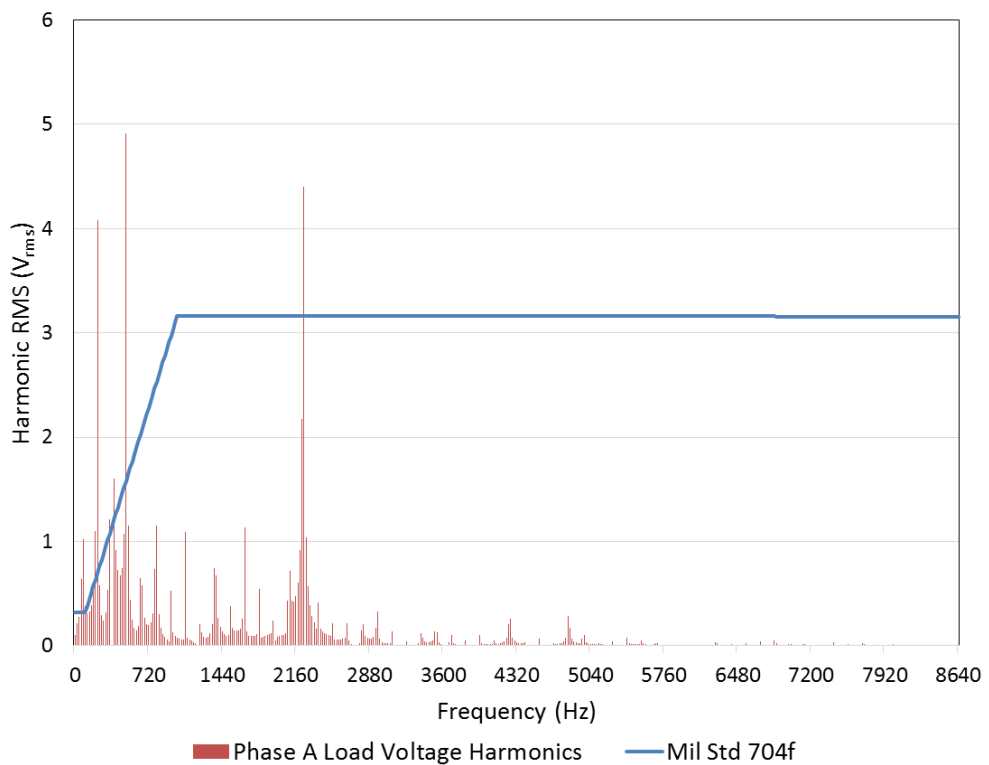


Figure 5.34 – 20% below VF range (4,320rpm) power winding phase A voltage FFT waveform with no skew with a 72Hz co-rotating  $14.14A_{rms}mm^{-2}$  control winding current and a load resistance of  $4.1\Omega$

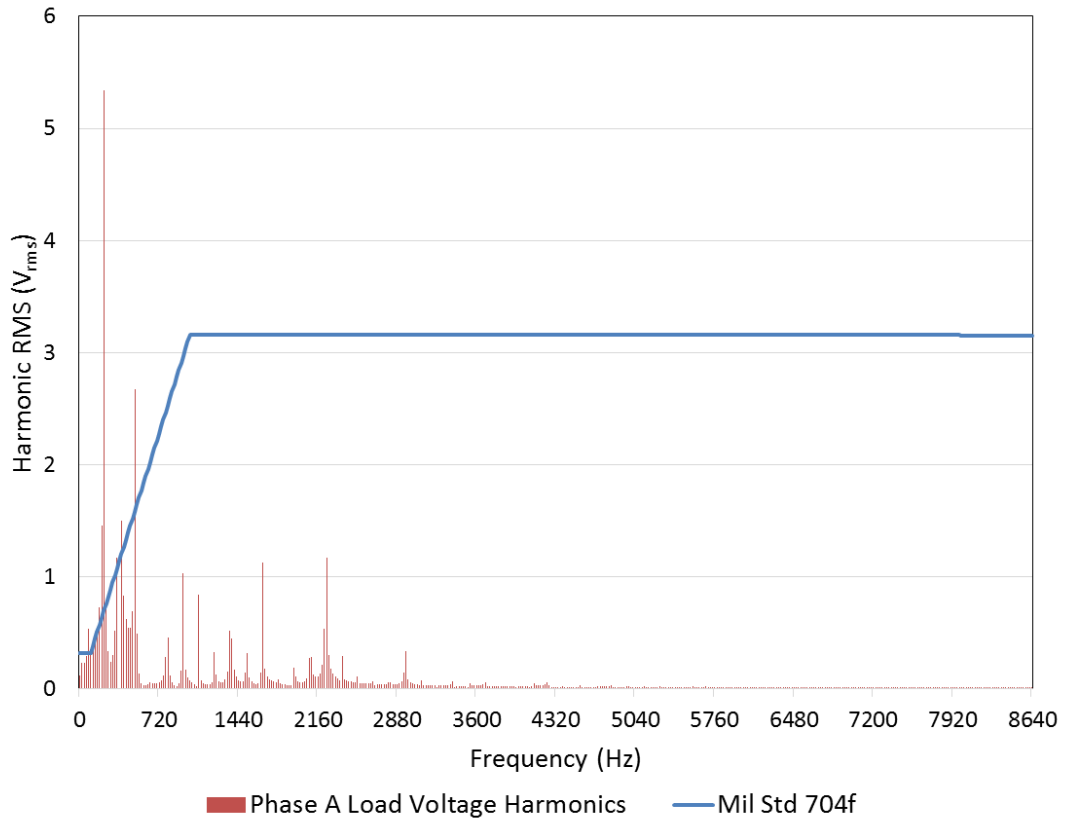


Figure 5.35 – 20% below VF range (4,320rpm) power winding phase A voltage FFT waveform with skew with a 72Hz co-rotating  $14.14A_{rms}mm^{-2}$  control winding current and a load resistance of  $4.1\Omega$

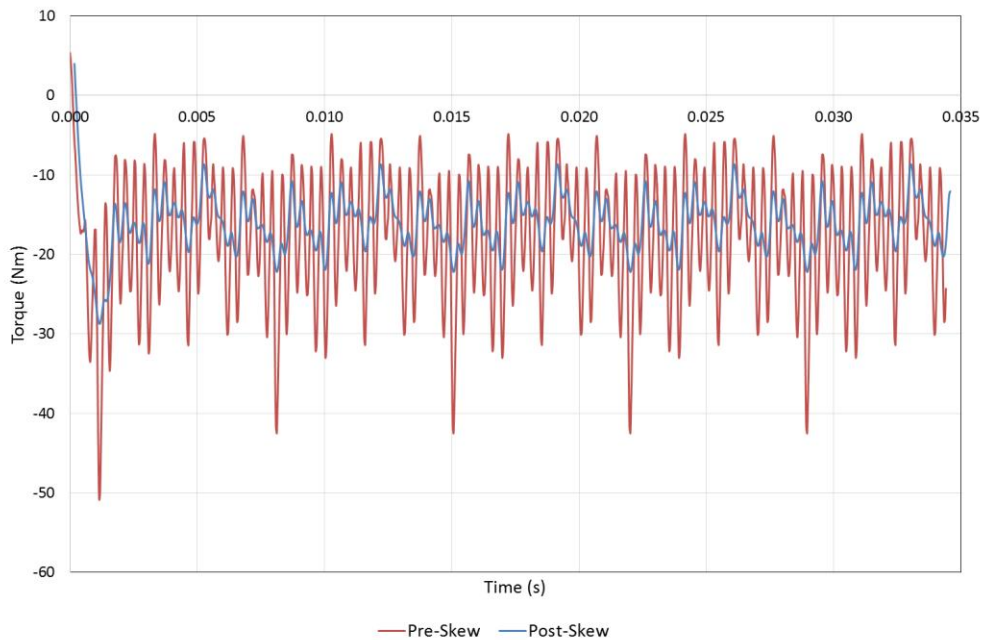


Figure 5.36 – 20% below VF range (4,320rpm) torque waveform with and without a skew with a 72Hz co-rotating  $14.14A_{rms}mm^{-2}$  control winding current and a load resistance of  $4.1\Omega$

### 5.9.2 SKEW TEST POINT AT 4,860RPM

The next test point which was considered is 10% below the synchronous speed range, which corresponds to a rotational speed of 4,860rpm, a control winding frequency of 36 Hz and a power winding frequency of 360Hz. The phase A power winding voltage for the case of a control winding current density of  $14.14A_{rms}mm^{-2}$  and a load resistance of  $4.2\Omega$  is shown in Figure 5.37. In this case both the 620Hz and 2,560Hz harmonics are reduced by 73% and 33% respectively as a result of skewing the rotor, as shown by the unskewed and skewed FFTs of Figure 5.38 and Figure 5.39 respectively.

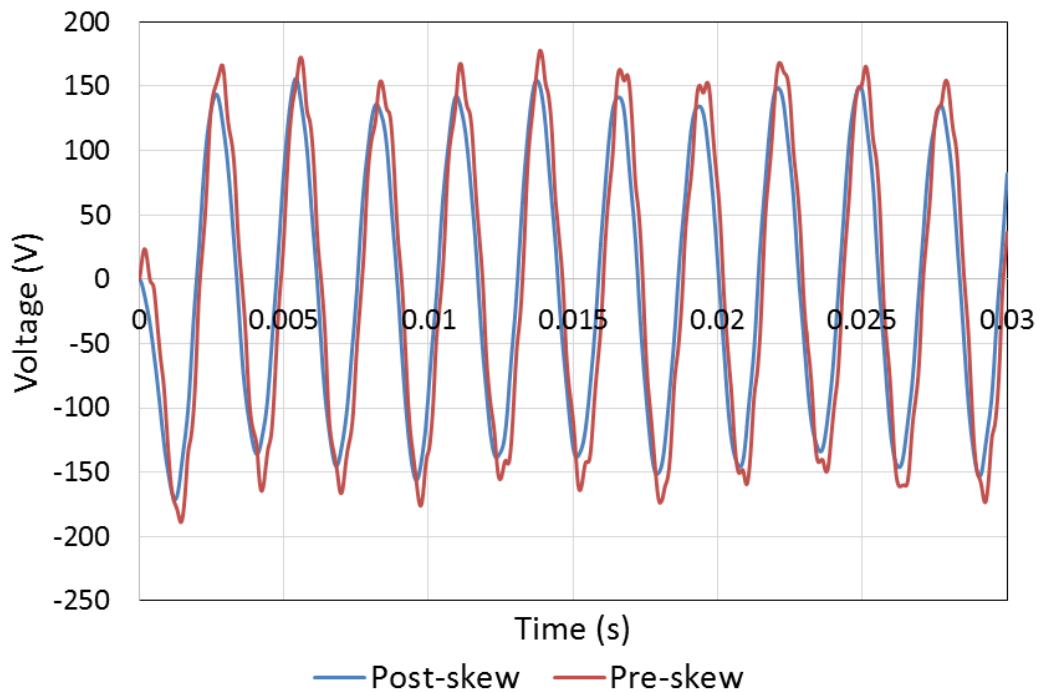


Figure 5.37 – FE calculated phase A power winding load voltage with a load of  $4.2\Omega$  and a control winding current density of  $14.14 A_{rms}mm^{-2}$  at a test point of 10% below the synchronous frequency range (4,860rpm)



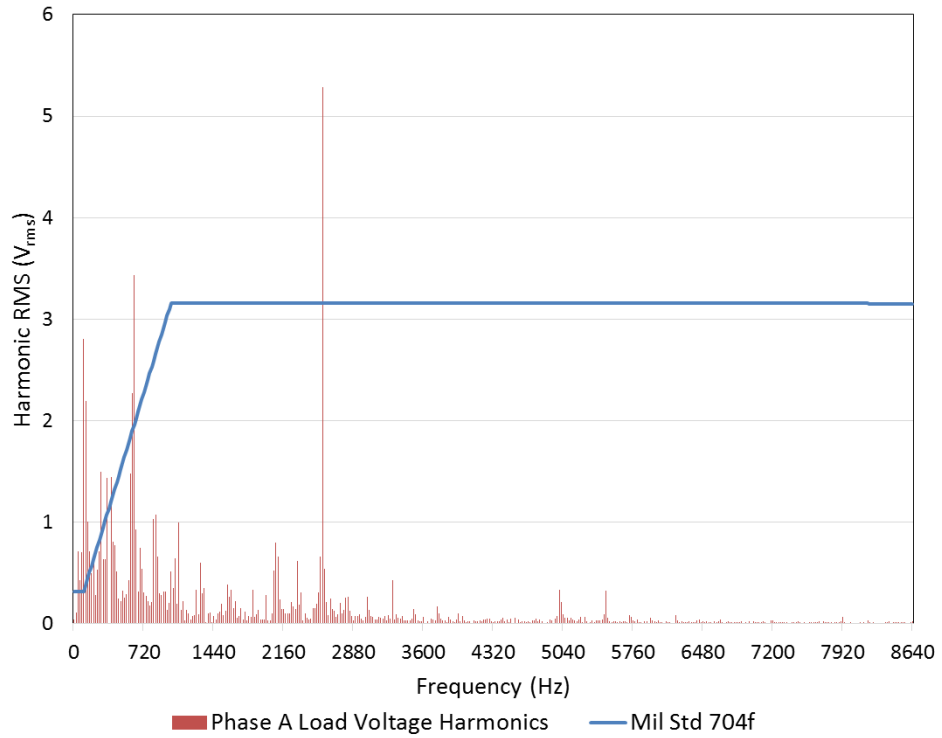


Figure 5.38 – FE calculated FFT of phase A power winding load voltage with a load of  $4.2\Omega$  and a control winding current density of  $14.14A_{rms}mm^{-2}$  at a test point of 10% below the synchronous frequency range (4,860rpm) with no skew

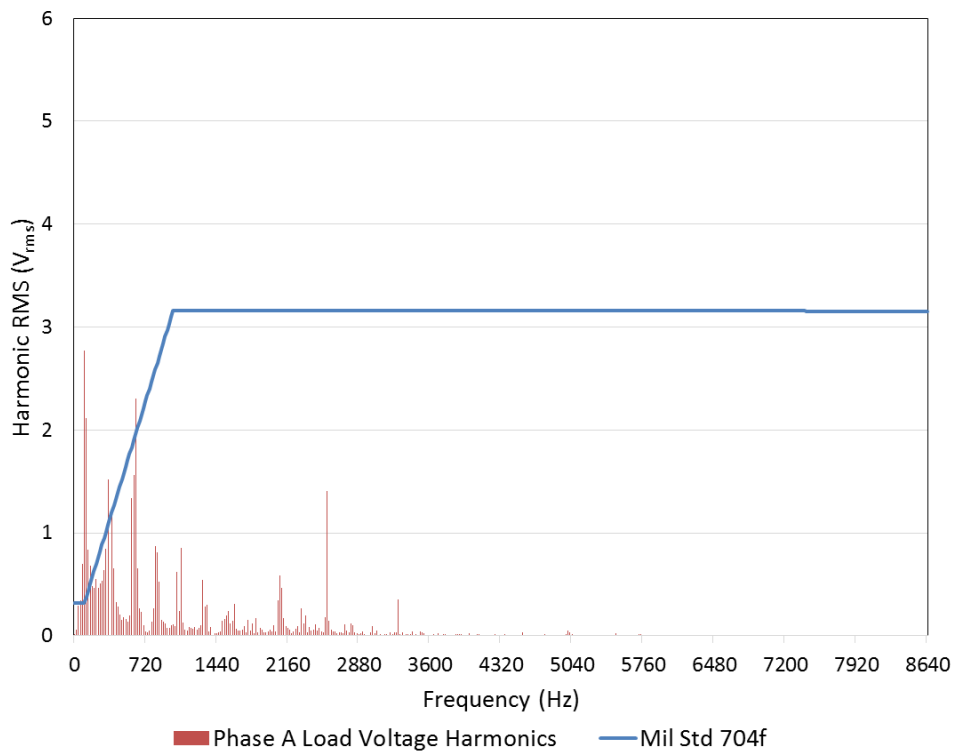


Figure 5.39 - FE calculated FFT of phase A power winding load voltage with a load of  $4.2\Omega$  and a control winding current density of  $14.14A_{rms}mm^{-2}$  at a test point of 10% below the synchronous frequency range (4,860rpm) with skew

### 5.9.3 SKEW TEST POINT AT 9,000RPM

For the mid speed range case, the control winding frequency was set to be zero, i.e. the three phase control winding currents were set to a fixed snapshot of a three phase sinusoid. The rotor speed was set to 9,000rpm which corresponds to a synchronous power winding frequency of 600Hz. Figure 5.40 shows the FE predicted phase A power winding voltage for both the unskewed and skewed cases. The slotting harmonic at 4,800Hz is reduced by 70% with the introduction of skewing to the rotor as shown in the FFTs of Figure 5.41 and Figure 5.42. This results in all of the harmonics in the voltage waveform dropping comfortably below the VF standard limit.

Another prevalent harmonic in Figure 5.41 is at 1,200Hz, which in fact is a second harmonic of the power winding fundamental frequency caused by the asymmetry of the application of the control winding current. With the application of a skew, this 2<sup>nd</sup> harmonic is seen to reduce significantly by 31%. Further information on this 2<sup>nd</sup> harmonic will be discussed in Section 6.7.

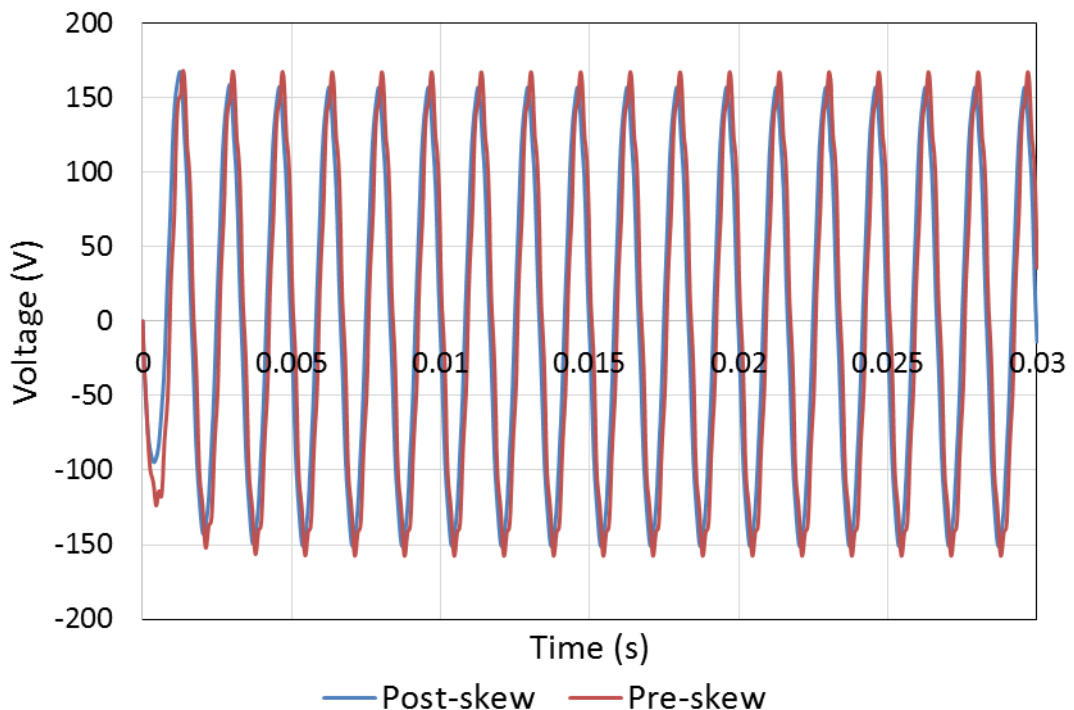


Figure 5.40 – FE calculated phase A power winding load voltage with a load of  $3.7\Omega$  and a control winding current density of  $14.14A_{rms}mm^{-2}$  at a DC test point in the middle of the speed range (9,000rpm)

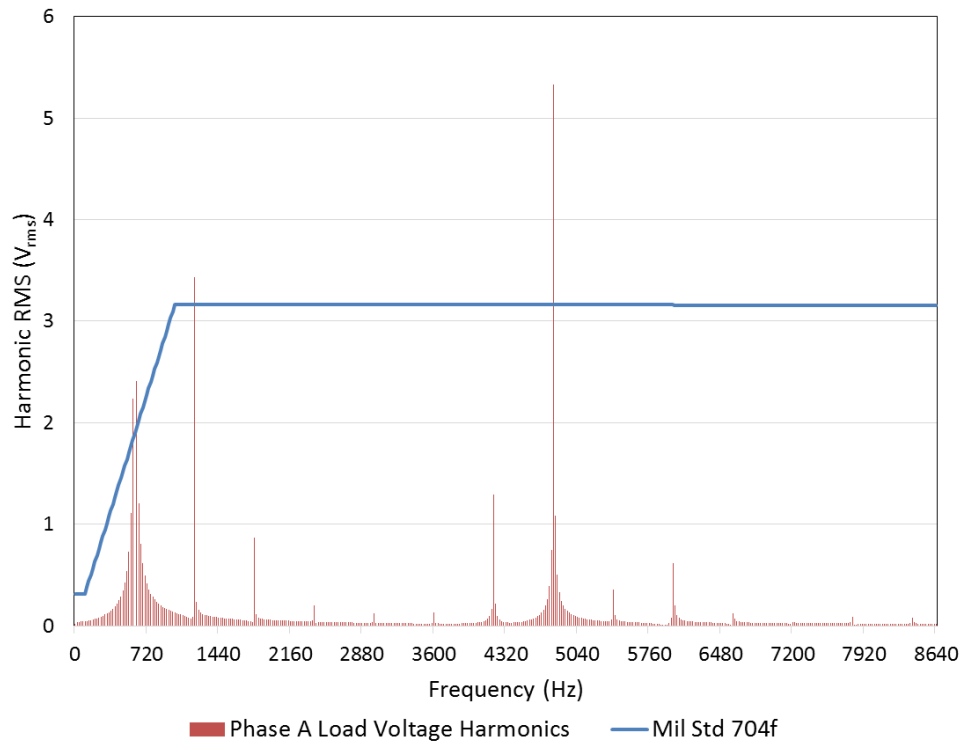


Figure 5.41 – FE calculated FFT of phase A power winding load voltage with a load of  $3.7\Omega$  and a control winding current density of  $14.14A_{rms}mm^{-2}$  at a DC test point in the middle of the speed range (9,000rpm) with no skew

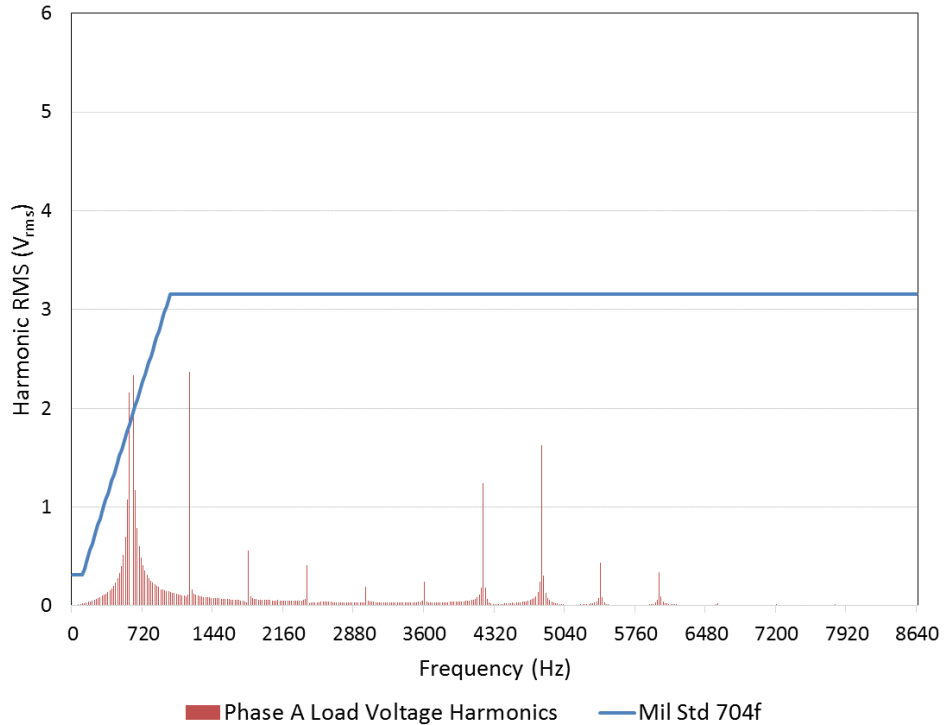


Figure 5.42 – FE calculated FFT of phase A power winding load voltage with a load of  $3.7\Omega$  and a control winding current density of  $14.14A_{rms}mm^{-2}$  at a DC test point in the middle of the speed range (9,000rpm) with skew

#### 5.9.4 SKEW TEST POINT AT 13,200RPM

The next case considered corresponds to a test point at 10% above the synchronous range, with a rotational speed of 13,200rpm and a control winding frequency of 80Hz leading to a power winding frequency of 800Hz. Figure 5.43 shows the phase A power winding voltage both with and without a rotor skew. The two key slotting harmonics here are at 1,840Hz and 7,120Hz, which are reduced by 29% and 72% respectively by skewing the rotor.

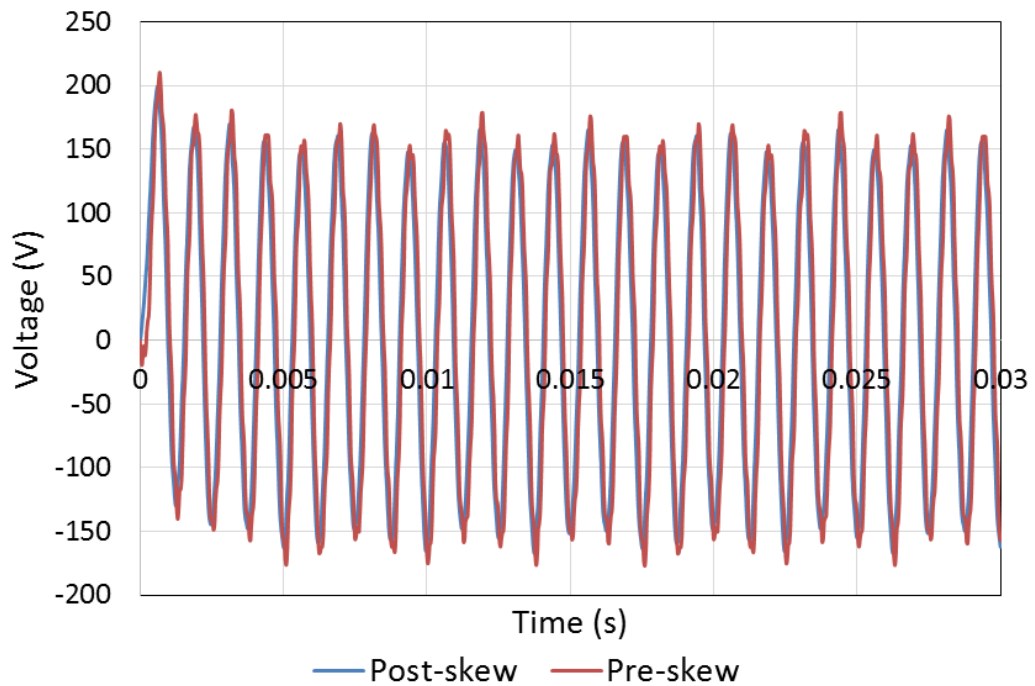


Figure 5.43 – FE calculated phase A power winding load voltage with a load of  $3.7\Omega$  and a control winding current density of  $14.14 \text{ A}_{\text{rms}}\text{mm}^{-2}$  at a test point of 10% above the synchronous frequency range (13,200rpm)

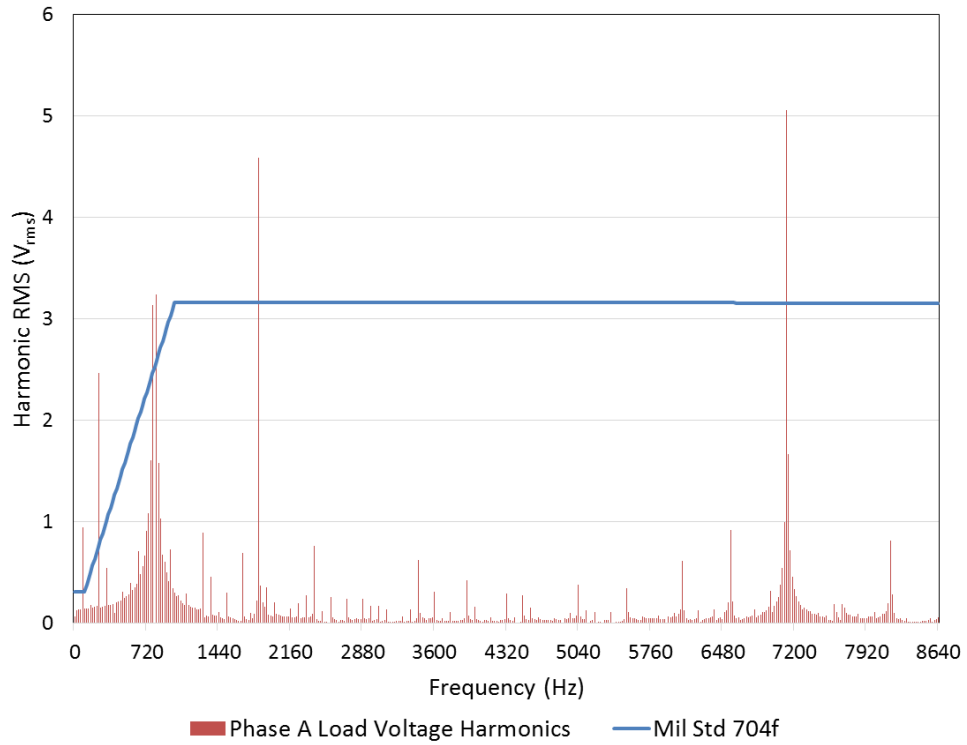


Figure 5.44 – FE calculated FFT of phase A power winding load voltage with a load of  $3.7\Omega$  and a control winding current density of  $14.14 \text{ A}_{\text{rms}}\text{mm}^{-2}$  at a test point of 10% above the synchronous frequency range (13,200rpm) with no skew

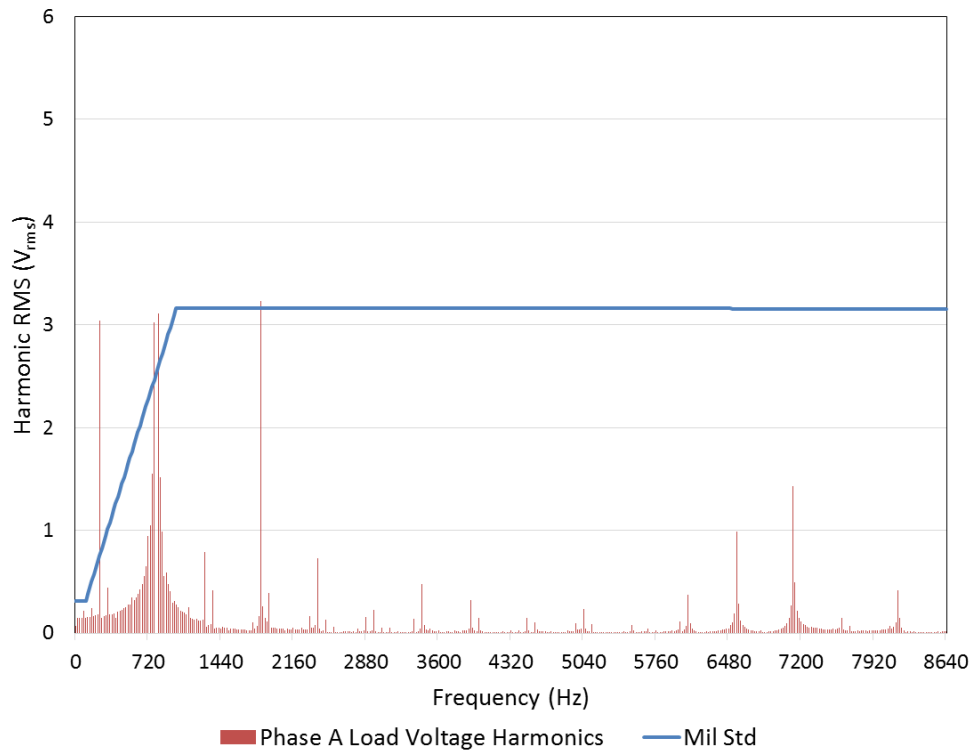


Figure 5.45 – FE calculated FFT of phase A power winding load voltage with a load of  $3.7\Omega$  and a control winding current density of  $14.14 \text{ A}_{\text{rms}}\text{mm}^{-2}$  at a test point of 10% above the synchronous frequency range (13,200rpm) with skew

### 5.9.5 SKEW TEST POINT AT 14,400RPM

The final test point considered is at the top of the speed range with a rotational speed of 14,400rpm and a control winding frequency of 160Hz leading to a power winding frequency of 800Hz. Figure 5.46 shows the power winding phase A load voltages both with and without the rotor skew. The key slotting harmonics at 2,080Hz and 7,840Hz are reduced by 27% and 71% respectively by skewing.

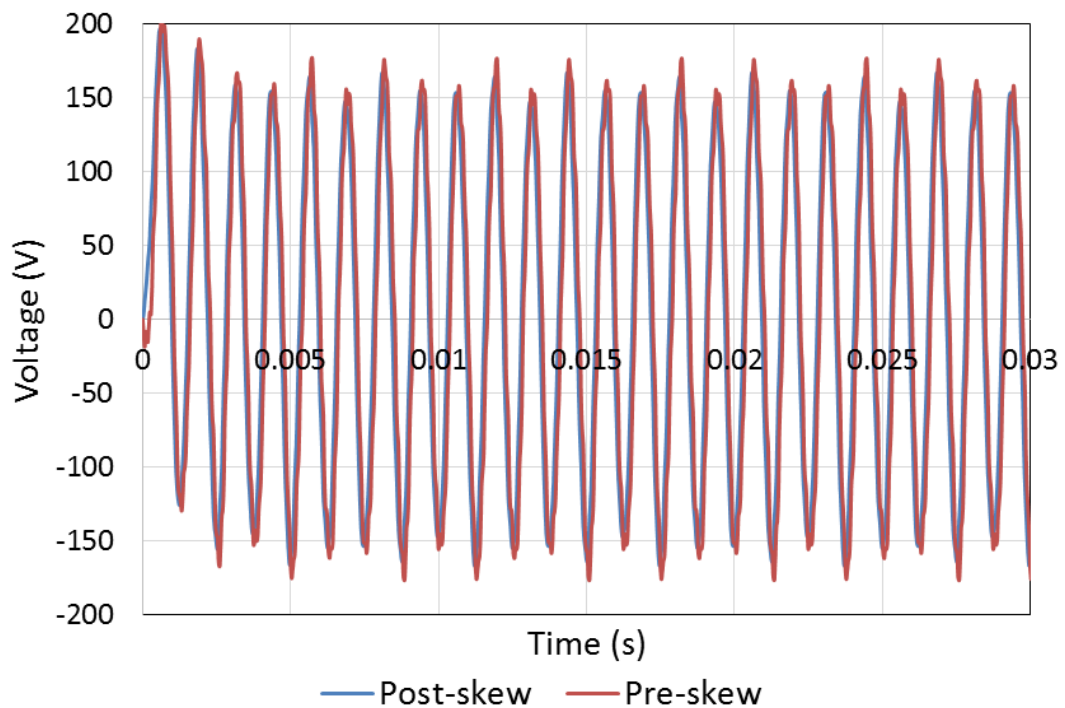


Figure 5.46 – FE calculated phase A power winding load voltage with a load of  $3.7\Omega$  and a control winding current density of  $14.14A_{rms}mm^{-2}$  at a test point of 20% above the synchronous frequency range (14,400rpm)

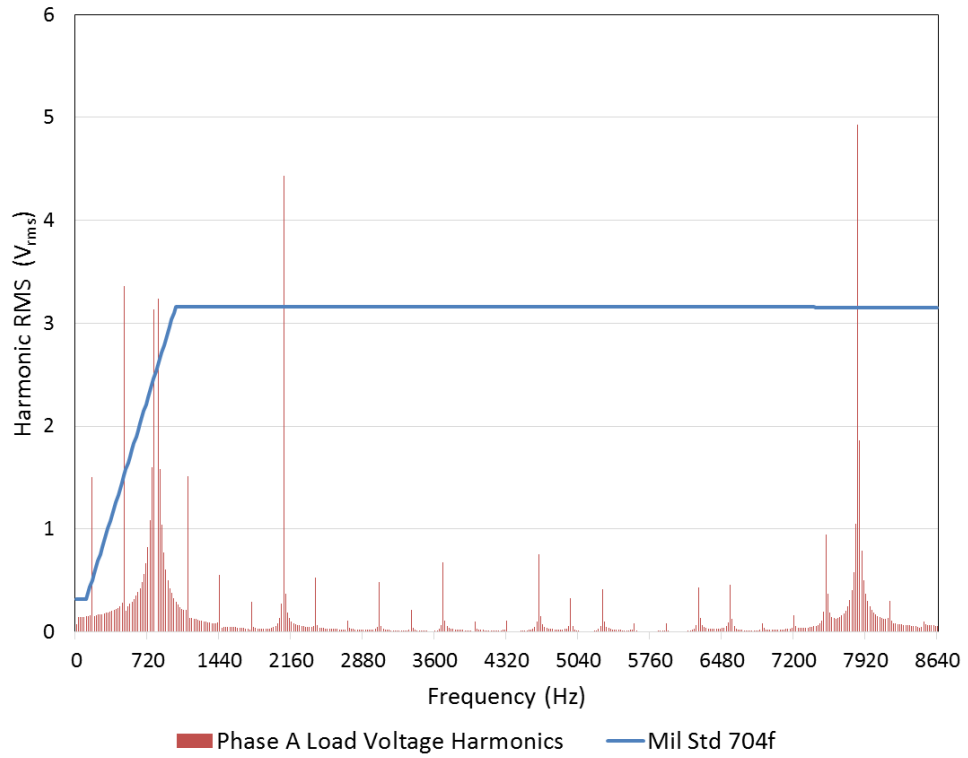


Figure 5.47 – FE calculated FFT of phase A power winding load voltage with a load of  $3.7\Omega$  and a control winding current density of  $14.14A_{rms}mm^{-2}$  at a test point of 20% above the synchronous frequency range (14,400rpm) with no skew

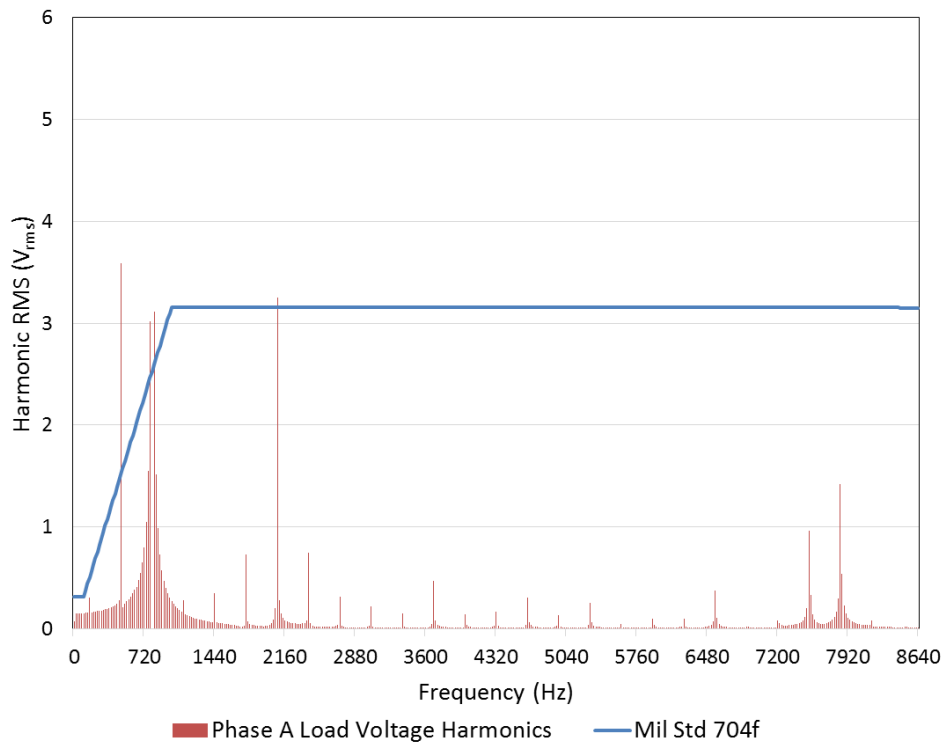


Figure 5.48 – FE calculated FFT of phase A power winding load voltage with a load of  $3.7\Omega$  and a control winding current density of  $14.14A_{rms}mm^{-2}$  at a test point of 20% above the synchronous frequency range (14,400rpm) with skew

These 5 operating points all show a clear benefit from skewing the rotor, specifically in terms of significant reductions in power winding slotting induced harmonics. Table 5.11 summarises the various reductions in key performance measures as a result of adopting a skew of one stator slot-pitch. To be able to operate the BDFRM in aerospace applications, strict VF standards must be adhered to, a requirement that can be met in terms of slotting harmonics by incorporating a one stator slot pitch skew to the rotor. Unfortunately, this leads to an inevitable reduction in the output power of the machine. An additional advantage to adding a rotor skew is to reduce torque ripple seen in the torque waveform.

One recurring harmonic seen in each of these cases (with the exception of the 0% correction case) is the sub-harmonic which is due to a saturation-induced 3<sup>rd</sup> harmonic of the control winding. This harmonic is a consequence of the choice of pole number combination for the BDFRM as discussed in detail in Chapter 2. The relationship between the magnitude of this 3<sup>rd</sup> harmonic and the control winding current density can be re-calculated to account for a skew of one stator slot pitch with the use of the Flux Skewed module for one test point at 4,860rpm. Figure 5.49 shows the resulting variation in this harmonic with increasing control winding current density. At lower current densities, the subharmonic reaches a peak of 5.3% of the fundamental magnitude due to the initial saturation of the rotor bridges. This then reduces at higher current densities as the level of saturation reaches a maximum.



Table 5.11 – BDFRM operating points as a result of a 10° skew and 14.14A<sub>rms</sub>mm<sup>-2</sup> control winding current

Excursion from VF range (%)	Operating point				
	-20	-10	0	+10	+20
Rotor speed (rpm)	4,320	4,860	9,000	13,200	14,400
Control winding frequency (Hz)	72	36	0	80	160
Reduction in phase A power winding fundamental voltage (%)	4.4	4.1	3.3	3.8	3.8
Reduction in phase A power winding load voltage THD (%)	20.2	30.3	32.2	22.0	21.4
Reduction in average torque (%)	9.2	8.6	7.8	8.4	8.8
Reduction in torque THD (%)	58.8	58.5	52.3	52.5	52.5
Reduction in 3-phase load power (%)	8.6	8.2	7.5	8.1	8.2

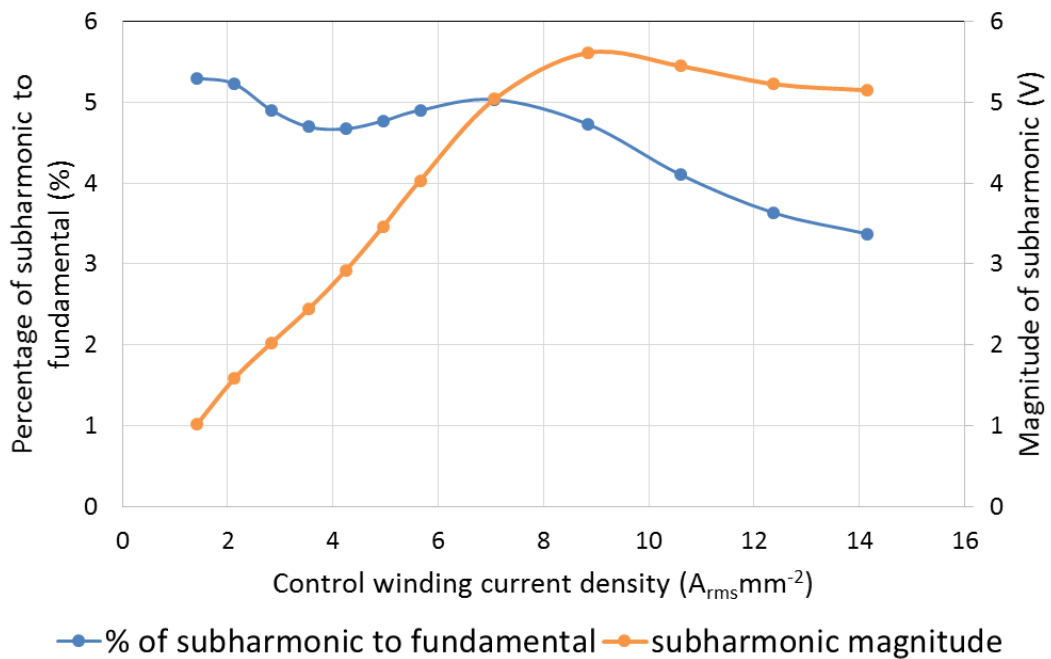


Figure 5.49 – FE predicted subharmonic content in phase A of the power winding voltage with a skewed rotor and a 4.2Ω load for a test point at 10% below the synchronous speed range (4,860rpm)

Returning to a more analytical approach and using the standard skew factor formula:

$$K_{sq} = \frac{\sin\left(v \cdot \frac{S}{\alpha_p} \cdot \frac{\pi}{2}\right)}{v \cdot \frac{S}{\alpha_p} \cdot \frac{\pi}{2}} \quad [10] \quad (5.2)$$

Where  $S$  is the angle of skew,  $\alpha_p$  is the pole pitch of the winding and  $v$  is the harmonic order, the skew factor for a BDFRM with this pole combination is found to be 0.9886 for the fundamental. Therefore the fundamental component of the load voltage is calculated to be reduced by 1.14%, but the results in Table 5.11 suggest that this figure could be as high as 4.4%. This discrepancy could be a result of saturation in the laminations of the machine.

### 5.10 FINAL SIMULATION OF PERFORMANCE FOR THE OPTIMISED DESIGN

Taking into account all of the above simulations and design choices (including the 10° rotor skew), a final operating performance at a range of test points are summarised in Table 5.12 for the final down-selected design, with a comprehensive list of dimensions provided in Appendix 4 (Section 8.4). It should be noted that not all operating points in Table 5.12 were included in the experimental test plan for the demonstrator due to limitations of the control winding converter (as will be discussed in Section 6.5).

Table 5.12 – Operating points for the final design

Correction (%)	Rotor speed (rpm)	Control frequency (Hz)	Power frequency (Hz)	Phase A load power (kW)
-20	4,320	72	360	2.8
-10	4,860	36	360	2.8
0	9,000	0	600	3.1
+10	13,200	80	800	3.3
+20	14,400	160	800	3.3

### 5.11 CALCULATION OF LOSSES AND EFFICIENCIES

The losses in electrical machines must be accurately modelled, to provide a meaningful basis for a comparison between the various models used and experimental results for the demonstrator. The main sources of losses in a BDFRM

are: stator copper losses, rotor and stator iron losses and mechanical losses comprising various contributions from windage and friction.

#### 5.11.1 METHOD FOR CALCULATING COPPER LOSS

The key to calculating the copper losses is a reliable means of calculating the resistance of each winding. The biggest challenge is a reliable model for calculating end-winding length. The presence of two windings of different pole numbers makes this more complex. The end-winding length and hence contribution to the resistance is calculated as follows:

- The slot area for each winding is multiplied by the packing factor (0.45) to obtain the cross-section of copper for each winding slot area
- The length of each end winding arc must then be calculated by referring to the average radius of each winding and the angle over which each arc occurs
- For the control winding three different arc lengths exist, indicated as orange, green and red in Figure 5.50 with arcs of 130°, 150° and 170° mechanical
- The power winding only has one arc length of 60° mechanical
- Using these arc lengths, the total end winding length for one turn can be calculated for each winding
- This area and length are then inserted into the equation for resistance (equation (5.3)) using the resistivity of copper as  $1.7 \times 10^{-8} \Omega\text{m}$

$$R = \frac{\rho l}{A} \quad (5.3)$$

Table 5.13 shows the predicted phase to neutral resistances at 20°C calculated using these methods. As will be demonstrated in Section 6.2.2, these values proved to be an underestimate of the resistance of the demonstrator manufactured.

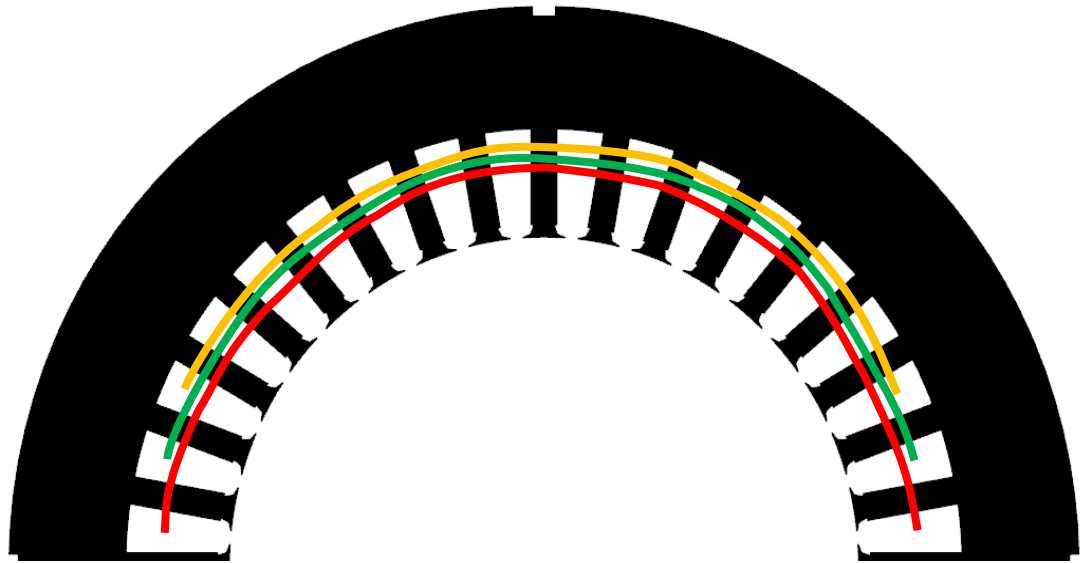


Figure 5.50 – End winding arrangement of one pole of one phase of the 2-pole control winding

Table 5.13 – Calculated winding resistances at 20°C

Winding	Active region resistance (mΩ)	End winding resistance (mΩ)	Total resistance (mΩ)
Power winding (phase to neutral)	127.9	161.1	288.9
Control winding (phase to neutral)	188.8	530.6	719.5

### 5.11.2 METHOD FOR CALCULATING IRON LOSS

Iron loss is often a significant contributor to the overall losses in electrical machines, and hence it is important to model this to a reasonable degree of accuracy if comparisons are to be drawn between a FE model and a demonstrator.

The calculation of iron loss is a complex process that is reliant on the availability of a great deal of material specific coefficients and constants. It is common practice to consider the overall loss as comprising of three components of loss: hysteresis loss, Eddy current losses and excess (or anomalous) losses:

$$P_{iron} = P_{hyst} + P_{eddy} + P_{anom} \quad (5.4)$$

The individual loss components can be estimated from well-established equations for arbitrary waveforms [11, 12]:

$$P_{hyst} = k_{hys} f B_{pk}^{a+bB_{pk}} \quad (5.5)$$

$$P_{eddy} = \frac{\sigma \delta_{lam}^2}{12} \frac{1}{T} \int_0^T \left( \frac{dB}{dt} \right)^2 dt \quad (5.6)$$

$$P_{anom} = \frac{k_{anom}}{T} \int_0^T \left| \frac{dB}{dt} \right|^{1.5} dt \quad (5.7)$$

These equations can be deployed on an element by element basis in a time-stepped magneto-static finite element simulation over one complete electrical cycle. Flux density waveforms in the radial and tangential directions for each element are extracted from the finite element simulations. The loss resulting for each individual flux density excursion is calculated using material specific loss constants contained in equations (5.4) to (5.7).

Table 5.14 lists the material specific constants for the NO20 Silicon Iron material selected for the stator and rotor cores. These values were taken from [12] while the post-processing of the series of finite element simulations was undertaken with a pre-existing MATLAB tool. Although this is able to accommodate non-sinusoidal flux density waveforms, it is not able to rigorously account for minor loop excursions.

Table 5.14 – Material specific constants for the NO20 material used for iron loss calculations [2]

Constant	Value
$k_{hys}$	0.0172
$B_{pk}$	1.8
a	1.21
b	0.85
$\sigma$	1923077
$\delta_{lam}$	0.2
$k_{anom}$	0.00025

The loss associated with minor hysteresis loops is affected by the magnitude, phase and order of the harmonic components [13]. In particular the 3<sup>rd</sup> harmonic of the fundamental frequency is seen to be as high as 15% [14, 15] of the fundamental, leading to a significant increase in the eddy current losses.

### 5.11.3 PREDICTED EFFICIENCIES

Having performed simulations at all the key operating points, including the calculation of losses, the efficiency of the final machine at various operating points was calculated. Table 5.15 contains a summary of the various contributions to the overall loss. When compared to permanent magnet machines of similar dimensions, where efficiencies up to 95% are commonplace, the values in Table 5.15 may seem to be relatively poor. This low efficiency is in part due to the requirement to use two separate 3-phase windings in BDFRMs, and therefore produce two separate copper losses. The increased slot area required for these two windings also increases the tooth length and hence increases the iron losses.

Table 5.15 – Efficiencies of the final skewed FEA design

Operating point	-20%	-10%	DC	+10%	+20%
Control winding frequency (Hz)	72	36	0	80	160
Rotor speed (rpm)	4,320	4,860	9,000	13,200	14,400
Power winding frequency (Hz)	360	360	600	800	8000
3-ph control winding real power (W)	3554	2511	1419	450	-139*
3-ph load power (W)	9163	9668	10148	10585	10577
Power winding copper loss (W)	767	700	921	974	973
Control winding copper loss (W)	1416	1416	1416	1416	1416
Iron loss (W)	58	59	127	231	271
Total Losses (W)	2235	2175	2465	2621	2660
Efficiency (%)	<b>71.5</b>	<b>76.7</b>	<b>78.0</b>	<b>79.5</b>	<b>80.1</b>

\*a negative number in this cell refers to a control winding power being sunk to the grid

### 5.11.4 CONTROL WINDING REACTIVE POWER REQUIREMENTS

A major practical drawback of operating these machines in non-grid connection mode is the amount of reactive power which needs to be accommodated by the control winding converter due to the coupling, via the rotor, of the two windings.

A good operating point to appreciate this effect is the mid speed band example with DC control current. In this case a static 3-phase DC pattern is set up by the control winding using three constant current sources. With a rotational speed of 9,000rpm and a 0Hz control winding frequency, the machine is effectively operating in synchronous mode, producing an output power winding frequency of 600Hz. If the

voltage across the control winding is then derived from the simulations (Figure 5.51), a DC offset and large ripple at 600Hz can be observed, therefore leading to a requirement for converter with an increased rating.

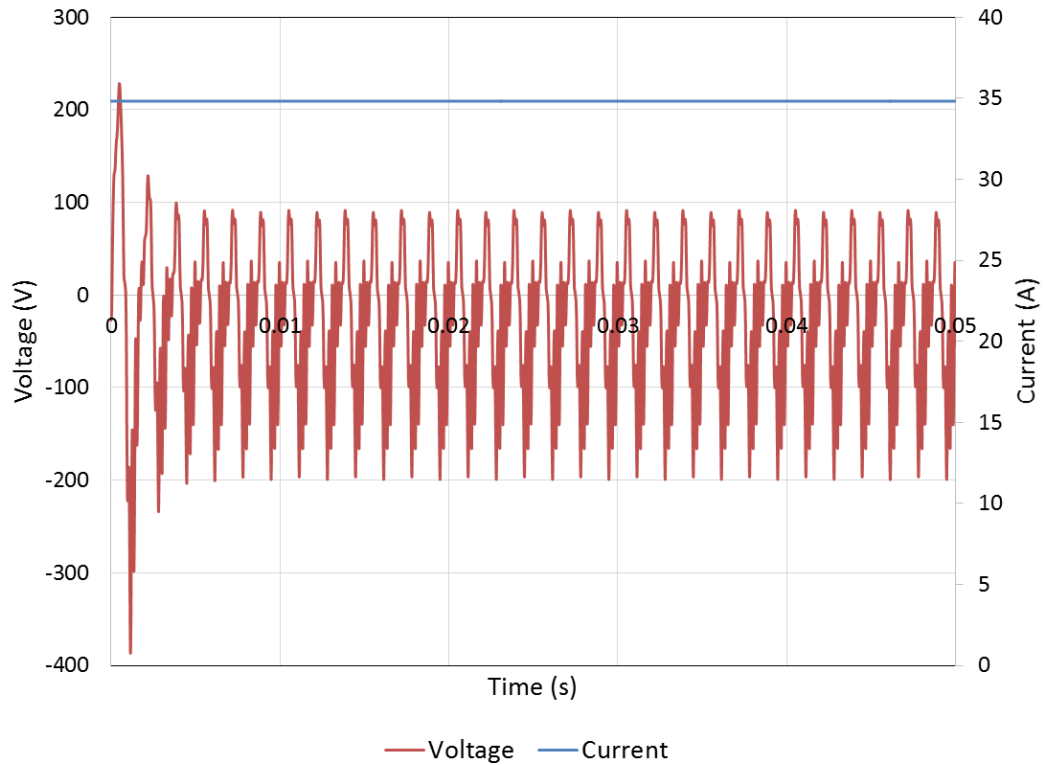


Figure 5.51 – Voltage across the control winding phase A current source at 0 Hz control frequency and control winding current density of  $14.14A_{rms}mm^{-2}$ , a rotor speed of 9,000rpm and a power winding load of  $3.7\Omega$

The control winding converter VA rating requirements at a range of operating points were calculated and are summarised in Table 5.16. As will be apparent, the partially rated converter which is often cited in many papers as a virtue of these machines, in fact turns in to an over rated converter in several cases, i.e. greater than the real power delivered at the load. A broadly linear correlation is observed between the frequency correction required and the VA requirement of the converter.

Table 5.16 – VA ratings of the control winding converter over a range of operating points

Frequency correction	Power winding frequency (Hz)	Rotor speed (rpm)	Phase A VA rating (kVA)
-20%	72	4,320	7.67
-10%	36	4,860	5.02
0	0	9,000	2.72
+10%	80	13,200	8.90
+20%	160	14,400	14.82

## 5.12 FURTHER STUDIES

Although the optimisation of the design was concluded in Section 5.8, further investigations were performed on two features that could offer some enhancement to this design.

### 5.12.1 SUBSTITUTION OF SILICON IRON BY COBALT IRON

As detailed in Section 5.2 of this chapter, the design and resulting simulations of performance presented in this chapter have been based on the stator and rotor core being manufactured from Silicon Iron. To establish the scale of the performance loss incurred by selecting Silicon Iron instead of Cobalt Iron (this being largely for cost reasons) a further simulation was undertaken at one of the reference operating points for a machine with Cobalt Iron in both the stator and rotor cores.

A summary of the relative performances of otherwise identical BDFRMs with Silicon Iron and Cobalt Iron cores is shown in Table 5.17, for a 13,200rpm operating point with a control winding current density of  $14.14A_{rms}mm^{-2}$  and a load resistance of  $3.7\Omega$ . As will be apparent by adopting Cobalt Iron, there is an increase of 14% in power winding voltage and a 26% increase in 3-phase power. With due account of the increased flux density of Cobalt Iron as compared to Silicon Iron, the power density increases by  $\sim 19\%$ . At this particular test point of 10% above the VF range, the active power density (stator, rotor and winding weights considered) achieved with Cobalt Iron is 0.52kW/kg, which is still modest in comparison to competing machine types.



Table 5.17 – BDFRM comparison of output characteristics with silicon iron and cobalt iron at a speed of 13,200rpm, a control winding current density of  $14.14A_{rms}mm^{-2}$  and a load of  $3.7\Omega$

	Silicon iron	Cobalt iron
Material owner	Sura	Vacuumschmelze
Material designation	NO20	VACOFLUX 50
Material density ( $gcm^{-3}$ )	7.65	8.12
Saturation magnetisation (T)	~1.80	~2.35
Control winding current density ( $A_{rms}mm^{-2}$ )	14.14	14.14
Power winding phase A load voltage ( $V_{rms}$ )	110.6	125.9
Power winding 3-phase power (kW)	9.9	12.5
Average torque (Nm)	-8.5	-10.9

### 5.12.2 ADDITION OF PMS TO THE BDFRM ROTOR

As discussed in Section 3.6, the addition of small pieces of permanent magnet into the rotor of a SyncRel leads to an increase in average torque, as well as a decrease in torque ripple. It is worth recalling, the addition of magnets into the SyncRel was not to provide hybrid excitation, but to manage the saturation within the cross-barrier supports. On this basis, it would seem that similar benefits might be achieved with a BDFRM. However, it should be noted that the rotor in the BDFRM is skewed along its length, and hence the incorporation of magnets would be challenging given the complex geometry of the flux barriers. An alternative would be to divide the rotor into a number of axial sections and adopt a step-skew approach. This would still produce a reasonable approximation to the required skew but allow straight magnet pieces to be used.

To reduce the potential computational time requirements of studying all operating points, only three operating points at -10%, mid-range and +10% were simulated for a BDFRM rotor incorporating PMs. To ensure the findings from this study are representative across the power range, two control winding current densities of 3.54 and  $14.14 A_{rms}mm^{-2}$  are considered at each speed point.

Table 5.18 summarises the predicted performance at a current density of  $14.14A_{rms}mm^{-2}$ . Introducing magnets into the rotating reference frame could produce a synchronous rotating field in the airgap, thus increasing torque ripple and

voltage THD. In fact, this behaviour is minimised by ensuring that the majority of the flux produced by the PMs remains within the rotor, passing in large part through the rotor bridges.

The percentages shown in Table 5.18 indicate the change resulting from the addition of PMs into the BDFRM, with green indicating an advantageous change and red a detriment. As will be apparent, the addition of magnets to a BDFRM operating at this highly saturated current level shows advantages in power winding voltage at all operating point and small increases in the 3-phase load power at two out of the three points. One major disadvantage of operating with the addition of magnets at this current density is the significant increase in voltage harmonics in the power winding voltage. Finally, in terms of torque ripple the addition of PMs results in only a modest reduction in the peak to peak ripple as a percentage of the average torque.

Table 5.18 – Operational comparison of the BDFRM at various test points with and without the addition of PMs at a current density of  $14.14A_{rms}mm^{-2}$

Operating point	BDFRM without magnets			BDFRM with magnets		
	-10%	DC	+10%	-10%	DC	+10%
Power phase A load voltage ( $V_{rms}$ )	108.92	108.00	110.57	119.49	108.73	111.51
	-	-	-	+10%	+1%	+1%
Power 3-phase load power (W)	8488.85	9263.48	9912.05	9140.72	9457.74	9851.40
	-	-	-	+8%	+2%	-1%
Power phase A load voltage THD (%)	5.70	4.88	6.86	7.46	7.13	7.99
	-	-	-	+31%	+46%	+16
Torque ripple (%)	89.31	145.05	220.48	90.05	139.39	197.33
	-	-	-	+1%	-4%	-10%

Table 5.19 – Operational comparison of the BDFRM at various test points with and without the addition of PMs at a current density of  $3.54A_{rms}mm^{-2}$

Operating point	BDFRM without magnets			BDFRM with magnets		
	-10%	DC	+10%	-10%	DC	+10%
Power Phase A Load Voltage ( $V_{rms}$ )	37.03	33.52	33.25	43.87	35.17	35.31
	-	-	-	+18%	+5%	+6%
Power 3-phase load power (W)	951.75	864.75	866.80	1207.51	987.28	987.72
	-	-	-	+27%	+14%	+14%
Power Phase A Load Voltage THD (%)	6.54	4.19	8.72	5.19	6.25	7.71
	-	-	-	-21%	+49%	-12%
Torque Ripple (%)	200	341	548	172	354	396
	-	-	-	-14%	+4%	-28%

Table 5.19 shows the corresponding results at a current density of  $3.54A_{rms}mm^{-2}$ , where greater advantages in power and voltage magnitude are evident. In particular, the voltage THD at 10% above and below the synchronous speed range shows a marked improvement, compared to the improvements in Table 5.18. This can be attributed to the onset of significant bulk saturation of the rotor and/or stator cores at higher current densities, thus reducing the advantageous effects of adding permanent magnet to promote localised saturation. The THD values for DC control winding current show an increase with the addition of PMs, which may be due to the inherent lack of airgap flux harmonics, due to operation with zero control frequency. Hence, harmonics introduced by the addition of magnets are now the dominant contributor to the overall harmonic distortion. The torque ripple shows an improvement when a non-zero control winding frequency is used, but a slight increase for the DC control winding case.

The effect of THD on the shape of the output voltage waveform can be gauged in Figure 5.52, which shows a comparison between the two phase A voltage waveforms of the DC mid speed range operating point at a current density of  $3.54A_{rms}mm^{-2}$ . Even

with an increase in voltage THD of 49% between the two cases the absolute THD is still only 6.25%, which is difficult to discern when comparing the two voltage waveforms.

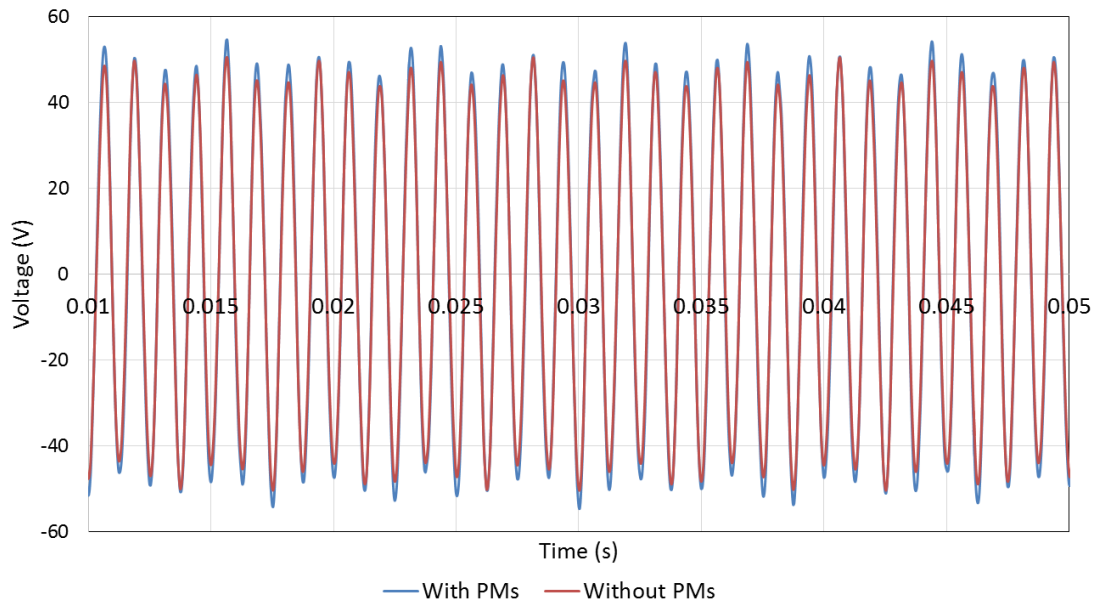


Figure 5.52 – Power winding phase A load voltage produced with and without the addition of PMs to the rotor at a current density of  $3.54A_{rms}mm^{-2}$  at a DC mid speed range (9,000rpm) operating point and a power winding load of  $3.7\Omega$

The addition of these 72 small magnet pieces into the flux barriers leads to increases of up to 27% in 3-phase output power and up to 18% increase in load voltage magnitude. In some cases, a detriment in voltage THD was observed, but the torque ripple is generally improved. The total weight of these additional PMs is only 417g, which corresponds to 1.75% of the active mass of the machine. So with a small increase in weight, the power and corresponding power density can be increased appreciably.

### 5.13 SUMMARY OF CHAPTER 5

This chapter has detailed the many parameters of the BDFRM which may be optimised, as well as providing detailed performance characteristics from simulations of the final design and several intermediate design steps during optimisation.

Firstly a detailed optimisation of the physical parameters was performed leading to a final design with parameters as detailed in Appendix 4 (Section 8.4).

A detailed study followed in to both the electromagnetic and mechanical design of the rotor structure, with the specification of providing sufficient mechanical strength whilst ensuring that the additional supports saturate at as low a current density as possible. The output characteristics of the electromagnetically and mechanically optimised rotors are then compared, and a significant reduction of up to 34% in output power is found by ensuring the rotor is mechanically sound at the maximum specified speed.

The effect of skewing the rotor on load voltage harmonics is then studied with the conclusion that slotting harmonics are significantly reduced by skewing the rotor. When introducing the harmonic limits imposed by aerospace standards, it is obvious that subharmonics in these machines are too great to be able to operate straight on to an aircraft grid, but mid to high frequency harmonics remain mostly below these limits.

The losses in the BDFRM are dominated by the copper losses, due to the lengths of the turns and the presence of two windings. The iron losses present in the BDFRM are predictably primarily due to eddy current losses especially at high speeds. This is an unsurprising result when one considers the amount of complex airgap harmonics prevalent in machines such as this. The efficiencies produced by this machine range between 72% and 80%, depending upon the chosen operating point.

The final part of this chapter contained two additional studies, the first is concerned with the effect of producing the BDFRM with more expensive cobalt iron laminations. This led to a predictable increase in 3-phase load power of 26% due to the significant saturation seen in these machines. The second study takes an idea from the SyncRel chapter (Chapter 3) with the addition of magnets to the AFB rotor. A significant potential increase in output power is found at certain test points with small detriments to the voltage THD.

Table 5.20 shows the power and torque densities of the final BDFRM design over a range of operating points. It is apparent from this table that even following

comprehensive optimisation, this final BDFRM design is not competitive in performance with alternative aerospace generator concepts such as high power dense PM machines. This said, it does retain the advantage of a direct line-connected machine with frequency correction capability.

Table 5.20 – Power and torque densities for the final design over a range of operating points at a fixed control winding current density of  $14.14A_{rms}mm^{-2}$

Operating point	-20%	-10%	0	+10%	+20%
Rotor speed (rpm)	4,320	4,860	9,000	13,200	14,400
Control winding frequency (Hz)	72	36	0	80	160
Power winding load ( $\Omega$ )	4.1	4.2	3.7	3.7	3.7
Power density (kW/kg)	<b>0.35</b>	<b>0.36</b>	<b>0.39</b>	<b>0.41</b>	<b>0.41</b>
Torque density (Nm/kg)	<b>0.67</b>	<b>0.68</b>	<b>0.45</b>	<b>0.36</b>	<b>0.35</b>

## 5.14 REFERENCES

- [1] T. Feehally and J. Apsley, "The doubly-fed induction machine as an aero generator," in *Energy Conversion Congress and Exposition (ECCE), 2014 IEEE*, 2014, pp. 1340-1347.
- [2] Cogent. Sura NO20 Data Sheet [Online]. Available: <http://cogent-power.com/cms-data/downloads/NO20.pdf>
- [3] Vacuumschmelze. Soft Magnetic Cobalt-Iron-Alloys [Online]. Available: [http://www.vacuumschmelze.com/fileadmin/Medienbibliothek\\_2010/Downloads/HT/PHT\\_004\\_Vacoflux-Vacodur\\_engl.pdf](http://www.vacuumschmelze.com/fileadmin/Medienbibliothek_2010/Downloads/HT/PHT_004_Vacoflux-Vacodur_engl.pdf)
- [4] J. S. Rao, *Rotor Dynamics*, 3rd ed. New Delhi: New Age International Limited, Publishers, 1983.
- [5] V. B. Bhamdari, *Introduction to Machine Design*, 2000 ed.: Tata McGraw-Hill Education, 2001.
- [6] T. Staudt, F. Wurtz, N. J. Batistela, and P. Kuo-Peng, "Influence of rotor design and geometric parameter variation on global performance of Brushless Doubly-Fed Reluctance Machines," in *Electrical Machines (ICEM), 2014 International Conference on*, 2014, pp. 537-543.
- [7] A. M. Knight, R. E. Betz, and D. G. Dorrell, "Design and Analysis of Brushless Doubly Fed Reluctance Machines," *Industry Applications, IEEE Transactions on*, vol. 49, pp. 50-58, 2013.
- [8] A. Vagati, M. Pastorelli, G. Francheschini, and S. C. Petrache, "Design of low-torque-ripple synchronous reluctance motors," *Industry Applications, IEEE Transactions on*, vol. 34, pp. 758-765, 1998.
- [9] U. D. o. Defense, "Aircraft Electric Power Characteristics - MIL-STD-704F," ed, 2004.
- [10] J. R. Hendershot and T. J. E. Miller, *Design of Brushless Permanent-Magnet Machines*, 2010.
- [11] C. A. Hernandez-Aramburo, T. C. Green, and A. C. Smith, "Estimating rotational iron losses in an induction machine," *Magnetics, IEEE Transactions on*, vol. 39, pp. 3527-3533, 2003.
- [12] J. Paulides, "High performance 1.5MW 20,000rpm permanent magnet generator with uncontrolled rectifier for 'more-electric' ship applications," PhD, Electronic and Electrical Engineering, University of Sheffield, Sheffield, UK, 2005.
- [13] J. D. Lavers, P. Biringer, and H. Hollitscher, "A simple method of estimating the minor loop hysteresis loss in thin laminations," *Magnetics, IEEE Transactions on*, vol. 14, pp. 386-388, 1978.
- [14] A. J. Moses and G. H. Shirkoohi, "Iron loss in non-oriented electrical steels under distorted flux conditions," *Magnetics, IEEE Transactions on*, vol. 23, pp. 3217-3220, 1987.
- [15] G. Bertotti, A. Boglietti, M. Chiampi, D. Chiarabaglio, F. Fiorillo, and M. Lazzari, "An improved estimation of iron losses in rotating electrical machines," *Magnetics, IEEE Transactions on*, vol. 27, pp. 5007-5009, 1991.

## **6 CHAPTER 6 – BUILD, TEST AND ANALYSIS OF A BDFRM DEMONSTRATOR**

---

### **6.1 INTRODUCTION**

This chapter describes the construction and testing of a demonstrator model of the BDFRM, including comparisons with FE predicted performance. Detailed information on the testing equipment is provided including information concerning the converter, signal processing, dynamometer and load bank. Some initial tests are completed to confirm the frequency correction properties of the BDFRM, followed by more detailed studies across the whole test range. Finally, a further study in to the presence of harmonics in the power winding voltage is completed by performing FFTs over a range of speeds and control winding frequencies.

### **6.2 DEMONSTRATOR MANUFACTURE**

A demonstrator machine for experimental testing was manufactured according to the dimensions and winding parameters specified in Appendix 4 (Section 8.4), after a comprehensive optimisation in Chapter 5. A full set of the resulting engineering drawings used to manufacture the rotor and stator laminations as well as the casing are contained in Appendix 5, 6 and 7.

#### **6.2.1 ROTOR AND STATOR CORES**

The rotor and stator cores were formed by individually laser cutting silicon iron laminations, which were then aligned, heated and compressed to form a bonded stack. The rotor lamination has a  $10^\circ$  (one stator slot pitch) skew, which led to each rotor lamination having a unique cross-section to ensure the key-way is straight along the length of the bore of the rotor. The stator and rotor laminations before winding and shaft insertion can be seen in Figure 6.1.



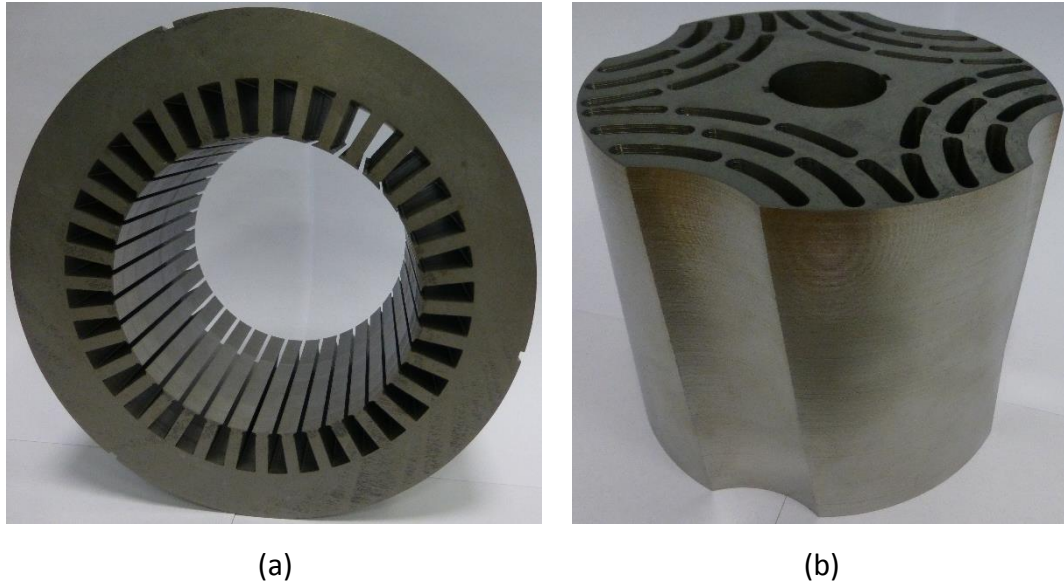


Figure 6.1 – Stator (a) and rotor (b) laminations of the BDFRM demonstrator

### 6.2.2 STATOR WINDING

The stator core was wound with both the control and power windings by an external contractor.

Six thermocouples are buried in the windings at various positions and in all phases around the periphery of the machine (as described in Table 6.1 with reference to the slot numbering in Figure 4.3). This ensures that all regions of the stator slots are sufficiently monitored across all phases and both windings. One thermocouple was attached to the casing via a thermal epoxy to obtain an accurate reading of casing temperature. The other three thermocouples measure environmental temperatures with two measuring the input and output air temperatures of the machine and the final one measuring the ambient air temperature. This arrangement of thermocouples ensures that all areas of the machine are being actively monitored to avoid any damage to the windings due to either hot spots or bulk heating in the machine.

Table 6.1 – Locations of thermocouples buried in the windings in relation to the machine cross-section of Figure 4.3

Winding and phase	Slot location
<b>Control Phase A</b>	1
<b>Control Phase B</b>	13
<b>Control Phase C</b>	25
<b>Power Phase A</b>	33
<b>Power Phase B</b>	19
<b>Power Phase C</b>	6

Placing the laminations in the casing before winding would seem like the logical step from both a winding and a mechanical point of view, in that it is much easier to heat fit the laminations into a casing without the presence of windings which impede the application of a press. Ordinarily this would be the preferred method, but in the case of this project, utilising both a high span 2-pole winding and two separate windings leads to a relatively large amount of end winding copper to be accommodated in the passive areas at both ends of the machine. This high amount of end winding copper leads to an increase in case length, which cannot be accounted for until the winding has been completed. Therefore, if the casing was constructed before the completion of the winding, an estimation would have to be made on the axial length required for the end windings. Making an error in this estimation may lead to either a casing extension being required or the original casing being cut which is much more difficult to achieve when the stator and windings are already thermally fitted into the casing.

As the casing would need to be oversized to allow for an unknown quantity of end windings, actually getting tools to each end of the stator to wind the machine would be prohibiting thereby increasing the winding time and therefore winding cost.

The chosen option was to construct a temporary clamp, which would ensure that the laminations would be under constant compression to eliminate the risk of damage, e.g. de-lamination, to the bonded stack. This method would improve access to the stack for ease of winding but may make the casing insertion slightly more complicated. A simple clamp design (Figure 6.2) was designed and constructed. The

clamp was constructed using four semi-circles in order to accommodate disassembly of the clamp post-winding, without the need for the end windings to pass through the clamp ring risking damage to the windings.



Figure 6.2 – Image of the temporary stator clamp and lamination stack

The final winding parameters are listed in Table 6.2. A copper wire of diameter 0.67mm was chosen as the nearest standard value to the nominal diameter required to match the numbers of turns and target packing factor of 0.45. The resulting calculated and measured phase resistances (which includes the end-windings) are shown in Table 6.3. The measured values were measured before final termination of the winding by a Cropico DO5000 microhmmeter. The discrepancy between the calculated and measured resistances is a consequence of the following:

- i) The use of the nearest standard wire diameter, i.e. 0.67mm instead of the 0.6656mm and 0.6739mm for the control and power winding respectively identified in Table 6.2. This accounts for a difference of 1.3% and 1.1% for the control and power windings respectively, i.e. simply the ratio of the squares of these diameters.
- ii) An underestimate of the end-windings mean length per turn. The calculated value was based on an assumption that the mean length was equal distance from the lamination around the whole turn. This leads to

a calculated mean length per turn of 3.6m for the control winding and 2.1m for the power winding, leading to a total end-winding mass of 2.44kg. In practice the need to pass the various coil interconnects past each other led to bulkier end-windings, contributing an extra 1.76kg to the mass. The mean path lengths per turn for the control and power windings inferred from the phase A resistance measurements are 4.9m and 3.3m. This corresponds to an increase in total path length of 42% from the calculated model to the measured windings.

- iii) The inter-connects and trailing wires of the demonstrator machine which were not accounted for in the original resistance calculations.

Table 6.2 – Final manufactured stator winding parameters

	Control winding	Power winding
Pole number	2	6
Winding configuration	Nested coils	Overlapping
Turns per coil	16	13
Slot cross-sectional area (mm <sup>2</sup> )	123.8	
Packing factor	0.45	
Slot cross-sectional area per winding (mm <sup>2</sup> )	61.9	61.9
Copper cross-sectional area per winding (mm <sup>2</sup> )	27.86	27.86
Copper cross-sectional area per turn (mm <sup>2</sup> )	1.74	2.14
Number of strands of 0.67mm diameter wire in parallel	5	6

Table 6.3 – Predicted and measured winding phase resistances

Resistance measurement	Predicted phase resistance		Measured phase resistance	
	Control	Power	Control	Power
Winding				
A – Star (mΩ)	719.47	288.92	778.8	340.5
B – Star (mΩ)	719.47	288.92	780.5	340.0
C – Star (mΩ)	719.47	288.92	777.4	340.6

The final wound and terminated stator is shown in Figure 6.3. As will be apparent, the end windings play a significant role in determining the overall length of the stator. The overall length of the wound stator is 220mm even though the active length of the stator core is only 100mm.

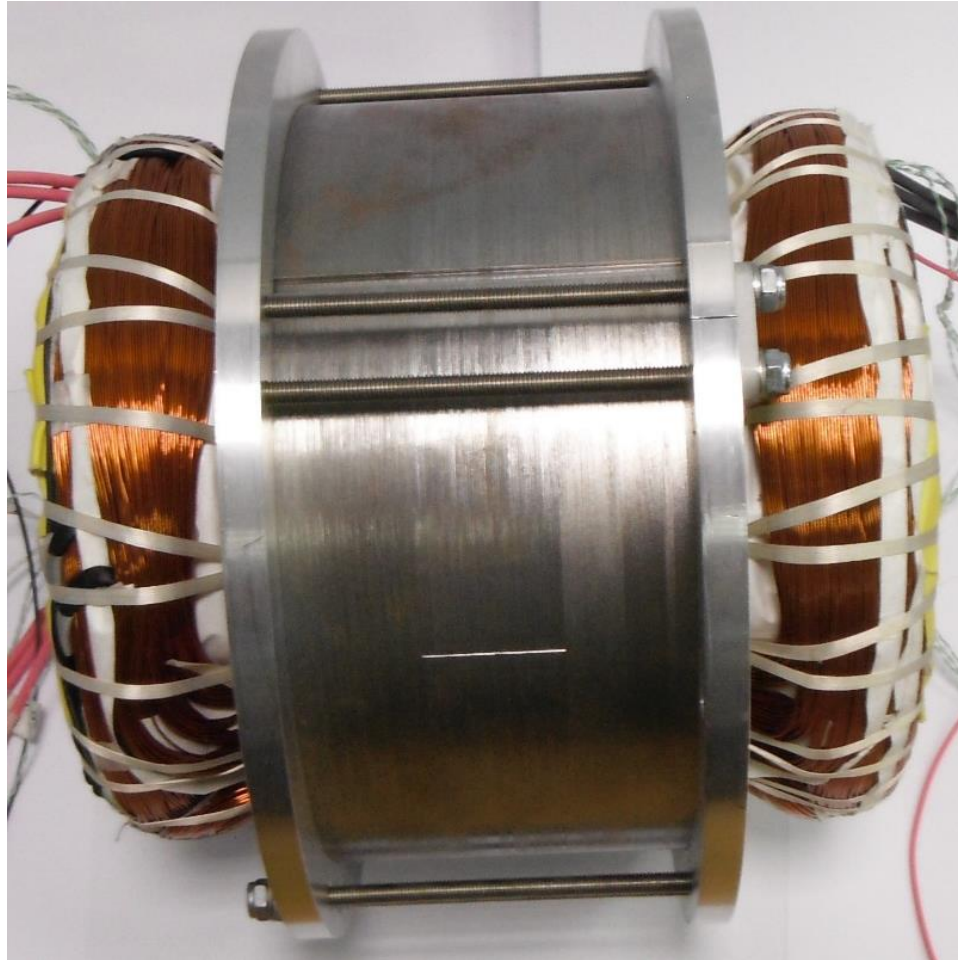


Figure 6.3 – Side view of the completed stator winding

The wound stator was varnished with HI-THERM BC-325 solvent borne polyester stoving varnish to provide mechanical rigidity and enhance heat transfer in the winding. Although heat transfer could be further enhanced with vacuum impregnation with a loaded resin, this was not warranted in this particular study since the thermal behaviour of the machine was not a high priority, it not being capable of sustaining a current density of  $14.14A_{rms}mm^{-2}$  in steady-state.

### 6.2.3 ROTOR SHAFT

The rotor was mounted onto the shaft by way of a sliding fit past two keys and a washer and nut assembly as seen in Figure 6.4. The rotor assembly was balanced at a speed of 850rpm up to a quality of G2.5 by means of applying small amounts of material into the rotor flux barriers as can be seen in Figure 6.5. Detailed mechanical drawings of the rotor shaft can be found in Appendix 5 (Section 8.5).

The bearings used between the rolling interface of the shaft and the casing are from the NSK series of high precision angular contact ball bearings, specifically the 7905 and the 7906 models. These are both open bearings, due to their high speed nature, so additional bearing covers were constructed from aluminium to eliminate the risk of the forced air cooling method dislodging the carefully measured bearing grease which was inserted in to the bearings. As angular contact ball bearings were chosen, a preload should be applied to improve the rigidity of the shaft. This was accomplished by the addition of an EMO EPL42 waved washer to give a 112N preload to the bearing.



Figure 6.4 – Shaft and rotor assembly with nut and washer arrangement



Figure 6.5 – View of the green weighting material used to balance the rotor assembly

#### 6.2.4 MACHINE CASING

Having established an overall length of the wound stator of 220mm, the axial length of the cylindrical section of the casing was set to 234mm. The casing was manufactured in aluminium through a combination of wire-erosion, milling and turning. A finned arrangement was used on the outside of the casing as shown in Figure 6.6. This increases the surface area and hence enhances heat transfer from the machine to the forced air. Two Mil-Standard connectors were incorporated in to the top-mounted termination block, as seen in Figure 6.7, to connect the power winding to the load bank and the control winding to the converter. On the other side of the termination block in Figure 6.8, 10 panel mount thermocouple connectors were incorporated to connect the embedded thermocouples to the data logging equipment used externally to the test cell.

The end-plates of the casing, which were also manufactured from aluminium, included a series of apertures which could be used to direct forced-air cooling into the stator, e.g. by using a conical cowling.

The whole casing, comprising of 14 pieces, was anodised to increase the corrosion resistance of the surface. Figure 6.9 shows the various casing components both before and after the anodising process.

Table 6.4 contains the key component weights of the demonstrator BDFRM with the active mass accounting for the rotor and stator laminations as well as both of the windings. The total machine mass is the final mass of the completed demonstrator before being fitted to the dynamometer.



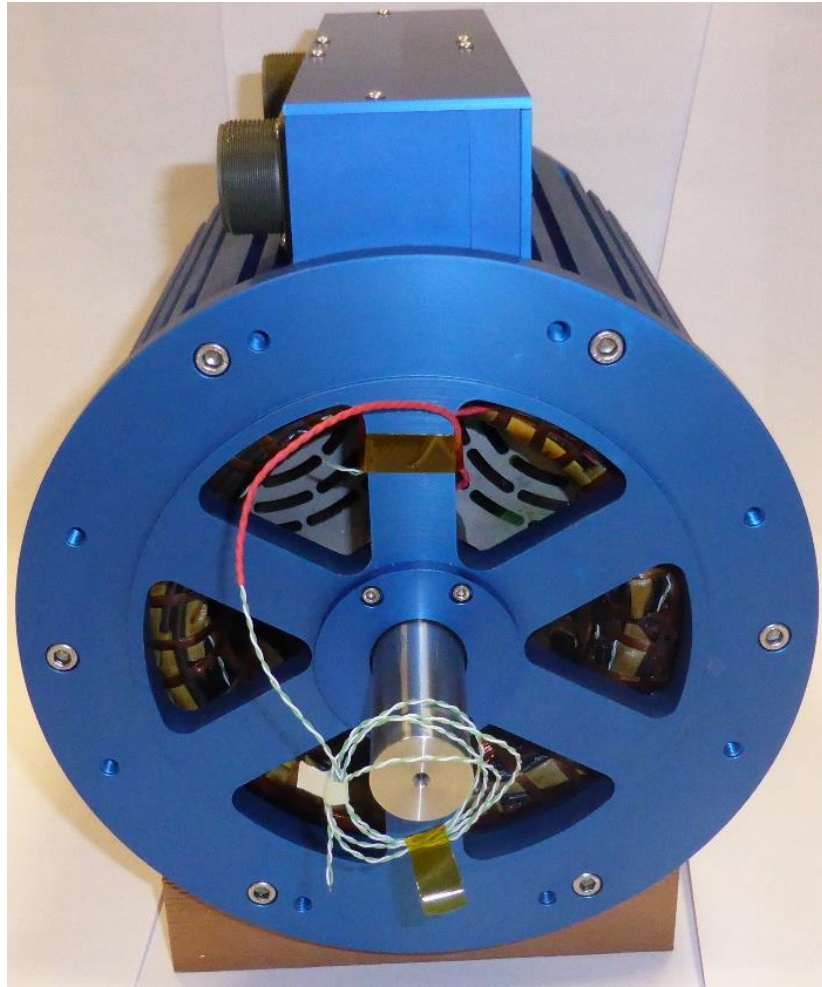


Figure 6.6 – End-plate view of assembled demonstrator



Figure 6.7 – The control and power winding Mil-Standard connectors

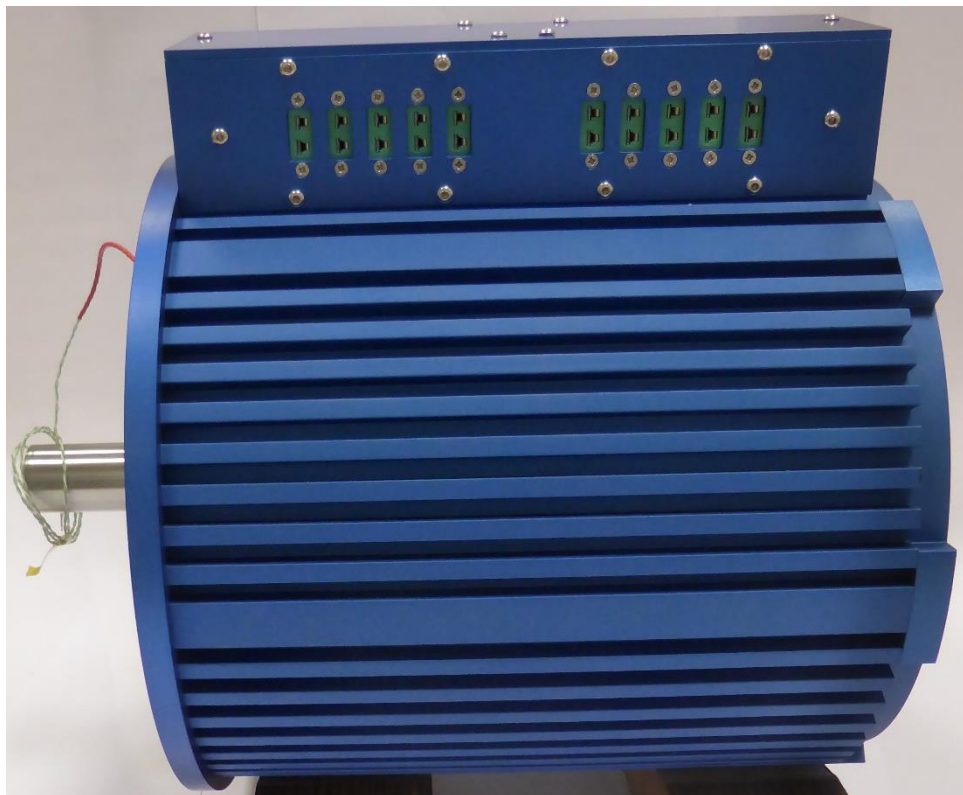


Figure 6.8 – The 10 thermocouple panel mount connectors

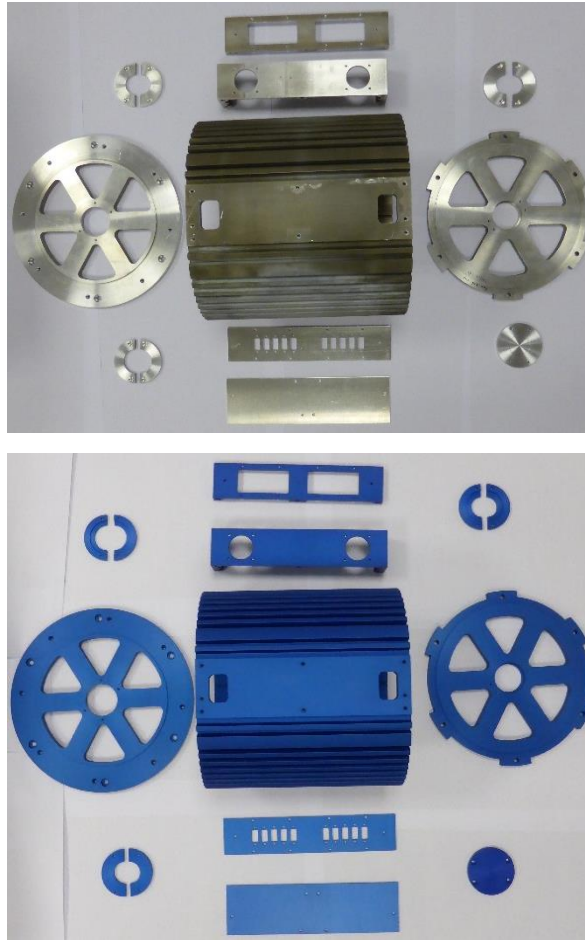


Figure 6.9 – The deconstructed casing before and after anodising

Table 6.4 – Measured weights of the various demonstrator components

Component	Mass (kg)
Stator laminations	12.66
Rotor laminations	4.96
Stator windings	6.00
Rotor shaft	1.79
Casing	8.40
<b>Total active mass</b>	<b>23.62</b>
<b>Total machine mass</b>	<b>33.81</b>

### 6.3 TESTING FACILITY

Figure 6.10 shows a block diagram of the testing arrangement used to measure the performance of the demonstrator. This provides an overview of how both the power and measurement channels are arranged.

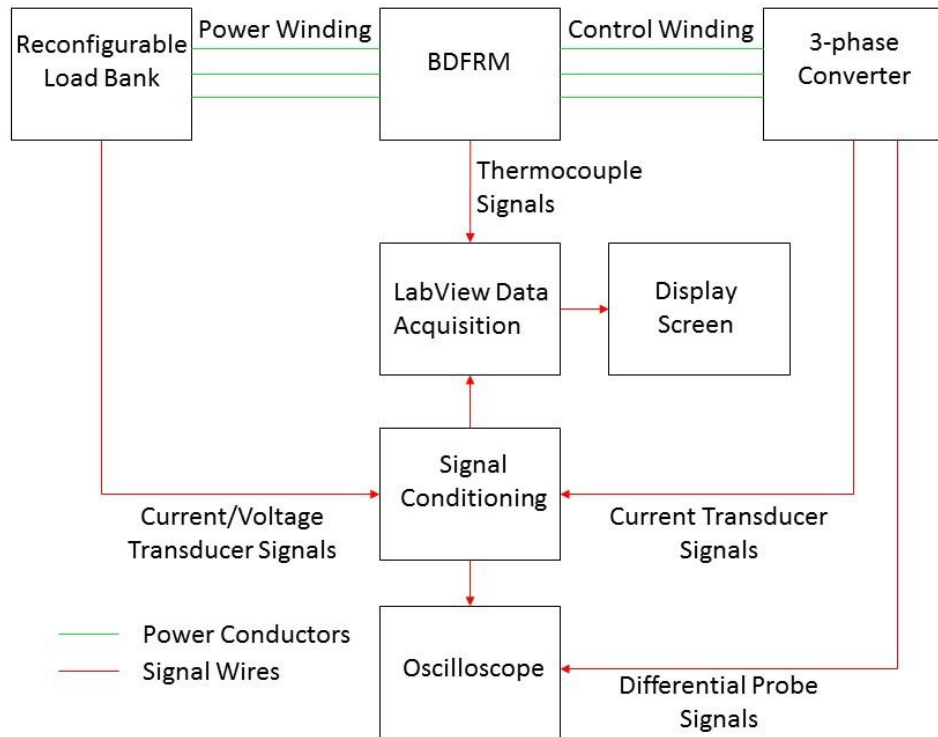


Figure 6.10 – Block diagram of the testing arrangement

### 6.3.1 AVL APA 102 DYNAMOMETER

The BDFRM demonstrator is coupled to the AVL dynamometer which provides both 4 quadrant torque-speed capability and built-in torque measurement. The torque-speed curve of the dynamometer is shown in Figure 6.11 along with the predicted operational envelope for the BDFRM demonstrator. As will be apparent the operating range fits comfortably inside the limits of the dynamometer. The torque is measured from the dynamometer display screen to an accuracy of 0.3%. For all of the tests performed, the dynamometer was operated in speed control mode.

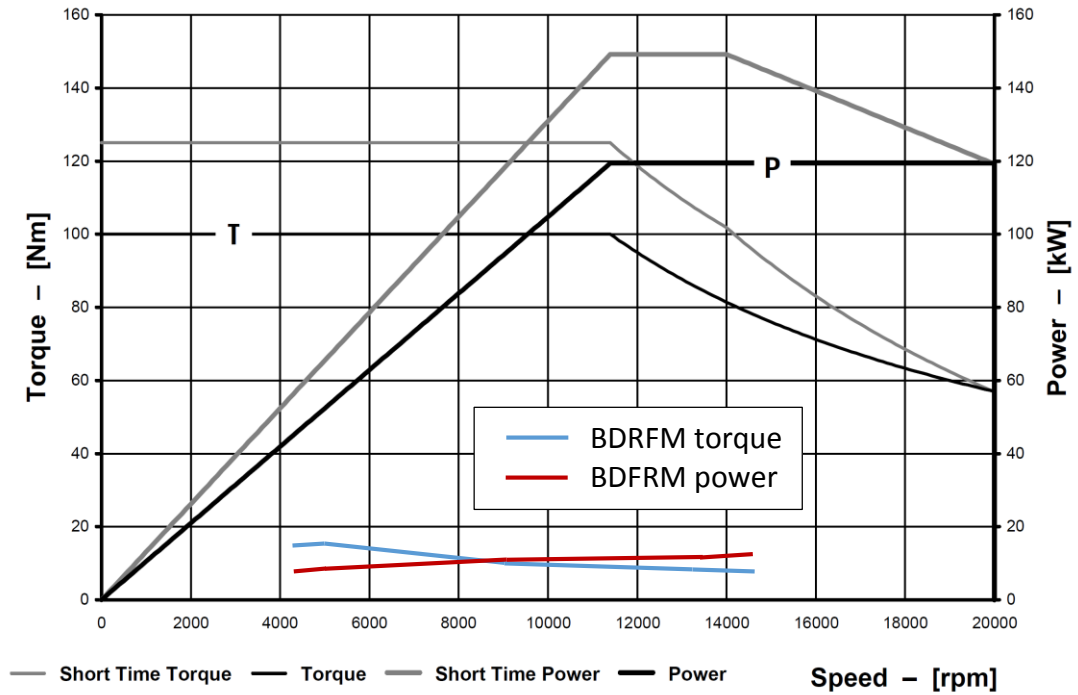


Figure 6.11 – Torque-speed curve of the AVL APA 102 dynamometer with the BDFRM demonstrator torque and power

### 6.3.2 LOAD BANK

In order to load the power winding of the BDFRM, the custom three-phase load bank shown in Figure 6.12 was designed and constructed. It includes a series of 6 power resistors per phase with the resistance values and power ratings summarised in Table 6.5. The load bank can be reconfigured by hard-wiring the resistors into groups to produce a range of discrete three-phase power ratings. For example, considering the operating point at 10% above the speed range (13,200rpm), the optimum load resistance was found (through finite element calculations) to be  $3.7\Omega$  so the resistor bank was configured to give this value as well as  $3.6\Omega$  and  $3.9\Omega$ . This ensured that  $3.7\Omega$  was in fact the optimum resistance for this operating point to provide maximum power with the required phase voltage.

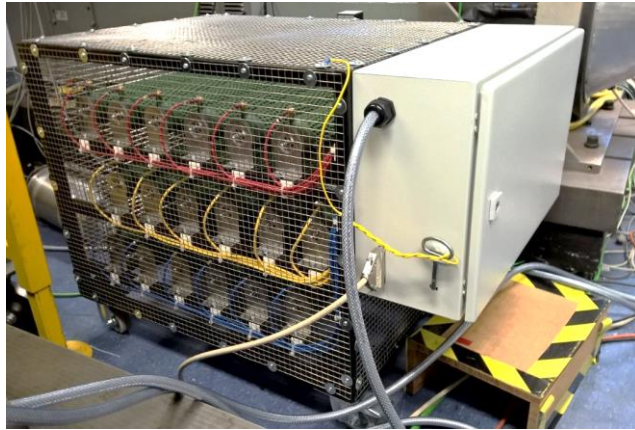


Figure 6.12 – Load bank external view

Table 6.5 Resistances per phase and power ratings of load bank

Resistance value ( $\Omega$ )	Number per phase	Power rating per resistor (kW)
1.0	1	2
2.2	2	2
4.7	1	2
10.0	2	2

### 6.3.3 POWER WINDING VOLTAGE AND CURRENT MEASUREMENT

In order to measure the BDRFM power winding voltage and current waveforms, three current transducers (LEM LA125-P rated at 141A<sub>rms</sub>) and three voltage transducers (LEM LV25-P rated at 212V<sub>rms</sub>) were incorporated into the load-bank, as seen in Figure 6.13.

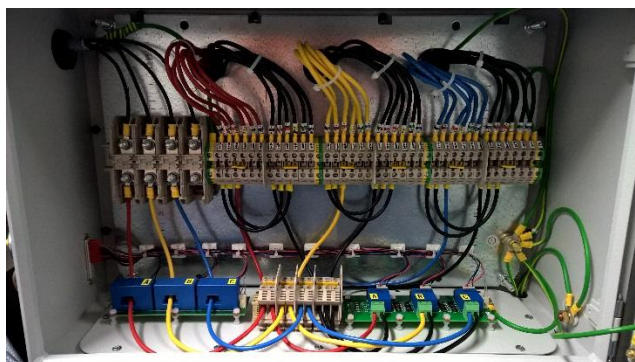


Figure 6.13 – Inside view of the load bank measurement and connection box

#### 6.3.4 CONTROL WINDING POWER CONVERTER

The converter used in the testing is a Control Techniques Unidrive SP2403 converter. The cabinet, which is shown in Figure 6.14 is part of a reconfigured cabinet used for a previous project. The main specifications of the Unidrive SP2403 are shown in Table 6.6.

Regarding these parameters, it is apparent that the BDFRM will not be able to run to its maximum calculated power due to limits in the current and voltage that would be needed to provide the predominantly reactive power for the control winding. None the less, a substantial set of results can still be acquired using this converter rig.

The SP2403 can be operated in several control modes:

- Open loop mode
  - Open loop vector mode
  - Fixed V/F mode
  - Quadratic V/F mode
- Rotor flux control mode
- Closed loop vector mode
- Servo mode
- Regen mode

For the purposes of this testing schedule a simple open loop control mode was used to avoid the need for position or speed feedback. The torque demand which corresponds to the control winding current magnitude alongside the frequency will be controlled from outside of the test cell via Ethernet connection using CTSOft software.

The cabinet contains three LEM LA125-P current transducers (rated current  $141A_{rms}$ ) and a pair of Tektronix P5210 differential voltage probes which are used to measure two of the three phase-to-neutral voltages produced by the converter (Figure 6.15).

Table 6.6 – Key operating parameters of the Control Techniques SP2403 converter [1]

<b>Parameter</b>	<b>Value</b>
<b>Voltage rating (V)</b>	400
<b>Max continuous output current (A)</b>	29
<b>Peak current (A)</b>	31
<b>Nominal power at 400 V (kW)</b>	15



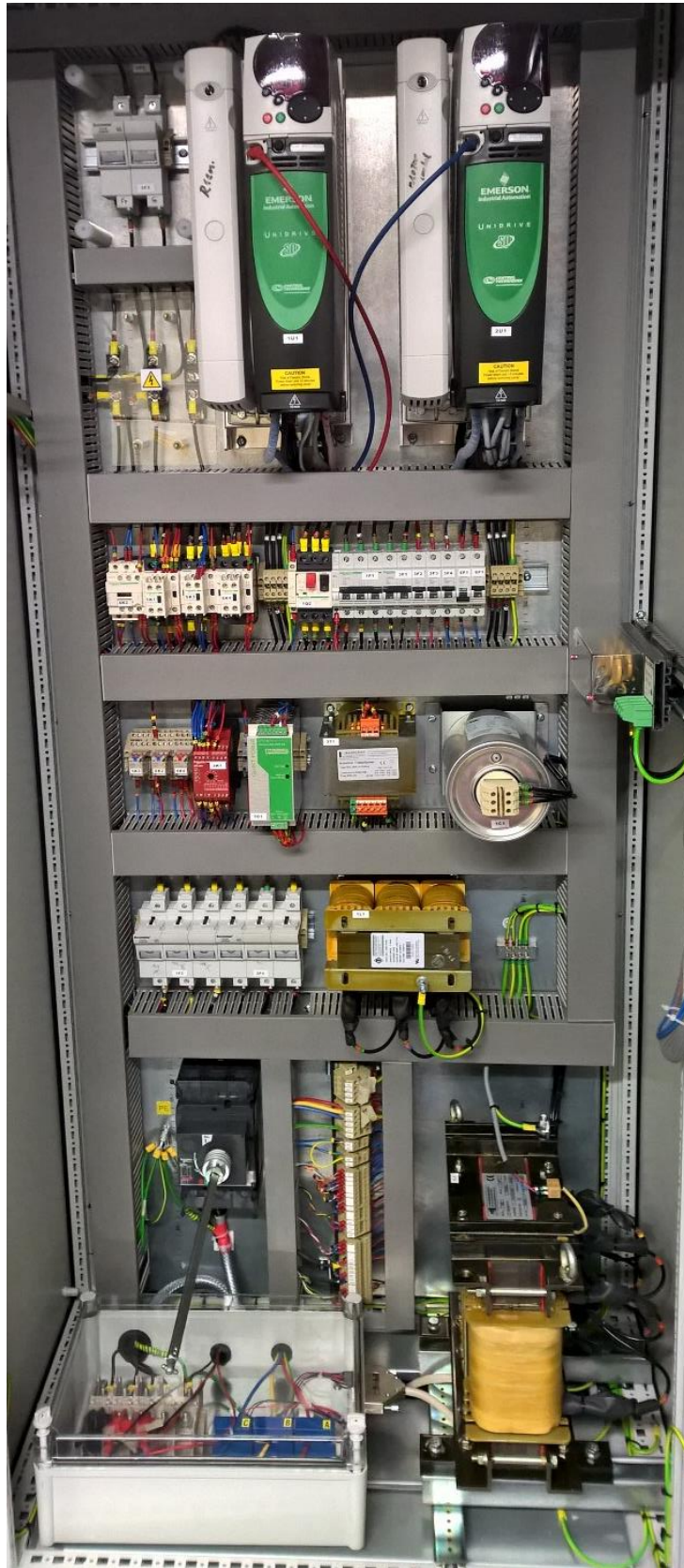


Figure 6.14 – Converter rig used in testing

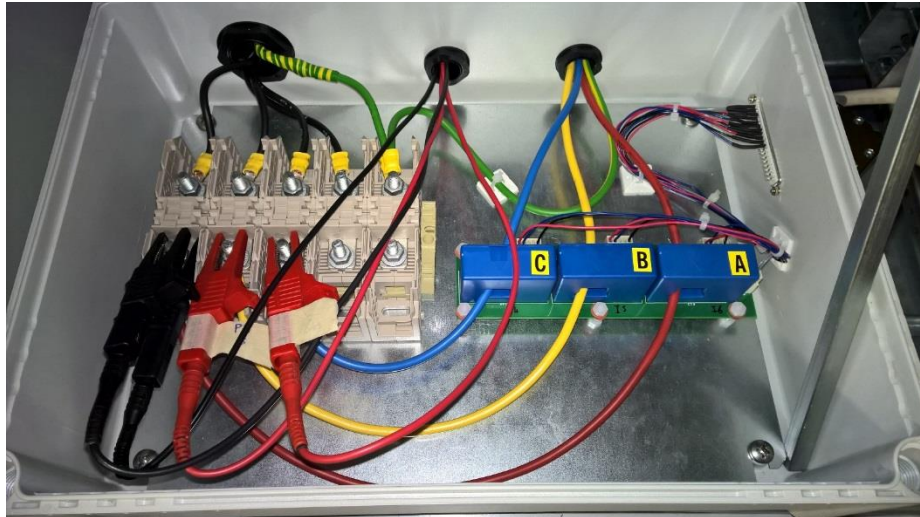


Figure 6.15 – Voltage and current measurements at the output of the converter

### 6.3.5 SIGNAL CONDITIONING

To condition the nine signals from the 3 power winding voltage transducers and the 6 current transducers, a signal processing PCB was designed and constructed as shown in Figure 6.16. This PCB incorporates Sallen-Key filters and unity gain op-amps to allow the current transducer to be displayed on a standard oscilloscope (Figure 6.17). The Sallen-Key filter was designed with a corner frequency of over 4kHz which is much higher than the fundamental frequency of either winding and any harmonics which would be of interest to this thesis. As the oscilloscope only has eight differential analogue inputs, 3 of the total 11 (9 transducer signals and 2 differential probe signals) outputs are fed into a LabView system so that all of the machine time-varying quantities can be displayed and recorded.

The LabView system also reads in and records the 10 values of temperature measured in and around the machine using the thermocouples discussed previously in Section 6.2.2. The thermocouple voltages are connected to a NI SCXI conditioning unit via a NI TC-2095 connector rack. The voltages which are to be recorded by the LabView script are input to a NI BNC-2110 connector block. The conditioning unit and connector block are then connected to a NI PXI-1000B, on which the LabView script to display and record the data is run.

A summary of the various measurements performed is shown in Table 6.7.

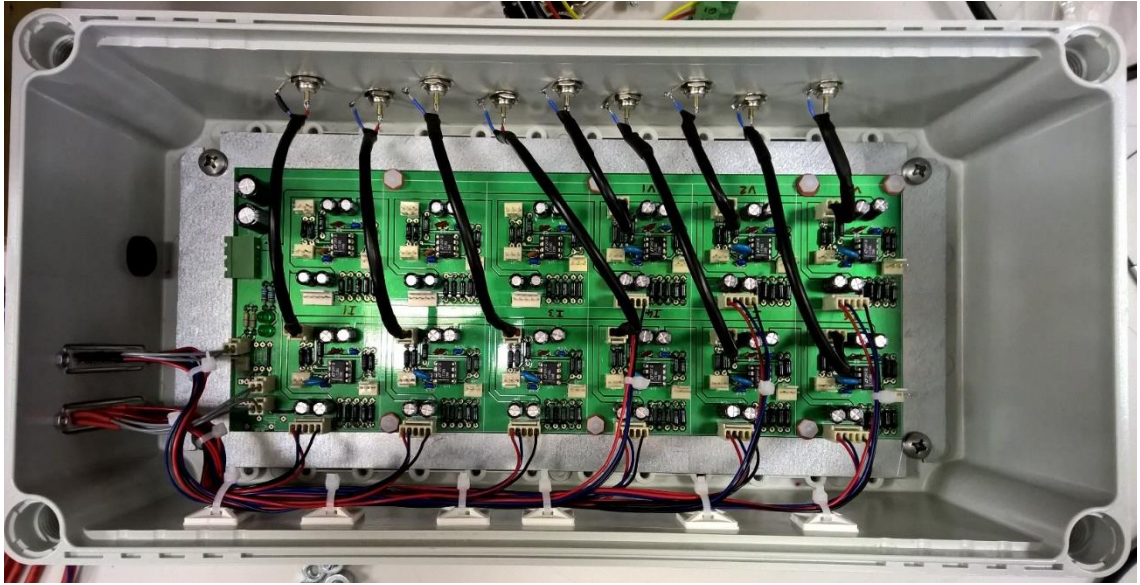


Figure 6.16 – PCB utilised for signal conditioning purposes

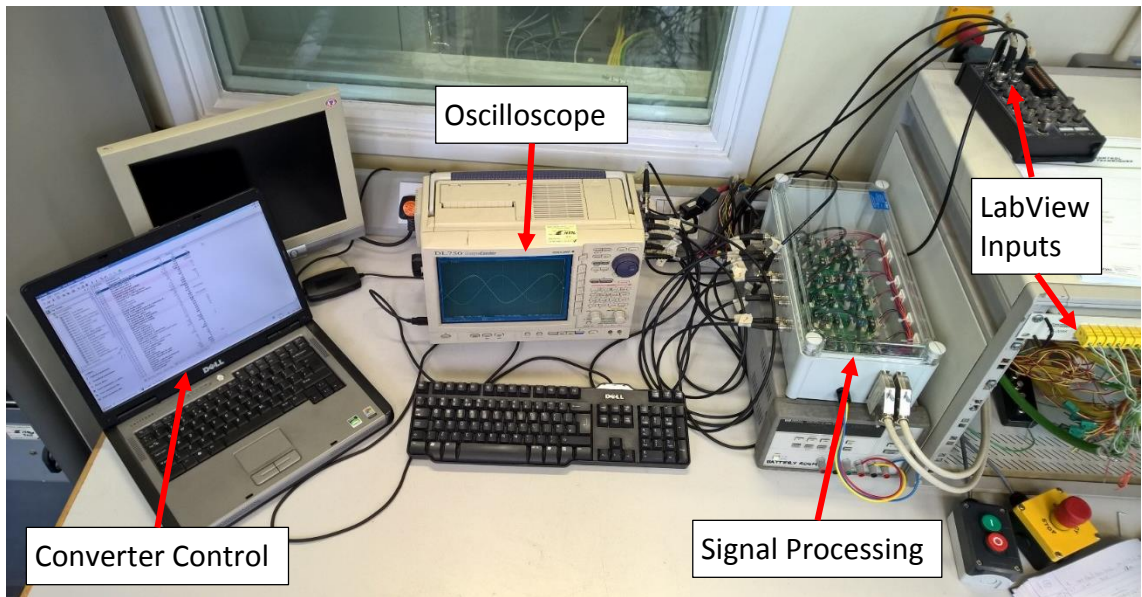


Figure 6.17 – Experimental set up for the signal processing, measurement display and converter control

Table 6.7 – A summary of the various measurements performed

Quantity	Sensor	Measurement range	Nominal accuracy	Data logging
Power winding phase voltage	LEM LV25-P voltage transducer	10-500V	±0.9%	Labview/ Oscilloscope waveform save
Power winding phase current	LEM LA125-P current transducer	0-300A	±0.6%	Labview/ Oscilloscope waveform save
Control winding phase voltage	LEM LV25-P voltage transducer	10-500V	±0.9%	Labview/ Oscilloscope waveform save
Control winding phase current	LEM LA125-P current transducer	0-300A	±0.6%	Labview/ Oscilloscope waveform save
Temperatures	k-type thermocouples	-50 to +1100 °C	±1.5°C	LabView
Torque	Dynamometer internal strain gauge	±125Nm	±0.3%	Manually observed and recorded

#### 6.4 BASELINE PERFORMANCE MEASUREMENTS

For the preliminary test results, the magnitude of the converter output current is purely incidental with only the output frequency controlled. For each test point the rated load resistance and two values around the rated value will be used to act as a load. This will ensure that a range of output voltages may be measured.

Two preliminary test points will be discussed in detail, with the rest of the results placed in a table and commented on.

#### 6.4.1 TEST POINT AT 20% BELOW SYNCHRONOUS SPEED RANGE (4,320 RPM)

At this test point, the rotational speed is set and controlled by the dynamometer to a fixed 4,320rpm, a speed which corresponds to a synchronous frequency of 288Hz, i.e. 20% below the 360Hz lower limit of the VF standard. With a 72Hz control current, the power winding output frequency is corrected to 360Hz.

At this operating speed and frequency correction, the three nominal load resistance values chosen were 4.3Ω, 4.7Ω and 5.0Ω. The actual measured resistance (including cables etc.) were 4.40Ω, 4.77Ω and 5.05Ω.

For this initial set of results, the converter connected to the control winding was operated in a closed-loop current control mode using the internal current controller and its default factory set gains. The nominal sinusoidal current set-point was set to 100% of the maximum rating at a frequency of 72Hz, which corresponds to a set point of 20.24A<sub>rms</sub>. The resulting measured control winding current for the particular case of a power winding load resistance of 4.40Ω, 4.77Ω and 5.05Ω for phase A, B and C respectively are shown in Figure 6.18. The rms current of 20.24A corresponds to a control winding current density of 11.62A<sub>rms</sub>mm<sup>-2</sup>. Figure 6.19 provides a Fourier transform of the control winding current found in Figure 6.18 which shows the higher harmonics present due to the voltage waveform. As will be evident, although the closed-loop current controller tracks the sinusoidal demand reasonably well, it does struggle to accommodate the significant harmonics at ~500Hz. This particular harmonic is also a dominant harmonic, among others, in the control winding FE calculated voltage at this 20% below the synchronous range test point, with Figure 6.20 providing an FFT of this waveform. This suggests that the ~500Hz harmonic could be due to the complex coupling process within this machine and is approximated by summing the power winding frequency and twice the control winding frequency, viz.  $360Hz + (2 \times 72Hz) = 504Hz$ .

The resulting measured 3-phase power winding voltages on this 4.7Ω load point are shown in Figure 6.21. With a 72Hz control winding frequency and the rotor rotating at 4,320rpm, measured power winding frequency is 360Hz as expected, thus confirming the basic operating behaviour of the BDFRM as a frequency modulator.

One notable feature of the voltage waveform of Figure 6.21 is the asymmetry between phases which is likely to be due to a low frequency subharmonic as will be discussed in Section 6.6. This is seen in the FFT chart of Figure 6.22 and is due to the third harmonic in the flux produced by the control winding.

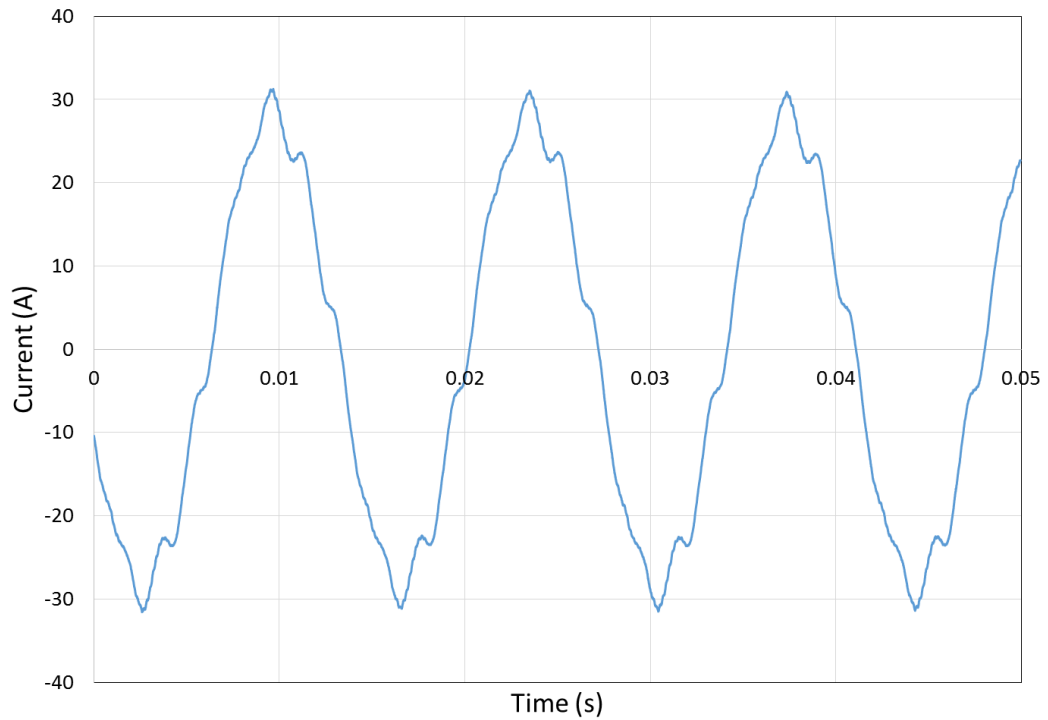


Figure 6.18 – Measured phase A control winding current for 20% frequency correction at the lower end of the synchronous range (4,320rpm) and a power winding load resistance of 4.40 $\Omega$ , 4.77 $\Omega$  and 5.05 $\Omega$  for phase A, B and C respectively

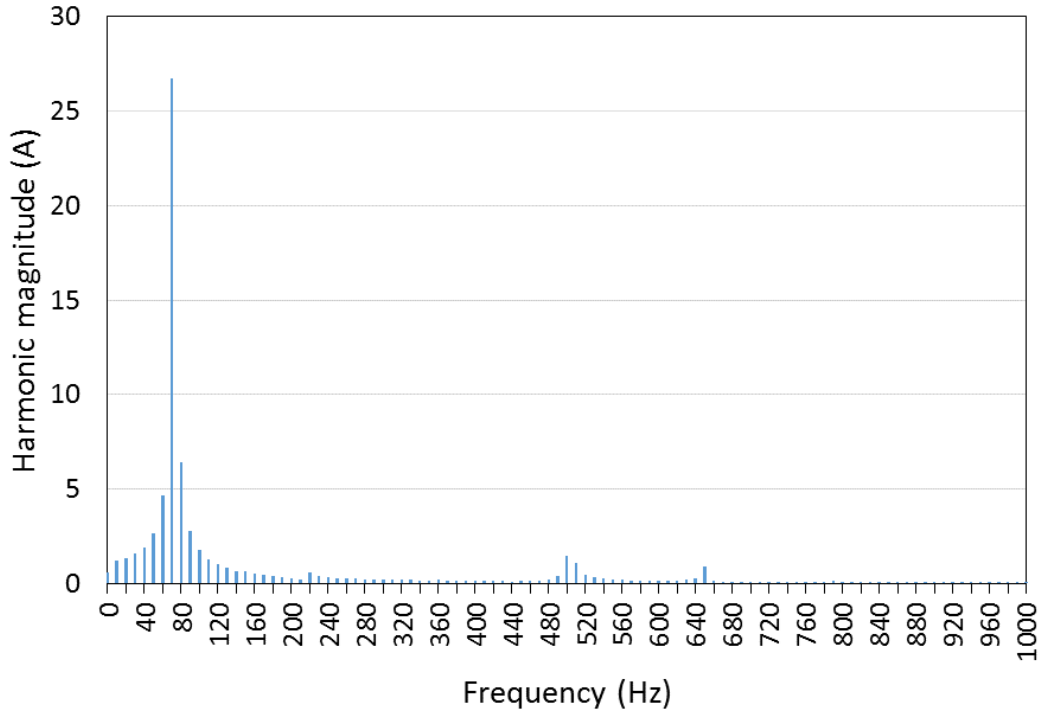


Figure 6.19 – FFT of measured phase A control winding current (Figure 6.18) for 20% frequency correction at the lower end of the synchronous range (4,320rpm) and a power winding load resistance of 4.40Ω, 4.77Ω and 5.05Ω for phase A, B and C respectively

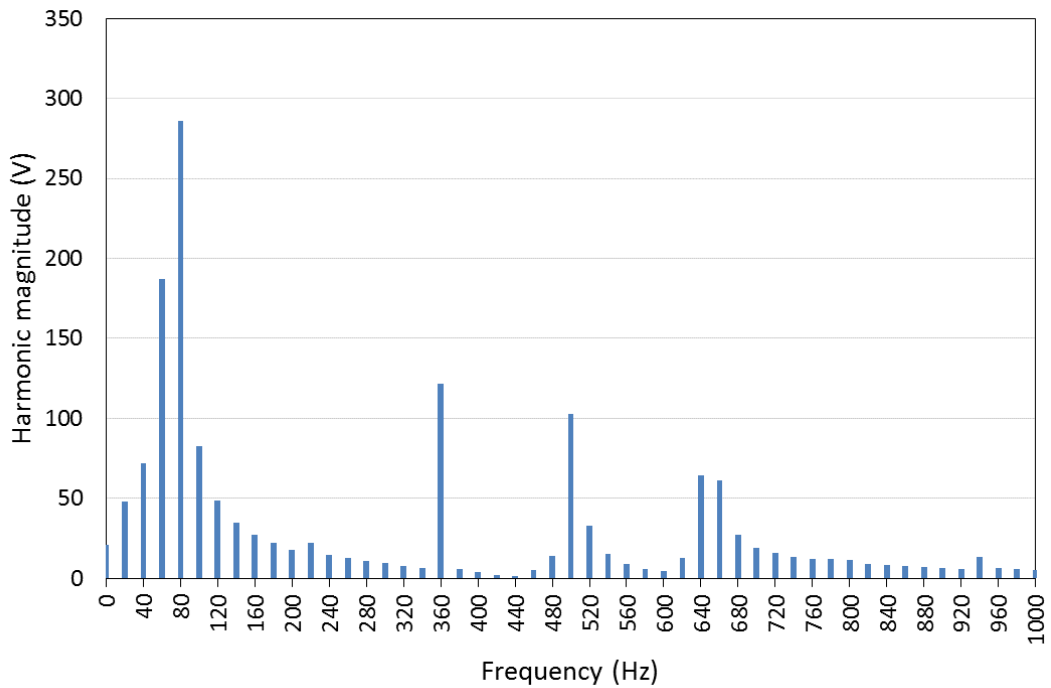


Figure 6.20 – FFT of FE predicted phase A control winding voltage for 20% frequency correction at the lower end of the synchronous range (4,320rpm) with sinusoidal control current at a current density of  $14.14A_{rms}mm^{-2}$  and a power winding load resistance of 4.7Ω

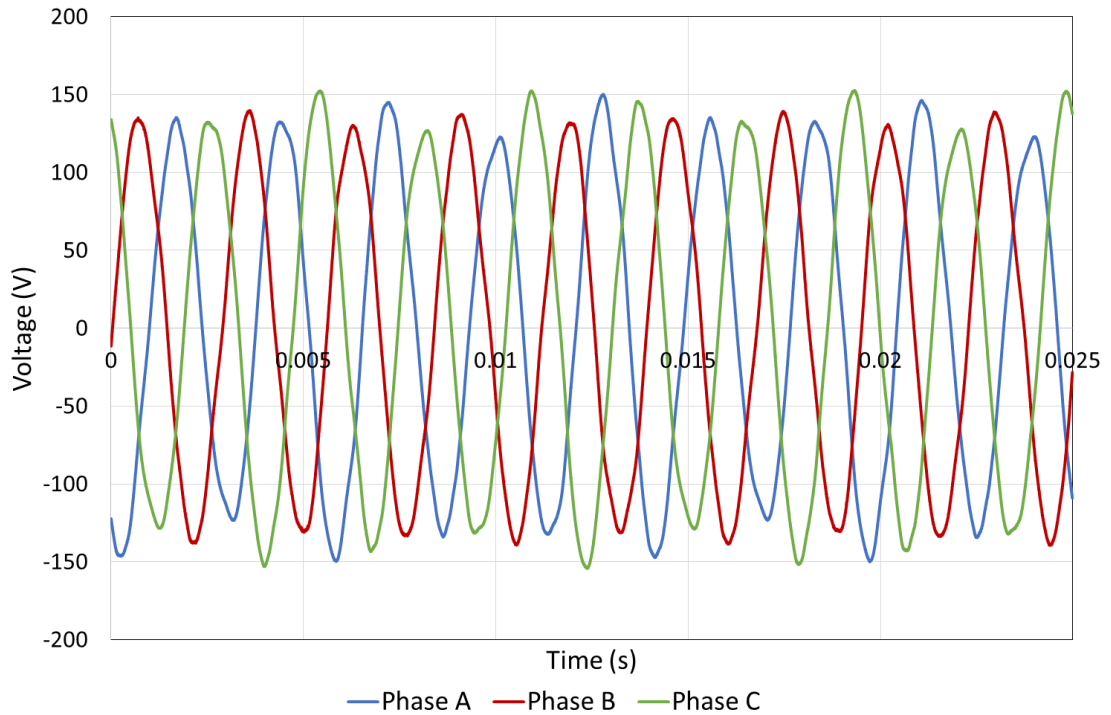


Figure 6.21 – Measured power winding voltage waveforms for 20% frequency correction from 4,320rpm with a power winding load resistance of 4.40Ω, 4.77Ω and 5.05Ω for phase A, B and C respectively and control winding current of Figure 6.18

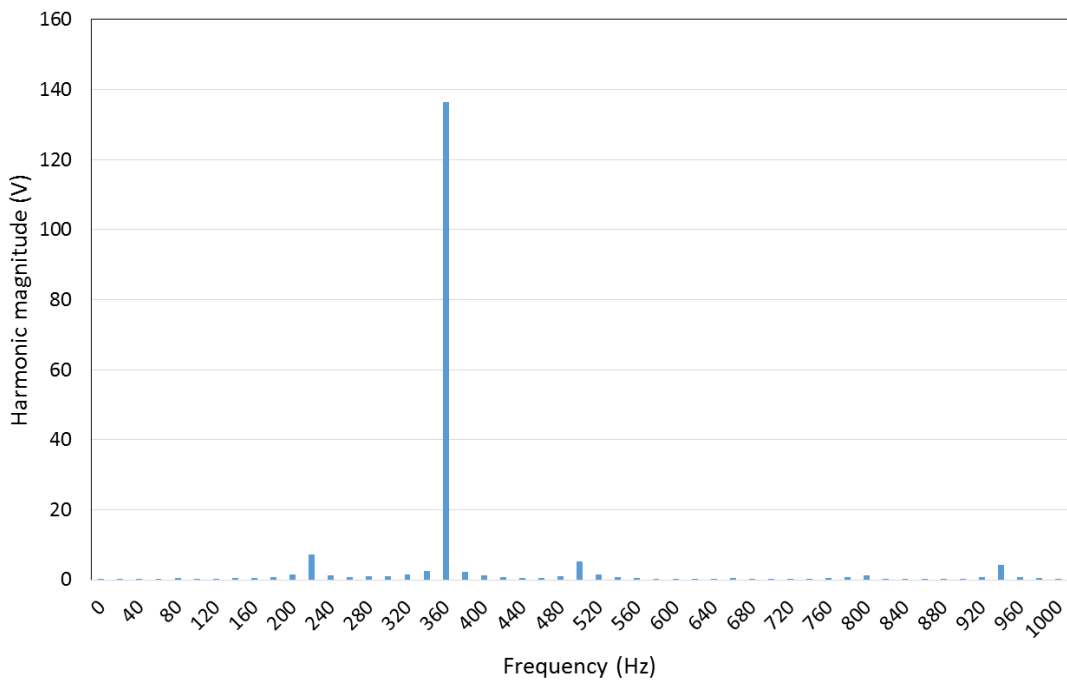


Figure 6.22 – Measured FFT of power winding phase A voltage waveform (Figure 6.21) for 20% frequency correction at 4,320rpm with a power winding load resistance of 4.40Ω, 4.77Ω and 5.05Ω for phase A, B and C respectively and control winding current of Figure 6.18



These measurements were repeated for the remaining values of load resistance of  $4.3\Omega$  and  $5.0\Omega$ , using the same converter voltage set point and frequency. Table 6.8 shows a summary of the measured performance. As will be apparent, all three power winding voltages in column 2 of Table 6.8 are below the VF voltage range. Therefore, to place this test point within the VF standard voltage magnitude range, a higher resistance would be required to increase this voltage further.

Table 6.8 – Summary of measured power winding performance for a test point at 20% below the synchronous speed range (4,320rpm)

Load resistance ( $\Omega$ )	Phase A power winding voltage ( $V_{rms}$ )	Phase A power winding current ( $A_{rms}$ )	3-phase power winding power (kW)
4.3	91.2	20.5	5.6
4.7	96.7	19.8	5.8
5.0	101.2	19.6	5.9

#### 6.4.2 TEST POINT AT 20% ABOVE SYNCHRONOUS SPEED RANGE (14,400RPM)

In this case, a correction of 20% at the upper end of the VF frequency range corresponds to a rotational speed of 14,400rpm, i.e. the maximum speed used for mechanical design in Chapter 5. In this case, a 160Hz control current waveform is required to ensure a maximum frequency of 800Hz in the power winding. Unfortunately, the maximum rated voltage of the converter is such that the peak current at this high speed operating point is limited compared to the current which can be achieved at lower speeds, specifically to a maximum of  $3.96A_{rms}$  as shown in Figure 6.23, which corresponds to a control current density of  $2.27A_{rms}mm^{-2}$ . This is thought to be due to a higher EMF and reactance at this higher frequency operating point, thus leading to a reduction in the current. As was the case in the test point considered in Section 6.4.1 the closed loop current controller is unable to impose a true sinusoidal current. As is evident from the corresponding FFT in Figure 6.24, the major harmonic content is at 480Hz and 1,120Hz. The 480Hz can be attributed to a saturation induced 3<sup>rd</sup> harmonic of the 160Hz fundamental. The 1,120Hz harmonic has parallels with the test point of Section 6.4.1 in which a 500Hz component was

significant, again being the sum of the power winding frequency and twice the control winding frequency, viz.  $800\text{Hz} + (2 \times 160\text{Hz}) = 1,120\text{Hz}$ .

The resulting measured power winding waveform for this control winding current waveform is shown in Figure 6.25, which again demonstrates the basic frequency correction functionality of this machine and the presence of significant sub-harmonics in the FFT of this waveform in Figure 6.26. A summary of performance for the 3 values of load resistance is shown in Table 6.9.

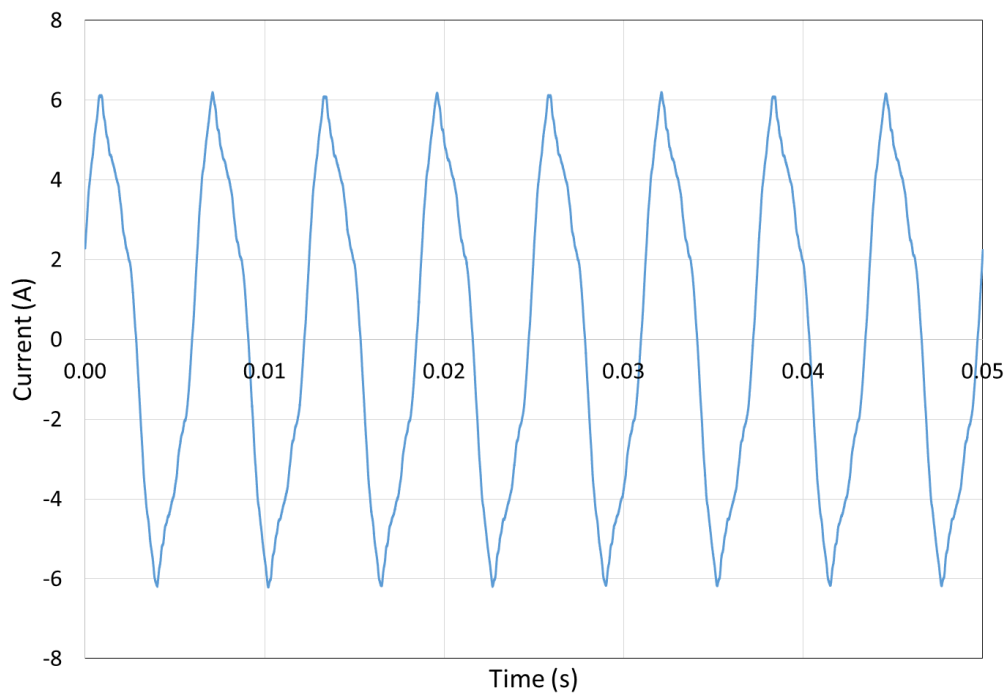


Figure 6.23 – Measured control winding phase A current for 20% frequency correction at the upper end of the synchronous range (14,400rpm) with a power winding load resistance of  $3.77\Omega$ ,  $3.77\Omega$  and  $3.80\Omega$  for phase A, B and C respectively

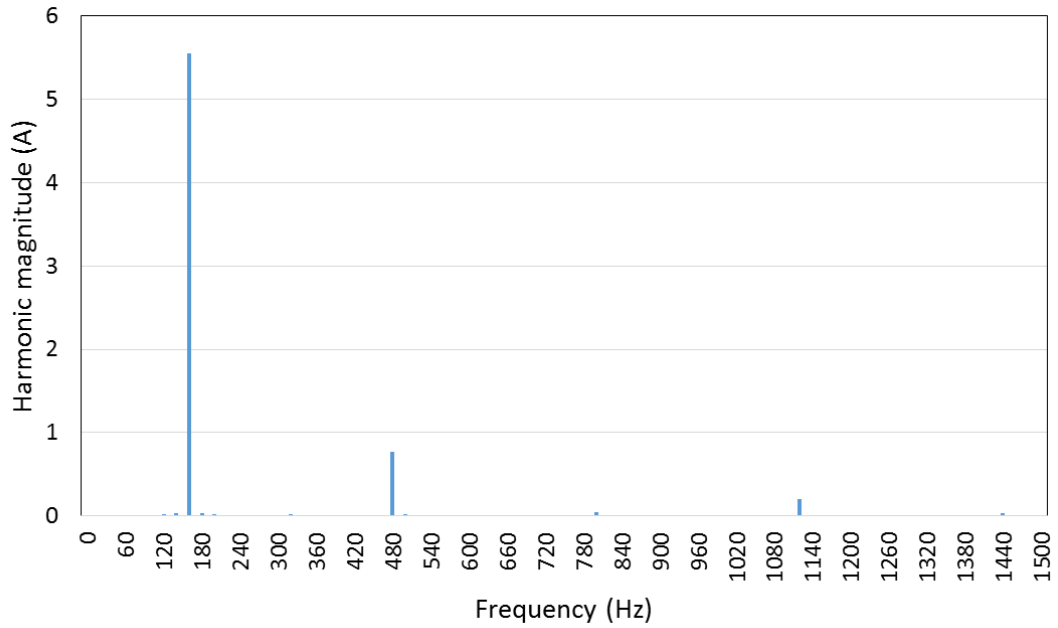


Figure 6.24 – Measured FFT of control winding phase A current in Figure 6.23 for a 20% frequency correction at the upper end of the synchronous range (14,400rpm) with a power winding load resistance of  $3.77\Omega$ ,  $3.77\Omega$  and  $3.80\Omega$  for phase A, B and C respectively

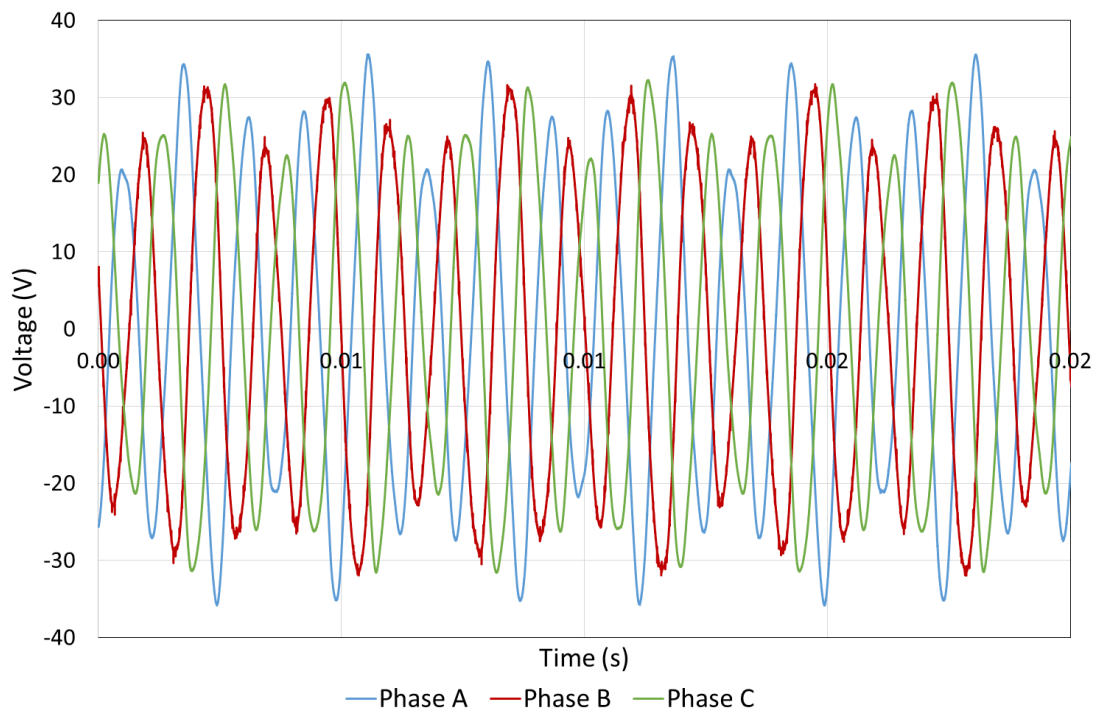


Figure 6.25 – Measured power winding voltage waveforms for 20% frequency correction from 14,400rpm with a power winding load resistance of  $3.77\Omega$ ,  $3.77\Omega$  and  $3.80\Omega$  for phase A, B and C respectively and a control winding current of Figure 6.23

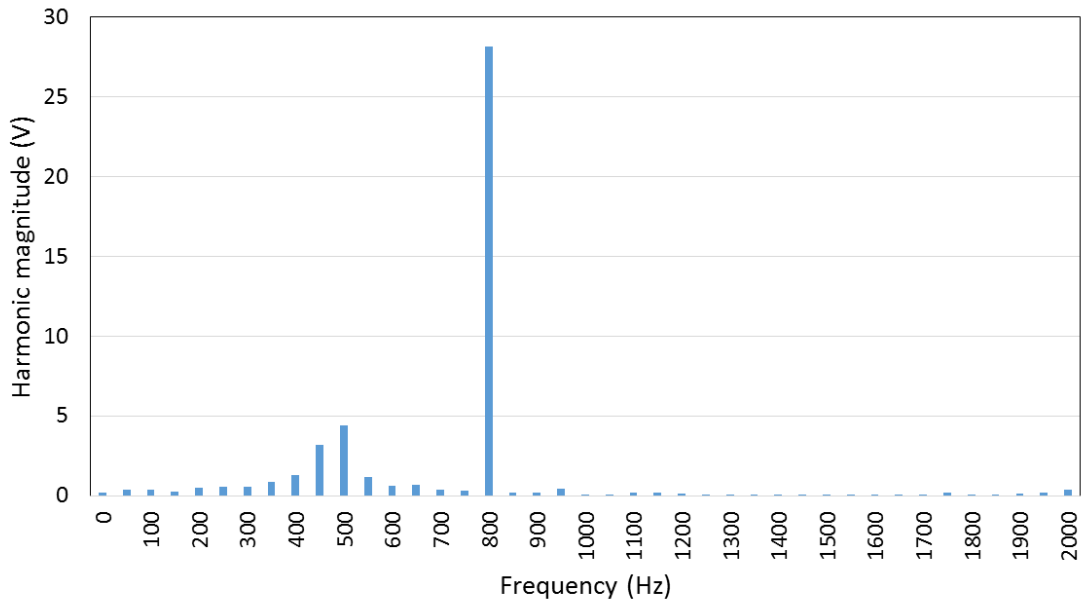


Figure 6.26 – FFT of measured phase A power winding voltage in Figure 6.25 for 20% frequency correction at 14,400rpm with a power winding load resistance of 3.77Ω, 3.77Ω and 3.80Ω for phase A, B and C respectively and a control winding current of Figure 6.23

Table 6.9 – Measured power winding characteristics for a test point at 20% above the synchronous speed

Load resistance (Ω)	Phase A power winding voltage (V <sub>rms</sub> )	Phase A power winding current (A <sub>rms</sub> )	3-phase power winding power (kW)
3.6	20.1	5.4	0.4
3.7	20.5	5.4	0.3
3.9	21.4	5.4	0.3

## 6.5 COMPARISON OF MEASURED RESULTS WITH FINITE ELEMENT PREDICTIONS

Whereas the operating points considered in Section 6.4 provided initial verification of the key behaviour of the demonstrator BDFRM, they do not provide a basis for direct comparison with the finite element models. To provide a more meaningful comparison, further simulations and measurements were performed on the basis of more comparable control winding current waveforms.

Two operating points were considered for a comparison between measured and finite element predictions at 10% above the VF range and 10% below the VF range. This corresponds to a rotor speed of 13,200rpm and 4,860rpm respectively, with a

control winding frequency of 80Hz and 36Hz respectively, to bring the power winding output frequency into the VF range of 360-800Hz.

As shown previously, the form of the control winding current which can be achieved in practice with the converter in the test-rig departs significantly from a sine-wave. Hence, in order to provide a direct comparison between measurements and finite element predictions, it is necessary to use the measured control current waveforms as an input to the time-stepped, electric-circuit coupled FEA model. Furthermore, the load resistances in the FEA model were also adjusted to match the net measured load resistances connected to the power winding terminals.

Unfortunately, at this point in the testing, the converter began to cause the wall-mounted 3-phase supply RCD to falsely trip due to the installed RCD being of the wrong type for this converter application. Thus the converter internal EMC filter was removed to reduce the surge current thought to be causing the trip error. Consequently, the converter now cannot operate at the high current densities such as those seen in Figure 6.18. This is not too much of an issue to the testing phase as in fact the control phase A current in Figure 6.18 is  $20.24A_{rms}$  which corresponds to a thermally unsustainable current density of  $11.63A_{rms}mm^{-2}$ .

#### 6.5.1 OPERATING POINT AT 13,200RPM

The measured control winding current waveform, which is used as an input to the finite element model, is shown in Figure 6.27. This current waveform corresponds to a peak current density of  $13.10Amm^{-2}$  and an RMS value of  $9.27Amm^{-2}$ .

A comparison between the measured and predicted power winding voltage waveforms for each phase are shown in Figure 6.28, Figure 6.29 and Figure 6.30 (for the purely resistive load, the power current waveforms are simply scaled versions of these waveforms). There is reasonable agreement in terms of the magnitude of the voltages, although there is some variation in this agreement between successive peaks. It is also apparent that the significant modulation of the peaks which is indicative of a substantial sub-harmonic is captured in both the measurements and the finite element model.

To obtain a more direct quantitative comparison of the harmonic content of the measured and FEA power winding voltage waveforms an FFT analysis was performed on the measured and predicted voltage waveforms of phase A, i.e. the waveforms shown in Figure 6.31. As expected there is a significant harmonic component at 240Hz (12.7% of the magnitude of the 800Hz fundamental) which can be attributed to the saturation induced 3<sup>rd</sup> harmonic of the control winding 80Hz current.

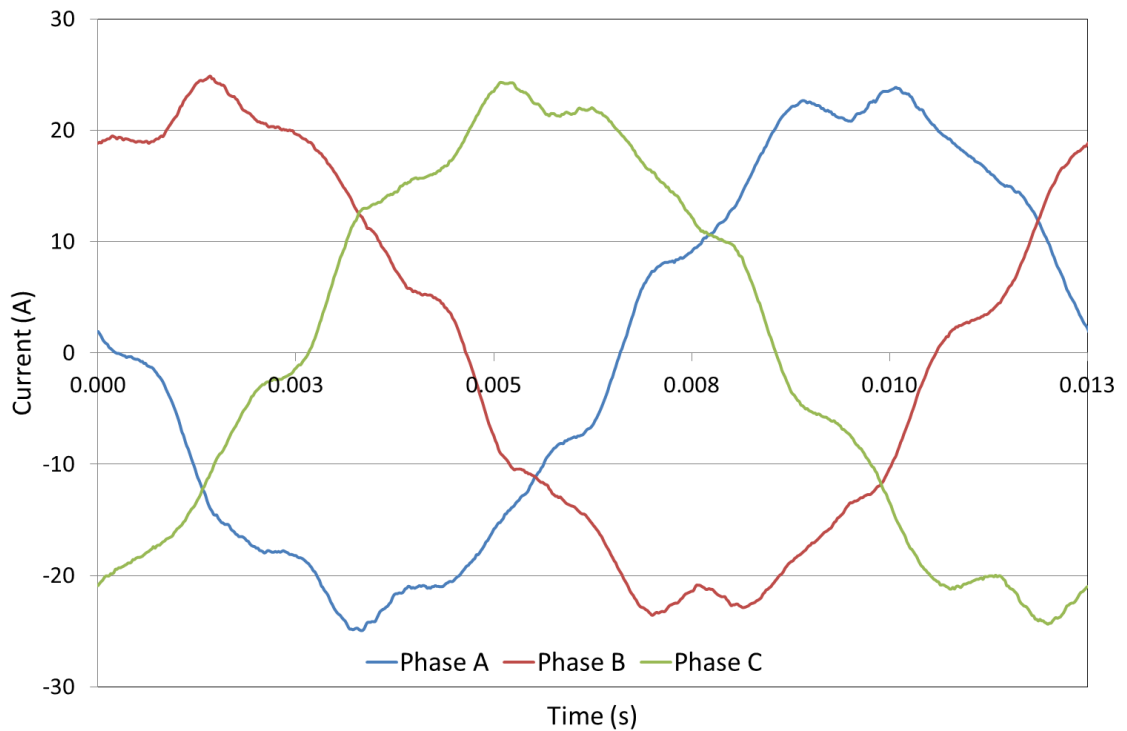


Figure 6.27 – Measured 3-phase control winding current used in FEA comparison for the test case of 10% above the VF range (13,200rpm) with load resistances of 3.77 $\Omega$ , 3.77 $\Omega$  and 3.79 $\Omega$  for phase A, B and C respectively

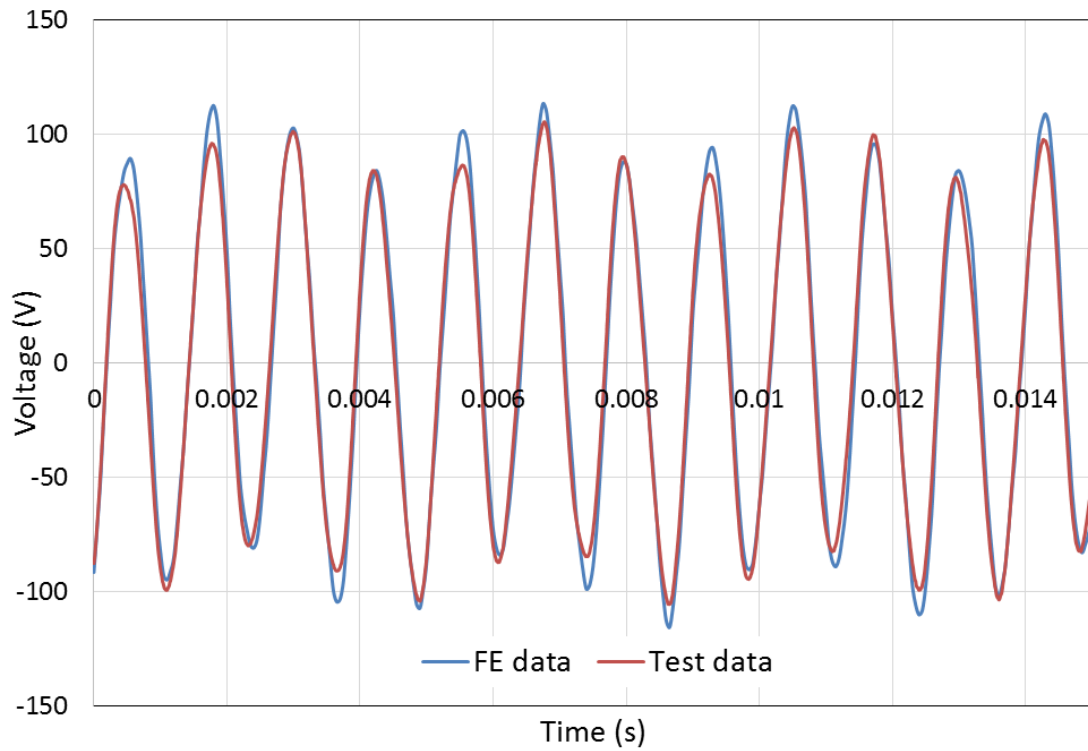


Figure 6.28 – FE predicted and test results of phase A load voltage for the test case of 10% above the VF range (13,200rpm) at a control winding current density of  $7.27A_{rms}/mm^2$  and a load resistance of  $3.77\Omega$ ,  $3.77\Omega$  and  $3.79\Omega$  for phase A, B and C respectively

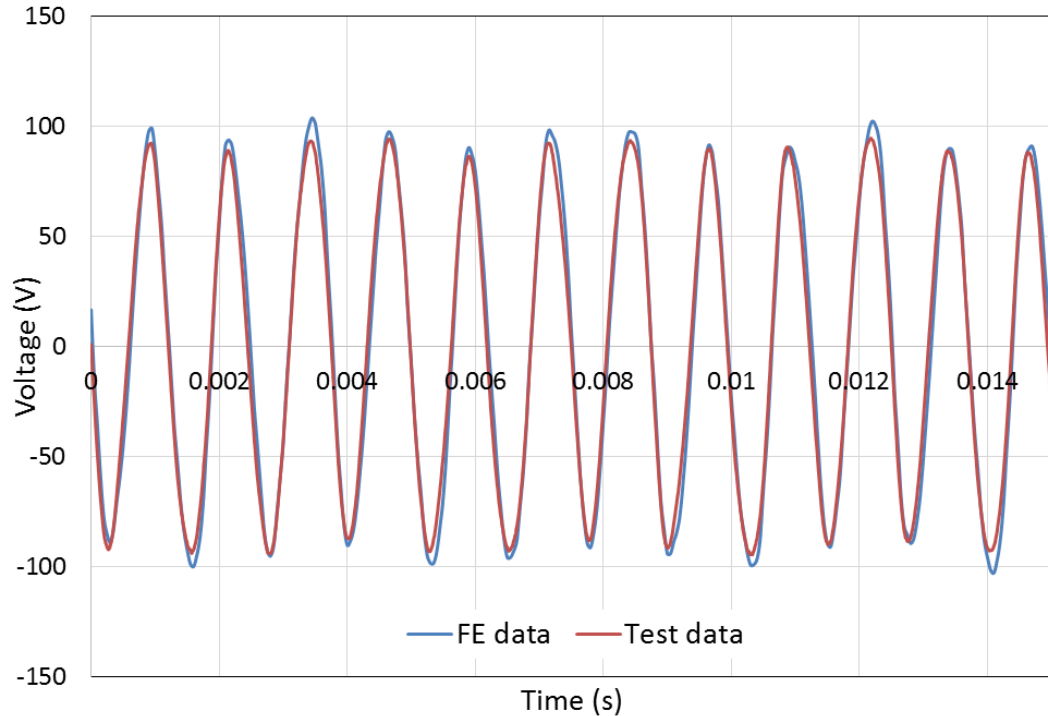


Figure 6.29 – FE predicted and test results of phase B load voltage for the test case of 10% above the VF range (13,200rpm) at a control winding current density of  $7.27A_{rms}/mm^2$  and a load resistance of  $3.77\Omega$ ,  $3.77\Omega$  and  $3.79\Omega$  for phase A, B and C respectively

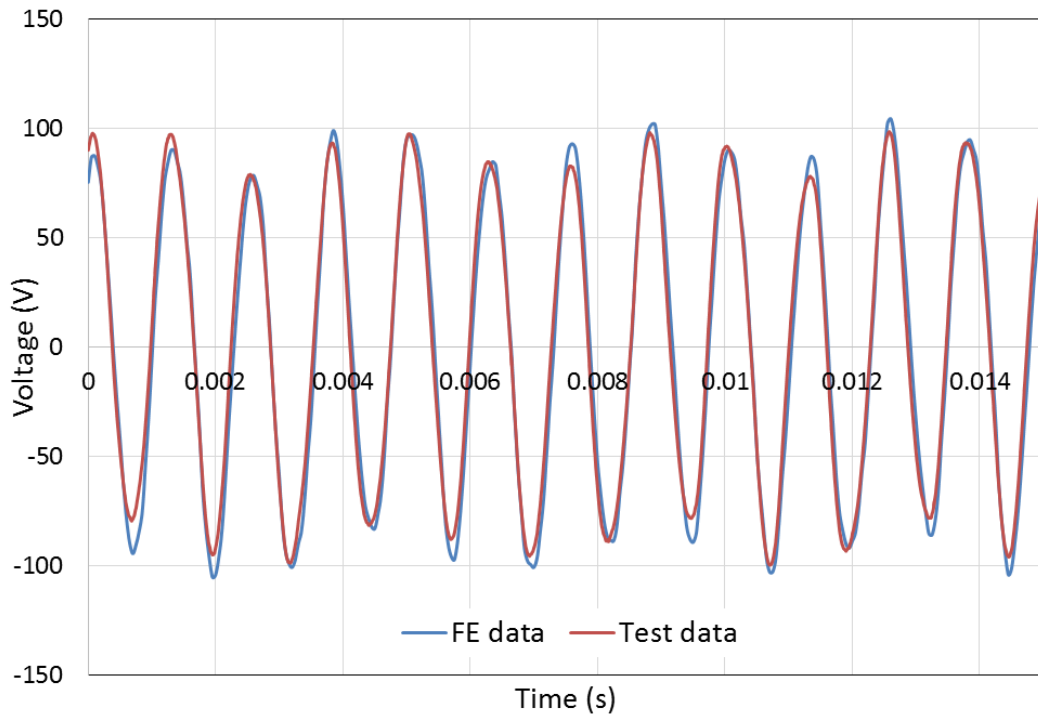


Figure 6.30 – FE predicted and test results of phase C load voltage for the test case of 10% above the VF range at (13,200rpm) a control winding current density of  $7.27A_{rms}mm^{-2}$  and a load resistance of  $3.77\Omega$ ,  $3.77\Omega$  and  $3.79\Omega$  for phase A, B and C respectively

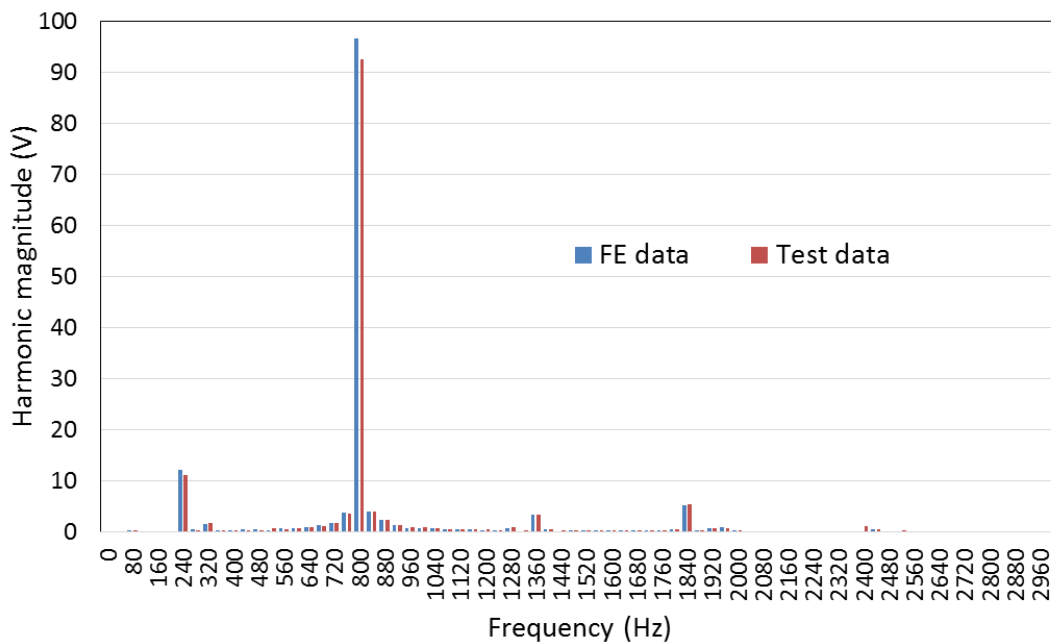


Figure 6.31 – FE predicted and test results for an FFT of phase A load voltage for the test case of 10% above the VF range (13,200rpm) at a control winding current density of  $7.27A_{rms}mm^{-2}$  and a load resistance of  $3.77\Omega$ ,  $3.77\Omega$  and  $3.79\Omega$  for phase A, B, C respectively



### 6.5.2 OPERATING POINT AT 4,860PM

Next, the test case at 10% below the speed range was modelled with a rotor speed of 4,860rpm and a co-rotating control frequency of 36Hz. Figure 6.32 provides the control winding current used in both the FEA and test which has a peak current density of  $9.36\text{Amm}^{-2}$  which corresponds to an RMS current density of  $6.62\text{Amm}^{-2}$ .

The power winding voltage waveforms are very similar in terms of magnitudes and harmonic content as found in Figure 6.33, Figure 6.34 and Figure 6.35 for phase A, B and C respectively. As expected a subharmonic of the power winding voltage is prevalent, seen here in phase A in Figure 6.36. At this operating point, the 108Hz subharmonic has a magnitude of 4.7% of the fundamental magnitude for the measured case. Conversely, the FE data of this power winding voltage FFT shows very little subharmonic content. This would suggest that the FE software is underappreciating the amount of saturation in the demonstrator machine, therefore eliminating the saturation induced subharmonic seen in the measurement results.

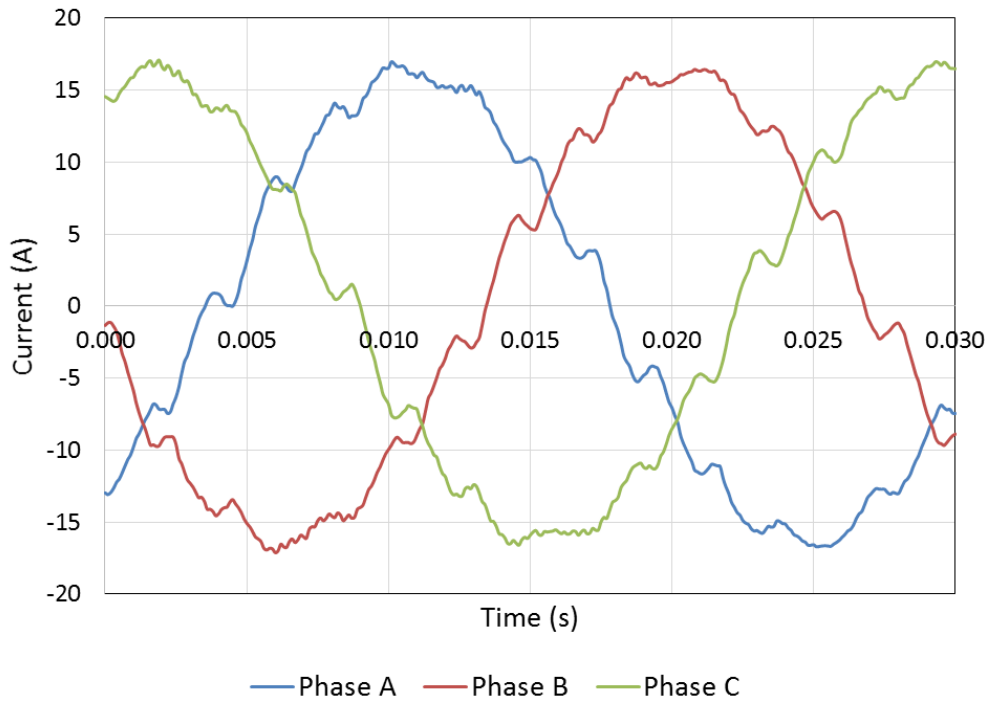


Figure 6.32 – Measured 3-phase control winding current used in FEA comparison for the test case of 10% below the VF range (4,860rpm) with load resistances of 4.76Ω, 4.75Ω and 4.79 Ω for phase A, B and C respectively

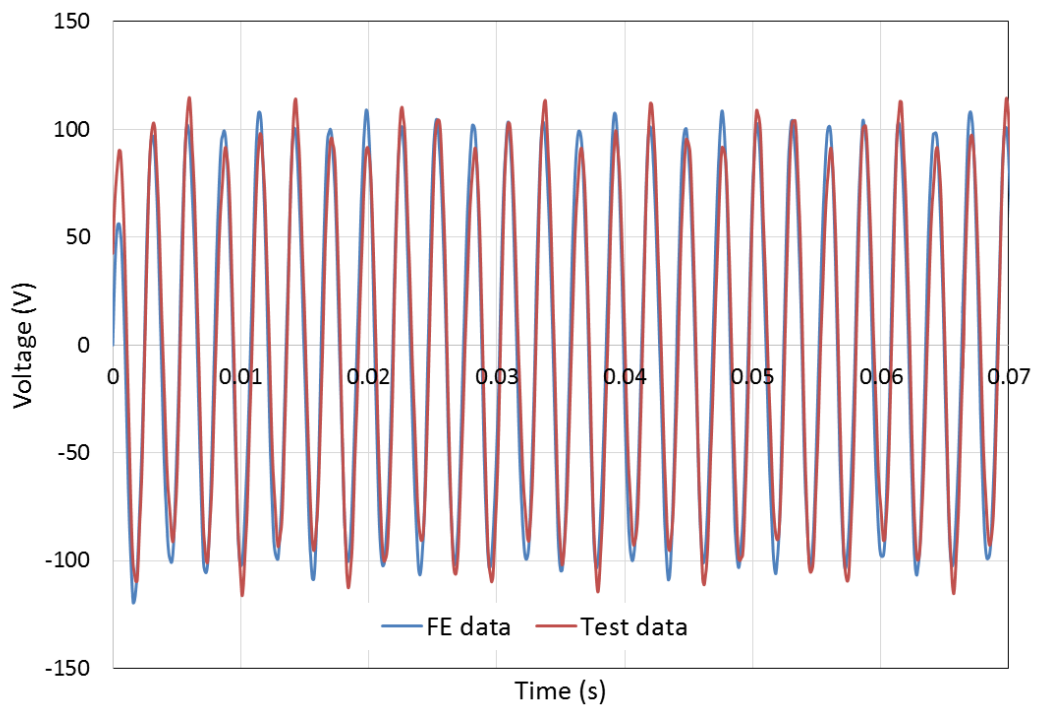


Figure 6.33 – FE predicted and test results of phase A load voltage for the test case of 10% below the VF range (4,860rpm) at a control winding current density of  $6.62A_{rms}mm^{-2}$  and a load resistance of 4.76Ω, 4.75Ω and 4.79Ω for phase A, B and C respectively

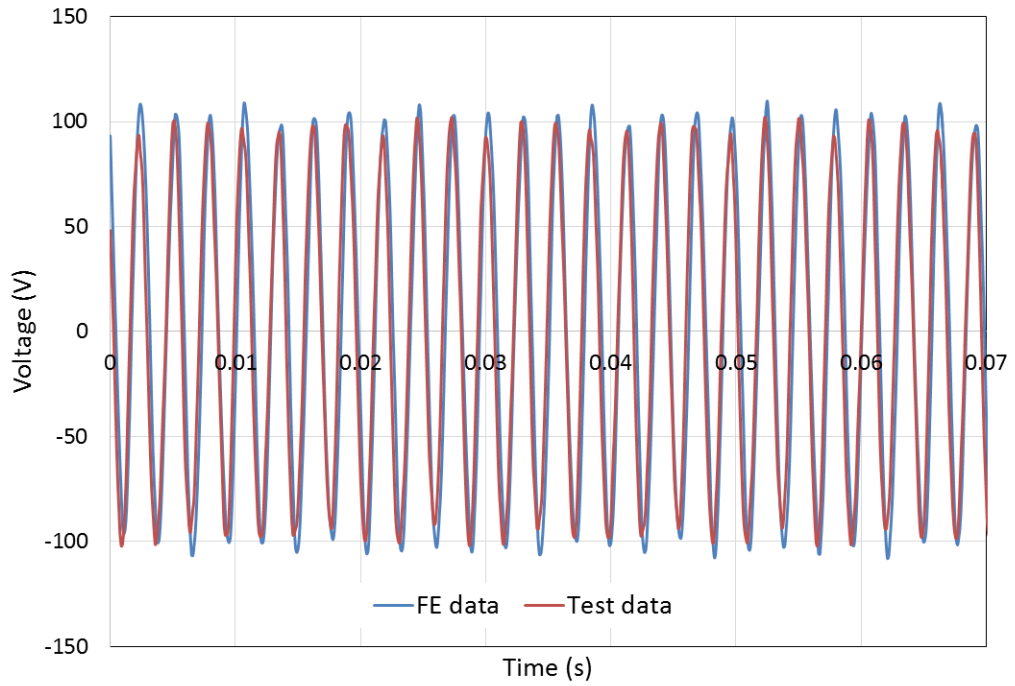


Figure 6.34 – FE predicted and test results of phase B load voltage for the test case of 10% below the VF range (4,860rpm) at a control winding current density of  $6.62A_{rms}mm^{-2}$  and a load resistance of  $4.76\Omega$ ,  $4.75\Omega$  and  $4.79\Omega$  for phase A, B and C respectively

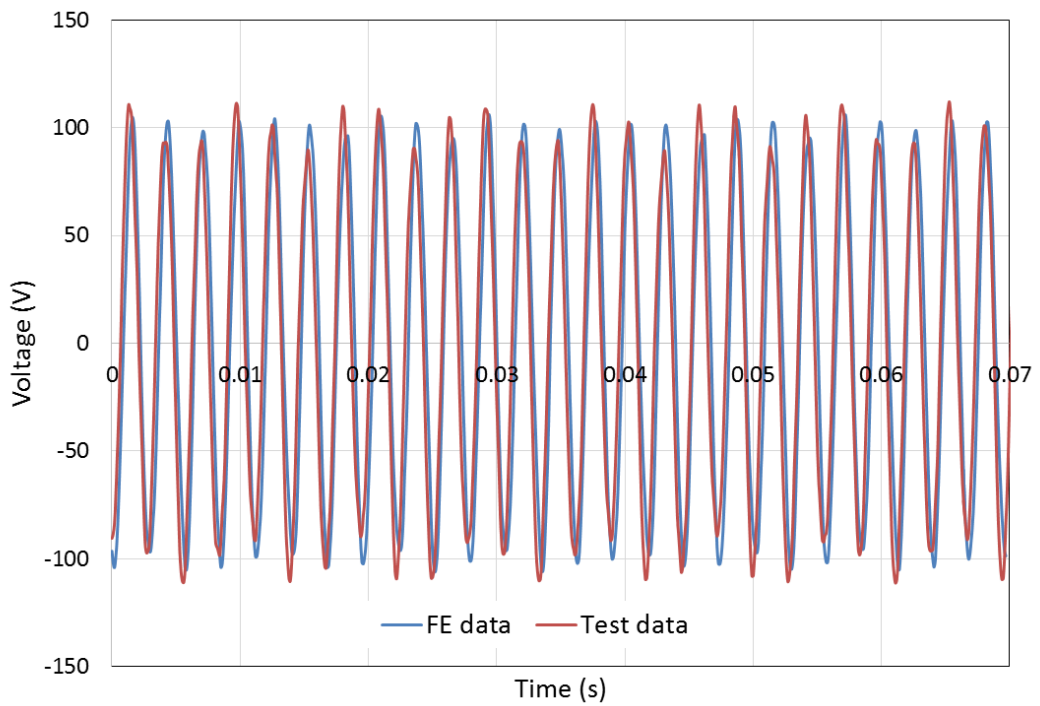


Figure 6.35 – FE predicted and test results of phase C load voltage for the test case of 10% below the VF range (4,860rpm) at a control winding current density of  $6.62A_{rms}mm^{-2}$  and a load resistance of  $4.76\Omega$ ,  $4.75\Omega$  and  $4.79\Omega$  for phase A, B and C respectively

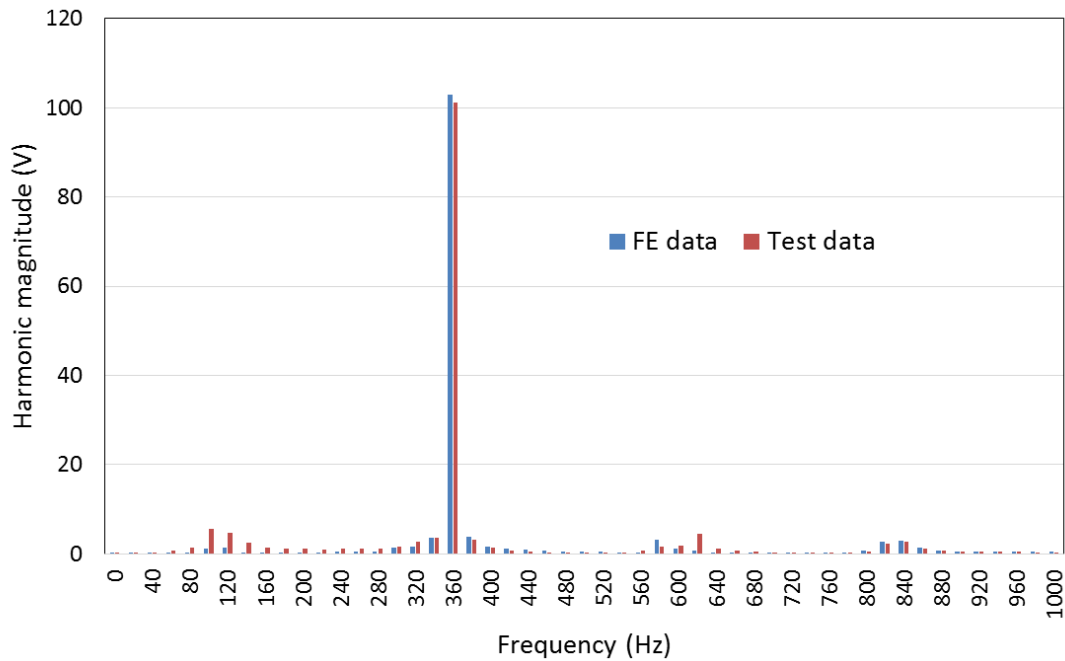


Figure 6.36 – FE predicted and test results for FFT of phase A load voltage for the test case of 10% below the VF range (4,860rpm) at a control winding current density of  $6.62\text{A}_{\text{rms}}\text{mm}^{-2}$  and a load resistance of  $4.76\Omega$ ,  $4.75\Omega$  and  $4.79\Omega$  for phase A, B, C respectively

## 6.6 FURTHER INVESTIGATION OF POWER WINDING SUB-HARMONICS

The comparisons between measured and predicted power winding voltages in Section 6.5 have both shown the presence of significant sub-harmonics. These sub-harmonics are of a magnitude that would give rise to problems in terms of meeting the allowable voltage variations in the VF standard (nominally  $\pm 5\text{V}$ ). This section investigates this behaviour in more detail.

As discussed and investigated in Sections 2.8.2 and 4.4 of previous chapters, the pole number combination chosen for this demonstrator has many advantages in terms of being the combination that allows the rotor to run at the maximum speed while remaining within the VF range and avoiding unbalanced magnetic pull. However, one drawback is that any saturation induced 3<sup>rd</sup> harmonic in flux produced by the control winding will link directly with the power winding, which will manifest itself in the power winding voltage waveform in the form of a subharmonic of a frequency three times that of the control winding fundamental frequency.

The FEA results presented in Chapter 5 indicate the magnitude of the subharmonic in the power winding voltage increases rapidly at the onset of saturation before levelling off at higher current densities.

#### 6.6.1 INFLUENCE OF CONTROL WINDING CURRENT ON POWER WINDING SUBHARMONIC AT 4,860RPM

For this test point, which requires a frequency correction of 10% to bring the output frequency up to 360Hz, the load bank was configured to provide a nominal  $4.7\Omega$  balanced load, a value which should lead to an output voltage within the VF frequency specification (108-118V<sub>rms</sub>). For this condition, Figure 6.37 shows the measured variation in the power winding output voltage with control winding current density. To provide an indication of the distortion in the actual control winding current waveforms which produced these results, Figure 6.38 and Figure 6.39 show the measured control winding waveforms at the upper and lower end of the range, i.e.  $0.29A_{rms}mm^{-2}$  and  $6.59A_{rms}mm^{-2}$ , while Figure 6.40 and Figure 6.41 show the corresponding power winding output voltage waveforms respectively.

Figure 6.42 shows the variation with control current density of both the percentage magnitude of the sub-harmonic relative to the fundamental and the absolute magnitude of the sub-harmonic for this 4,860rpm.

Figure 6.43 shows the corresponding FEA predicted variations with a skewed rotor for ideal sinusoidal current (as previously discussed in Section 5.9). Although there is some broad agreement in terms of the overall shape, it is apparent that there are several interesting differences when comparing the skewed FEA predicted results to the measured results, notwithstanding the fact that the control winding currents in the measured results are not sinusoidal. Although both graphs feature an initial significant increase in subharmonic, in the measured data there is a marked reduction at higher current densities. This is present but less pronounced in the FEA characteristics. As will be apparent from the continued rise in the harmonic itself, this reduction in the percentage of subharmonic is due to the harmonics being more affected by saturation than the fundamental, which continues to rise more or less linearly up to  $6.59A_{rms}mm^{-2}$  as shown previously in Figure 6.37. Figure 6.43

demonstrates a much lower percent of third harmonic than Figure 6.42, which suggests that the saturation within this machine has been under predicted in the FE modelling compared to the test data, although again it should be noted that the measured control winding current includes harmonics due to the limitations of the converter.

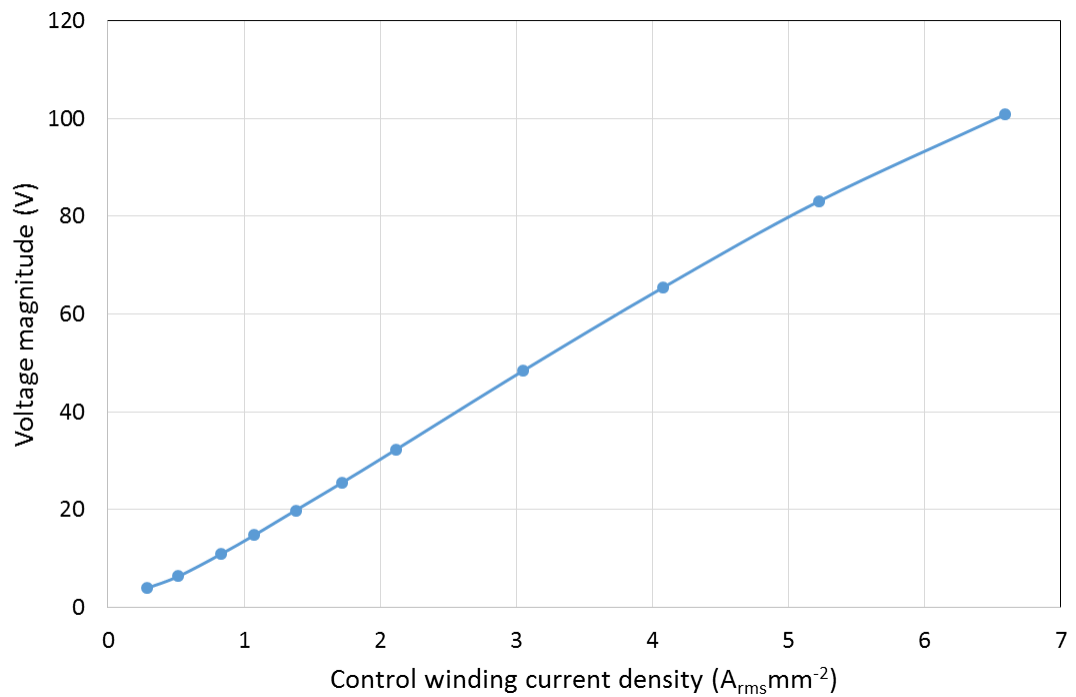


Figure 6.37 – Measured variation in power winding voltage fundamental magnitude with control winding RMS current density for a rotor speed of 4,860rpm and a co-rotating 36Hz control current with a power winding load of 4.76 $\Omega$ , 4.75 $\Omega$  and 4.79 $\Omega$  for phase A, B and C respectively

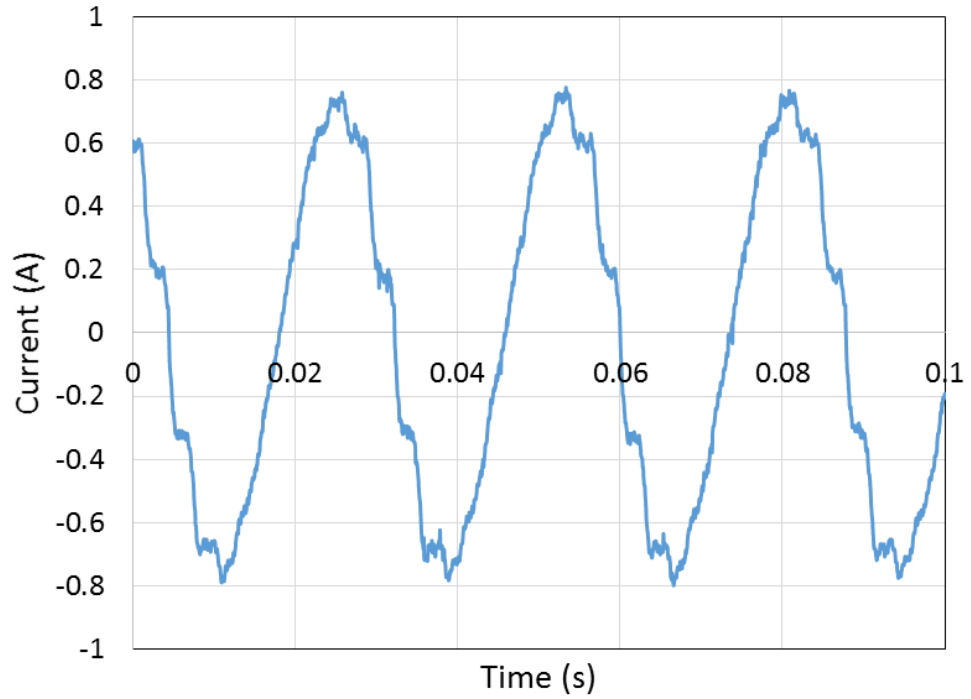


Figure 6.38 – Measured phase A control winding current for the test case of 10% below the VF range (4,860rpm) with load resistances of 4.76Ω, 4.75Ω and 4.79 Ω for phase A, B and C respectively at a control winding current density of  $0.29A_{rms}mm^{-2}$

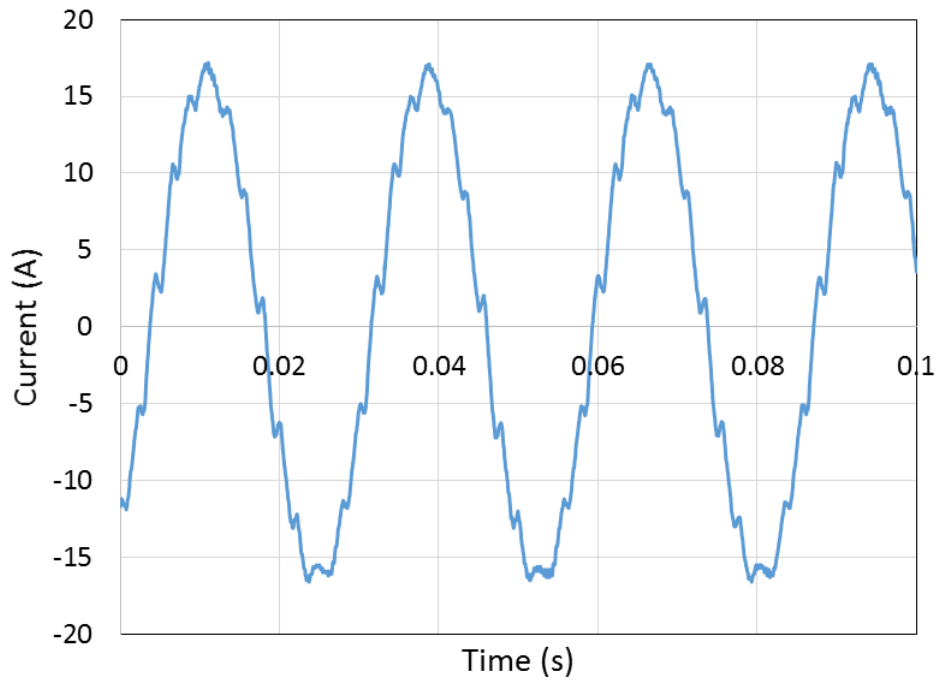


Figure 6.39 – Measured phase A control winding current for the test case of 10% below the VF range (4,860rpm) with load resistances of 4.76Ω, 4.75Ω and 4.79 Ω for phase A, B and C respectively at a control winding current density of  $6.59A_{rms}mm^{-2}$

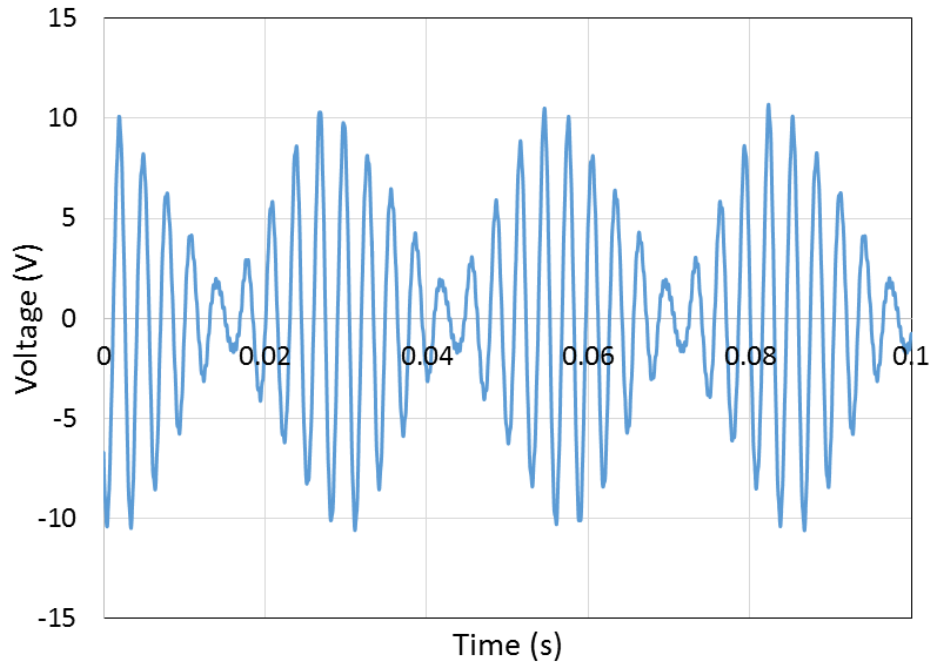


Figure 6.40 – Measured phase A power winding voltage for the test case of 10% below the VF range (4,860rpm) with load resistances of 4.76Ω, 4.75Ω and 4.79 Ω for phase A, B and C respectively at a control winding current density of  $0.29A_{rms}mm^{-2}$  (as of Figure 6.38)

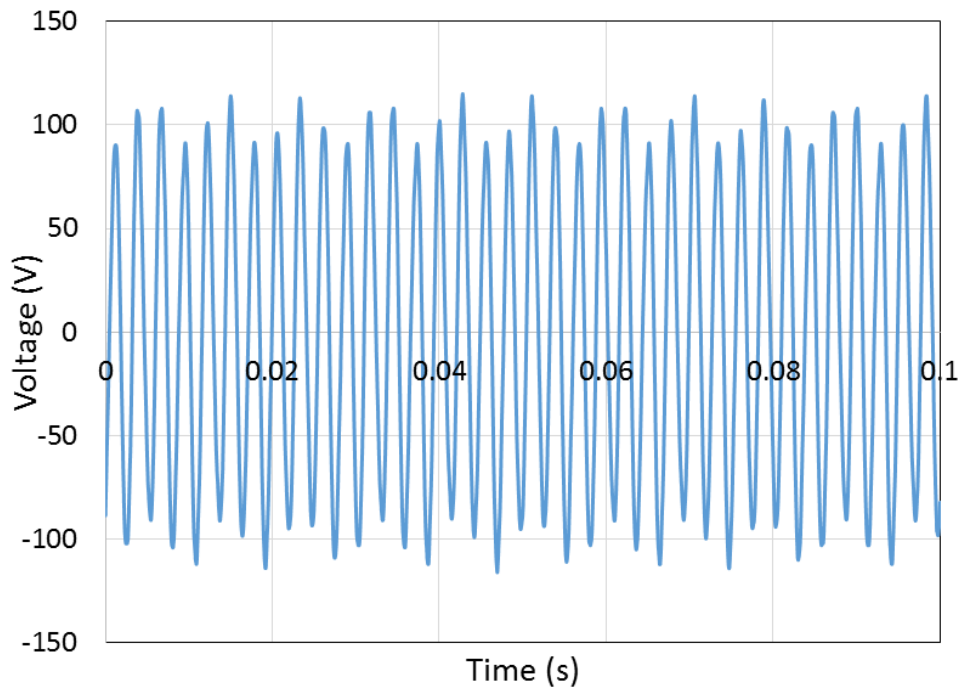


Figure 6.41 – Measured phase A power winding voltage for the test case of 10% below the VF range (4,860rpm) with load resistances of 4.76Ω, 4.75Ω and 4.79 Ω for phase A, B and C respectively at a control winding current density of  $6.59A_{rms}mm^{-2}$  (as of Figure 6.39)



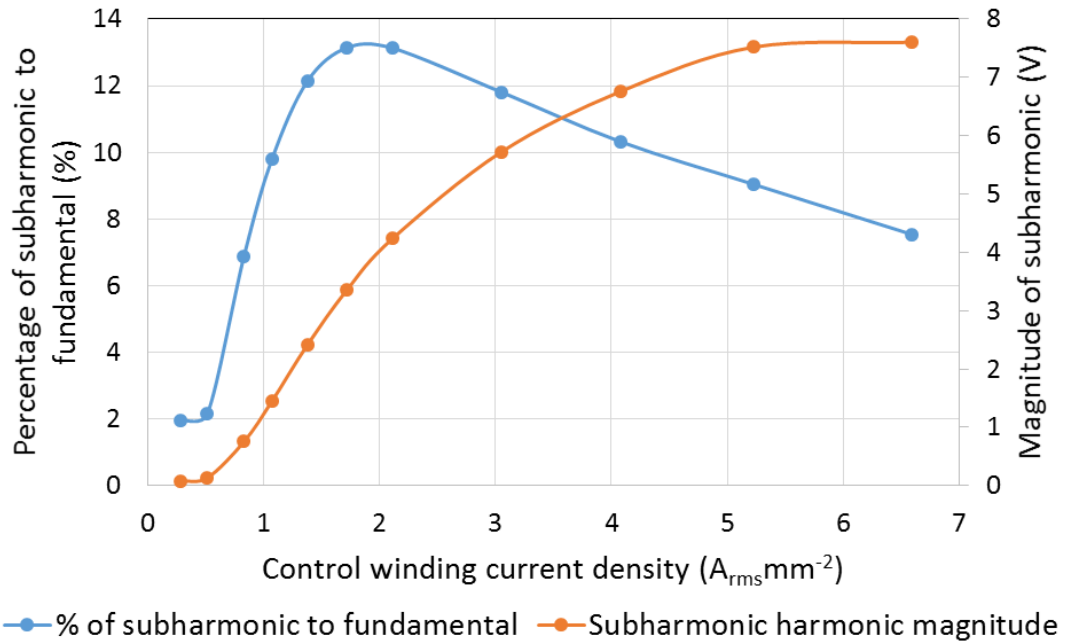


Figure 6.42 – Measured variation in sub-harmonic magnitudes with control winding current density for a rotor speed of 4,860rpm, a co-rotating 36Hz control current and load resistances of 4.76Ω, 4.75Ω and 4.79Ω for phase A, B and C respectively

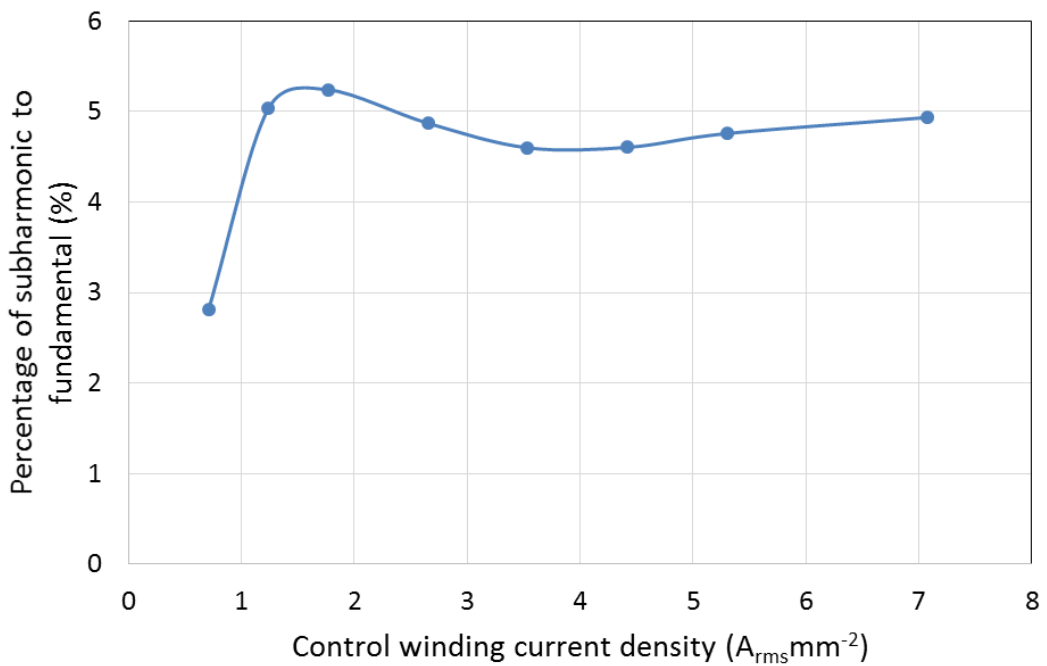


Figure 6.43 – 4,860rpm rotor speed of current density vs. % of 3<sup>rd</sup> harmonic as found in Chapter 5 using skewed finite element software with sinusoidal control current and load resistances of 4.76Ω, 4.75Ω and 4.79Ω for phase A, B and C respectively

## 6.6.2 INFLUENCE OF CONTROL WINDING CURRENT ON POWER WINDING SUBHARMONIC AT 13,200 RPM

A series of further measurements were taken for the high speed case of 13,200rpm which corresponds to a point 10% above the synchronous speed range. The resulting variation in the percentage of subharmonic with respect to the fundamental and the subharmonic magnitude as a function of control winding current density are shown in Figure 6.44. Although the curves are similar in shape to those for the low speed operating point described in Section 6.6.1, the higher speed point contains significantly higher percentages of saturation induced subharmonic. This can be attributed in large part to the increased power winding output current, as found in Figure 6.45 for phase A, leading to an increase in flux and therefore saturation in the magnetic circuit.

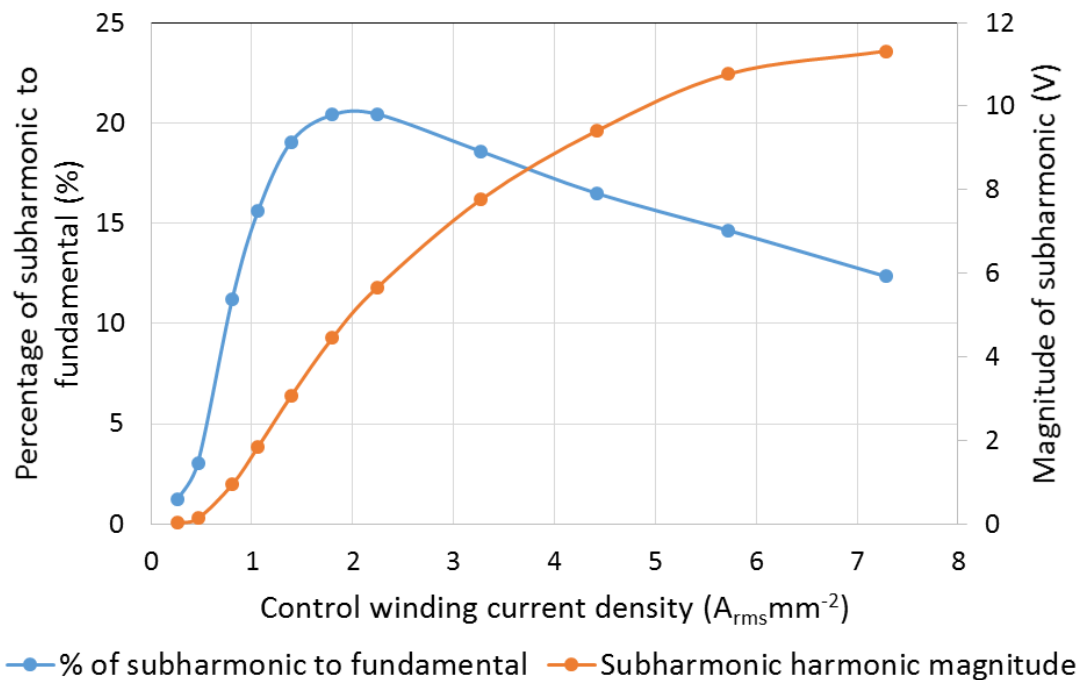


Figure 6.44 – Measured power winding voltage saturation induced subharmonic content as a percentage of the fundamental for a rotor speed of 13,200rpm and a contra-rotating 80Hz control current and load resistances of 3.77Ω, 3.77Ω and 3.80Ω for phase A, B and C respectively

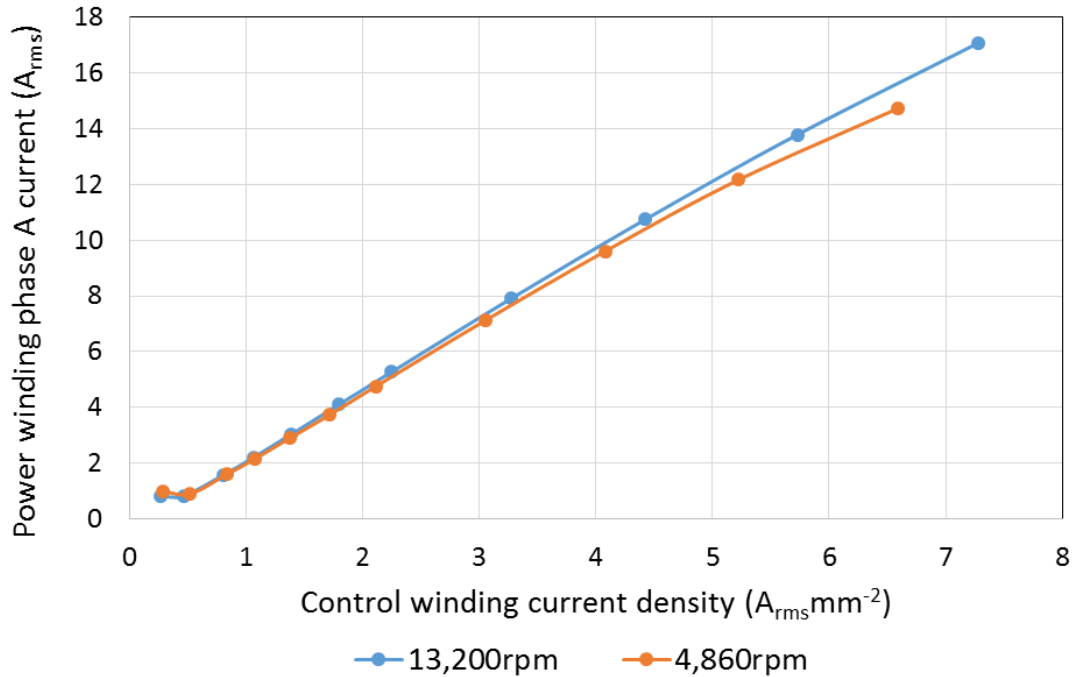


Figure 6.45 – Measured power winding phase A current with respect to the control winding current density of the 4,860rpm case of Figure 6.42 and the 13,200rpm case of Figure 6.44

### 6.6.3 INFLUENCE OF SPEED AND CONTROL FREQUENCY ON SUBHARMONICS

The next series of measurements of harmonics involved fixing the power winding frequency at 800Hz, while varying the rotor speed and therefore required control winding frequency. For an operating power winding frequency of 800Hz (which is the top of the VF range and corresponds to a synchronous rotor speed of 12,000rpm), the speeds considered were 12,600rpm, 13,200rpm and 14,400rpm corresponding to 5%, 10% and 20% above the synchronous speed. These operating points required control winding frequencies of 40Hz, 80Hz and 160Hz to maintain the 800Hz output.

Figure 6.46, Figure 6.44 and Figure 6.47 show the percentage of subharmonic to the fundamental, as well as the magnitude of subharmonic for the 5%, 10% and 20% operating points respectively, as mentioned previously. There is an apparent trend in which an increase in the degree of correction required leads to an increase in the percentage of control winding subharmonic appearing in the power winding voltage. This is due to a higher power winding current at comparable control winding current densities when a higher degree of correction factor is required.

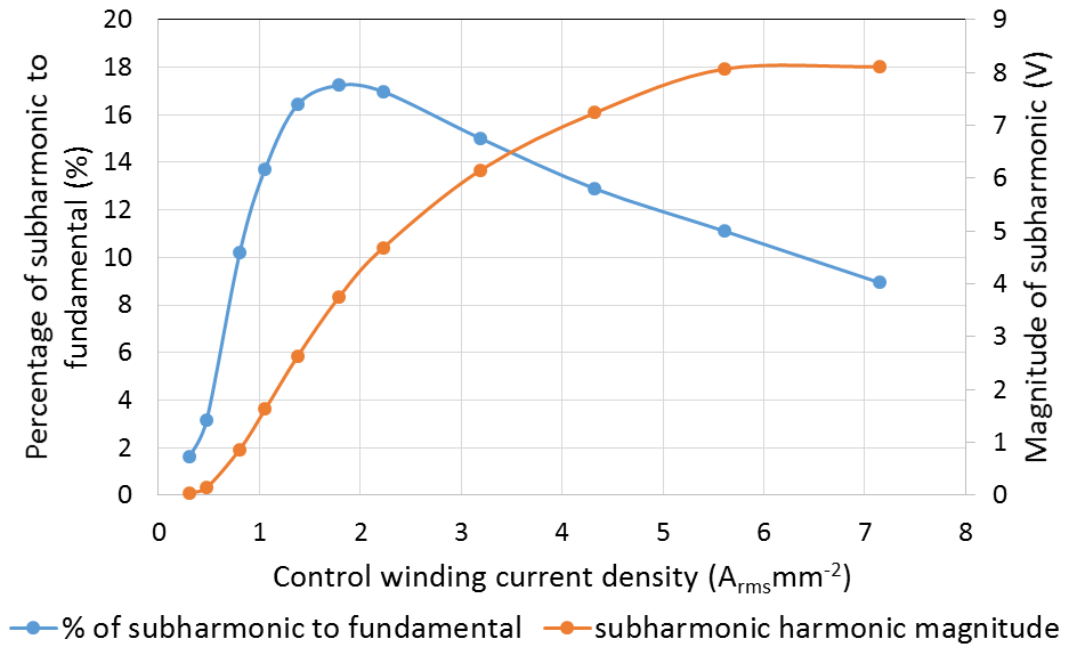


Figure 6.46 – Measured power winding voltage saturation induced subharmonic content as a percentage of the fundamental for a rotor speed of 12,600rpm, a contra-rotating 40Hz control current and load resistances of 3.77Ω, 3.77Ω and 3.80Ω for phase A, B and C respectively

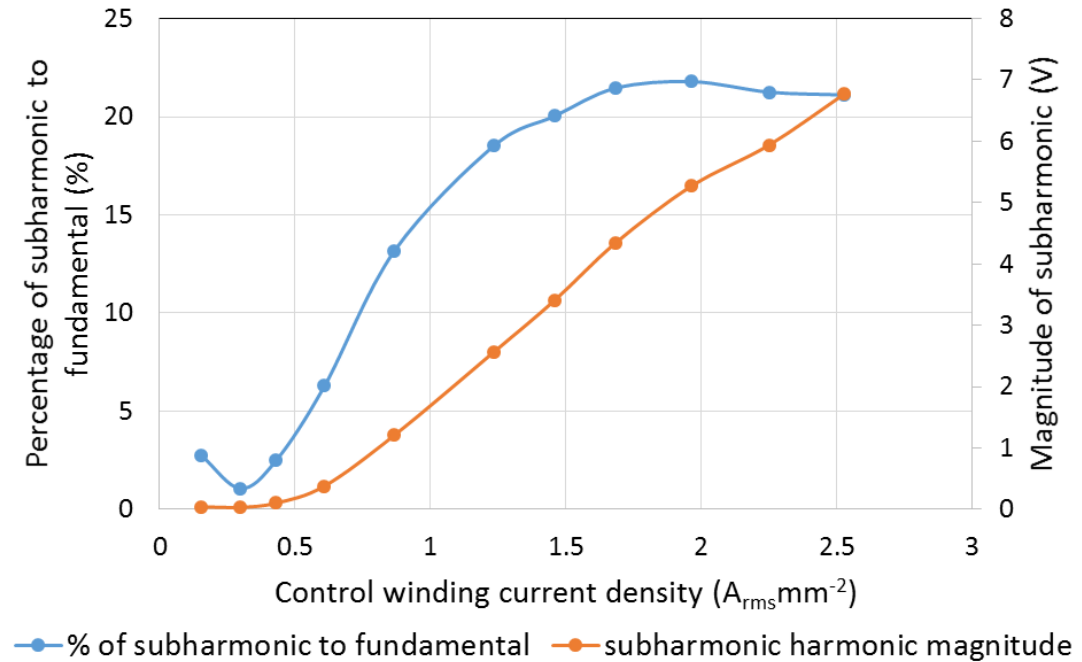


Figure 6.47 – Measured power winding voltage saturation induced subharmonic content as a percentage of the fundamental for a rotor speed of 14,400rpm, a contra-rotating 160Hz control current and load resistances of 3.77Ω, 3.77Ω and 3.80Ω for phase A, B and C respectively

#### 6.6.4 INFLUENCE OF CONTROL FREQUENCY VARIATIONS ON SUBHARMONIC CONTENT

The final series of measurements undertaken in this section of the chapter involved fixing the rotor speed at 6,000rpm, whilst adjusting the control winding correction from 10% to 5% below the synchronous frequency of 400Hz. This corresponds to a power winding fundamental frequency of 360Hz and 380Hz for the 10% and 5% correction respectively.

Figure 6.48 shows the subharmonic content in the case of a 10% reduction in power winding frequency, which is achieved with a contra-rotating 40Hz control winding current. As expected the harmonic content exceeds 16% of the fundamental voltage magnitude as seen in operating points of similar percentage corrections (Figure 6.44).

By adjusting the power winding frequency by only 5%, as seen in Figure 6.49 by introducing a 20Hz contra-rotating control winding current, the magnitude and relative percentage of the fundamental is much lower. Therefore, it can be concluded that increasing the correction factor leads to an increase in the percentage of subharmonic in the power winding voltage waveform. This is primarily due to the extra slip power required to enable a higher degree of correction in the power winding frequency.

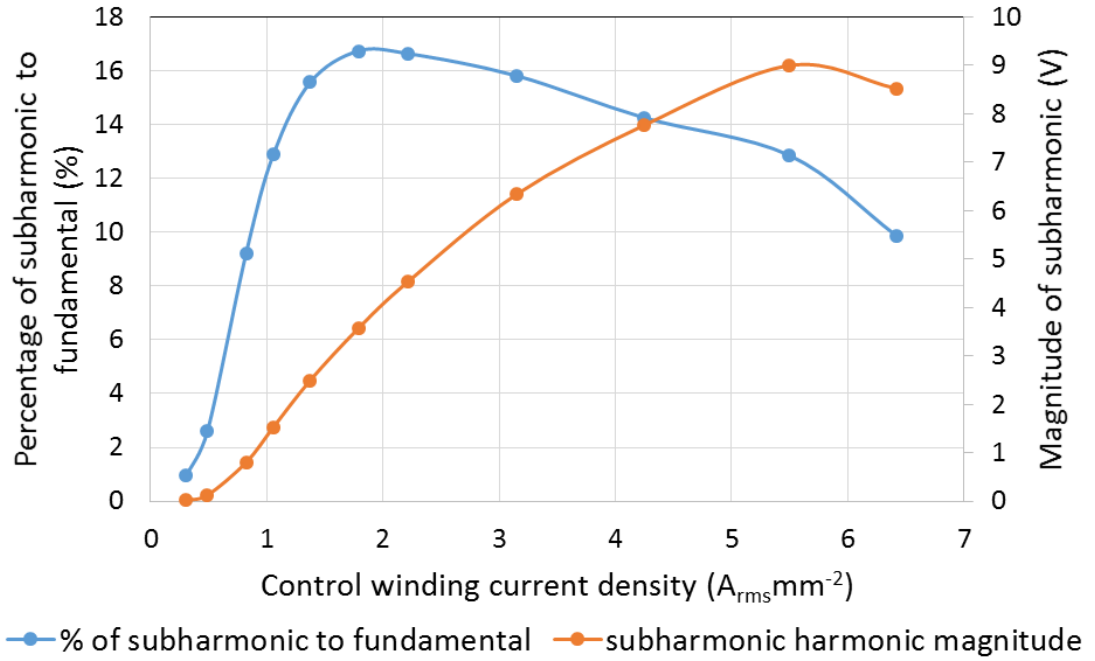


Figure 6.48 – Measured power winding voltage saturation induced subharmonic content as a percentage of the fundamental for a rotor speed of 6,000rpm, a contra-rotating 40Hz control current and load resistances of 3.77Ω, 3.77Ω and 3.80Ω for phase A, B and C respectively

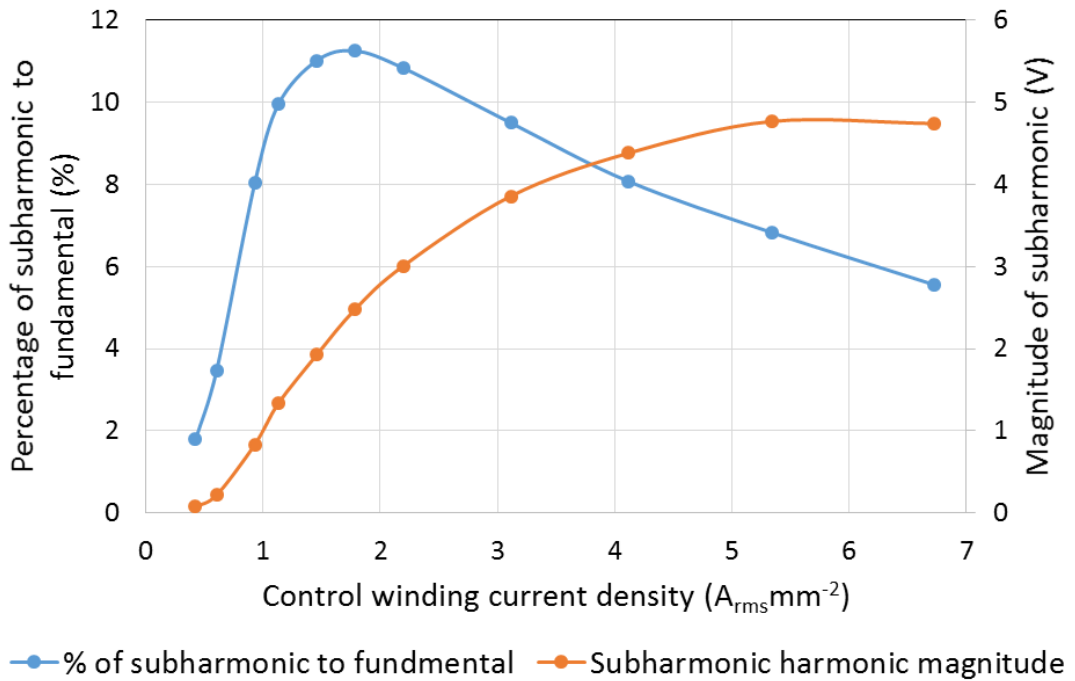


Figure 6.49 – Measured power winding voltage saturation induced subharmonic content as a percentage of the fundamental for a rotor speed of 6,000rpm, a contra-rotating 20Hz control current and load resistances of 3.77Ω, 3.77Ω and 3.80Ω for phase A, B and C respectively

## 6.7 INVESTIGATION INTO SYNCHRONOUS PERFORMANCE

To investigate aspects of performance when no frequency correction is used, the demonstrator was run with a nominally static control winding current. In order to avoid asymmetric localised heating of the star-connected control winding, a control winding frequency of 0.1Hz was used rather a true static DC current combination.

The machine was driven at a speed of 6,000rpm which should result in a power winding output voltage with a frequency of 400Hz. The measured power winding voltage with a 0.1Hz,  $0.56A_{rms}mm^{-2}$  control current is shown in Figure 6.50, while the resulting FFT of the phase A power winding load voltage is shown in Figure 6.51. As will be apparent, there is no meaningful subharmonic present, but there is a notable harmonic (order of 10.17% of fundamental) at  $\sim 800Hz$ . It is worth noting that this test point is at a very modest current density at which the sub-harmonic, even with frequency correction, would not be expected to be prominent.

The interesting 800Hz component in the FFT cannot be attributed to the slotting harmonics as these are of the order of 4,850Hz.

To confirm the presence of this 2<sup>nd</sup> harmonic and eliminate the possibility that it is a consequence of some complex slotting artefacts, several other synchronous test points were considered, viz. 4,800rpm, 7,800rpm and 9,000rpm, in all cases at the same control winding current density of  $0.56A_{rms}mm^{-2}$ . The resulting measured power winding output voltages are shown in Figure 6.52, Figure 6.54 and Figure 6.56 respectively, while the corresponding FFTs are shown in Figure 6.53, Figure 6.55 and Figure 6.57. These FFTs all confirm the presence of a significant second harmonic for these various synchronous operating points.

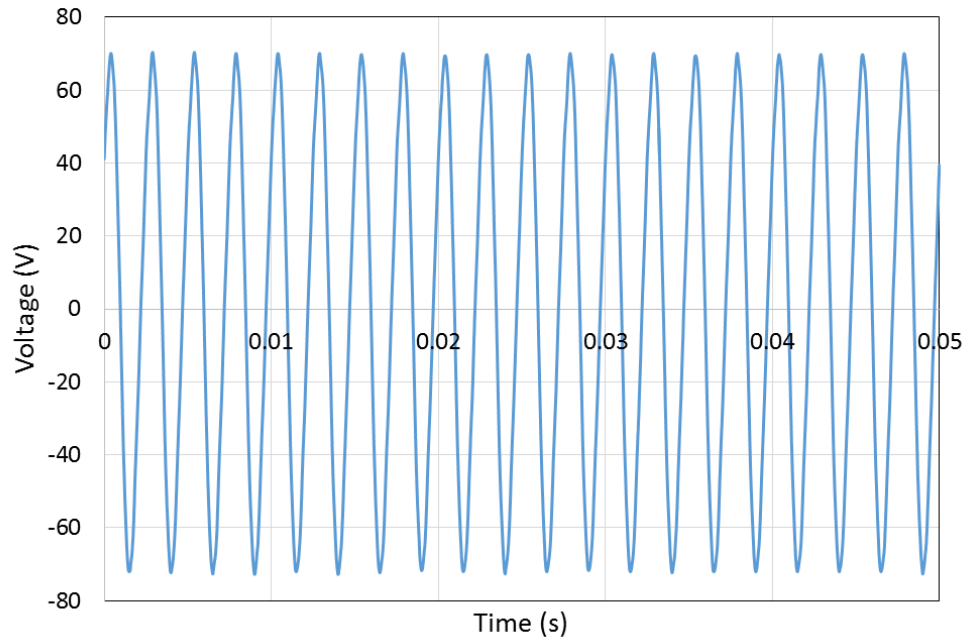


Figure 6.50 – Measured test results of phase A load voltage for the 0.1Hz control winding test case at 6,000rpm with a control winding current density of  $0.56A_{rms}mm^{-2}$  and a load resistance of  $3.77\Omega$ ,  $3.77\Omega$  and  $3.80\Omega$  for phase A, B and C respectively

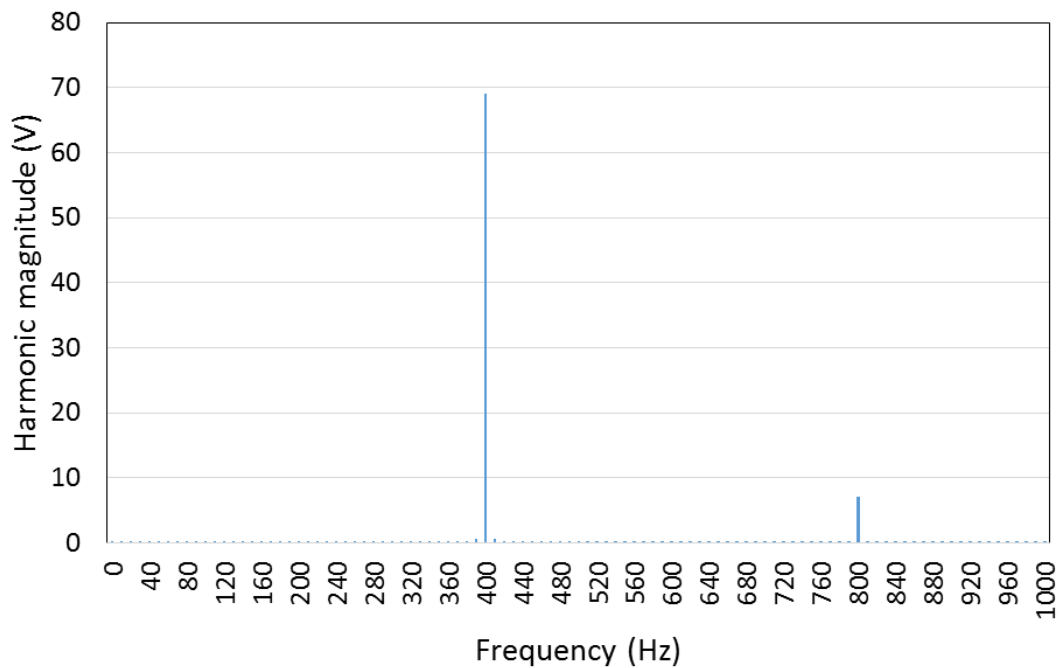


Figure 6.51 – Measured test results of phase A load voltage FFT for the 0.1Hz control winding test case at 6,000rpm with a control winding current density of  $0.56A_{rms}mm^{-2}$  and a load resistance of  $3.77\Omega$ ,  $3.77\Omega$  and  $3.80\Omega$  for phase A, B and C respectively



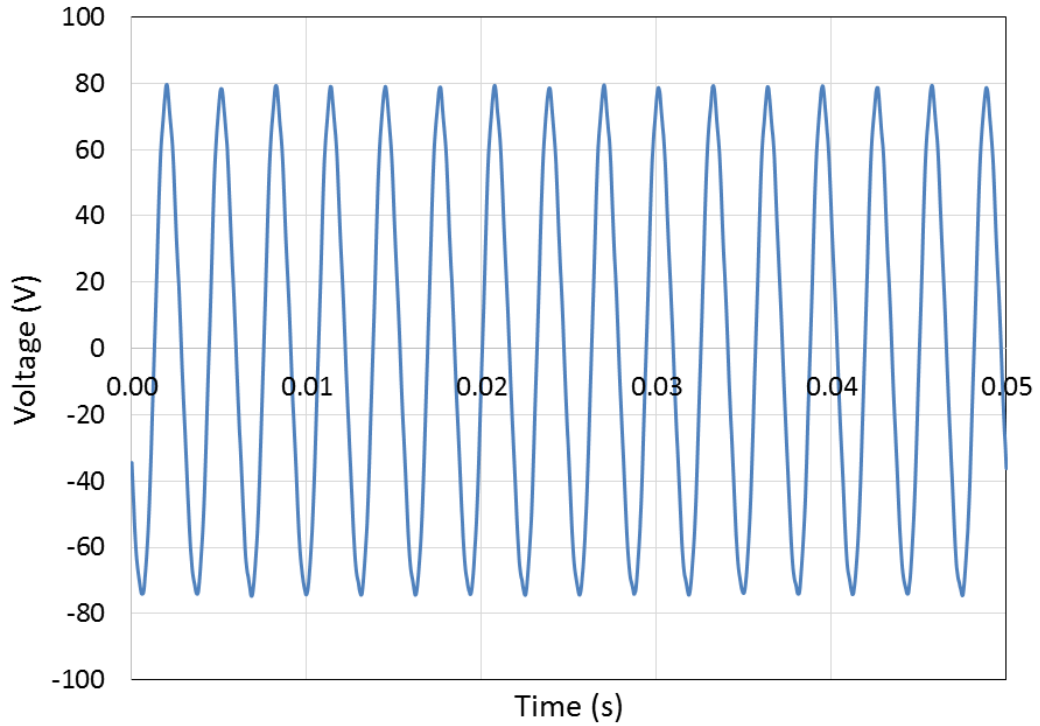


Figure 6.52 – Measured test results of phase A load voltage for the 0.1Hz control winding test case at 4,800rpm with a control winding current density of  $0.56A_{rms}mm^{-2}$  and a load resistance of  $3.77\Omega$ ,  $3.77\Omega$  and  $3.80\Omega$  for phase A, B and C respectively

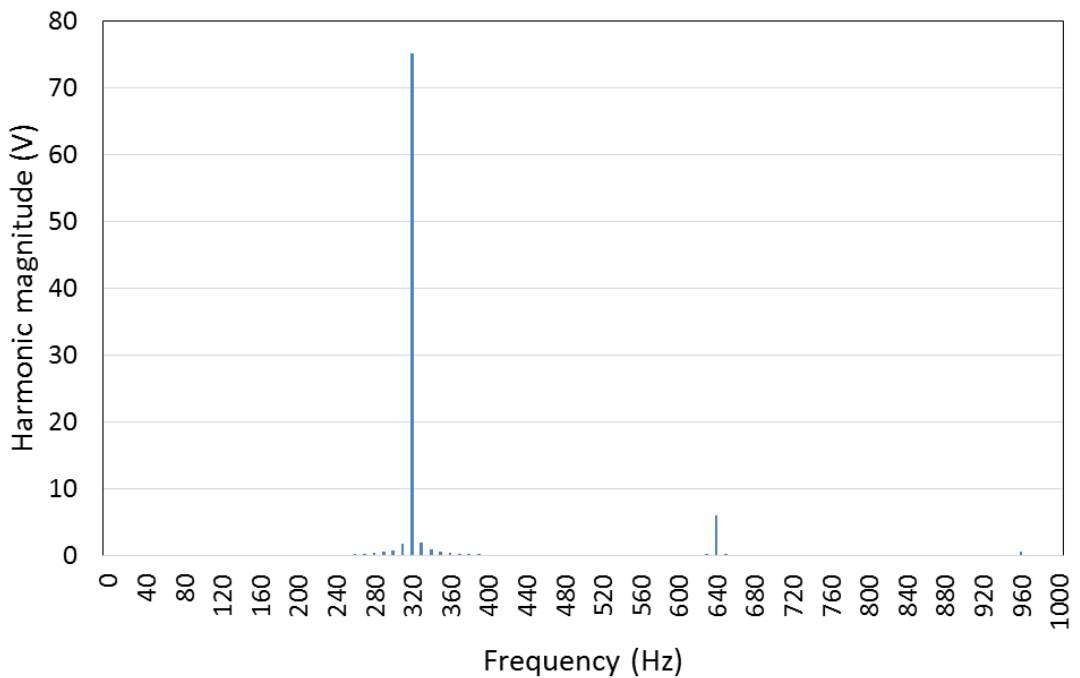


Figure 6.53 – Measured test results of phase A load voltage FFT for the 0.1Hz control winding test case at 4,800rpm with a control winding current density of  $0.56A_{rms}mm^{-2}$  and a load resistance of  $3.77\Omega$ ,  $3.77\Omega$  and  $3.80\Omega$  for phase A, B and C respectively

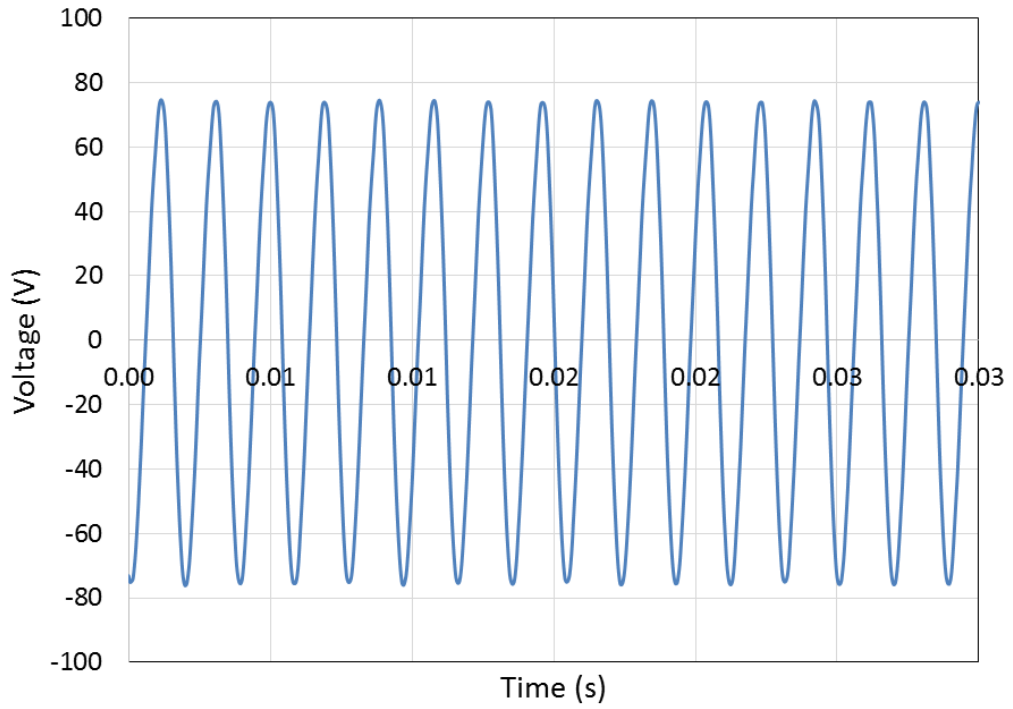


Figure 6.54 – Measured test results of phase A load voltage for the 0.1Hz control winding test case at 7,800rpm with a control winding current density of  $0.56A_{rms}mm^{-2}$  and a load resistance of  $3.77\Omega$ ,  $3.77\Omega$  and  $3.80\Omega$  for phase A, B and C respectively

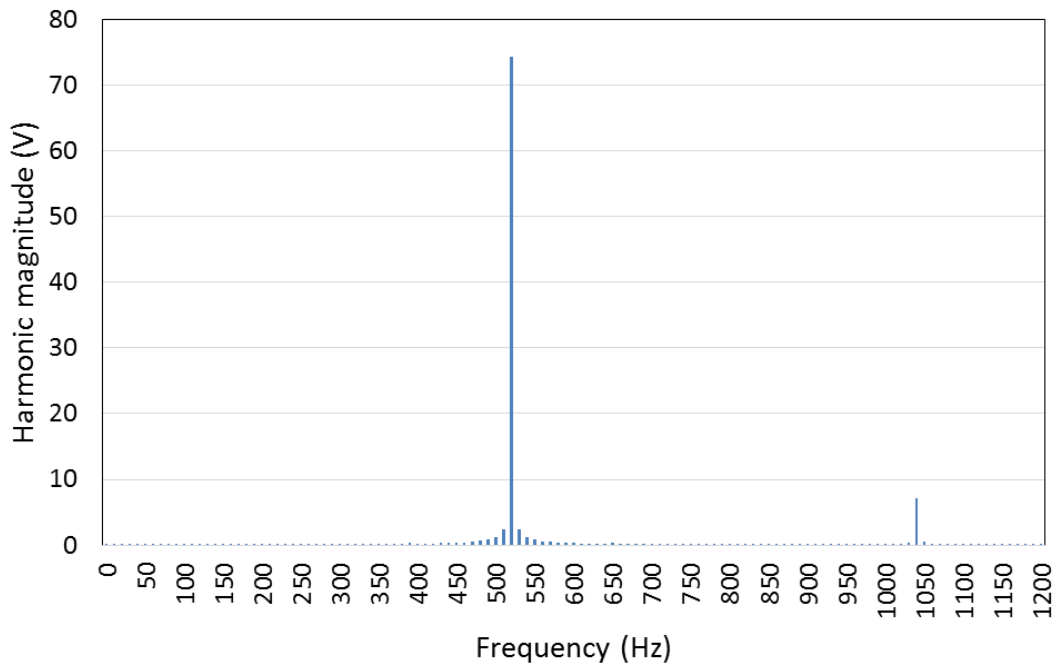


Figure 6.55 – Measured test results of phase A load voltage FFT for the 0.1Hz control winding test case at 7,800rpm with a control winding current density of  $0.56A_{rms}mm^{-2}$  and a load resistance of  $3.77\Omega$ ,  $3.77\Omega$  and  $3.80\Omega$  for phase A, B and C respectively

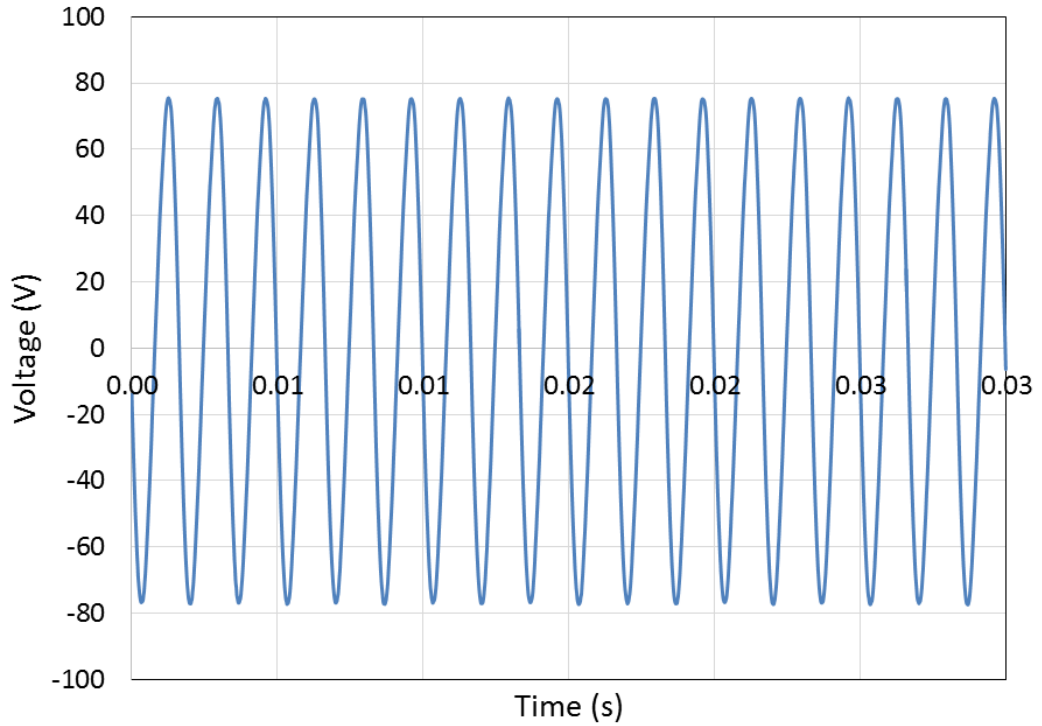


Figure 6.56 – Measured test results of phase A load voltage for the 0.1Hz control winding test case at 9,000rpm with a control winding current density of  $0.56A_{rms}mm^{-2}$  and a load resistance of  $3.77\Omega$ ,  $3.77\Omega$  and  $3.80\Omega$  for phase A, B and C respectively

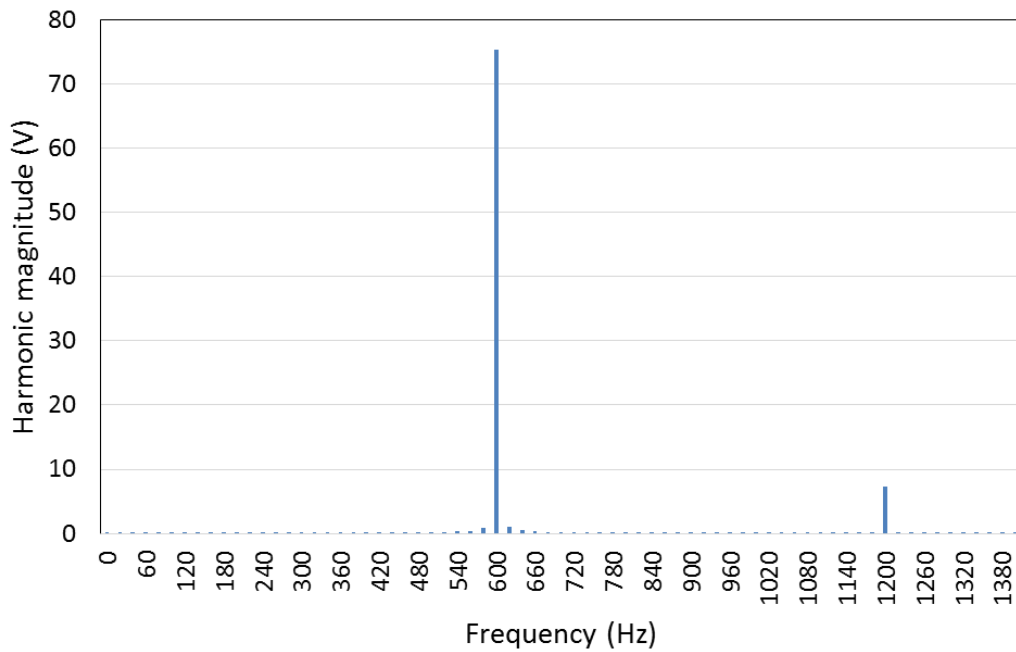


Figure 6.57 – Measured test results of phase A load voltage FFT for the 0.1Hz control winding test case at 9,000rpm with a control winding current density of  $0.56A_{rms}mm^{-2}$  and a load resistance of  $3.77\Omega$ ,  $3.77\Omega$  and  $3.80\Omega$  for phase A, B and C respectively

The presence of 2<sup>nd</sup> harmonics is unusual in 3-phase balanced systems since the symmetry of 3-phase systems usually cancels out all even harmonics [2, 3]. In the general case, the main reason for the appearance of second harmonics is when the positive and negative half cycles of the waveform have different forms. Examples of such cases include half-wave rectification, arc furnaces and the presence of geomagnetically induced currents within the power system.

In the case of the BDFRM, close inspection of the measured power winding voltage waveforms show an asymmetry between the positive and negative half-cycles as summarised for phase A in Table 6.10. This imbalance in the output voltages is the source of the 2<sup>nd</sup> harmonic seen in the previous FFTs.

Table 6.10 – Measured voltage magnitudes of the positive and negative half-cycles of the phase A power winding voltage for several synchronous operating conditions with a control frequency of 0.1Hz and load resistances of 3.77Ω, 3.77Ω and 3.80Ω for phases A, B and C

Rotor speed (rpm)	Phase A power winding voltage (V)	
	+ve peak	-ve peak
4,800	79.68	-74.08
6,000	70.07	-72.04
7,800	74.68	-75.06
9,000	75.52	-76.73

The source of this imbalance is the inherent asymmetry between the axis of the control winding field at any given time (which is to all practical purposes static over the duration of the waveforms shown), and the three individual power winding phase windings. To confirm this behaviour, two otherwise identical FEA simulations with a 0.1Hz control winding current were performed, except that a phase shift of 30° electrical was applied to the control winding current in the second simulation. Over the duration of the simulations (0.02s) the rotation of the axis of the field produced by the control winding is negligible (~0.72°) and so the 30° acts to simply shift the spatial axis of the control winding field. The resulting power winding output voltage waveforms and the resulting FFTs for these two cases are shown in Figure 6.58, Figure 6.59, Figure 6.60 and Figure 6.62.

When comparing Figure 6.58 and Figure 6.60 it is apparent that adding a phase offset to the near static control winding current changes the asymmetry between the three power winding voltages as summarised in Table 6.11. This behaviour is consistent with the notion of spatial asymmetry. This behaviour is most apparent with this near static case, but would also be a factor with a low frequency correction, i.e. a few Hz. It should be noted that this 2<sup>nd</sup> harmonic phenomena also occurs in FE results at zero frequency as well as with a 0.1 Hz control winding current as can be seen in the power winding voltage plot of Figure 6.62 and the corresponding FFT of Figure 6.63.

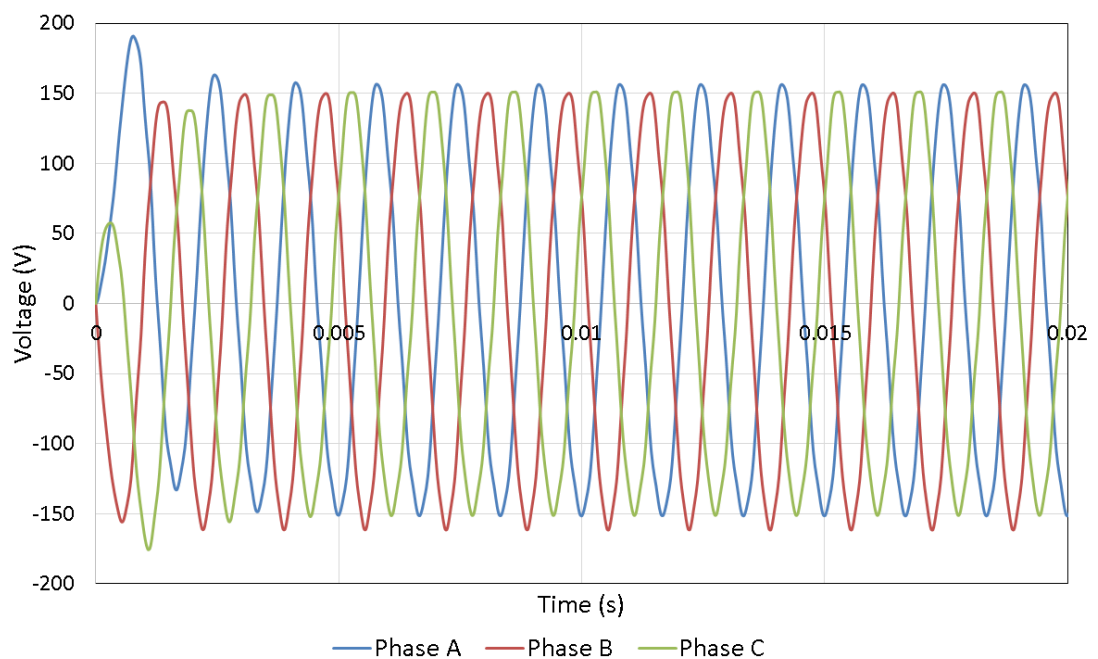


Figure 6.58 – FE calculated 3-phase power winding load voltages with a control winding frequency of 0.1 Hz, control winding current density of  $14.14A_{rms}mm^{-2}$ , a  $3.7\Omega$  load and a rotor speed of 4,800 rpm ( $0^\circ$  phase case)

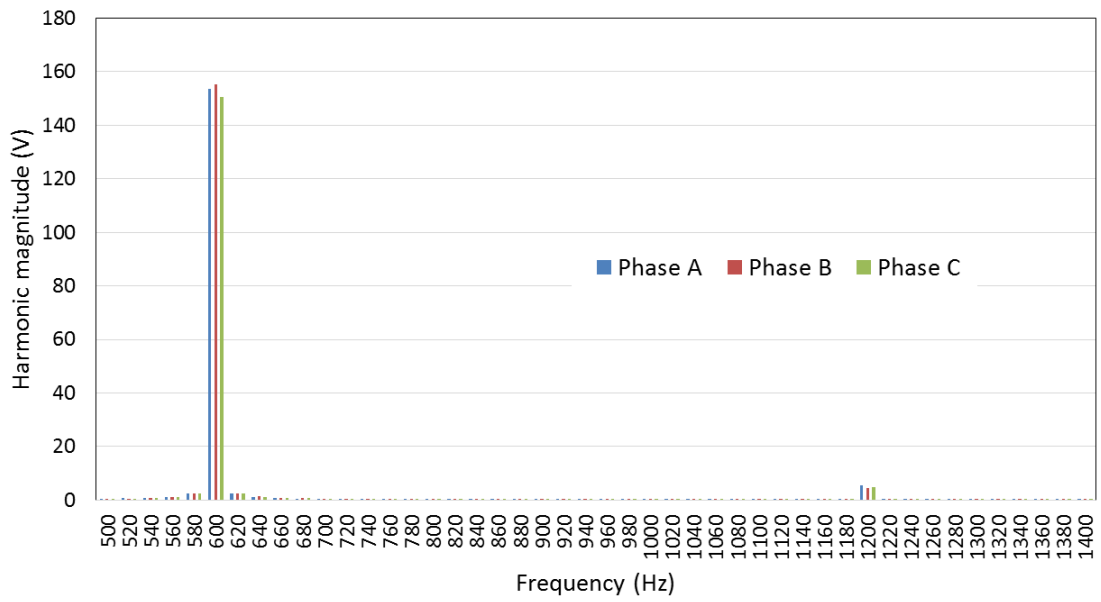


Figure 6.59 – FFT of FE calculated 3-phase power winding load voltages (Figure 6.58) with a control winding frequency of 0.1 Hz, control winding current density of  $14.14A_{rms}mm^{-2}$ , a  $3.7\Omega$  load and a rotor speed of 4,800 rpm

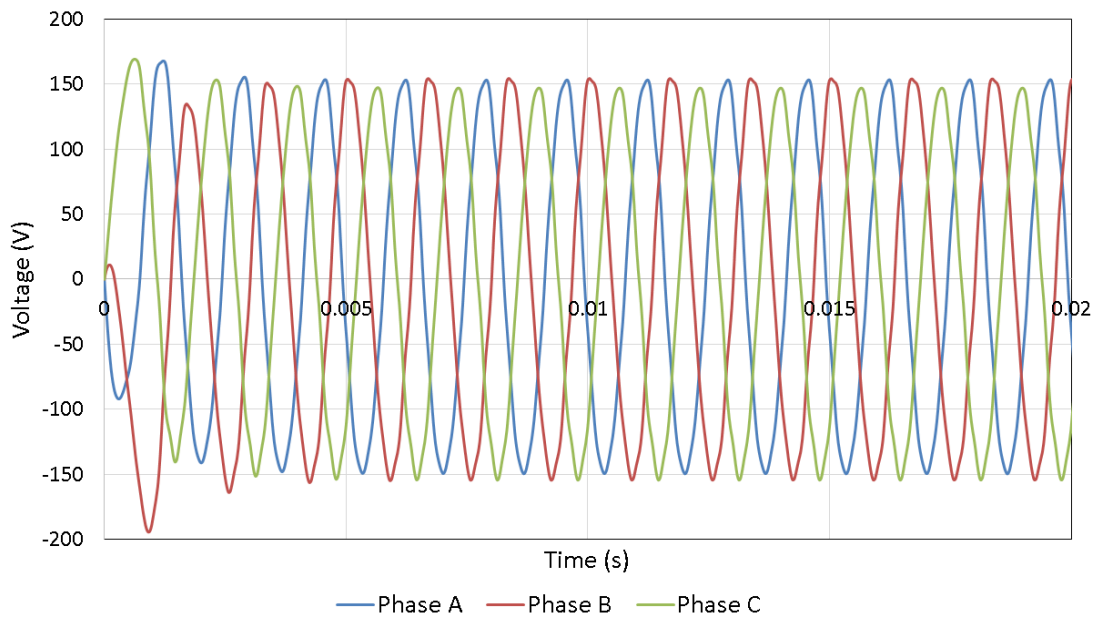


Figure 6.60 – FE calculated 3-phase power winding load voltages with a control winding frequency of 0.1 Hz, control winding current density of  $14.14A_{rms}mm^{-2}$ , a  $3.7\Omega$  load and a rotor speed of 4,800 rpm with a control winding current offset of  $30^\circ$  electrical

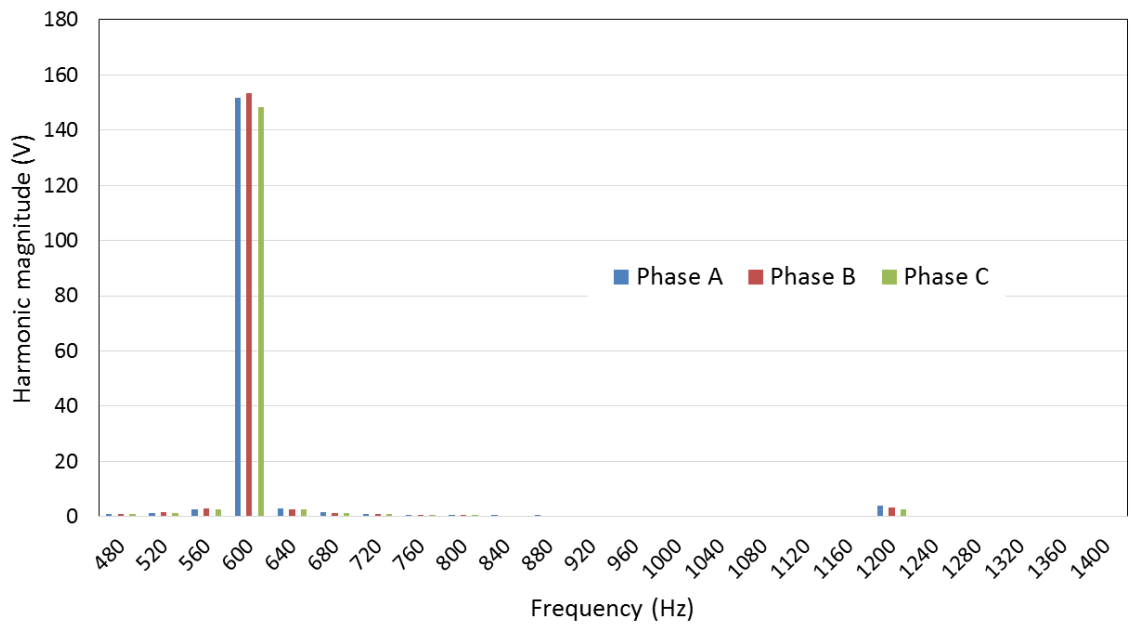


Figure 6.61 – FFT of FE calculated 3-phase power winding load voltages (Figure 6.60) with a control winding frequency of 0.1 Hz, control winding current density of  $14.14A_{rms}mm^{-2}$ , a  $3.7\Omega$  load and a rotor speed of 4,800 rpm with a control winding current offset of  $30^\circ$  electrical

Table 6.11 – FE calculated 3-phase power winding 2<sup>nd</sup> harmonic magnitudes for the FFTs in Figure 6.59 and Figure 6.61 with a control winding current offset of 0 and  $30^\circ$  electrical

2 <sup>nd</sup> harmonic magnitude (V)	0° Control current offset	30° Control current offset
Phase A	5.58	3.93
Phase B	4.39	3.14
Phase C	4.66	2.58

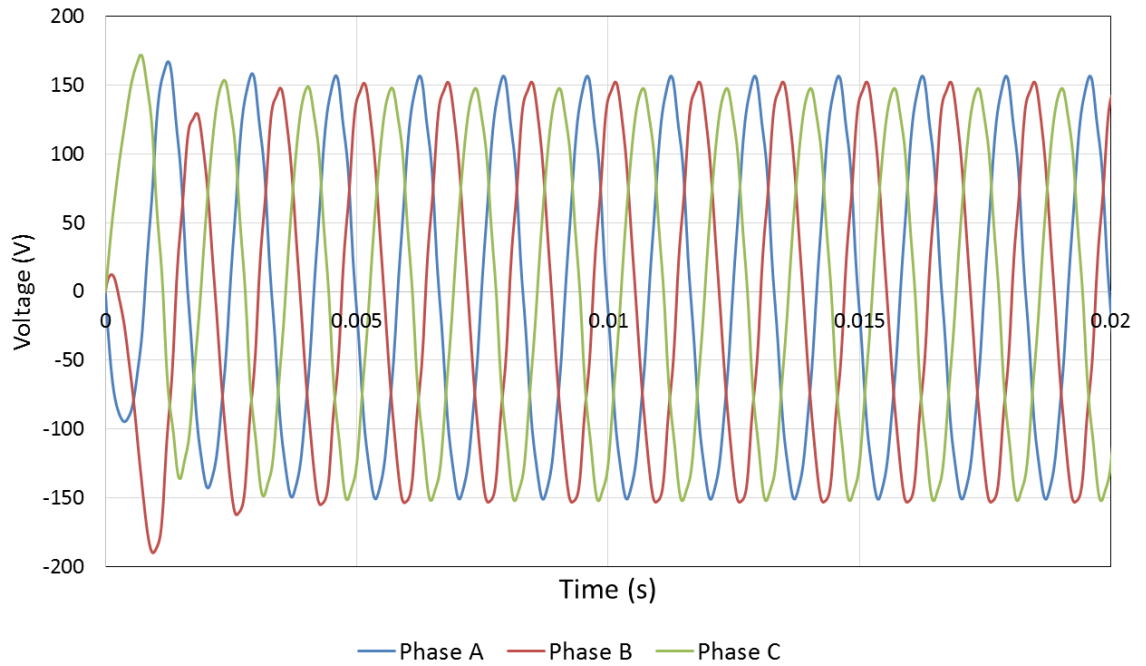


Figure 6.62 – FE calculated 3-phase power winding load voltages with a DC control winding of nominal current density of  $14.14A_{rms}mm^{-2}$ , a  $3.7\Omega$  load and a rotor speed of 4,800 rpm

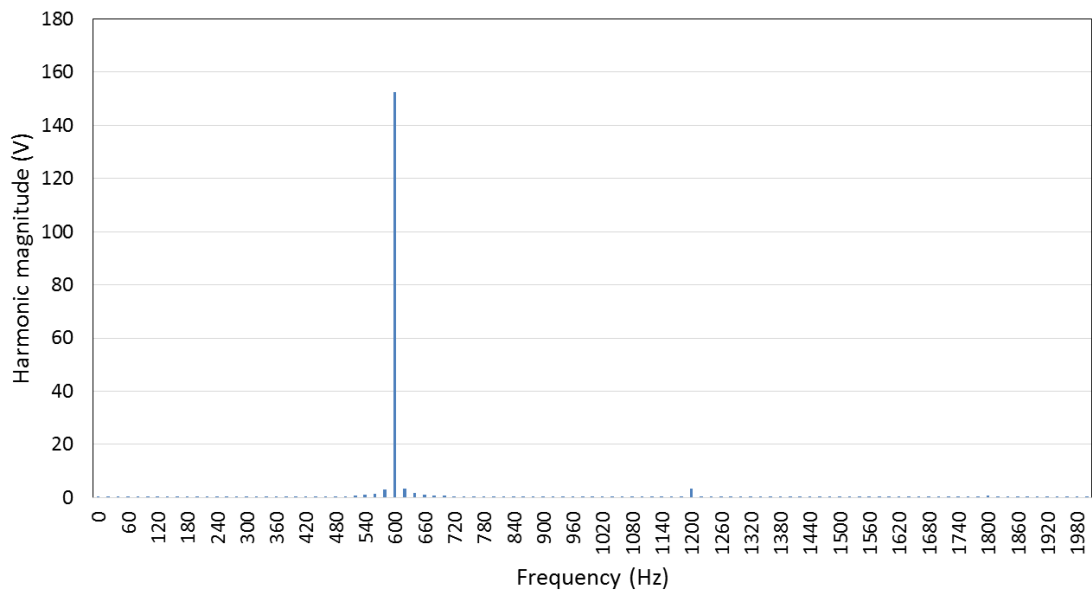


Figure 6.63 – FFT of FE calculated phase A power winding load voltages with a DC control winding of nominal current density of  $14.14A_{rms}mm^{-2}$ , a  $3.7\Omega$  load and a rotor speed of 4,800 rpm



## 6.8 OPERATION AT A VF STANDARD OPERATING POINT

According to VF standards, the magnitude of variable frequency AC voltage on an aircraft grid must lie between 108 and 118  $V_{rms}$ . To find an operating point which satisfies this specification with the particular winding design implemented, a load point 10% below the synchronous speed range was selected (4,860rpm), then a load resistance of  $10.1\Omega$  was selected to obtain a load voltage of  $115.89V_{rms}$  (the actual load seen by the machine in practice including interconnects etc. is  $10.23\Omega$ ).

The measured phase A load voltage at this operating point is shown in Figure 6.64. As in previous cases, the subharmonic which is clearly evident can be attributed to the saturation induced 3<sup>rd</sup> harmonic from the control winding flux.

The harmonic content of phase A of the power winding voltage at this operating point is shown in the FFT of Figure 6.65, onto which has been superimposed the VF standard limit for harmonics. The subharmonic is clearly evident at 108Hz, the fundamental at 360Hz and higher frequency components which are the result of the modulation process and slotting.

As will be apparent, in common with the earlier test points studied in this chapter, the subharmonic is appreciably higher than the allowable VF limit. Setting aside the fundamental at 360Hz, three of the harmonics are higher in magnitude than the limits allow. This is due to both the presence of a subharmonic as well as the penalty paid by operating at the lower end of the frequency range where the harmonic standard is much more stringent than the higher frequency end.

In terms of 3-phase output power at this operating point 3.83kW was measured across the load resistors. Although not in its self a very high figure in comparison with other measured test points (5.9kW in Section 6.4.1), with only  $6A_{rms}mm^{-2}$  flowing through the control windings, this test point provides a useful operating point for the demonstrator machine in terms of continuous operation with the limited cooling provision incorporated into the demonstrator.

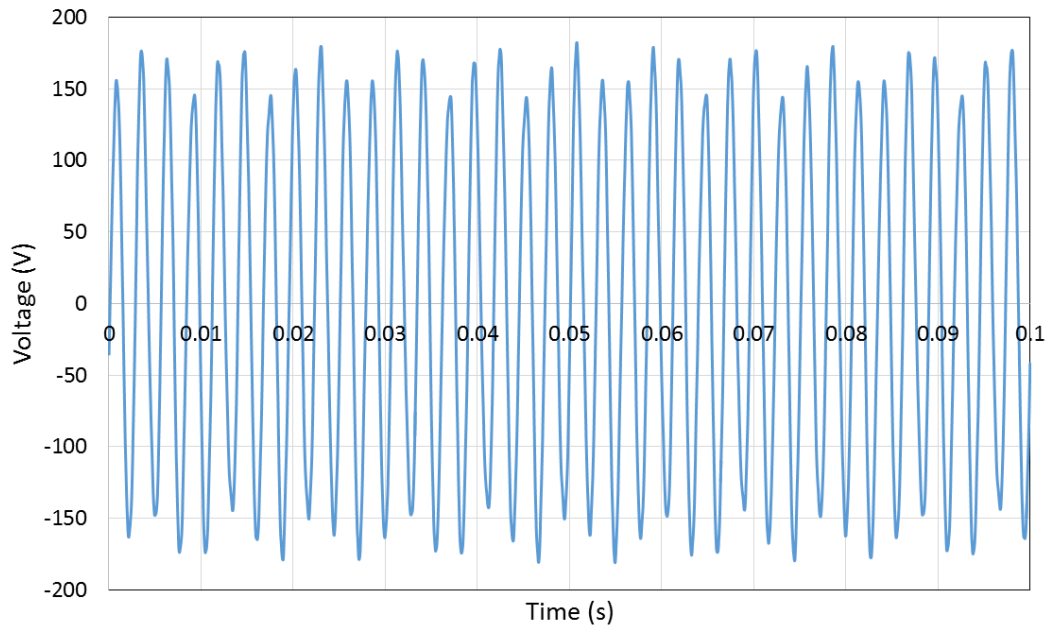


Figure 6.64 – Measured phase A load voltage for a test case at 10% below the VF range (4,860rpm) with a control winding current density of  $6.3A_{rms}mm^{-2}$  and a load resistance of 4.76Ω, 4.75Ω and 4.79Ω for phase A, B, C respectively

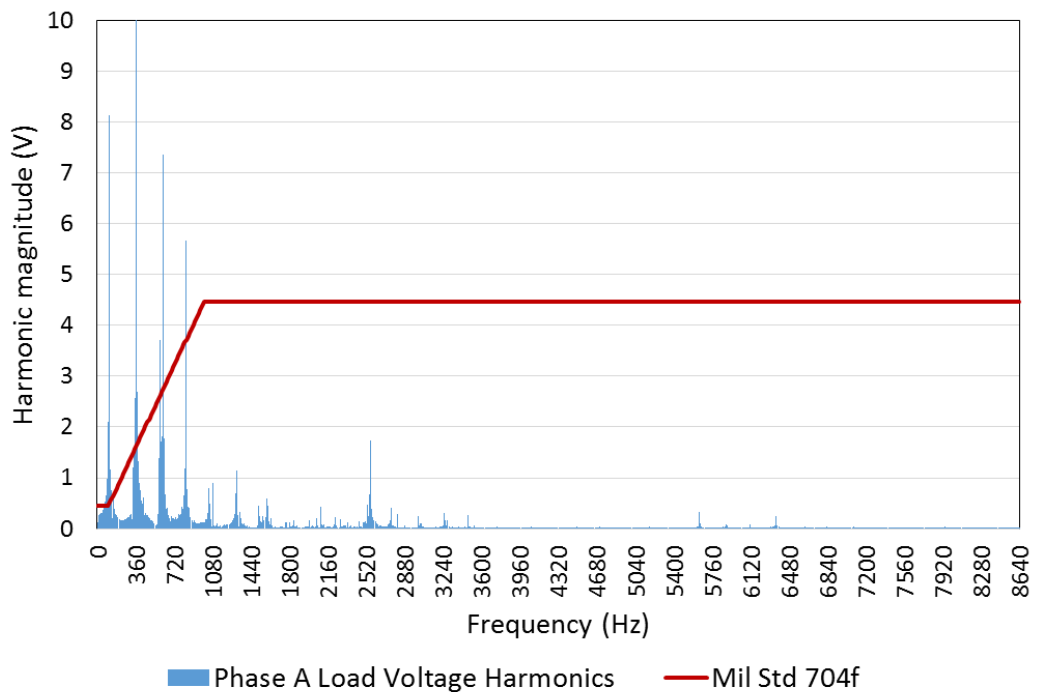


Figure 6.65 – FFT of measured phase A load voltage (Figure 6.64) for a test case at 10% below the VF range (4,860rpm) with a control winding current density of  $6.3A_{rms}mm^{-2}$  and a load resistance of 4.76Ω, 4.75Ω and 4.79Ω for phase A, B, C respectively with the VF harmonic limit

### 6.8.1 THERMAL CHARACTERISTICS OF EXAMPLE OPERATING POINT

As discussed previously, the demonstrator machine was only equipped with limited cooling capability. Some forced airflow through the stator cavity is possible via an external fan and apertures in the end-caps. This would not be sufficient for continuous operating with current densities of the order of  $15A_{\text{rms}}\text{mm}^{-2}$ , where flood-cooling or at least liquid jacket cooling would be required. Providing an appropriate converter was employed, these higher operating points could be tested on a transient basis.

Although the demonstrator machine may not be fully representative of a machine operating at the highest levels of current density, it is still important to have a broad understanding of the thermal capabilities of the demonstrator machine. To this end, thermal measurements were performed at several points within the machine over a representative cycle starting from an ambient steady state, through a converter activation phase to thermal steady state and then returning to ambient steady state again.

The cooling method used in this set of measurement was forced air produced via a single phase centrifugal fan, mounted on the test bed in front of the BDFRM as shown in Figure 6.66.

A summary of the operating conditions during the converter activation phase is shown in Table 6.12

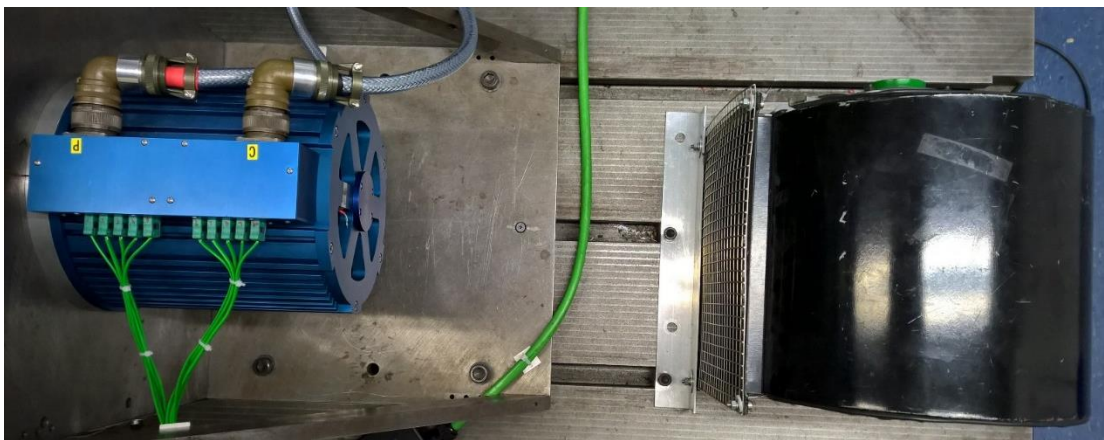


Figure 6.66 – Arrangement of the cooling fan and machine

Table 6.12 – Operating conditions used for the thermal test of the BDFRM demonstrator

Parameter	Value
Speed (rpm)	4,860
Frequency correction (Hz)	36
Load resistance ( $\Omega$ )	10.1
Current density in control winding ( $A_{rms}mm^{-2}$ )	5.93
Estimated 3-phase copper loss in control winding at steady-state temperature of 54°C (W)	282.35
Current density in power winding ( $A_{rms}mm^{-2}$ )	6.32
Estimated 3-phase copper loss in power winding at steady-state temperature of 49°C (W)	137.83

The measurements of temperature for each winding were obtained by capturing and averaging 2,000 samples over two seconds and recording this value in a text document along with the time, voltage measurements and additional user-inputted data. The locations of each of the thermocouples are detailed in Section 6.2.2 with the winding slot positions detailed in Table 6.1.

Figure 6.67 shows the temperature in each winding throughout the specified operating cycle. As would be expected, the temperature in the control windings is higher than that in the power winding, due to the higher winding resistance ( $\sim 780m\Omega$  rather than  $\sim 340m\Omega$  in the power winding). Also added to Figure 6.67 is the ambient temperature to show that the windings had in fact reached thermal steady state, relative to the ambient temperature.

Figure 6.67 can facilitate the calculation of the thermal time constant of the control and power windings by finding the time taken for the machine temperature to reach  $1 - \frac{1}{e}$  ( $\approx 63.2\%$ ) of its final steady state value. Taking the control winding thermal data of a 26°C starting point and a 55°C steady thermal state the thermal time constant is found to be 5.97 minutes. This long time constant suggests that an element of short-term over rating should be possible at this particular operating point without risking thermal damage to the machine. Due to the power winding having the same thermal mass and comparable heat sinking behaviour to the core and casing as the control

winding, it can be reasonably assumed that the thermal time constants of the two windings would be broadly similar.

Considering the temperature rise in the control winding at a known current density, the maximum allowable control winding current density can be found, whilst remaining below the 240°C limit in the Polyimide coated windings [4]. To find this maximum current density, the change in control winding temperature under this fixed  $5.93A_{rms}mm^{-2}$  must be calculated. For this operating point the change in control winding temperature between rest and thermal steady state is 29°C. The change in temperature from rest to thermal steady state considering a 240°C winding temperature limit is 7.38 times greater than the change in temperature found in Figure 6.67. Next, the resistivity of the copper must be calculated at both the winding initial temperature of 26°C and the steady state control winding temperature of 55°C using equation (6.1).

$$\rho = \rho_{20}(1 + \alpha_{cu}\Delta T) \quad (6.1)$$

The resistivity at 26°C and 55°C are calculated as  $1.77e^{-8}\Omega m$  and  $1.96e^{-8}\Omega m$  respectively.

These values may then be inserted in to equation (6.2) to calculate the maximum control winding current density, which may be used with the forced air cooling method used in this thesis. In this case the maximum sustainable current density is estimated to be  $15.28A_{rms}mm^{-2}$ , which leads to the conclusion that forced air cooling would be sufficient to operate this machine at high current densities at the expense of a reduction in the lifetime of the enamel coating of the windings. It should be noted that these calculations presume that the dominant losses are due to copper losses rather than core losses.

$$7.38 \times J_{Meas}^2 \rho_{Meas} = J_{Max}^2 \rho_{Max} \quad (6.2)$$

$$J_{Max}^2 = \frac{7.38 \times J_{Meas}^2 \rho_{Meas}}{\rho_{Max}}$$

This process could be repeated for the power winding, however as demonstrated in Chapter 5, the combined effect of significant saturation, lack of saliency ratio and

winding reactance dictates that the maximum current density in the control winding is the limiting factor in power winding output power. Therefore, the peak temperature in the windings will be dominated by the higher current density control winding. With this in mind, future designs could review the balance between the slot areas of the two windings.

The air flow temperature into and out of the machine casing can be found in Figure 6.68 to give an indication of the amount of thermal energy absorbed by the forced air.

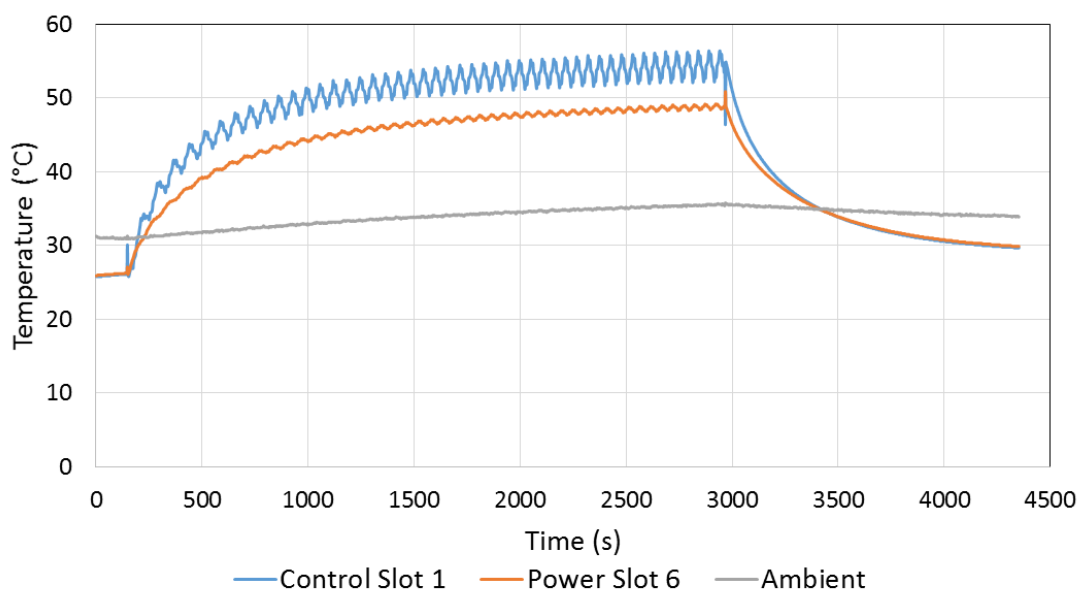


Figure 6.67 – Measured control winding and power winding slot temperatures for a cycle at 4,860rpm

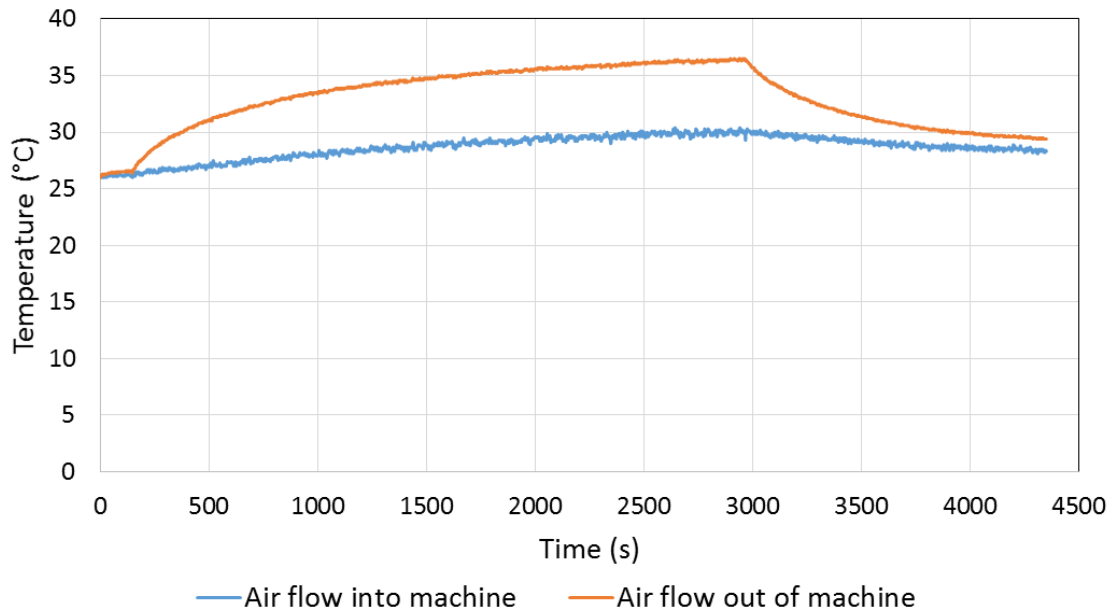


Figure 6.68 – Measured temperature of the air flowing into and out of the machine casing for a test cycle at 4,860rpm

## 6.9 SUMMARY OF CHAPTER 6

This chapter has provided detailed information on the process of building and testing the prototype BDFRM demonstrator.

The two windings both have a higher resistance than was predicted analytically, but this can be attributed to the simplification of end windings, as well as the trailing wires and interconnects of the wound machine which were not considered in the analytical model.

The testing arrangement was detailed with confirmation that the dynamometer is more than capable in terms of power and torque of operating with the demonstrator BDFRM.

Several preliminary tests were performed at a range of load resistances and correction factors to confirm the frequency correction ability of the demonstrator machine. This was then followed by a comparison of two test points, with the finite element calculated results to compare the critical power winding voltage frequency content.

A detailed power winding subharmonic study followed to view the effect of speed and correction factor on the percentage of this subharmonic to the fundamental.

The second harmonic in the power winding voltage harmonics in the synchronous cases were then studied. This was found in both the FEA and test results and is confirmed to be due to the asymmetry in the current waveforms, caused by operating the machine with DC or pseudo-DC control winding current.

An example operating point was then studied with the aim of producing a power winding voltage of between 108 and 118  $V_{rms}$ , as per the VF standards. This power winding voltage waveform was then taken to the frequency domain to define the present harmonics. It is interesting to note at this stage how much of a penalty is paid with the large low frequency harmonic content by operating at the lower end of the frequency spectrum range. Finally, the steady state thermal analysis of the BDFRM is completed to obtain relevant thermal constants.



## 6.10 REFERENCES

- [1] Emerson, "User guide: Unidrive SP Model sizes 0 to 6," 14 ed, 2013.
- [2] E. Fuchs and M. A. S. Masoum, *Power Quality in Power Systems and Electrical Machines*, 2nd ed., 2015.
- [3] J. Barros, M. Apraiz, and R. Diego, "Analysis of second order harmonic voltages in power systems," *International conference on renewable energies and power quality*, 2007.
- [4] MWS, "Magnet Wire Insulation Guide," ed, 2014.

## **7 CHAPTER 7 – CONCLUSIONS**

---

This thesis has described a series of investigations into the performance of brushless doubly fed reluctance machines, within the context of an extend speed range aerospace generator, where high power densities are necessary in order to be competitive. In contrast to the majority of research on BDFRMs reported in the literature, this thesis has focussed on the electromagnetic analysis and design rather than control methods and circuit analysis.

### **7.1 SUMMARY OF KEY FINDINGS**

The key elements of novelty in the research and the major findings are:

#### **7.1.1 SYNCREL – INFLUENCE ON PERFORMANCE OF ROTOR FLUX BRIDGE GEOMETRY**

A systematic study of rotor bridge features (Section 3.3) demonstrated the critical role of saturation, in realising acceptable levels of saliency ratio and identified that a single-piece rotor lamination with bridges spanning the flux-guides near the airgap compromises performance significantly, as compared to an electromagnetically optimal rotor with entirely open flux guides.

#### **7.1.2 SYNCREL – INFLUENCE OF DIMENSION SCALING**

A scaling study has been undertaken to establish the influence of scaling all of the linear dimensions of the SyncRel on the torque and power densities (Section 3.5). It was shown that whereas power density increased for larger machines, benefits do tail off at higher scaling factors. It was also noted that the aspect ratio plays a role in determining the extent to which end winding mass influences the power density.

#### **7.1.3 BDFRM – BEHAVIOUR ON A NON-STIFF AC NETWORK**

All published literature on BDFRM performance have considered the case of the power windings being connected to a voltage-stiff AC network, which is a reasonable approximation for a utility grid. However, as discussed in detail in Chapter 1, an aircraft grid is not voltage stiff. It has been demonstrated both through simulation and experiment, that large quantities of reactive power are required in the control

winding current even at modest frequency correction factors when operating on such a network, even with a unity power factor load.

#### 7.1.4 BDFRM – DEMONSTRATION OF LIMITED POWER CAPABILITY

Although the basic functionality of frequency correction has been demonstrated both through simulation and by experiment, the overall machine power density of the BDFRM has been shown to be modest (max. of 0.41kW/kg achieved for the frame size considered in this thesis). It has also been demonstrated, that unlike some competing machine types, this limited power density cannot be overcome by increasing the current density in the windings to higher values, due to the very dramatic effects of magnetic saturation. Even in the case of the optimised design in Chapter 5, increased output power was achieved at a very diminishing rate for control winding RMS current densities beyond 5A/mm<sup>2</sup> or so.

#### 7.1.5 BDFRM – PRESENCE OF SIGNIFICANT SECOND HARMONIC WHEN OPERATED IN SYNCHRONOUS MODE

It has been shown through simulation (Section 5.9.3) and experiment (Section 6.7), when the BDFRM is run in a synchronous mode, i.e. with a DC or pseudo-DC control winding current, a significant second harmonic is present in the power winding voltage due to the instantaneous asymmetry in the field produced by the control winding.

#### 7.1.6 BDFRM – SATURATION INDUCED SUB-HARMONICS

Although the presence of saturation induced subharmonic in the power winding voltage has been noted in several publications, this phenomenon has been explored quantitatively in much more detail in this thesis and has been observed and characterised experimentally. Moreover, test results have demonstrated that this subharmonic increases with increasing degrees of frequency correction and with increasing rotor speed.

### 7.1.7 BDFRM – INCORPORATION OF PERMANENT MAGNETS IN SYNCREL AND BDFRM ROTORS

It has been demonstrated through simulation (Sections 3.6 and 5.12.2) that incorporating small quantities of PM in to the rotor of both a synchronous reluctance machine and a BDFRM in order to introduce pre-saturation can lead to appreciable improvements in power density, average torque and torque ripple. For the electromagnetically optimised rotor design, a mere 139g of PMs were used (corresponding to less than 1% of the machine active mass), yet the average torque was increased by 10% and the corresponding torque ripple was reduced by 10%. For the more mechanically robust rotor, which included a series of structural ribs, an increase of average torque of up to 55% is possible at the lower end of the current density range. A corresponding reduction in torque ripple of 39% at this operating point confirms the advantage of adding PMs to the rotor structure.

### 7.1.8 COMPARISON OF BDFRM POWER DENSITY WITH SYNCREL MACHINES

Design studies undertaken for a reference frame size have shown that BDFRMs are only capable of producing a modest fraction of the power capability of an equivalent SyncRel, e.g. ~32% in a comparison between the BDFRM design of Section 5.10 and the SyncRel design of Section 3.5.

### 7.1.9 COMPARISON OF A CONVENTIONAL SINGLY-SALIENT BDFRM WITH A DOUBLY-SALIENT VARIANT

Doubly-salient variants of the BDFRM were compared with a more conventional singly-salient variant in Section 4.7. Although the doubly-salient design was not optimised and some small further increments in performance might be derived, the poor utilisation of the airgap periphery led to a power density and a reference operating point which was 56% lower than its singly-salient counterpart.

### 7.1.10 BDFRM – SCALING EFFECTS

The effect of scaling a BDFRM design was studied systematically in Section 4.5 for both 2/4/6 and 4/6/8 pole combinations. Compared to the same investigation

performed for a SyncRel, the power and torque densities tend to reach a peak at a lower scaling factor with the BDFRM. Furthermore, although the 2/4/6 and 4/6/8 combinations yield comparable torque densities, the ability to drive the 2/4/6 at a much higher speed while remaining within the VF range, yields a considerably higher power density throughout the scaling range.

#### 7.1.11 BDFRM – OPTIMISATION OF THE NUMBER OF FLUX GUIDES

During the optimisation of a BDFRM equipped with an AFB rotor, it was noted that the key features which impacted on torque density are the number and thickness of rotor flux guides. Published literature suggests benefits in using five or more flux guides in BDFRMs, but the findings in Section 5.4.4 for the optimised BDFRM suggest that there were no electromagnetic benefits in designing a BDFRM with more than three flux guides.

#### 7.1.12 BDFRM – MECHANICAL OPTIMISATION OF THE ROTOR

Published literature indicated that an AFB rotor needs to include additional internal structural elements to operate at high speeds. The mechanical rotor optimisation reported in Section 5.6 demonstrated that an electromagnetically optimised design would not be capable of operating beyond ~5,000rpm. This led to a final rotor design which could operate across the whole speed range up to 14,400rpm but with a significant reduction of up to 34% in the output power.

#### 7.1.13 BDFRM – LOSS AUDIT

As would be expected, the losses in the optimised BDFRM design, computed at a range of test points, are dominated by the copper losses due to the length of the distributed coils in each winding. This led to a very modest efficiency of ~80% in this particular design.

#### 7.1.14 INFLUENCE OF ROTOR SKEWING

The rotor was skewed by one stator slot pitch in order to reduce the high frequency slotting harmonics in an attempt to satisfy the harmonic standards for aerospace. At most simulated operating points, a skewed rotor successfully reduced the high

frequency slotting harmonics sufficiently to satisfy the VF aerospace standard. The harmonic limits become more stringent at lower harmonics, therefore the subharmonic present in the power winding voltage fails to fall below these standards at all test points.

## **7.2 KEY OVERALL CONCLUSION**

This thesis has explored, through extensive FE simulation and testing of a prototype, the design and performance of a BDFRM. Although this type of machine offers potentially attractive functionality for a wide speed range generator, it suffers from many performance limitations, which become particularly pronounced at high electric loading. Hence, its drawbacks in terms of modest power density (maximum of 0.41kW/kg) and poor efficiency (80% - which has significant implications for the cooling system), and control winding converter rating result in it not being remotely competitive in an aerospace generator application with, for example, a PM generator with a fully-rated back to back converter.

## **7.3 PROPOSALS FOR FURTHER RESEARCH**

The research described in this thesis has studied several aspects of the electromagnetic performance of BDFRMs, and arrived at an overall conclusion that the power density and power quality achieved for this type of machine is unlikely to be competitive for the most demanding aerospace applications. Saturation of the stator and rotor cores, and the high winding loss densities being the two major factors that limit performance.

There are, however, several aspects of their performance that would benefit from additional investigations:

**Use of PMs in the demonstrator machine** – It has been proven, through FE analysis, that improvements in power and torque density, as well as torque ripple, can be achieved by the addition of PMs to the rotor supports to assist pre-saturation of the rotor bridges. It would be interesting to use the demonstrator with a modified PM rotor to experimentally assess the performance of this option.

**Further experimental measurements with a bespoke and optimised power converter** – The main emphasis in the research reported in this thesis was electromagnetic design and analysis and hence a standard high-performance commercial 3-phase inverter was employed in testing. However, the limited scope to tune the converter control loops and some internal protection features precluded the full range of testing, and in many cases resulted in some compromise in the level of control winding excitation that could be employed. The development of a bespoke converter, which is better suited to regulating a precise current in the control winding, would allow a more comprehensive series of tests to be performed. The converter could also be sufficiently monitored to accurately measure the converter losses.

**Exploitation of the variable frequency nature of the network to enhance power density** – All the studies undertaken in this thesis have been concerned with steady-state operating points. However, the VF standard allows the output frequency to transiently vary at a rate up to 250Hz/s. Hence, there is scope to rapidly vary the control frequency to more effectively manage the effective field alignment in the machine with the potential to increase torque, e.g. by sweeping the frequency over some specified range. This would be an entirely novel approach to controlling BDFRMs, exploiting a degree of control freedom which is not available in conventional grid connected machines.

## 8 APPENDICES

### 8.1 APPENDIX 1 – FINITE ELEMENT ANALYSIS

Throughout this PhD finite element analysis has been a key enabler in discovering the potential for BDFRMs to operate on non-stiff AC grids. The software used for these studies is Cedrat Flux2D version 12, along with a Flux Skewed add-on for calculating the effect of skewing of the rotor.

Static solvers are used to calculate initial torque, but the predominant FEA method used throughout this thesis are transient circuit-coupled solvers. The circuit contains resistors to represent winding resistance and, towards the end of thesis, phase inductors to represent the end-winding inductances. Figure 8.1 provides an example of this FE-coupled circuit. The top three-phase circuit represents the current source fed control winding and the bottom circuit represents the three-phase power winding.

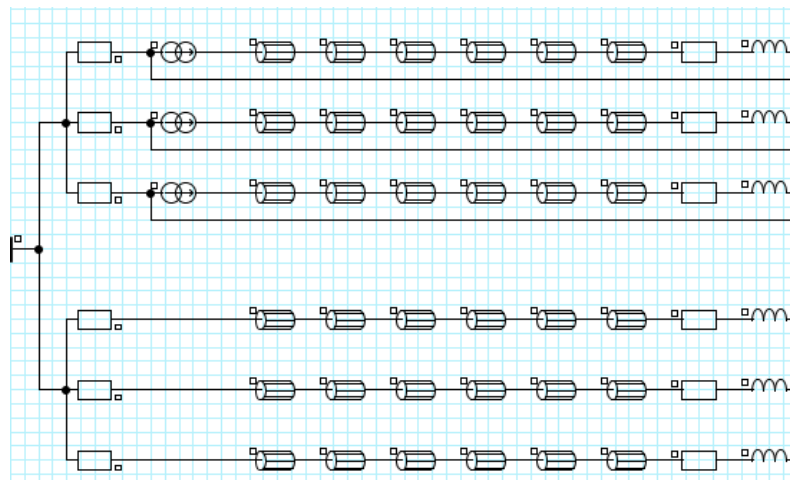


Figure 8.1 – Coupled circuit design used for the BDFRM

The meshing used in the FEA is predominantly the in-built aided mesh of Flux2D, but for areas of particular interest, or high flux density, it is important to use a finer mesh. This ensures that an accurate picture of the flow of flux in the airgap and rotor flux guides is achieved. Figure 8.2 and Figure 8.3 provide an overall and close-up view of the meshing used throughout this thesis.



At a diameter of 150% of the stator outer diameter, a boundary condition is applied of zero flux. This ensures that any fringing fields that are present outside of the stator laminations are still considered therefore improving the accuracy of the model.

The non-linear solver uses a Newton-Raphson algorithm with an accuracy threshold of  $1 \times 10^{-4}$ . The torque is calculated by differentiating the system energy with respect to an angular displacement. The power is calculated post-process in a spreadsheet by finding the average  $V \cdot I$  over a cycle or  $V_{rms} \cdot I_{rms}$  for the real and apparent power respectively. The copper losses are calculated by multiplying the  $V_{rms}$  by the  $I_{rms}$  over one cycle across a resistor representing the winding resistance.

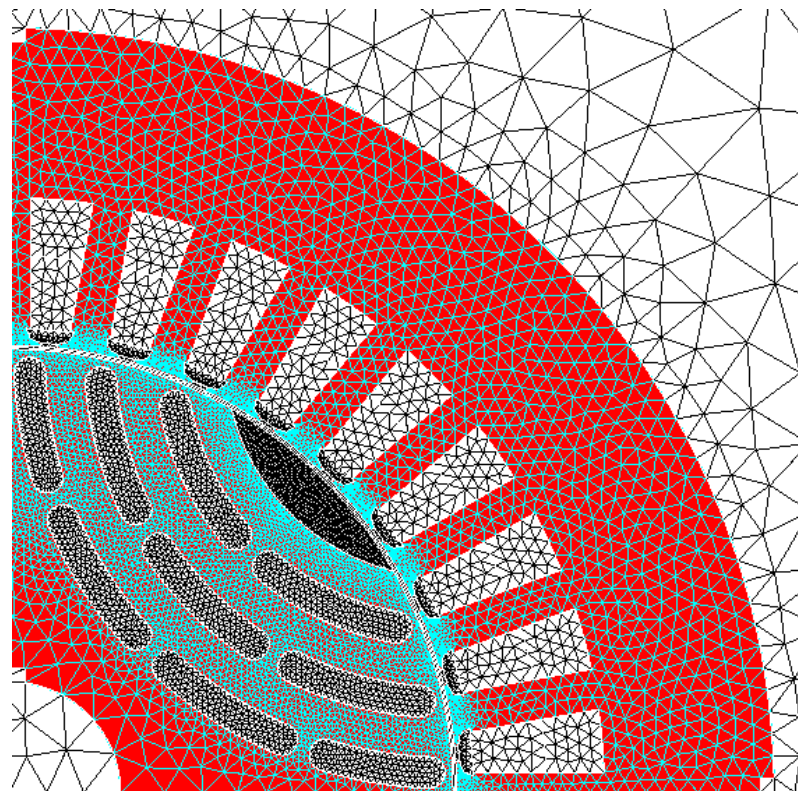


Figure 8.2 – Mesh used in the FEA simulations

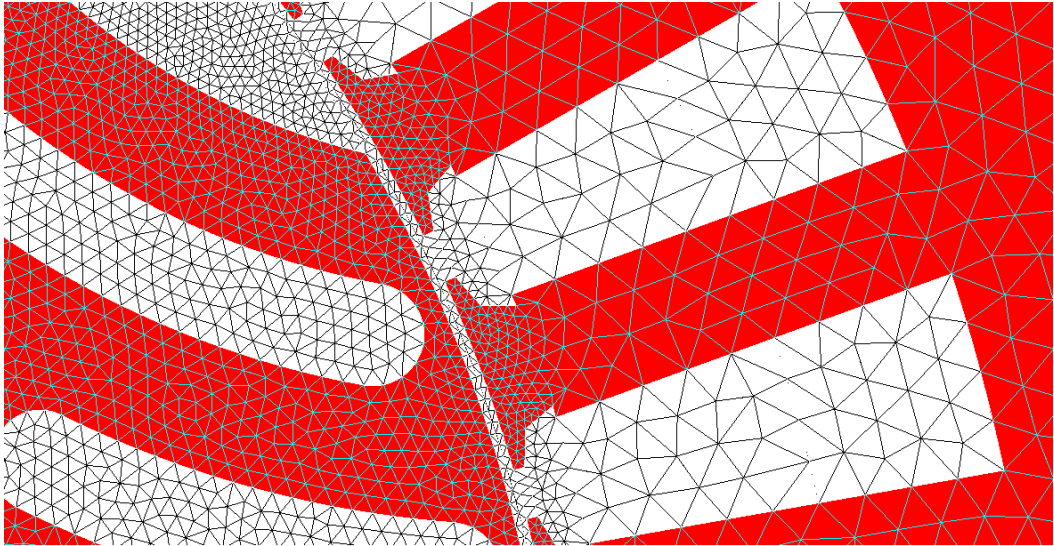


Figure 8.3 – Close up of the airgap and tooth-tip mesh used in the FEA simulations as highlighted in Figure 8.2

## 8.2 APPENDIX 2 – FOURIER TRANSFORM

Extensive use is made in this thesis of analysis in the frequency domain (both temporal and spatial) as it provides a useful insight into machine behaviour, e.g. in dealing with complex airgap harmonics and in assessing compliance with voltage harmonics standards.

The MATLAB FFT (Fast Fourier Transform) function will be used throughout this thesis due to both its proven accuracy and relatively low computational overheads.

However, whereas such a FFT is well suited to the analysis presented in this thesis, it is important to recognise that artefacts in the waveform and/or limitations in the transform can generate potentially misleading outcomes.

Firstly, only discrete frequency steps can be specified. If a particular frequency of interest exists in the interval between two adjacent frequency steps, surrounding lobes would be formed. To overcome this shortcoming, it is common practice amongst some authors to present FFT spectra such that they only contain the frequencies of interest, i.e. the data is in effect 'cleaned-up' to omit side-lobes, which in many respects aids the clarity of the spectrum. However, when quantifying total harmonic distortion these lobes also add to this distortion thereby leading to an inaccurate measure of harmonic content. Therefore, it is of paramount importance to ensure that the sample period contains an exact multiple of the fundamental frequency.

One option to reduce these lobes is to use an alternative window function to the standard rectangular shape in the time domain before progressing to the frequency domain. These window functions come in many shapes, which give rise to various advantages in decreasing the lobes. One major downside of these advanced window functions is the decrease in resolution due to the increased bandwidth required to widen the major lobe [1]. This may lead to adjacent harmonics merging and therefore a loss of frequency domain data. In addition, the fundamental magnitude of each waveform is also decreased when advanced windowing functions are used. This is a major drawback for later in the thesis when accurate readings of harmonic magnitudes are required to study the harmonic effects of skewing the rotor. For

these reasons, only a standard rectangular window will be used as a time domain sample window.

It is also important to ensure a sufficiently long data sample is used to cover the Nyquist limit of the highest expected frequencies.

### References

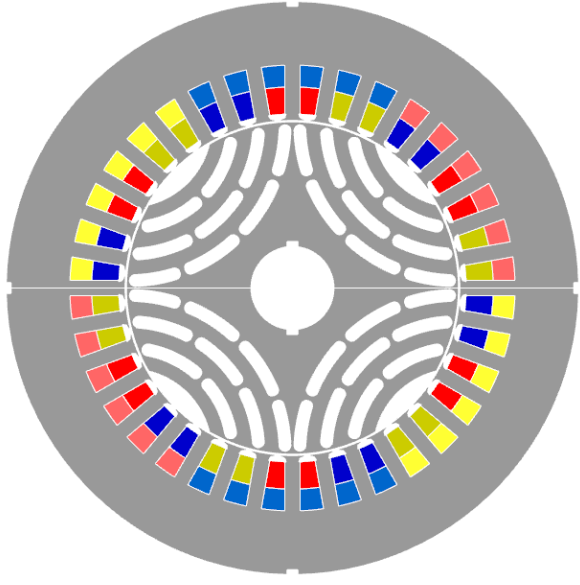
- [1] R. W. Ramirez, *The FFT - Fundamentals and Concepts* vol. 1. USA: Prentice-Hall, 1985.

### 8.3 APPENDIX 3 – DESIGN SPECIFICATION

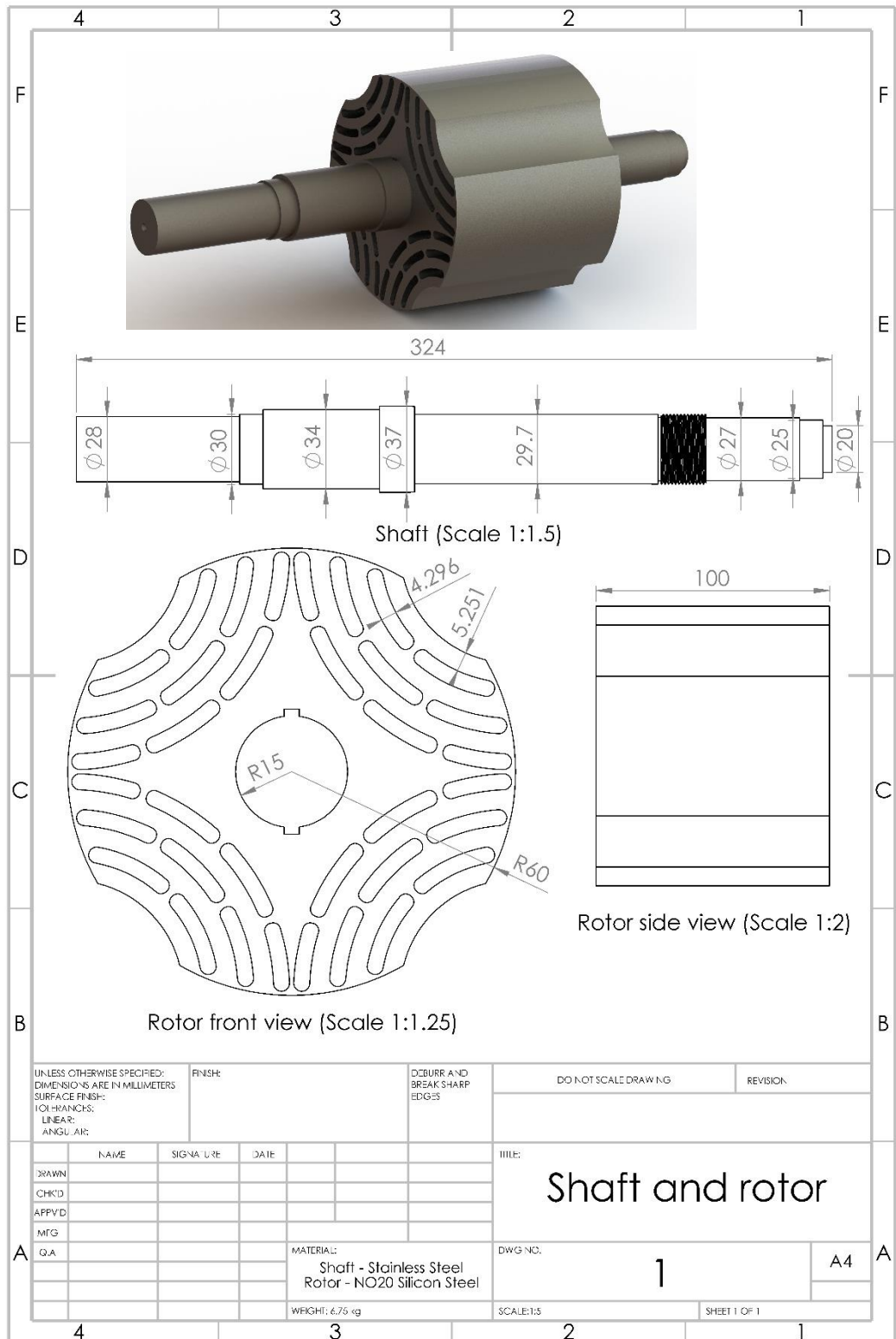
The demonstrator BDFRM must adhere to the following specifications:

- An output frequency of between 360 and 800 Hz to abide to Mil-Std-704f
- The control, rotor and power poles will be 2, 4 and 6 respectively
- The BDFRM should be able to correct frequencies at up to 20% above and below the synchronous speed range
  - This leads to a speed range of 4,320rpm to 14,400rpm
  - The rotor must be structurally sound at the top of this speed range
- The output voltage must be directly connected to the aircraft grid therefore should follow strict Mil-Std-704f standards for harmonic content.
- The output voltage magnitude should be controlled to be between 108 and 118  $V_{rms}$  as per Mil-Std-704F
- Silicon Iron will be used for both the rotor and stator laminations
- A packing factor of 0.45 will be used to provide a realistic value for in-situ winding
- The machine must be of a power, torque and size so as to be compatible with the available AVL dynamometer
- The machine will be forced air cooled, so current density should be limited accordingly
  - But a thermal steady state does not have to be reached so high current short tests may be accommodated
- The machine must be sufficiently instrumented to monitor temperature in various locations in the windings and in the rest of the static structure
- The star point of each winding should be accessible to accommodate measurement of phase voltages

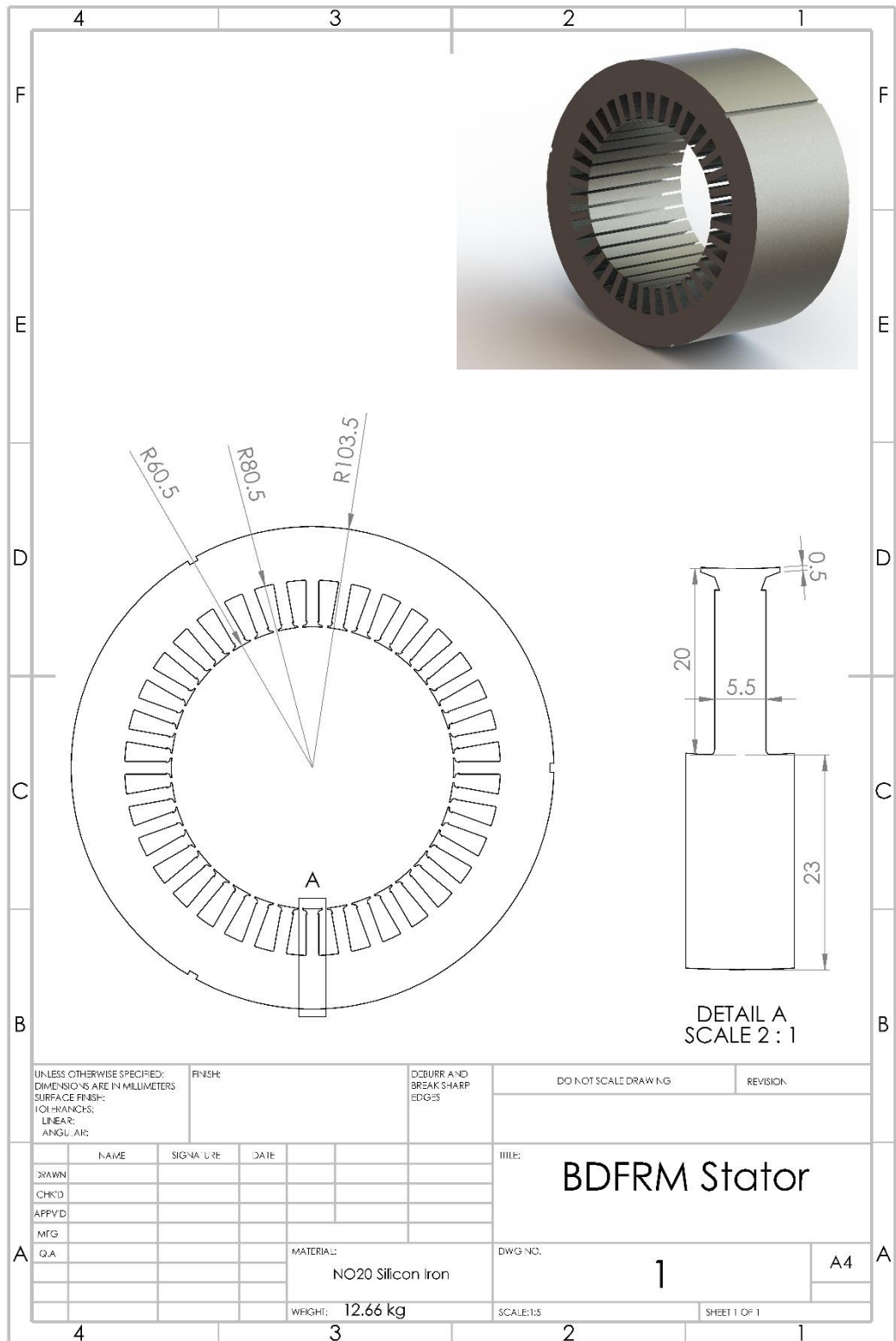
## 8.4 APPENDIX 4 – FINAL DESIGN PARAMETERS

<b>Rotor dimensions</b>			
Parameter	Value (mm)		
Shaft diameter	30		
Outer diameter	120		
Barrier thickness	4.29		
Guide thickness	5.25		
Airgap length	0.5		
Number of flux guides	3		
<b>Stator dimensions</b>			
Parameter	Value (mm)	Stator material	NO20 Silicon Iron
Inner diameter	121	Rotor material	NO20 Silicon Iron
Outer diameter	207		
Total tooth height	20	Axial length	100 mm
Tooth body width	5.5	Proportions of slot occupied by winding (power:control)	1:1
Tooth tip height	0.5		
Tooth shoulder height	0.5	Control poles	2
Back iron thickness	23	Power poles	6
Number of teeth	36		
Tooth tip to slot pitch ratio	0.8		

## 8.5 APPENDIX 5 – BDFRM ROTOR AND SHAFT TECHNICAL DRAWING



## 8.6 APPENDIX 6 – BDFRM STATOR TECHNICAL DRAWING





## 8.7 APPENDIX 7 – BDFRM CASING TECHNICAL DRAWING

